This electronic thesis or dissertation has been downloaded from Explore Bristol Research, http://research-information.bristol.ac.uk

Author:
Al Hooti, Khalil J M

Title:
Analysis of microseismicity during thermally-assisted gas oil gravity drainage in a heavy oil field in the Sultanate of Oman

General rights
Access to the thesis is subject to the Creative Commons Attribution - NonCommercial-No Derivatives 4.0 International Public License. A copy of this may be found at https://creativecommons.org/licenses/by-nc-nd/4.0/legalcode This license sets out your rights and the restrictions that apply to your access to the thesis so it is important you read this before proceeding.

Take down policy
Some pages of this thesis may have been removed for copyright restrictions prior to having it been deposited in Explore Bristol Research. However, if you have discovered material within the thesis that you consider to be unlawful e.g. breaches of copyright (either yours or that of a third party) or any other law, including but not limited to those relating to patent, trademark, confidentiality, data protection, obscenity, defamation, libel, then please contact collections-metadata@bristol.ac.uk and include the following information in your message:

- Your contact details
- Bibliographic details for the item, including a URL
- An outline nature of the complaint

Your claim will be investigated and, where appropriate, the item in question will be removed from public view as soon as possible.

Analysis of microseismicity during thermally-assisted gas oil gravity drainage in a heavy oil field in the Sultanate of Oman

By

Khalil Juma Al Hooti

School of Earth Science
University of Bristol

A dissertation submitted to the University of Bristol in accordance with the requirements of the degree of Doctor of Philosophy in the Faculty of Science.

April 2021

Advisor

Prof. J.-Michael Kendall & Dr. James Verdon

ABSTRACT

The objective of this thesis is to evaluate the use of microseismic monitoring to assess Thermally-Assisted Gas-Oil Gravity Drainage (TA-GOGD) in an oilfield in the Sultanate of Oman. The reservoir units are carbonate rocks of high porosity but low matrix permeability, and the field contains heavy oil. Pilot tests proved that heating the oil decreases its viscosity, increasing the recovery factor through the process of TA-GOGD, and lead to field-scale use of this Enhanced Oil Recovery (EOR) method. However, the field is shallow, and there have been growing concerns about felt seismicity and surface deformation. A microseismic monitoring program detected roughly 7200 events between April 2011 and August 2015. A processing workflow is established to analyze the data, which includes determining sensor orientation, noise filtering, automatic travel time picking, 3D velocity model building, and event location and characterization. Located events cluster around two major fault systems, oriented NW-SE and NE-SW. The induced microseismic events are related to fracture initiation around these faults, reflecting the local stress state. Events locations are concentrated in the reservoir units where the steam injection is taking place, and there is no evidence of seismicity into the overburden. This means that steam is not leaking into the shallower layers, and there is little pressure buildup in the caprock. The seismicity also reveals an active fault that was not detected in seismic reflection surveys. Moment magnitude varies from -0.18 to -3.12 with an average of -1.75. Estimated b-values for different event clusters range from 1.5-2.2, indicating swarms of fluid-induced low-magnitude events and the diffusion of fluids into fractures. Calculated d-values for each event cluster are between 1 and 2, implying that they are mostly clustering in a planner manner (fault plane), or related to steam flow. Microseismic monitoring of TA-GOGD shows the caprock and fracture network system's integrity during prolonged exposure to steam injection.

DEDICATION AND ACKNOWLEDGEMENTS

> *"Are those who have knowledge and those who have no knowledge alike? Only the men of understanding are mindful. "*
>
> — (Holy Quran, 39:9)

I praise The Mighty Allah for the endurance and patient he bestowed upon me while being away from home during my PhD studies. I ask him for help, guidance and ease of work.

I would like to express my deepest gratitude and appreciation to my supervisor Prof. Mike Kendall who was like a friend and teacher to me for the last four years. He was the source of inspiration and the driving force towards the accomplishment of my project. Without his guidance, continuous advice and suggestions, this thesis would not have been completed. I am sincerely thankful to him for the help he provided in formulating the project outline and securing the dataset through Petroleum Development of Oman (PDO). His invaluable constructive criticism, friendly advice, and rigorous discussion throughout my Ph.D. study ignited the enthusiasm to acquaint myself with the necessary skills and knowledge towards being a better geophysicist and a research scientist.

I am also grateful to Dr. James Verdon for acting as a second supervisor and allowing me to use his Matlab BUMPS software in analyzing the microseismic data. I am thankful to him for the time he spent teaching me how to use these codes and deploy them for my own use, and for answering my questions related to the software and microseismic analysis techniques in general. Besides my advisors, I would like to thank the rest of my thesis committee, Dr. James Wookey and Prof. Juliet Biggs, for their encouragement and insightful comments.

I would like to acknowledge individuals at PDO, namely Dr. Othman Al Harrasi, Saif Al Azri and Qais Al Siyabi for the assistance provided in regard to data provision and answering all my technical inquiries related to the project dataset. Dr. Othman acted as my external supervisor and was always helpful to me in reviewing results at all stages of the project and providing suggestions on how to improve.

Appreciation is due to Itasca Consulting Group, Inc. Company for granting me a licence to the Insite software, which I used extensively in picking and locating microseismic events. It was thoughtful of personnel at Itasca for all the support they provided with special thanks to Jon Haycox and Philip Usher who were always ready to reply my emails, and offer in-house software training.

The datasets are provided by PDO after obtaining release approval from the Ministry of Oil and Gas in the Sultanate of Oman. I was also privileged by the company to conduct a summer internship program in their offices, which was beneficial in understanding the scope of dataset. Therefore, I thank them for their endless support and permission to use the microseismic data. My sincere thanks to the Ministry of Higher Education at the Sultanate of Oman sponsoring my Ph.D. program and covering my tuition and maintenance fees.

I thank my fellow roommates in room G10.b for stimulating discussions on various topics of geology and geophysics and for all the entertainment in the last four years. I pay special tribute to the Bristol Geophysics Group. The bi-weekly coffee break seminars organized by the group were of a great source of knowledge to strengthen and expand my perception of various geophysical topics, particularly seismology.

Last but not least, I would like to thank all my family members for supporting me spiritually throughout my life.

AUTHOR'S DECLARATION

I declare that the work in this dissertation was carried out in accordance with the requirements of the University's Regulations and Code of Practice for Research Degree Programmes and that it has not been submitted for any other academic award. Except where indicated by specific reference in the text, the work is the candidate's own work. Work done in collaboration with, or with the assistance of, others, is indicated as such. Any views expressed in the dissertation are those of the author.

SIGNED: .... DATE: ....

TABLE OF CONTENTS

Page

List of Tables xi

List of Figures xiii

Acronyms and Symbols xix

1 Introduction 1

1.1 Project overview and objectives 1
1.2 Microseismic role in unconventional reserves 5
  1.2.1 Unconventional oil and gas resources 5
  1.2.2 Heavy oil development 7
  1.2.3 Thermally-assisted gas oil gravity drainage 8
1.3 Overview of passive seismic monitoring 9
  1.3.1 Microseismic monitoring of hydraulic fracturing 9
  1.3.2 Microseismic monitoring for risk mitigation 11
1.4 Passive seismic data methodology 12
  1.4.1 Microseismic data acquisition 13
  1.4.2 Processing microseismic events 13
  1.4.3 Interpretation of microseismic events 16
1.5 Seismicity in Oman 17
  1.5.1 Natural seismicity in Oman and the surrounding area 17
  1.5.2 Microseismic monitoring programs in Oman 18
  1.5.3 Previous studies of induced seismicity in Oman 20
1.6 Thesis structure 21

1.7 Declaration 22
1.8 Conclusion 23

2 Geology of The Field 25

2.1 Tectonic setting 25
2.2 Sedimentary facies 32
2.2.1 Nahr Umr Formation 35
2.2.2 Shuaiba Formation 37
2.2.3 Kharaib Formation 40
2.3 Petroleum system 42
2.3.1 Trap system 42
2.3.2 Seal 43
2.3.3 Source rock maturation and migration 43
2.4 Production challenges 44
2.5 In-situ stress 45
2.6 Fracture characterization from subsurface and outcrop data 48
2.6.1 Subsurface data 48
2.6.2 Outcrop data 49
2.7 Conclusion 50

3 Data Processing and Preparation 51

3.1 Microseismic equipment setup at Field X 52
3.2 Polarization analysis for geophone orientation determination 59
3.2.1 Introduction 59
3.2.2 Theoretical background 61
3.2.3 Application to Oman dataset 68
3.2.4 Conclusion 72
3.3 Waveform Filtering for Noise Reduction 84
3.3.1 Introduction 84
3.3.2 Oman dataset quality 85
3.3.3 Filters design 86
3.3.4 Filter application 93

3.4 Conclusion . . . 101

4 **Travel Time Picking and Velocity Analysis** **103**

4.1 Travel time picking . . . 103

4.1.1 Introduction . . . 103

4.1.2 P- and S-wave automatic arrival time picking . . . 105

4.1.3 Discussion on the performance of the methods . . . 110

4.2 Velcity model building . . . 119

4.2.1 Introduction . . . 119

4.2.2 Sonic log data . . . 120

4.2.3 Sonic log data smoothing and blocking . . . 121

4.2.4 S-wave velocity derivation using neural network . . . 126

4.2.5 3-dimensional velocity modeling . . . 127

4.2.6 Uncertainties in the velocity model . . . 132

4.3 Conclusion . . . 136

5 **Microseismic Location** **137**

5.1 Microseismic event location algorithms . . . 138

5.1.1 Seismic source location definition . . . 138

5.1.2 Location methods used in the Oman dataset . . . 142

5.1.3 Application to a sample dataset . . . 146

5.2 Testing location algorithms using a 1D velocity model . . . 152

5.3 Conclusion . . . 163

6 **Characterization of microseismic location results** **165**

6.1 Event locations characterization . . . 165

6.2 Seismicity correlation with surface surveillance data . . . 179

6.3 Source parameters estimation . . . 183

6.4 Reflection of results on Field X development . . . 190

7 **Conclusion and recommendations** **191**

7.1 Recommendations . . . 191

7.2 Future work . . . 192

7.3 Assessment of microseismic monitoring for TA-GOGD 192
7.4 Summary 193

References **197**

LIST OF TABLES

TABLE **Page**

1.1 Acquisition frequency of monitoring methods 3
1.2 Classification of crude oil 7

2.1 Shuaiba reservoir petrophysical properties 42

3.1 Operational status of the downhole geophones 54
3.2 The y-component orientation due north estimated using the RMS amplitude max for 8 different vibrator shots at one of the monitoring wells. The variance is zero for all geophones. 72

4.1 Signal to Noise Ratio (SNR) statistics of 50 events for P- and S-wave phases picked manually 106
4.2 P- and S-wave statistics describing the difference between manual and auto-picking methods 111
4.3 Cross-correlation between P-wave, S-wave and density logs 127

5.1 Summary of tested location methods. 147

LIST OF FIGURES

FIGURE **Page**

1.1 Location of the Sultanate of Oman in the world map 2
1.2 Heavy and extra heavy petroleum basins in the world 6
1.3 A schematic diagram showing the process of TA-GOGD 9
1.4 Rapid increase in the number of microseismic related publications in the period from 1980 to 2019 12
1.5 Three different microseismic array configurations 14
1.6 Threshold triggering system mechanism 15
1.7 Illustration of STA/LTA triggering method 15
1.8 The processing workflow adapted for this project 16
1.9 Tectonic boundaries of the Arabian plate 18
1.10 Earthquakes moment magnitudes map around the major tectonic boundaries surrounding Oman in the period from 1904 to 2008 19

2.1 Shuaiba depth map 28
2.2 Map view of Oman salt basins 29
2.3 Stratigraphic column of Oman geology 30
2.4 Simplified geologic cross-section along with major subsurface Formations in central Oman 31
2.5 Stratigraphic column of upper Kahmah and overlaying Nahr Umr in Central and North Oman 32
2.6 Gamma ray logs at four wells in the field X 34
2.7 Seismic section perpendicular to the main graben structure 36
2.8 Isopach map of Nahr Umr 37

2.9 Geologic cross-section across along the Wasia and Kahmah Groups of the Cretaceous rocks 39
2.10 Isopach map of Kharaib 41
2.11 Present-day insitu stress orientation in Oman Salt Basin 46
2.12 Rose diagrams of faults, fractures and insitu stress in the subject field 47
2.13 Reservoir fracture model from integrated study of borehole and 3D seismic data . . . 49

3.1 Microseismic monitoring wells surface map 53
3.2 A cross-sectional illustration of the geophones setup in each microseismic well 55
3.3 Microseismic data transmission flow path from subsurface to contractor's headquarter 56
3.4 Layout of the microseismic monitoring wells and the associated vibrator shots 57
3.5 Layout of the geophones in the monitoring well within the geological framework. The production and injection wells are also displayed 58
3.6 A schematic diagram of the ray and source vectors between a geophone and a vibrator shot 74
3.7 The difference between ordinary least square and orthogonal distance regression. . . 75
3.8 Layouts of the vibrator shots with respect to microseismic wells 76
3.9 A waveform of a vibroseis shot record 77
3.10 The orientation difference between new and old vibroseis data acquisition 78
3.11 Orientation results of polarization analysis using different techniques 79
3.12 circular variance in y-component orientation per each polarization methods 80
3.13 Plot of SNR and rectilinearity 81
3.14 Impact of rotation window 82
3.15 Effect of placing vibrator shot at a close proximity to well-head on orientation circular variance 83
3.16 Impact of dead component on geophone orientation 83
3.17 Background noise level of a waveform recorded during equipment testing and event triggering parameter setting 86
3.18 An example of a microseismic event waveform recorded by three wells before application filtering 87
3.19 Frequency content of the P, S-wave and noise 88
3.20 A Sonogram (Spectrogram) plot of frequency versus time for a raw waveform 89

3.21 Application of an adaptive notch filter developed by Wuestefeld et al. (2010) 90
3.22 FFT amplitude spectrum of a wavefrom filtered by the adaptive notch filter of Wuestefeld et al. (2010) 91
3.23 Peak detection of notch frequencies on a frequency spectrum 92
3.24 Application of multi-notch and bandpass filter on a microseismic event data (Original) 95
3.25 Application of multi-notch and bandpass filter on a microseismic event data (Filtered) 96
3.26 Application of multi-notch and bandpass filter on a microseismic event data (Difference between original and filter) 97
3.27 An example of a waveform before filter application 98
3.28 The same data from Figure 3.27 99
3.29 Histogram of SNR before and after application of notch and Bandpass filters 100

4.1 An example of manual picking in a high SNR waveforms 112
4.2 An example of manual picking in an average SNR waveforms 113
4.3 A move-out display of a moderate SNR event in MSW-7 114
4.4 A waveform shows two possible events from already triggered events 115
4.5 A waveform containing three possible events 115
4.6 The effect of STA and LTA windows size on the STA/LTA curve 116
4.7 STA/LTA curve produced using the recursive method on a good SNR 117
4.8 CF functions for all auto-picking methods 118
4.9 Location of the wells used to build the 3-dimensional velocity model 122
4.10 Well-section view of the wells from which P- and S-wave sonic logs are used to build the velocity models 123
4.11 Application of a smoothing filter to the original sonic log data to remove spikes 124
4.12 Averaging (blocking) the sonic logs reading within each major formation 125
4.13 The final number of velocity zones in the 1-dimensional velocity model 126
4.14 Derived S-wave cross-validation at wells 77 (left) and 84 (right) 128
4.15 A cross-plot between smoothed S-wave velocity and the derived one at wells 77 and 84 129
4.16 The relationship between variogram and covariance 131
4.17 Normal score transformation 132
4.18 Estimated P-wave velocities at the top of the lower reservoir unit 133
4.19 Estimated S-wave velocities at the top of the lower reservoir unit 134

4.20 Smoothing the 3D velocity models 135

5.1 Epicentral location of an earthquake determined graphically using the "circle and chord" method 139

5.2 An example of the Wadati diagram. Interception of the best fitting line with the x-axis defines the origin time 140

5.3 Simplex is a tetrahedron defined by four vertices F in 3D space 144

5.4 Location results from Geiger (1912) method 148

5.5 Location results from Falls (1995) method 149

5.6 Location results from Yue and Xiao-Fei (2005) method. The velocity used is shown in Figure 4.13. A total of 465 events are located 150

5.7 Location results from Vinje et al. (1993) method. The velocity used is shown in Figure 4.13. A total of 61 events are located 151

5.8 Four zones velocity model (right). The travel time curves from geophone eight from MSW-4 (left) from the WFC method. The P-wave and the S-wave are shown as black and green curves, respectively, at a time equal to 150 ms 154

5.9 Travel time grid using BUMPS software 155

5.10 Travel time grid using FSM in Insite software package 155

5.11 Comparison of location result between Fast Sweeping Method (FSM) and BUMPS . . 156

5.12 Comparison of location result between FSM and WFC 157

5.13 Comparison of location result between FSM and Tian ray-tracing 158

5.14 Difference in location results for 7 selected event 159

5.15 Depth range of of events calculated by all four method 160

5.16 Location error from FSM. The figure from left to right are uncertainty in north, east and depth domain, respectively. 161

5.17 Time residual (top) and location errors (bottom) from FSM 162

6.1 Monthly event frequency chart 168

6.2 Histogram of event frequency and correlation with injection times. Other spikes in seismicity are associated with surface activity or drilling 169

6.3 Map view of the located microseismic events displayed on the top surface of the reservoir170

6.4 Events shown in vertical E-W cross section (Figure 6.3) and color coded as a function of time. They align vertically and are generally confined to the complex graben and horst structures 171
6.5 A 3D view of located events around wells array 7, 11, 4 172
6.6 Structural analysis of events around well array 4, 8, 17 173
6.7 Left: a plane showing all projected events on the cross-section. Right: a map view of event. clustering of events along planner features A, B, C are highlighted 174
6.8 This is similar to the Figure 6.7 but events are limited to 100 meters from the cross-section line (black line to in the right-side plot) 175
6.9 Development of microseismic events with respect to time at three time-lapses (2011-Oct-1, 2012-Jan-1 and 2012-Jul-1) 176
6.10 Development of microseismic events with respect to time at three time-lapses (2013-Jan-1, 2013-Jul-1 and 2014-Jan-1) 177
6.11 Development of microseismic events with respect to time at three time-lapses (2014-Jul-1, 2015-Jan-1 and 2015-Aug-1) 178
6.12 Optical leveling measurement at three different time periods. The measurements from different periods indicate an uplift of 9 mm observed at the same surface location where the seismic activity is at the highest level 180
6.13 InSar data shows a slight uplift of 3 mm in the period from February 2010 to July 2013. In the northern area of Field X, a depression occurred due to excessive production of water from the brackish aquifer for steam generation. Well names are masked for confidentiality reasons 181
6.14 Global Positioning System (GPS) elevation change between November 2011 to November 2013. The blue circles are normalized injected volume of steam around the flank and the crest of the reservoir 182
6.15 Mw values as a function of time 185
6.16 Moment magnitude histogram 186
6.17 Moment magnitude spatial distribution 187
6.18 A plot of magnitude versus distance from the nearest geophones 188
6.19 Calculation of b-value 189

Acronyms and Symbols

Acronyms

API	The American Petroleum Institute gravity, is a measure of a petroleum viscosity. 6, 7, 43
AVOA	Amplitude versus Offset and Azimuth. 49
CCS	carbon capture and storage. 11
EOR	Enhanced Oil Recovery. i, 2, 44, 50, 192
FSM	Fast Sweeping Method. xvi, 132, 135, 137, 142, 145, 146, 147, 152, 153, 156, 157, 158, 161, 162, 163, 165, 166, 194
GPS	Global Positioning System. xvii, 2, 3, 179, 182
HFS	Hydraulic fracture stimulation. 9
InSAR	Interferometric Synthetic Aperture Radar. 2, 3, 179
OWC	Oil Water Contact. 44, 58, 167
PDO	Petroleum Development of Oman. iii, 2, 3, 22, 23, 36, 51, 53, 54, 56, 85, 86, 111, 180, 181, 182
QVOA	Quality Factor Versus Offset and Azimuth. 49
RMS	Root Mean Square. 20, 22, 66, 70, 72, 73, 105, 109, 111, 147, 194
SNR	Signal to Noise Ratio. xi, xiv, xv, 12, 13, 14, 21, 51, 52, 68, 70, 72, 85, 88, 93, 94, 99, 100, 101, 104, 105, 106, 108, 110, 112, 113, 114, 117, 194
STOIIP	Stock Tank Oil Initially In Place. 44
TA-GOGD	Thermally-Assisted Gas-Oil Gravity Drainage. i, xiii, 1, 2, 9, 21, 23, 41, 44, 48, 50, 165, 190, 192, 193
UER	Umm er Radhuma. 34, 38, 55
VSP	Vertical Seismic Profiling. 61, 62, 119, 132

Units

bbl	bbl; An abbreviation for oilfield barrel, a volume of 42 galUS [0.16 m^3]. 7
cP	centiPoise; cP = 0.001 kg/m/s. 7, 42, 44
dB	deciBel; vibration intensity compared to a given level on a logarithmic scale. 81, 105
mD	milliDarcy; Darcy = 0.9869233 μm. 8, 40, 42, 44
sm^3	Cubic meter at a temperature of 15° Celsius and a pressure of 101.325 kPa (Kilopascal). 42

CHAPTER 1

INTRODUCTION

> *"If wells are constructed right and operated right, hydraulic fracturing will not cause a problem. . . . Our natural gas supplies would plummet precipitously without hydraulic fracturing."*
>
> — Scott Anderson

Microseismic monitoring has recently seen a rapid expansion in its utilization for various industrial applications. Conventionally, microseismicity refers to an earthquake of magnitude less than 2.0. These are, therefore, events that can be detected using sensitive seismic instruments. In the oil industry, the technique is still growing. There is great potential for this method in the characterization and exploitation of unconventional resources existing in various parts of the world. In this thesis, I use the microseismic monitoring method to characterize an oil field in Oman undergoing continuous steam injection. The overall aim of this thesis is to investigate the use of microseismic monitoring in an oilfield undergoing Thermally-Assisted Gas-Oil Gravity Drainage (TA-GOGD). This is the first use of permanent microseismic monitoring in such a setting (Glegola et al., 2015; Penney et al., 2007; Wilson et al., 2013). This chapter provides an overview of this novel technique and gives some insight into its potential.

1.1 Project overview and objectives

The oilfield that is the focus of this thesis referred henceforth as **Field X** for confidentiality reasons is located in the central part of the Sultanate of Oman (Figure 1.1). It is operated by

PDO and is technically a challenging field for development and hydrocarbon production. The complexity comes from several factors, two of them being the nature of the oil contained in the high porosity and low permeability rock matrix and the heterogeneity of the interconnected fracture system, with highly variable permeability. After lengthy pilot tests, PDO decided to use a sophisticated Enhanced Oil Recovery EOR technique for the full field development plan in the field's tertiary stage to increase its life span. TA-GOGD is the EOR method used. This program's long-term success will be considered a blueprint for application to nearby fields characterized with similar reservoir properties. The TA-GOGD technique involves the injection of steam at high volumes and rates into the field's crest. The steam injection will likely alter the stress and strain regime of the reservoir units. Consequently, Field X requires a multidisciplinary monitoring approach to understand how its static and dynamic properties react when subjected to prolonged steam injection.

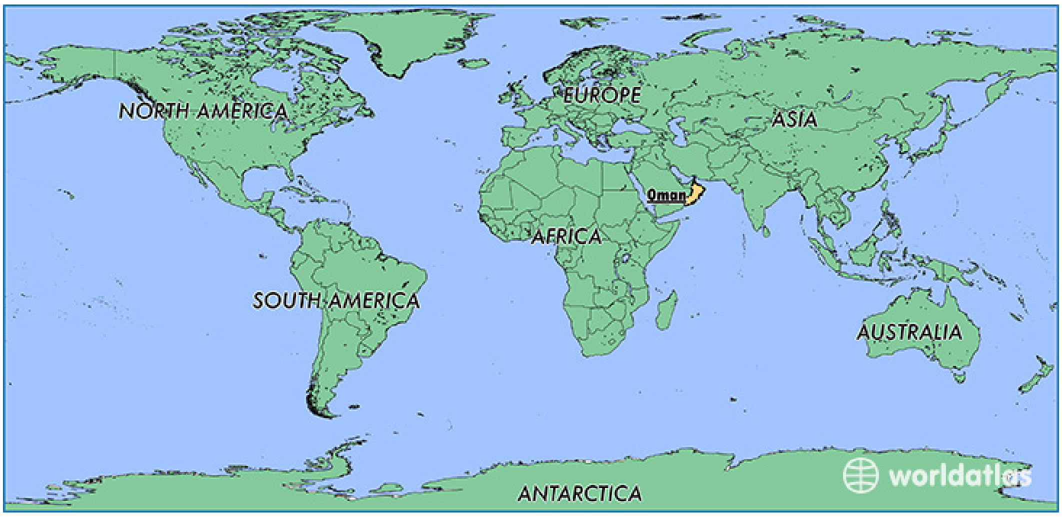

FIGURE 1.1. Location of the Sultanate of Oman in the world map.

The reservoir monitoring system used in Field X is a combination of microseismic monitoring and surface surveillance. The latter consists of many different surveillance types, namely Interferometric Synthetic Aperture Radar (InSAR), optical leveling, GPS, and microgravity survey. Table 1.1 describes the acquisition frequency for some of these techniques. The GPS method uses 64 established stations distributed around the field X and where water supply wells exist in the north-east. Shallow aquifers (Tertiary rocks) located above the reservoir's level supplied water for steam generation. Optical leveling has a total number of 78 measurement points more concentrated around Field X. Microseismic monitoring is made possible by 13 vertical wells; each contains eight 3-component geophones drilled at the crest and the flanks of Field X.

TABLE 1.1. Acquisition frequency of monitoring methods.

Method	**Acquisition frequency**
Microseismic	Real time
InSAR	Monthly
GPS	Quarterly
Optical leveling	Twice or once a year

One of the reasons for microseismic monitoring at Field X is that an increasing number of low magnitudes earthquakes were felt by people working in structurally and stratigraphically similar nearby fields undergoing fluid injection programs. In these fields, fluid injection and water extraction from shallow aquifers introduced subsidence in some areas and uplift around other regions. The maximum subsidence observed is as high as 40 cm (Sze, 2005). Compaction and surface subsidence could trigger fault reactivation, leading to well casing failures and integrity problems (De et al., 2000; Mahajan et al., 2018; Wu et al., 2016). Wellbore failures cost oil and gas companies billions of dollars yearly. They also have environmental impacts, such as groundwater contamination which is the primary source of drinking and irrigation water in Oman. Sherwood et al. (2016) conclude that well barrier failures are the leading cause of migration and leakage of hydrocarbon into shallow layers in the Denver-Julesburg Basin of Colorado.

Microseismic monitoring in Field X has three main objectives. The first aim is to provide near real-time distributions of microseismic events location and their magnitudes in the reservoir units and the overlying layers related to steam injection and oil production. The geometry of events can be used to infer how pore pressure changes in response to heat flow. It may also indicate bypassed oil zones close to injection wells through areas of low seismicity. Knowledge of event distributions will help monitor sustainable steam injection and retain the matrix and caprock integrity during prolonged heat exposure.

The second objective is the assessment of earthquake hazards and risks to surface and subsurface infrastructure. If events magnitudes exceed a certain threshold, PDO would temporarily cease the injection program until the seismicity drops below the threshold. After shutdown, the operator conducts a geomechanical assessment to understand the reason for large-magnitude events. However, if events' magnitudes are frequently above the threshold, seismic retrofitting must be required based on a seismic reference design. Probabilistic and deterministic seismic hazard maps for Muscat municipality have helped improve building design and reduce seismic risk (Deif et al., 2013; El-Hussain et al., 2012). A similar approach might be considered for Field X. It is worth noting that Field X is located in an unpopulated desert area. Nevertheless, microseismicity can pose a high risk to wellbores stability and surface infrastructure.

Finally, the project aims to integrate microseismic analysis with surface surveillance data to delineate reservoir characteristics better. High seismicity zones well presumably show a positive correlation with steam injection areas. Rocks volume expansion due to steam injection should be localized within the reservoir zones with a minimum impact on the overlying seal layer.

If created as a by-product of steam injection, induced fractures will enhance reservoir permeability and thus allow further heat expansion and subsequently lower the viscosity of the oil contained in the rock matrix. Induced faults and fractures represent weaknesses in the rock framework, which will break when the rock cannot sustain the subjected stress. A microseismic event marks their point of failure. Therefore, locating microseismic events and analyzing the associated source parameters (e.g., moment magnitude) will help understand dynamic reservoir properties. Reservoir complexity is controlled by structural elements, facies heterogeneity, and variations in reservoir permeability and porosity. These heterogeneities might impede steam expansion or fluid flow. The analysis and interpretation of microseismicity will help characterize the reaction of the reservoir units to human-induced disturbance. The goal is to be able to adjust drilling and field operations to maximize steam expansion and distribution in the reservoir units and ultimately increase the efficiency of the operation for better production and injection well placement.

In this thesis, I will process and analyze microseismic data to obtain the following deliverables:

1. Filter the microseismic data to enhance the signal-noise ratio
2. Find the orientation of downhole geophone
3. Build a representative velocity model
4. Pick P-wave and S-wave first arrivals
5. Locate microseismic events
6. Interpret microseismic events cloud and correlate them with other geological data
7. Analyze microseismic source parameters
8. Integrate microseismic results with surface surveillance

The approach I follow in project data analysis is to test different techniques in each step to obtain more reliable results. I developed a new method for both noise filtering and geophone orientation analysis individually. I perform different types of automatic arrival time picking and compare them with manual picking and choose the one which produces the lowest difference. Various location algorithms are also tested and quantified to find more authentic microseismic location results based on their alignment with preexisting faults and location errors. After processing the microseismic data with the selected method at each stage, I correlate the microseismic events' locations with geologic and surface data to determine the likelihood of reservoir compaction. I also assess the main cause of microseismicity. The plausible candidates are:

1. The reactivation of the main graben faults
2. Initiation of new fracture
3. Pore pressure increases due to steam injection and fluid expansion

1.2 Microseismic role in unconventional reserves

1.2.1 Unconventional oil and gas resources

The world's demand for fossil fuel energy and the depletion of conventional easily-accessible oil fields have shifted the oil industry into exploring and exploiting unconventional hydrocarbon resources such as shale gas, heavy oil, tight sands, and coalbed-methane (Arthur and Cole, 2014). Although these types of reservoirs are abundant and vast in volume (Yuko and Kazuo, 2001), they present challenges because they need advanced technology to bring their recovery factor to a profitable level. In comparison to conventional plays, their reservoir properties exhibit inferior porosity, permeability, and very high viscosity, as is the case of heavy oil. Successful exploration and production from such fields require an integrated, holistic approach in their development and the need for advanced technologies such as those associated with viscosity reduction, hydraulic fracturing, and sophisticated drilling methods (Ahmed and Meehan, 2016; Zhu, 2016). The field I am studying is a heavy oil carbonate reservoir. Passive seismic monitoring is relatively a new technology applied to the development of heavy oil reservoirs.

Figure 1.2 shows the heavy oil basins around the world color-coded based on the reported accumulations. In the Middle East, vast unconventional heavy oil and tight reservoirs have not been exploited. The most substantial volume of heavy oil is located in the western hemisphere, while the eastern hemisphere contains mostly light oil (Freeman, 2007).

Unlike conventional fields, heavy oil fields usually have to be studied comprehensively since the development strategy used in one field cannot be directly applied to another one without first examining all play aspects such as geological framework, mineralogy, and total organic content, stress regime, and nature of the host rocks (Santos et al., 2014). In North America, the technology has matured, and the production from the heavy oil and other unconventional resources has seen a tremendous surge since the last decade (Hein, 2006). Crude oil is classified based on API into four categories, as shown in the table below:

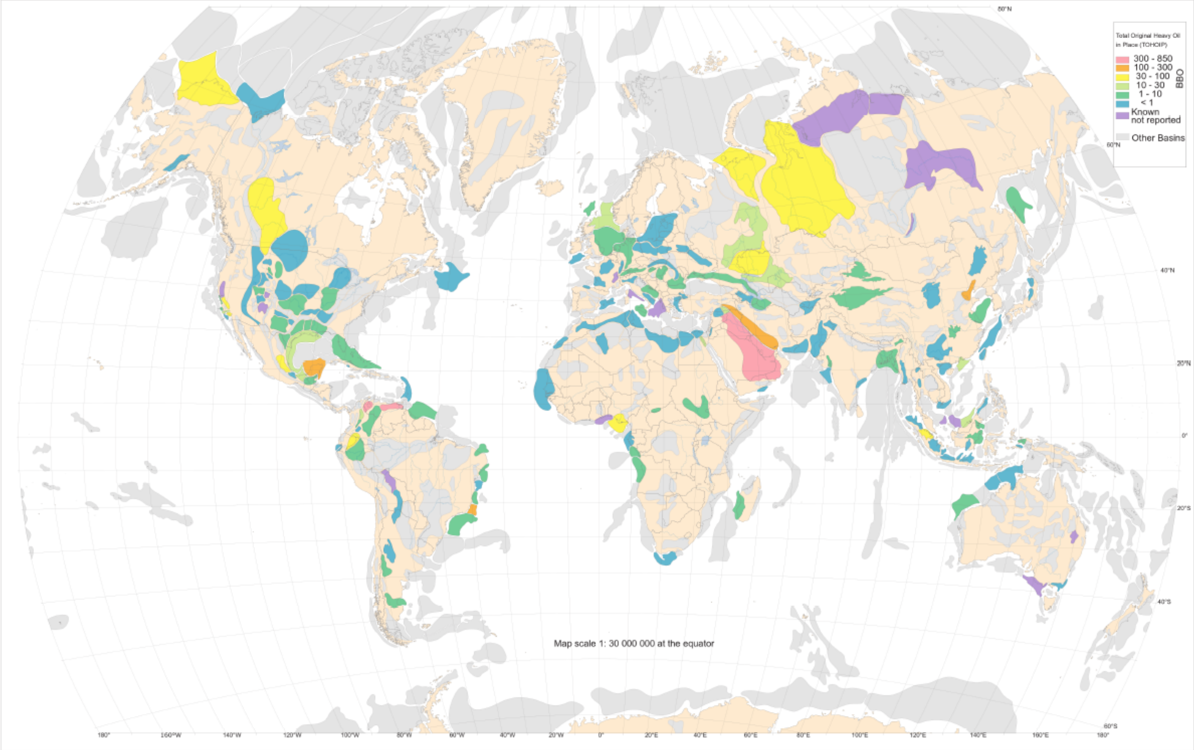

FIGURE 1.2. Heavy and extra heavy petroleum basins in the world reported in billion barrels. The Middle East has great potential to develop and exploit this unconventional resources. Figure courtesy of IHS (Whaley, 2008).

Microcosmic monitoring was successfully applied to numerous fields to gain critical information about their geological and structural properties. For example, Walters and Zoback (2013) monitored cyclic steam injection into a heavy oil field. The field experienced measurable surface deformation above the reservoir zone. The microseismic events were concentrated within the

TABLE 1.2. Classification of crude oil.

Categorization	**API**
Light	API > 31.1
Medium	22.3 < API < 31.1
Heavy	10.0 < API < 22.3
Extra Heavy	API < 10.0

reservoir zones and were attributed to the reactivation of shallow faults. Duhault et al. (2018) mapped microseismic events in a very tight clastic Cardium Halo play in Alberta with an average porosity as low as 2%. Their study highlighted methodologies to enhance oil production and increase the ultimate recovery.

1.2.2 Heavy oil development

What defines heavy oil apart from other unconventional resources is its viscosity under ambient reservoir conditions. Heavy oil viscosity range is greater than 100 cP and the estimated heavy oil in place in the world is about 4 trillion bbl (Briggs et al., 1988; Thakur et al., 1997). There are many deriving forces toward exploitation of heavy. Heavy oil resources are abundant, and their exploration cost is usually lower than conventional resources. Depletion of conventional hydrocarbon fields and the increase in the oil prices will eventually make the production of heavy oil profitable. Several development strategies tested feasible are thermal, chemical, and gas injection (Ali, 2003; Briggs et al., 1988; Guo et al., 2016). Successfully developing heavy oil reserves is an integrated approach that requires geoscientists and engineers working in harmony with downstream teams. Significant sustainable increase in recovery factor depends on a cost-effective and efficient completion method that is attainable through collaborative work to understand the correlation between multi-disciplinary data including geophysical, geological, engineering, and geomechanical field information (Fair et al., 2008).

Darcy's law is the principle that controls the mobility of hydrocarbon in porous media. This law states that the fluid flux is directly proportional to the pressure gradient (hydraulic head) and rock permeability but inversely related to viscosity. Steam-flooding can reduce the viscosity and improve the recovery rate. However, its efficiency is highly dependent on monitoring thermal expansion front movement direction and speed. The accumulating injection pressure changes the stress field in the reservoir units and can produce fractures at the steam front's edge. Passive seismic monitoring can track the spatial and temporal locations of induced fractures occurring at the heat-front, enabling operators to learn about the steam-flooding program's effectiveness. Operators can make better decisions to drill infill wells to minimize the cost and guarantee the development plan's longevity. This will also allow to image any rapid changes in the reservoir's stress and prevent caprock failure or compromising well casing integrity.

1.2.3 Thermally-assisted gas oil gravity drainage

Heavy oil is commonly drained from highly fractured carbonate rocks of low matrix permeability via the mechanism of gravity drainage, which depends on the density variation between fluids in the matrix and the fracture network. GOGD is the process by which gas when introduced into oil-bearing fractures system, causes an unbalanced hydrodynamic state. This disequilibrium allows gravity forces to drain oil downward in the matrix system if the permeability of the matrix is relatively high. However, when the matrix permeability is low, but the adjacent fracture systems are vertically continuous, and there are no lateral barriers, a pressure gradient develops between gas in the fractures and oil in the matrix. Gas will replace oil in the matrix when the pressure gradient exceeds the oil capillary-entry pressure. Once the oil is in the fracture system, it will continue sinking due to gravity until it reaches the newly developed fracture gas-oil contact (FGOC). The described process is controlled by Darcy's law ($q = -\frac{k}{\mu}\nabla p$, where q is the flux k is the permeability, μ is the viscosity, and ∇p is the pressure gradient). Thus, the process is extremely slow for a reservoir with a matrix permeability below $10mD$ but can be accelerated by injecting steam instead of gas into the crest of the reservoir unit to reduce the viscosity of the oil. The steam injection also inverts the wettability of the reservoir from oil-wet to water-wet, which further enhances water imbibition into the rock matrix, replacing oil in the pores.

The technique is very dependent on rock matrix block sizes surrounded by fractures. Therefore, the higher the fracture's density and the more open they are, the better is the process of the heat front expansion to heat the rock surface area as much as possible. Usually, the process is associated with dissolved gas breaking out of solution and occupying the upper part of the reservoir (Al-Hadhrami and Blunt, 2001; Dreher et al., 1986; Mahmoodi et al., 2009; Nabipour et al., 2007). The process is described as steam in oil out. Figure 1.3 depicts how this process works. From the figure, we find that the fractures are filled with fluids (oil in the oil rim zone and disloved gases in the upper part of the field). The production of oil elevates the water level higher inside the fracture system. Nabipour et al. (2007) states that TA-GOGD will reverse this phenomenon and maintain the reservoir pore pressure.

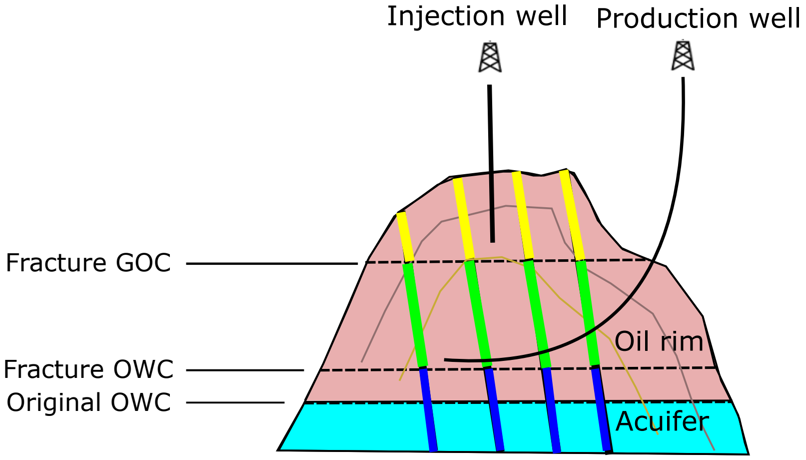

FIGURE 1.3. A schematic diagram showing the process of TA-GOGD. Fractures play a key role in the success of this process. Their density, openness, and interconnectivity will greatly enhance the expansion of the temperature front into the rock matrix. The blue-colored bar is the water column entering into the fracture network after oil production. The green bars are the oil contained inside the fracture network from where oil production happens. The secondary gas cap (yellow color) is produced when dissolved gasses come out of the solution.

1.3 Overview of passive seismic monitoring

1.3.1 Microseismic monitoring of hydraulic fracturing

Hydraulic fracture stimulation (HFS) has recently seen a rise in use, particularly in North America. Hydraulic fracturing is the main reason the USA has overtaken Saudi Arabia as the largest gas producer, and it will soon also be the largest oil exporter in the world. It is principally used to enhance fluid flow into production wells by increasing effective reservoir permeability. It involves the fluid injection into the reservoir rock at high volumes and rates to create fractures (Curtis, 2002). Proppant, usually a sand material, is added to the mixture to keep the fracture open during or after fracturing treatment (De Campos et al., 2018). The mixture is created so as the proppants travel as far as possible into the induced fractures and also to clear the pathways for fluid flow into the production wellhead (Jennings, 1996).

In recent years, due to an increase in hydraulic fracturing operations, especially in North America, there has been a growing fear from the public and media about the damage hydraulic fracturing can cause to the environment. Numerous studies correlate between hydraulic fracturing and different negative impacts such as contamination of groundwater (Llewellyn et al., 2015; Osborn et al., 2011) and earthquakes happening at proximity to sites experiencing hydraulic fracturing (Holland, 2013; Skoumal et al., 2015). Microseismic monitoring is useful for both regulators and operators. Regulatory measurements are set to manage the fracturing operation to mitigate any associated seismic risks (Bommer et al., 2006; Kendall et al., 2019). For instance, the traffic light regulation in which continuous monitoring of fracturing job is conducted and the operation is either stopped, amended, or continued based on a threshold magnitude. For example, in the United Kingdom, this threshold is set at a 0.5-moment magnitude. Whenever such an event is detected, the fracturing operation will be ceased to avoid any larger events (Red light). The regulation mandates the operators to lower the injection volume or rate if the detected magnitudes of events are in the range between zero and 0.5 (Yellow light). The operation carries outwith disruption when magnitudes of events are below zero (Green light).

From the operator's point of view, microseismic monitoring is used to evaluate the extent of fracture growth and complexity. It can help to appraise how much rock volume has been stimulated (Maxwell et al., 2010b) and thus plan each fracturing stage accordingly. Stimulated reservoir volume is a measure of the created fracture network's cloud size in a 3D sense during hydraulic fracking (Mayerhofer et al., 2010). Fractures, once initiated, radiate radially expanding seismic energy, which can be recorded by sensors placed in nearby monitoring well or at the surface. Fractures might also initiate without releasing seismic waves in a phenomenon known as aseismic creep or slip (Guglielmi et al., 2015; Maxwell, 2014). Another advantage of microseismic analysis is the possibility of integrating geomechanical models into static reservoir models by comparing synthetic events generated in forward modeling as a response to a particular geomechanical scenario (e.g., Mohr-Coulomb type rock failure criterion) with those really mapped by microseismic monitoring (Kettlety et al., 2019; Maxwell et al., 2015; Tarrahi et al., 2015). Such multidisciplinary integrations are crucial to the success of field development plan, cost-cutting, and seismic hazard mitigation.

Microseismic monitoring is the process of recording low magnitude earthquakes by very sensitive sensors, typically below a moment magnitude of zero, generated as a response to human disturbance. The microseismic analysis provides information about events' locations and distributions using P-wave and S-wave first arrivals detected by an array of sensors. Many industries use microseismic monitoring. The list below outlines some of its applications:

1. Mining industry for disaster prediction (Yang et al., 2007)
2. Geothermal investigation for energy generation (Okamoto et al., 2018)
3. Carbon capture storage to reduce greenhouse effect (Verdon, 2011)
4. Heavy oil reservoir monitoring (Al Hooti et al., 2019)
5. Underground tunnel construction (Tang et al., 2018)
6. Reservoir dam monitoring (Piccinelli et al., 1995)
7. Nuclear waste storage (Hente et al., 1984; Paul Young and Martin, 1993)
8. Wellbore stability (Kristiansen et al., 2000)

1.3.2 Microseismic monitoring for risk mitigation

One of the vital uses of passive seismic monitoring is its capability to make quick assessments to hazard and risk usually associated with many different large-scale projects that can cause harm to humans or the environment. The microseismic survey was first conducted in the mining industry as a tool for risk appraisal and prevention of fatalities from mine collapse (Ge, 2005; Jiang et al., 2006; Obert and Duvall, 1945). The implementation of microseismic acquisition permits appropriate actions for safe operation and risk mitigation in the mining industry (Ghosh and Sivakumar, 2018). In fact, the majority of microseismic processing and event location algorithms were first developed for the mining industry and later have been adapted in other industries. The largest interest in microseismic technology coincided with the booming in shale gas exploration in North America since the beginning of the current century (Figure 1.4).

The growing public concern over global warming has made governments proactive toward projects that can reduce the greenhouse effect. Carbon dioxide storage in deep subsurface formation is one of the methods that can stabilize the increasing mean earth temperature. A suitable site for carbon capture and storage (CCS) is seismically inactive zones. However, induced fractures create pathways for the carbon dioxide to escape and consequently lead to the failure of the storage program. Thus, microseismic monitoring is a viable technology to evaluate the geomechanical response of the caprock in CCS projects (Pawar et al., 2015; Stork et al., 2015; Verdon et al., 2011; Vilarrasa, 2016).

Induced fractures and fault reactivation are the major reasons for well casing deformation. The compaction or expansion of the reservoir and the overlying rock units can possibly occur in all stages of oilfield life-span from exploration, appraisal until development (Kristiansen et al., 2000). Microseismic analysis infers the geomechanical response of dormant faults or fractures cutting through well casing that can be reactivated during hydraulic fracking or steam injection. Microseismic monitoring plays a crucial role in mitigating the risk of well casing breakout (Chen et al., 2019; Lolla et al., 2019). Disasters like BP deepwater horizon oil spill in 2010 and Campos Basin oil spill in offshore Brazil in November 2011 mandate oilfield operators to deploy reservoir monitoring system initial stage of field exploration.

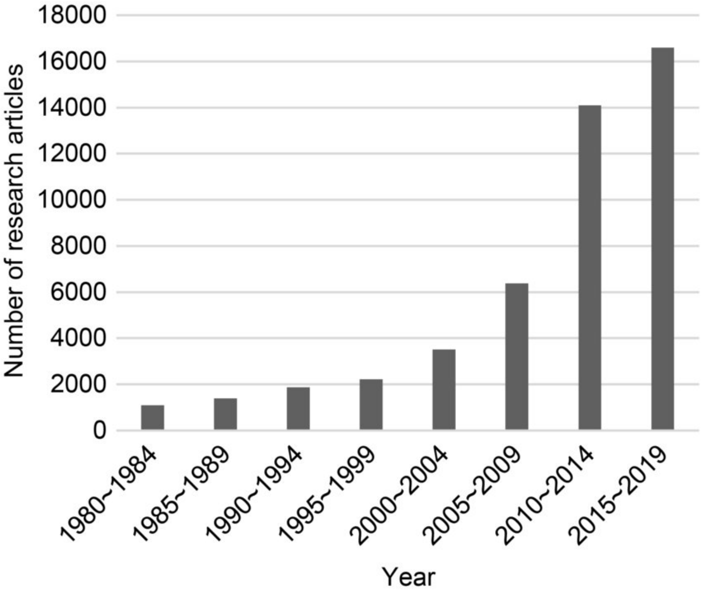

FIGURE 1.4. Rapid increase in the number of microseismic related publications in the period from 1980 to 2019 (Li and Chang, 2020).

1.4 Passive seismic data methodology

This section describes some fundamental knowledge of microseismic data acquisition and processing. The validity and reliability of microseismic events could, representing initial point of fault or fracture initiation in 3D space, produced from microseismic data are scrutinized based on how accurately the data are acquired and processed. Therefore, it is essential to understand how to acquire microseismic data and process them to enhance SNR.

1.4.1 Microseismic data acquisition

Microseismic data acquisition can be made using different array configurations based on field development requirements, as well as operational, geological, and economic constraints (Maxwell, 2014). Ideally, a configuration made of surface and downhole arrays gives more accurate hypocentral location results (Figure 1.5). Downhole geophone arrays usually have higher SNR than shallow geophones. However, they suffer from inherent 180° ambiguity in microseismic location when the events are detected by only one vertical well, as is usually the case in hydraulic fracturing jobs. They are also more expensive than shallow installations because of the requirement to drill monitoring wells.

Additionally, compared to surface arrays, deep arrays provide inadequate coverage of the radiated seismic waveforms from different directions (sampling of the focal sphere). Therefore, focal mechanism or moment tensor inversion techniques do not provide a unique solution with downhole arrays (Eyre and van der Baan, 2017). Surface arrays can be deployed with hundreds of geophones at a lower cost than buried or downhole arrays. Surface arrays have the potential to locate microseismic events using semblance stacking techniques without the need for first arrival picking due to the fact that a large number of geophones are spread across the surface with a wide aperture (Duncan and Eisner, 2010). Surface and near-surface arrays require static correction to eliminate the low-velocity effects of the unconsolidated surface layer and topographic variations (Diao et al., 2015). Downhole arrays are more sensitive to lateral velocity variation than surface arrays since the ray path has a higher horizontal component in their travel path. Hence, downhole arrays can better be suited to detect fracture-induced anisotropy (Baird et al., 2017; Verdon et al., 2009).

1.4.2 Processing microseismic events

There is a difference in the processing workflow adapted for each of the surface and downhole microseismic acquisition systems. This thesis focuses only on the downhole microseismic method. The provided data have already been triggered, and each event is contained in a single seg-y file. The triggering system works by comparing the amplitude of P- and S-wave signals to a background noise level. The events triggering methods used for this project are amplitude threshold and short-term over long-term average ratio STA/LTA ratio (Allen, 1978). Two triggering methods are used to ensure that the maximum possible number of events are recorded.

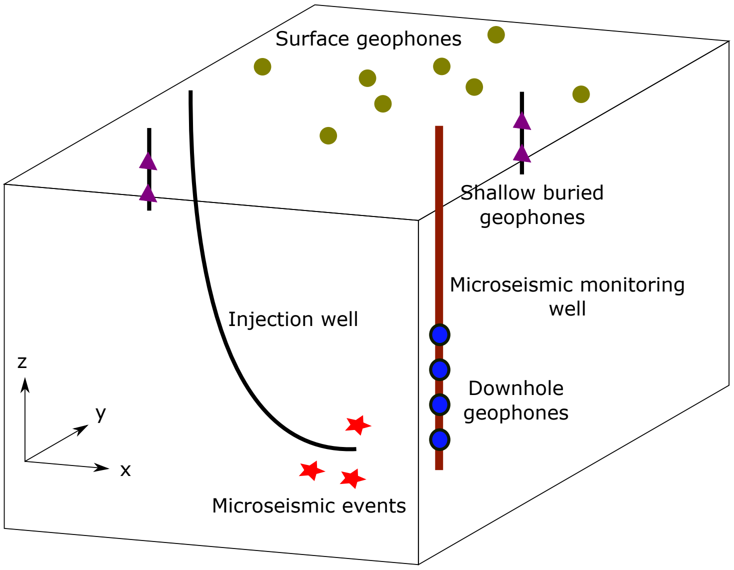

FIGURE 1.5. The figure shows three different microseismic array configurations. Downhole arrays are placed in a monitoring well close to the injection wells to detect as much events as possible.

The amplitude threshold triggering system works by using a predefined threshold limit to be compared with P-wave or S-wave amplitudes. Whenever the amplitudes of the signal are higher than the threshold, the system records a microseismic event. The triggering must be detected in a predefined number of channels to eliminate the detection of false events. For example, in Figure 1.6, an event is detected since five channels have their signal amplitudes above the triggering threshold.

The STA/LTA ratio method calculates the ratio of the average amplitudes between short-term trailing windows and the long-term leading window. When this ratio is greater than a predefined value, an event will be triggered. For Field X, the value is set at three. Figure 1.5 illustrates the mechanism of the STA/LTA triggering method. LTA window is set to 400 msec, and the STA window is set to 100 msec in Field X.

Figure 1.8 shows the processing workflow developed for this project. Raw data are filtered using bandpass and adaptive notch filters to remove unwanted noise and enhance SNR. I use vibrator shots to determine the geophone orientations. A representative velocity model of the subsurface is created using wireline P-wave and S-wave sonic longs. Usually, velocity model calibration is performed using a controlled shot in the subsurface. Here the model cannot

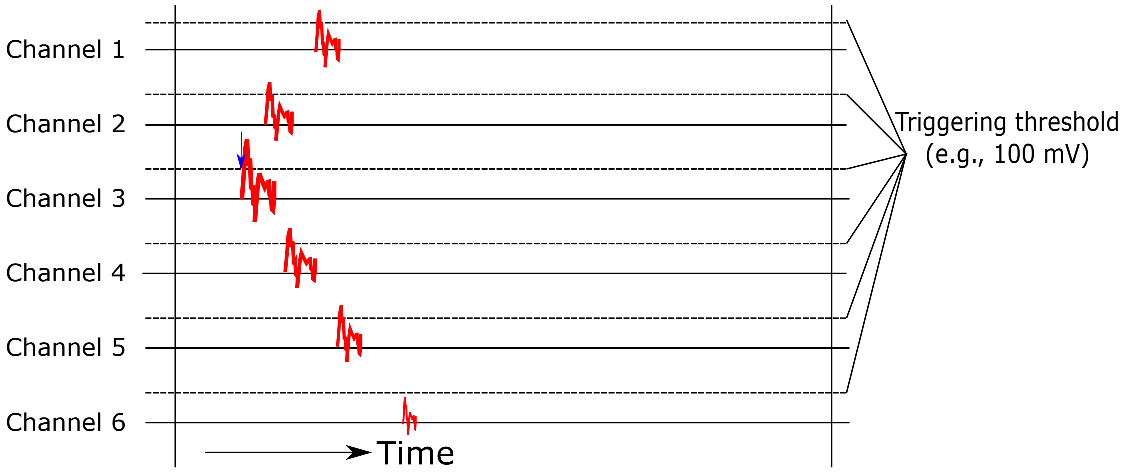

FIGURE 1.6. Illustration of the threshold triggering system mechanism. The solid horizontal line is the zero amplitude reference line.

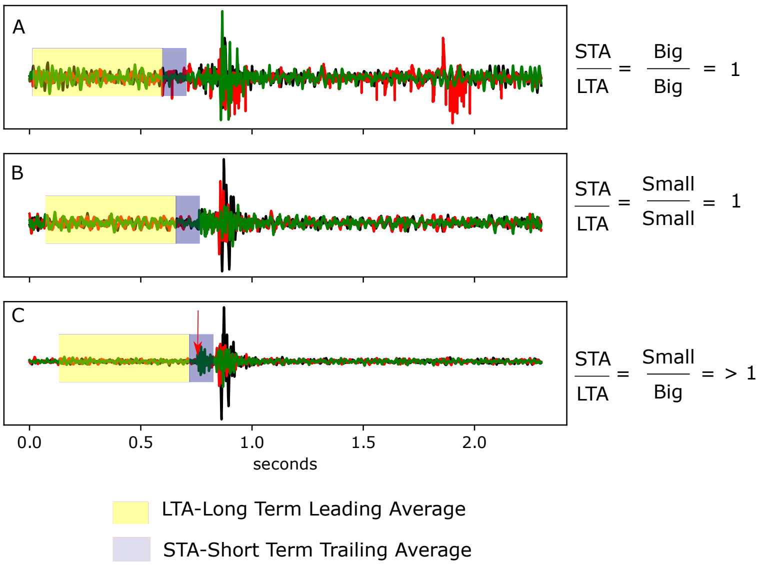

FIGURE 1.7. Illustration of STA/LTA triggering method. The red arrow indicateds P-wave arrival. The green, red and black waveform are the measurements from the geophones' three component.

be calibrated with vibrator shots. The reason is that the ray path from the vibrator shots to geophones does not image the reservoir units from where microseismic events originate. Also, no downhole controlled shots are provided. I tested different techniques of first arrival picking, and the one that best agrees with manual picking is used. I also tried various microseismic location algorithms. The location method inputs are the P-wave and S-wave arrival times, geophone location, and the velocity model. Finally, I calculated moment magnitude of the located events.

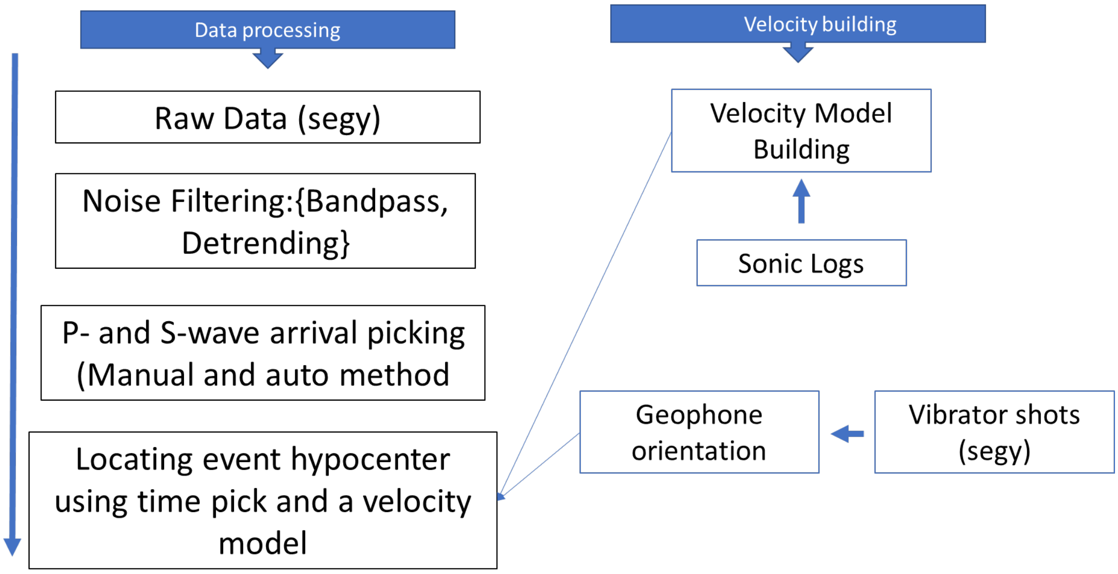

FIGURE 1.8. The processing workflow adapted for this project.

1.4.3 Interpretation of microseismic events

Microseismic interpretation is a broad term that encapsulates the analysis of the microseismic events' clusters to infer induced fracture network geometry, length, and width. It examines the creation of new faults or the reactivation of preexisting ones. Additionally, the interpretation can be expanded to analyze the microseismic source parameters such as magnitude, focal mechanism, stress drop, and fault radius. Downie et al. (2010) show that events' magnitudes can infer whether faults are contributing to the observed dimension of the microseismic cloud. They state that events' magnitudes can evaluate induced fracture behavior. Cipolla et al. (2011) state that microseismic analysis should not only be limited to hypocentre location investigation and source parameter analysis but preferably include geomechanical modeling and must be well integrated with the volumes of hydrocarbons produced and steam injected into the reservoir units. Microseismic events cluster and surface seismic attributes such as inversion of seismic reflection data when combined can evaluate why seismic clouds concentrate at specific zones in the reservoir. Advanced techniques of shear wave splitting and moment tensor inversion are nowadays common practice in most microseismic monitoring projects. Shear wave splitting analysis can infer reservoir velocity anisotropy and determine fracture length and width (Al-Harrasi et al., 2011; De Meersman et al., 2009; Teanby et al., 2004). Verdon and Kendall (2011) mapped multiple aligned fracture sets using shear wave splitting. Kendall et al. (2011) provide various potential applications of microseismic monitoring in the oil and gas industry of which this thesis focuses on:

1. Identify induced faults or fractures orientation
2. evaluate the stress direction
3. Integrating reservoir surface deformation with injection volumes and microseismic clouds
4. Assessing caprock integrity
5. Magnitude estimation and assessment to seismic hazard

1.5 Seismicity in Oman

1.5.1 Natural seismicity in Oman and the surrounding area

The Arabian plate constitutes most Arab countries located on the Asian continent and is bounder by various ranges of plate boundaries. Oman is located on the southeastern side of this plate. The Indian plate bounds the Arabian plate from the eastern direction along the Owen transform fault. The Red Sea rift separates the Arabian plate from the African plate in the western direction along a divergent boundary. To the northeast, the Makran subduction zone is created by the Arabian plate's collision with the Eurasian plate. Both the north Oman mountain ranges and the Zagros mountains in Iran are experiencing uplift due to this collision. To the south, the Gulf of Aden rift is comprised of en échelon transform faults (Figure 1.9).

Figure 1.10 shows the seismicity of the region, revealing that most earthquakes are concentrated at the plate tectonic boundaries. The highest concentration of seismicity occurs in the Zagros mountain belt and along the Gulf of Aden. There have been no recent devastating earthquakes in Oman (El-Hussain et al., 2012). The Owen transform fault has not yet produced any recorded earthquakes having magnitudes higher than 6. Since it is a transform fault, it is unlikely that earthquakes generated at this boundary will create Tsunamis.

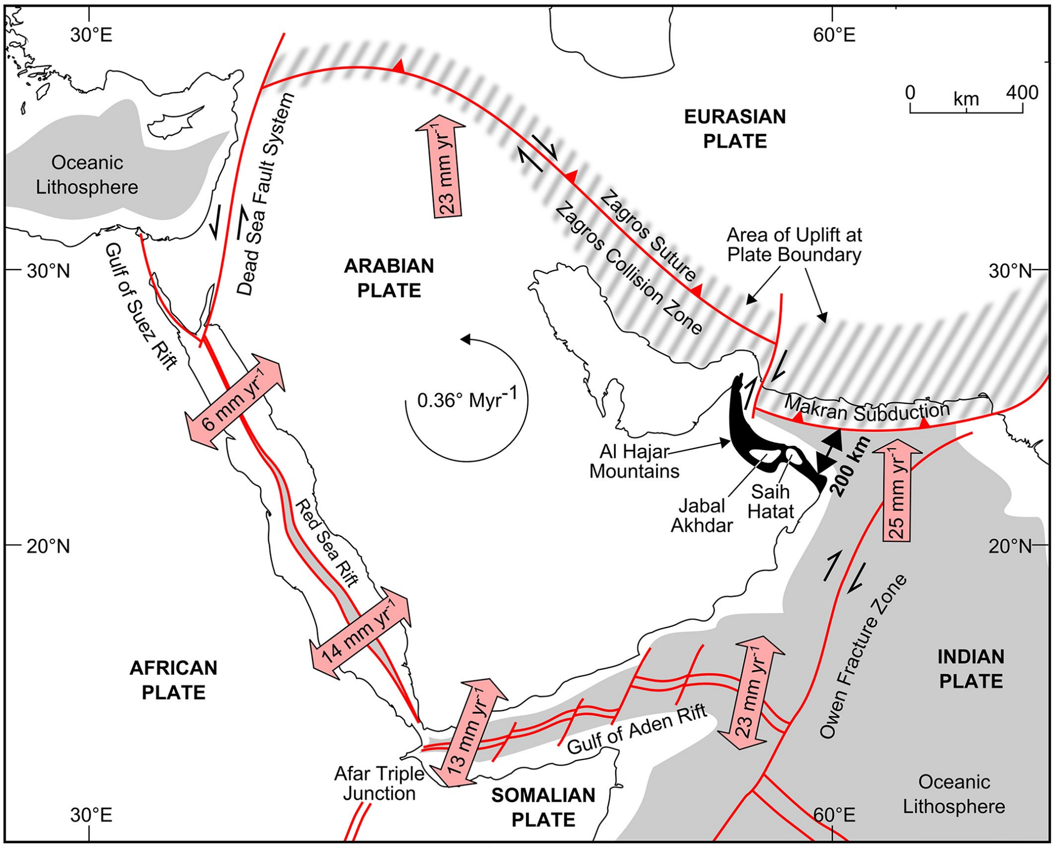

FIGURE 1.9. Tectonic boundaries of the Arabian plate. Adapted from Hansman and Ring (2018).

1.5.2 Microseismic monitoring programs in Oman

Permanent microseismic monitoring campaigns in Oman started during the late 90s targeting oil development projects with PDO and other oil operating companies. Some of these programs were still at that time in the pilot stage, and others were in the initial development phase. During the next decade, they proved very successful in achieving field development goals and delivering critical answers to confronted challenges in optimizing and maximizing hydrocarbon production. These projects provided geoscientists and engineers with the knowledge to make better decisions towards optimized field development plans. The technology has currently seen growth in utilization at different oil fields in Oman, ranging from shallow reservoirs (heavy oil) to deeply buried ones (tight rocks). In the north and central Oman, the targeted reservoir units are carbonate rocks, while in the south of Oman, they are clastic rocks. The development plans for these fields are water, steam, or chemical injections. Short period hydraulic fracturing jobs,

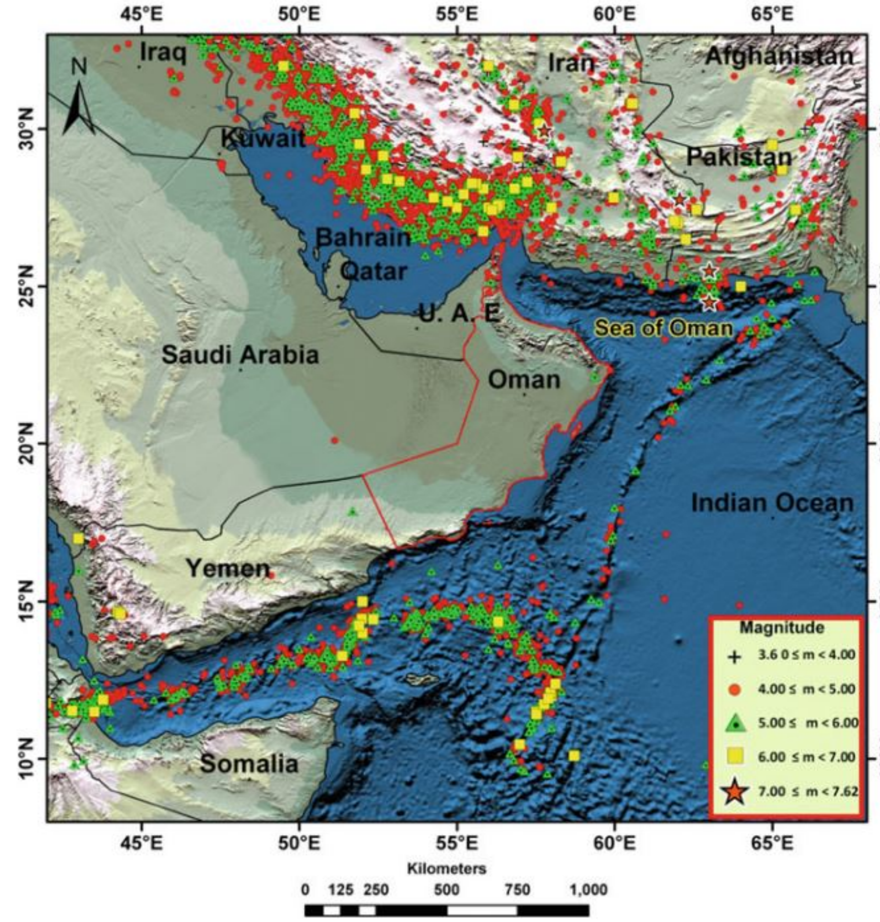

FIGURE 1.10. Earthquakes moment magnitudes map around the major tectonic boundaries surrounding Oman in the period from 1904 to 2008. Adapted from El-Hussain et al. (2012).

however, started quite later in 2010. Their primary purpose is quite different from permanent monitoring. They deliberately aim to break apart the rock to create fractures for oil and gas to flow easier into the production wells. The permanent microseismic monitoring targets deep gas fields. The reservoir types addressed by the hydraulic fracturing are mostly clastic tight rocks, except for one field in the central of Oman, which is a shallow carbonate.

The permanent microseismic monitoring and hydraulic fracturing planning and execution involve first a feasibility study whereby numerical simulations are conducted to evaluate events detectability and uncertainties. The next step is to prepare the surface arrays' layout or find a suitable injection or production wells to be converted into a microseismic monitoring well. Before starting the actual monitoring programs, the vibrator shots are acquired if necessary, the sonic logs are prepared, and the noise level is measured. The typical challenges confronted in the planning phase are finding nearby monitoring well, harsh topography for surface arrays, and the high temperature of the reservoir rock, which could damage the sensors. High temperatures in the reservoir zone below 3500m resulted in the failure of some monitoring project in Oman. Noise is also a very crucial challenge since most fields are under continuous operations. The type of noises in these fields usually are drilling, injection, and surface civil noise. Several challenges are also present in the processing phase. For example, the reliability and the quality of vibrator and controlled perforation shots are sometimes poor for geophone orientation and velocity modeling, respectively. In fact, Field X has the vibrator shots reacquired because the data from the first acquisition are of limited frequency bandwidth and poor quality. It is also relatively cumbersome to generate an accurate velocity model for highly complex structural reservoirs having heterogeneous facies proportions. The sonic logs are usually scarce and only limited to the reservoir zone, making the velocity model's quality questionable. The industry nowadays dedicates more attention toward integrating microseismic results with geologic, petrophysical, geomechanical, and active seismic data to bring engineering deliverable for better injection and production wells placement and field development and completion design.

1.5.3 Previous studies of induced seismicity in Oman

Microseismic monitoring is an emerging technology with millions of dollars investments hoping to increase oilfields recovery factor. The aim is to maximize hydrocarbon production and thus boost the economy of Oman, which is almost entirely dependent on oil export. Therefore, a common theme found in various literature is the anonymity of the investigated oil fields due to the confidentiality agreement signed with the Ministry of oil and gas in the Sultanate of Oman.

Several doctoral research studies have been conducted on microseismic monitoring on various oil fields in Oman. They investigated different aspects of microseismic monitoring. For instance, Sze (2005) applied three location algorithms techniques to some 405 microseismic events recorded in 20 months. He assessed the variation in location results from the different techniques by analyzing the smallest RMS location errors and the alignment of events along a major graben structure found in the studied oilfield. He finally examined the temporal and spatial characteristics of the located events. Al-Anboori (2005) conducted shear wave splitting analysis on the producing reservoir units in the Yibal oilfield. He observed a transition in the faulting from strike-slip to pure thrusting and from strike-slip to normal faulting in the reservoir and the caprock, respectively. His study determined the stress direction and the density, and the width of the fractures in the reservoir units and the overlying seal rock. Sarkar (2008) focused on the best strategies to obtain reliable location results with an emphasis on the effect of the velocity model on the accuracy of the location results. His study revealed faults and fractures initially unmapped from the active seismic method. Al-Harrasi (2010) applied shear wave splitting technique to analyze anisotropic behavior in an oilfield in Oman to determine the fractures' strike direction, size, and density. To validate the results, he applied a rock physics model to understand the observed anisotropy nature. He concludes that the anisotropy is controlled by the rock's lithology and the proximity to preexisting faults. Li and Others (2013) applied a newly developed method of source mechanism to find the focal mechanism of 40 events from an oilfield in Oman. The location results combined with the focal mechanism suggest that preexisting faults' reactivation is the primary source of microseismic events.

1.6 Thesis structure

In the introductory chapter, I presented the aim and objectives of this thesis and what deliverables it brings to the scientific community and the company which operates Field X. I gave a brief overview of the microseismic analysis technique. I discussed natural and induced seismicity in Oman. I conclude the chapter with the description of the TA-GOGD and microseismic equipment setup in Field X.

In Chapter 2, I discuss the tectonic setting and geological framework of the Field X with an emphasis on the structural elements that controlled the development of Field X. I explain the petrophysical and facies properties and heterogeneities found in the reservoir units. I exploit various research studies to decern the present in-situ stress direction and relate them to the observed fracture orientation deduced from other scholarly studies.

Chapter 3 focuses on pre-processing the microseismic data to prepare them for the location algorithms. The microseismic data are contaminated with unpredictable monochromatic noises, for which I developed an adaptive notch filter to increase SNR. I also developed a new fast, and reliable approach for geophone orientation analysis. I compared this approach with other established techniques to assess its validity.

In Chapter 4, I analyze different techniques for arrival times picking of the P- and S-waves and propose a methodology to identify arrival times from Characteristics Functions (CF) of the STL/LTA instead of using a user-defined constant threshold value which performs poorly in noisy seismograms. The method which provides the lowest mean difference from the manually picking is applied to the dataset. In the same chapter, I review the compressional and dilatational wireline sonic logs to build a representative velocity model as an input to the forward location algorithms. The final accepted velocity model is a 3D heterogeneous model. The 3D velocity is accepted since the complex structural styles (Graben and domal shape) of the field juxtaposes low-velocity shale layers and high-velocity carbonate rock side by side.

Chapter 5 discusses 5 location algorithms used to find the hypocentres of microseismic events. The main inputs for all the methods are the travel time picks and the generated velocity model. However, the velocity model for some of these algorithms is a homogeneous one, while others accept 1D or a fully 3D model. I compare location results from these methods and assess their accuracy by highlighting clustering of located events around preexisting faults and their alignment with fracture orientation mapped using formation microimager data from other studies. Their validity is also assessed by the values of associated RMS location errors.

In Chapter 6, I interpret the hypocenter of events to associate them with possible fracture and fault initiation or fault re-activation. I correlate the microseismic results with surface surveillance measurement to identify the potential reasons for the surface deformations observed on and around the surface of the field. I study the source parameters of the microseismic events to determine any seismic hazard related to the injection program. Magnitude values are evaluated spatially and temporally to find spurious trends or concentrations of relatively high magnitudes at a particular region in the subsurface. b-values are used to infer what caused the events (faults or fractures). Mapping of d-values for a different cluster can tell the degree of alignment of the events along faults' planes.

I summarize the thesis in chapter 7 by reviewing each chapter's content and providing recommendations based on the overall success of the microseismic monitoring program in imaging-induced fractures and faults.

1.7 Declaration

I received the data in raw formats without any pre-processing being applied by PDO. In Chapter 3. PDO provided me with vibrator shots as seg-y files that I used to determine the orientation of geophone sensors. I conducted manual P-wave picking on the vibrator shots. The data as provided are contaminated with noise that made first arrival picking impossible. Chapter 3 describes both the process of geophoen orientation determination and noise filtering. I picked the first arrivals of P- and S-wave using automatic and manual picking methods described in chapter 4. I built the velocity models using sonic and density logs provided by PDO (Chapter 4). Other dataset PDO provided to me are x, y and z location of every microseismic sensors located in 13 monitoring wells. PDO also provided me with surface depth maps of Nahr Umr, Shuaiba and Kharaib formations. The microseismic event data (7200) are provided as triggered events in seg-y formats.

1.8 Conclusion

In this chapter, I provided an overview of the objectives of this thesis and what is the deliverable I try to achieve. I reviewed the microseismic monitoring method, its potential, and its applications. I discussed the acquisition aspects, processing routine, and interpenetration methods of downhole microseismic events. Oman is located in a quite aseismic zone with no major devastating earthquakes in its recent history. Induced seismicity has a lot of applications in the oil and gas industry in Oman. Many major fields of various recovery methods in Oman use the microseismic technique for better delineation of reservoir properties and eventually recovery maximization. The number of research conducted on microseismic data from Oman has seen an increase, and the research types focus on different aspects of microseismic technology. TA-GOGD is a novel technique used in highly fractured carbonates containing heavy oil to accelerate the gravity drainage recovery method. In Field X, this method is the first of its type in the world to be applied on the full-field scale. I conclude the chapter by describing the equipment setup used in Field X. 13 microseismic wells equipped with 3C-component geophones continuously monitor induced fracture and faults.

CHAPTER 2

GEOLOGY OF THE FIELD

> *"There is earth below your earth, a deep room where gas and oil, rock and stone, circulate like slow blood through a body."*
>
> — Mathew Henderson

The field X is located in the northern part of Oman with a distance of nearly 350 km from the capital Muscat. It was discovered in the early 1970s, and production started in the same period. It is producing oil from highly faulted and fractured carbonate sequence of the Shuaiba and Kharaib Formations, which are overlain by a thick shale layer named the Nahr Umr Formation. (Figure 2.1) shows the top structural map of the Shuaiba reservoir unit, depicting the shape of a dome, trending NE-SW.

This chapter will discuss the production challenges confronted in the early stages of field development. It describes sedimentary facies of the subsurface rocks, particularly the Kahmah Group, to which reservoir rocks of the Shuaiba and Kharaib Formations belong, and their structural and stratigraphic framework with particular emphasis on the fracture network system.

2.1 Tectonic setting

The structural elements of the field are mainly controlled by a deep-seated salt basin (Schröder et al., 2003) that formed during the Neoproterozoic–Early Cambrian age in a stage of rifting and subsidence from 600 to 540 Ma (Figure 2.2). In this stage, the earliest sedimentary rocks were deposited in Oman (Husseini and Husseini, 1990). The salt basin is known as Ara salt, which forms the upper part of the Huqf Supergroup (Figure 2.3), and it extends vastly across Oman but is divided into three basins separated by structural highs (Al-Kindi and Richard, 2014). In Ghaba Salt Basin, the thickness of the Salt Basin exceeds 1000 m (Peters et al., 2003) (Figure 2.2) also outlines several major oil fields either located inside the areal extent of these salt basins or at their eastern flank, as is the case with the South Oman Salt Basin (Claringbould et al., 2013). Oil fields located in the northern Ghaba and Fahud Salt Basins have similar structural and stratigraphic characteristics (Rollinson et al., 2014).

The deposition of the Huqf Supergroup had ceased by the assemblage of Gondwanaland during the Neoproterozoic and Paleozoic (Meert and Van Der Voo, 1997), rising the Earth surface above mean sea level and led to the major Angudan unconformity (Figure 2.3). From the middle Cambrian until the end of the Ordovician, salt layer diapirism started due to differential loading of the overlying sedimentary succession of thick continental clastic rock of the Haima Supergroup, a mixture of aeolian, fluvial, and shoreface deposits (Droste, 1997; Loosveld et al., 1996), (Figure 2.4). The Haima Supergroup was fed by sediments from both basement rocks and Huqf Supergroup. Reactivation of existing extensional faults of the basement rocks trending NE-SW, parallel to the longest axis of the Salt Basin, also contributed to salt halokinesis and the fault systems extending into the Huqf Supergroup Formations. During the Permian period, the end of the ice age is marked by the waning glaciation from Gondwanaland (Crowell, 1995) giving rise to a glacio-fluvial depositional environment and Formation of Haushi Group (Braakman et al., 1982) (Figure 2.3). The area is later subjected to a period of tectonic inactivity during the Mesozoic in which carbonates of the Hajar Supergroup were deposited on a shallow-marine carbonate platform at the north-eastern flank of the Arabian Peninsula opposite to the Neo-Tethys sea (Pratt, Brian and D. Smewing, 1993). Closure of Neo-Tethys sea during the Late Cretaceous (Searle and Cox, 1999) resulted in obduction of the Semail Ophiolite on top of the Hajar Supergroup in north Oman, and the subsequent creation of NW-SE transtensional faults (Filbrandt et al., 2006). Obduction triggered reactivation of the salt rims, leading to further diapirism into the upper part of the overlaying Haima Supergroup and propagation of basement faults into shallower layers. Two types of deformation occurred in the north and central Oman during the Late Cretaceous (Ophiolite emplacement): strike-slip and NW-SE trending normal faulting. The opening of Red Sea from the Middle Cenozoic to present day has led to the obduction of the northern part of the Arabian plate beneath Eurasia along the Makran trench, and the current state of uplift observed in the Oman mountains.

Hydrocarbon fields that exist in the northern salt basins produce from several reservoir rocks of varying hydrocarbon viscosity. In general, deep clastic reservoirs of the Gharif and Khalata Formations (Figure 2.3) comprise light oil, whereas the shallow carbonate reservoirs rocks of the Shauiba and Natih contain heavier oil with higher viscosity. The Natih Formation is extensively eroded in the Ghaba Salt Basin compared to the Fahud Salt Basin. The only members of the Natih Formation present in Field X are Natih-E, Natih-F, and Natih-G. In contrary to Northern Oman, the Kahmah Group, to which the Shuaiba and Kharaib Formations belong to is absent in the South Oman Salt Basin (Droste, 1997). The Ara Salt consists of a prolific carbonate intra-salt stringer in South Oman Salt Basin, but the Group is not targeted for hydrocarbon in the Ghaba nor the Natih Salt Basins (Al-Siyabi, 2005).

The gross rock volume of the field X from the deepest spill point to the top of Shuaiba Formation is $6.74 \times 10^8\,\mathrm{m}^3$, and the three-dimensional surface area is $1.01 \times 10^7\,\mathrm{m}^2$. The dome is elongated in the NE-SW orientation, similar to the underlying salt basin. The slope at the flanks of the field varies drastically from one direction to another. For instance, it has a very gentle slope of about 5° at the north to the north-eastern edge, whereas it increases to 12° in the southern and eastern directions. In the western flank, it becomes quite steep, with a slope value of about 30°. Faults are shown as gray color polygons in (Figure 2.1) are high-angle normal faults having two perpendicular strike directions. Major faults oriented NW-SE formed during the Cretaceous and reactivated in the Tertiary. In contrast, NE-SW trending faults have been active since the Cambrian. Both fault systems have dip angles between 65° to 85° and two opposing dip directions perpendicular to their strike axis. The NW-SE trending faults create a major graben structure at the center of the field, juxtaposing the Nahr Umr Shale with the underlying Shauiba and Kharaib Formation with a maximum fault throw and heave of approximately $35\,m$ and $10\,m$, respectively, at the crest of top reservoir unit. Most of the injection wells are drilled into the adjacent horst structures since they constitute the shallowest depth zones in the reservoir units.

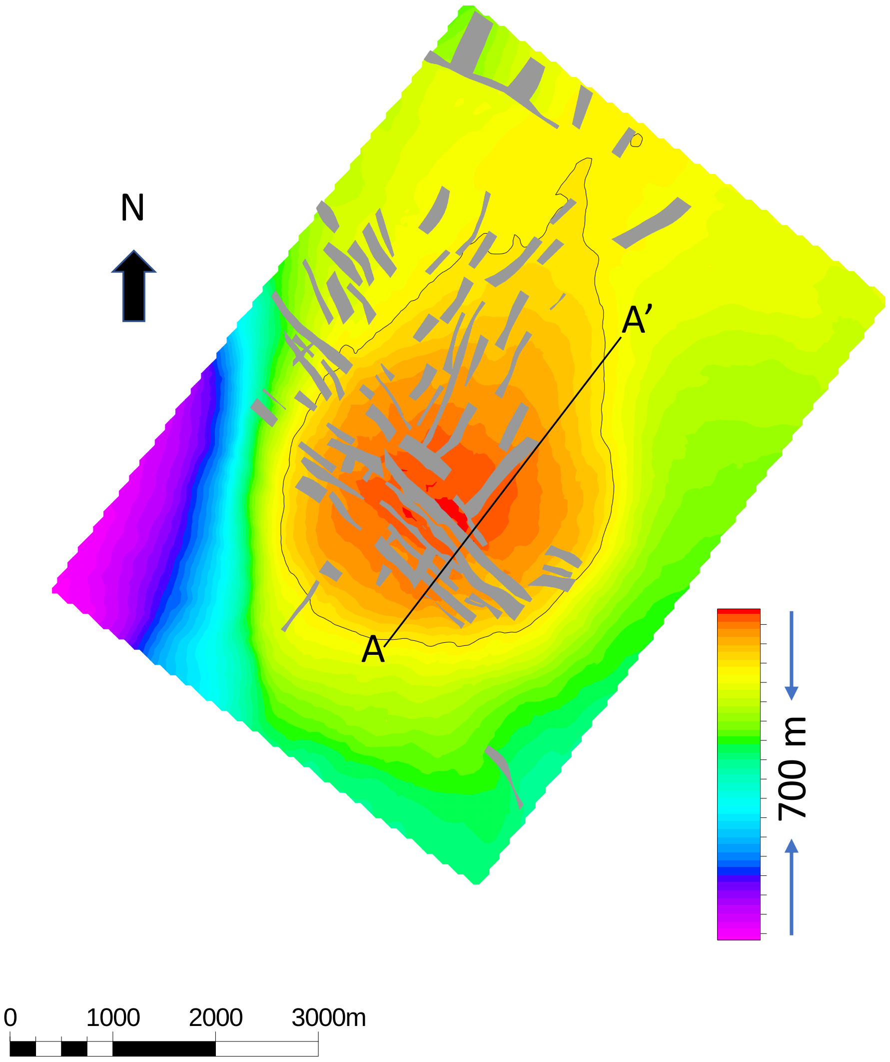

FIGURE 2.1. Depth map of the Shuaiba Formation as mapped from 3D seismic volume after conversion from time to depth domain. The gray-colored elongated shapes are the major seismically interpretable faults. The thicker their aperture, the gentler their dip is. The difference in meters from the crest of the reservoir to the deepest point in the map is about 700 meters. The black contour line marks spill point. Faults have two trends: major NW-SE developed during the Cretaceous and reactivated in the Mesozoic; perpendicular NE-SW faults extend from the deep crystalline basement rocks having a trend parallel to salt basin's major elongation axes. The NW-SE-oriented faults make series of graben structures at the center of the field. The line A-A' marks the location of the the seismic cross-section shown in (Figure 2.7).

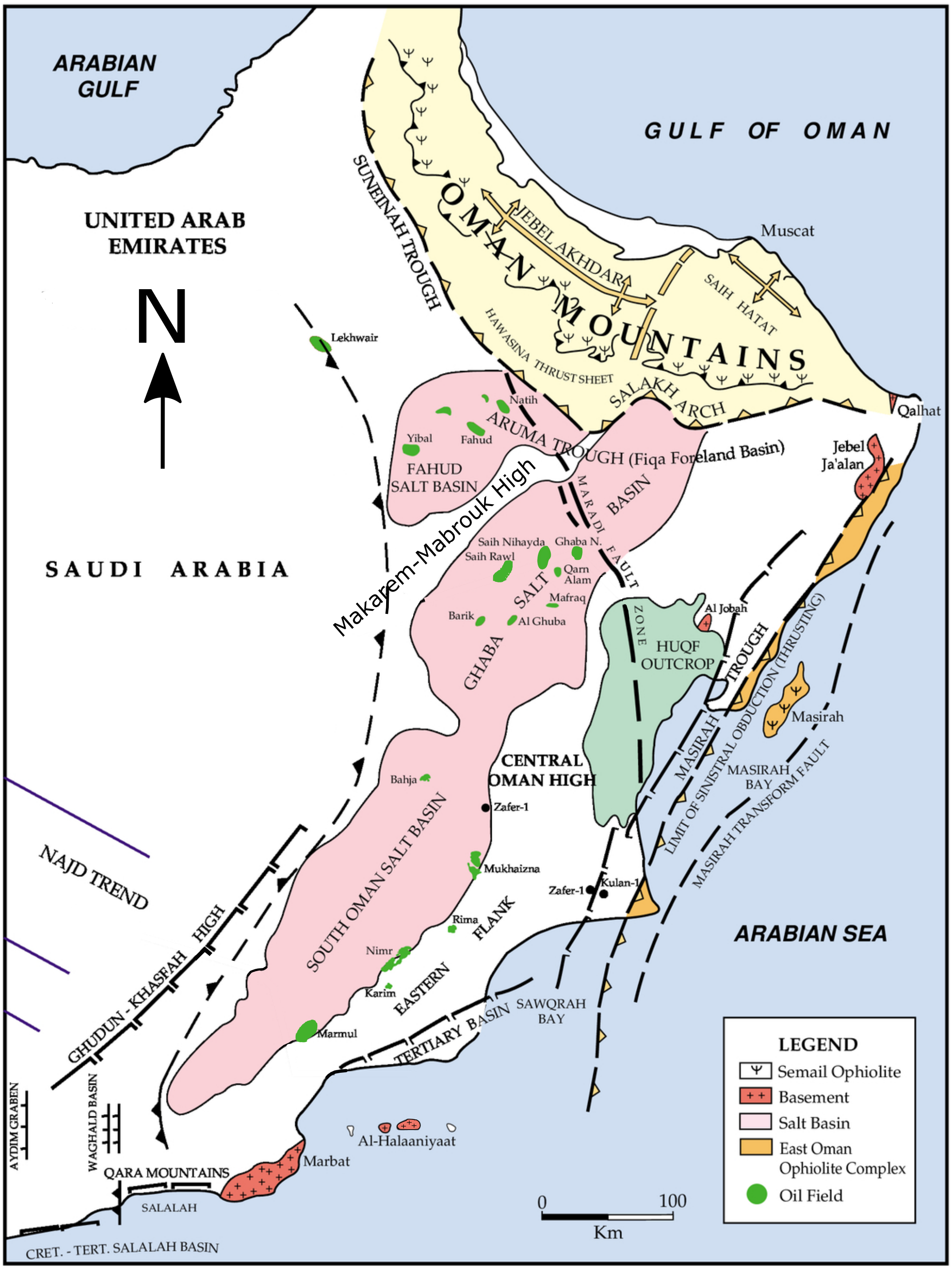

FIGURE 2.2. Three salt basins exist in Oman, each separated by structural highs. The Central Oman high separates the south Oman Salt Basin from Ghaba Salt Basin. The latter is divided from Fahud Salt Basin by Makarem-Mabrouk high. Surface-piercing of Ara Salt is observed at many localities within the Ghaba Salt Basin e.g., Qarat Kibrit. The Precambrian and Palaeozoic rocks outcrop in Huqf-Haushi Highs. Surface exposure of Shuaiba and Kharaib can be observed along with Salakh Arch. Adopted and slightly modified from (Loosveld et al., 1996).

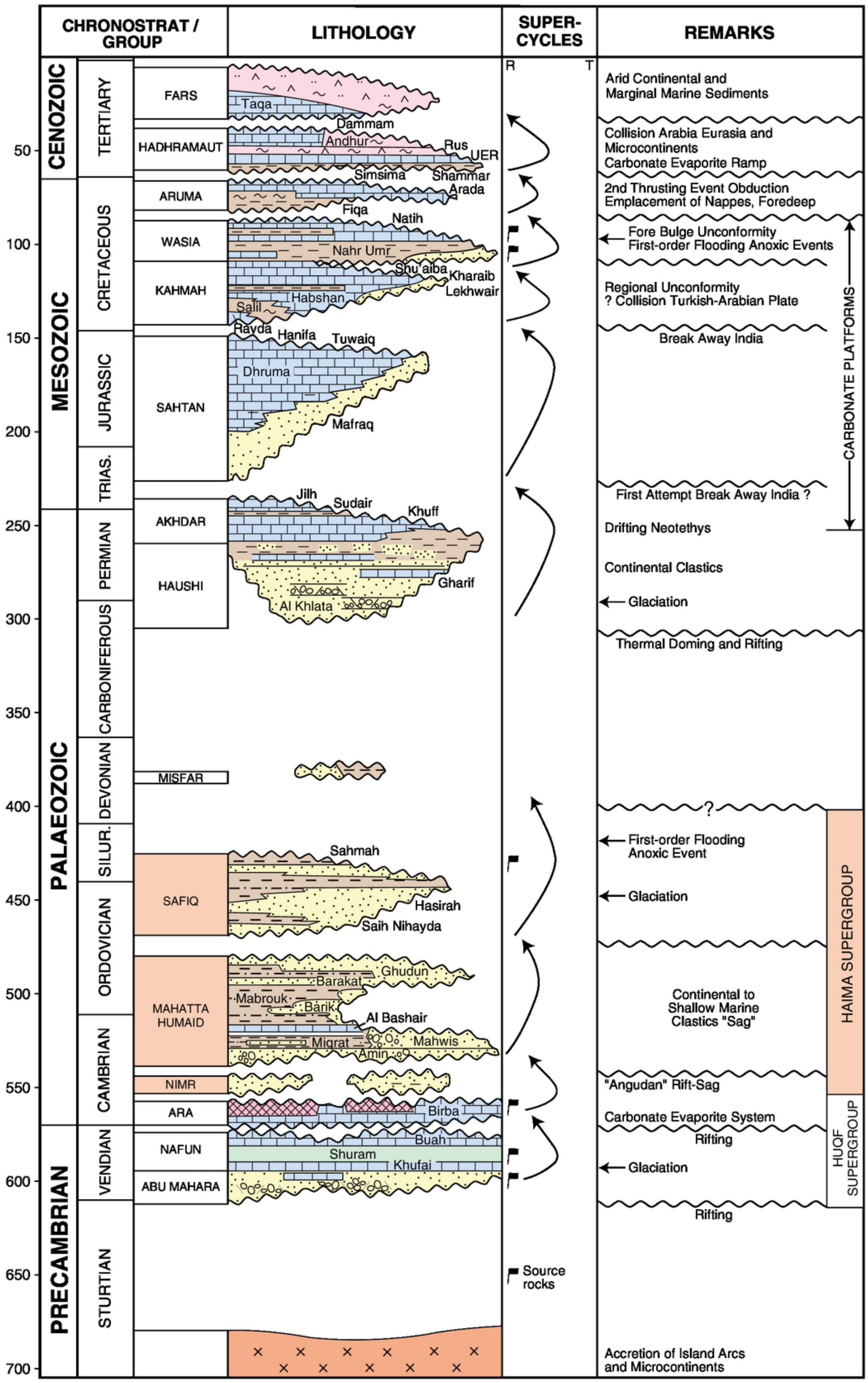

FIGURE 2.3. Stratigraphic column of Oman geology. This project focuses on Kahmah and Wasia Groups of Cretaceous Period. The first consists of both reservoir units of Shuaiba and Kharaib Formations while the latter contains the seal rock Nahr Umr Formation. Adopted from Droste (1997).

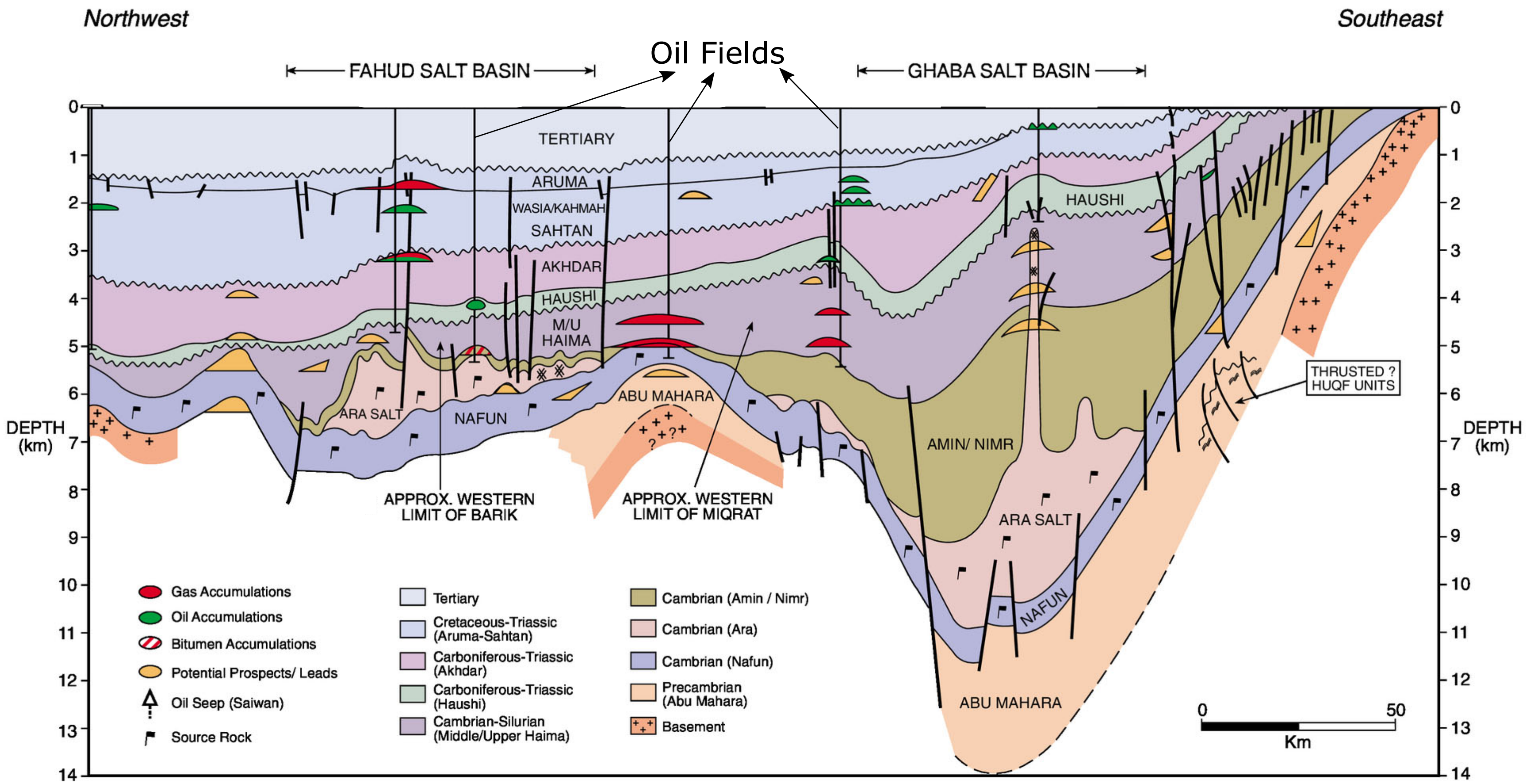

FIGURE 2.4. Simplified geologic cross-section along major subsurface Formations central Oman. Ara Salt in north Oman is thicker and deeper than in south the Oman Salt Basin. The reservoir units and the overlaying seal rock in this study are located within Kahmah and Wasia Groups, respectively. The Cretaceous platform forms Hajar Supergroup. Adopted and modified from Droste (1997).

2.2 Sedimentary facies

Shuiaba and Kharaib Formations belong to the Kahmah Group of Late Hauterivian to Aptian in age (Haan et al., 2008) (Figure 2.3). The Group has widespread existence in Oman, UAE, Saudia Arabia, and Qatar, but is known as Thamama in Arab Gulf countries other than Oman. It is one of the main hydrocarbon-bearing rock units in the Middle East, contributing around 25-30% of total oil production in Oman. In fact, Most North Oman oil fields have the Kahmah Group as the main target zone. Its lithological description in Oman was first attempted during the 1960s based on surface outcrops in Jabel Akhdar's culmination, where its best type locality is found at Wadi Kahmah. It comprises a sequence of varying thickness carbonates ranging increasingly from drowned platform pelagic porcelanite, clay, and cherts at the bottom to active platform ramp chalky rudist rich oolitic limestone at the Shuaiba level (Frost et al., 1983). This shoaling-up phase of forced regression (seaward movement of the shoreline) culminates the emergence and partial erosion of Shuaiba in the field X, whereas all Formations of the Kahmah Group are preserved to the western direction approaching the center of Bab Basin in UAE (Rameil et al., 2012), (Figure 2.5).

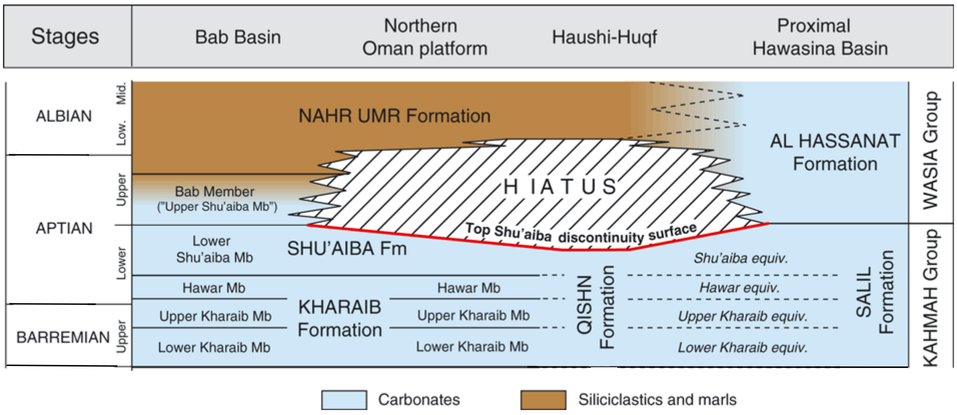

FIGURE 2.5. Kahmah Group deposited on a continental margin. In Central and North Oman, a shoaling-up sequence is observed in sedimentation grain size from fine-grained shallow-marine in the Aptian, to coarse grain wackestone deposits at the upper the Group. A hiatus is created with the emergence of Shuaiba above sea level happened in the eastern side of the Bab Basin. The sequence is followed by Albian transgression and the deposition of the Nahr Umr Formation. Outcrop of the Qishn Formation in the Huqf area is time-equivalent to upper Kahmah Group. Adopted from (Rameil et al., 2012).

the stacked shoaling-up process in which the sedimentation rate exceeds subsidence, is evident in gamma-ray logs shown in (Figure 2.6). A gradual decrease of gamma-ray intensity is observed from below the Lekhwair to the Shuaiba top marker, but occasionally interpreted by short periods of high gamma-ray strikes related to 5^{th} order eustatic sea-level rise. Shallow marine deposits of Sahtan Group stratigraphically and conformably underlays the Kahmah Group at the bottom contact.

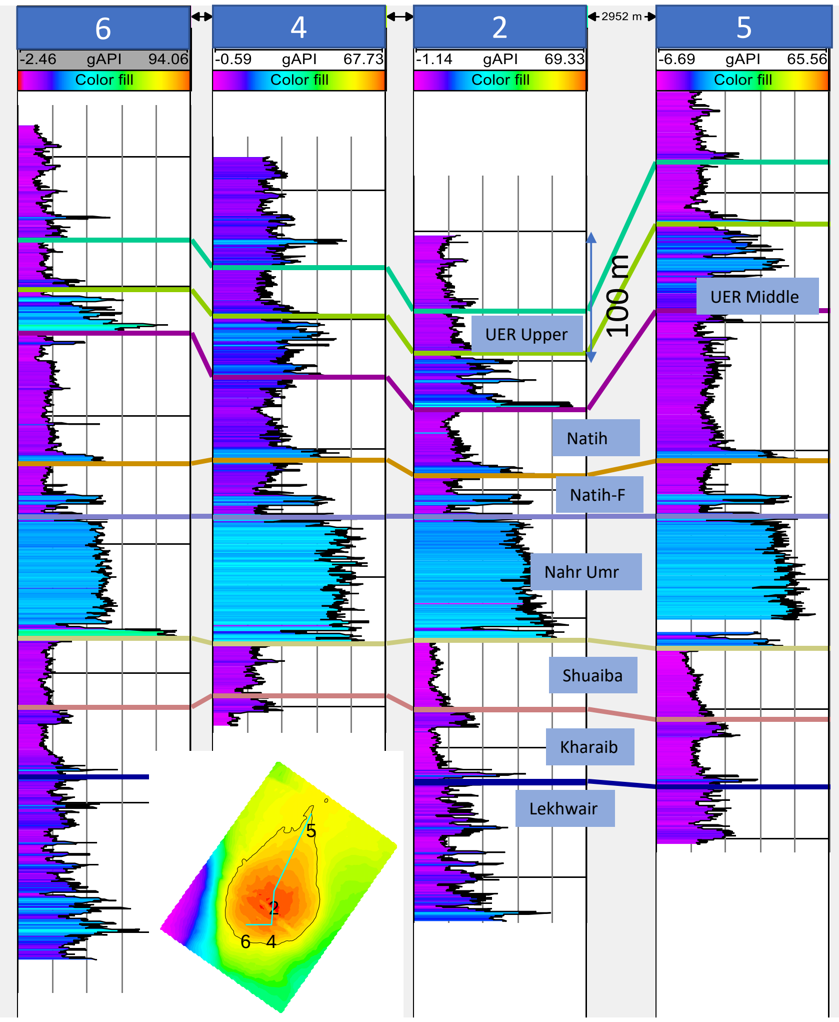

FIGURE 2.6. Gamma ray logs at four wells in the field X. The Kahmah Group is a shoaling-up sequence occasionally interpreted by 5th order eustatic sea-level rise, interpreted as short period strikes of a comparatively high gamma-ray intensity. Natih thickness is variable, getting thinner at the crest of the reservoir and thicker outward. Two rock lithologies can be discerned: (1) Low gamma-ray intensity of the Kahmah Group, Natih units, Upper UER and shallow Tertiary rocks, (2) High gamma-ray intensity, radioactively rich shale units of Nahr Umr and Middle UER. The relative increase in gamma-ray reading at the top of the Kharaib Formation is interpreted as dense limestone of the Hawar Member. Note that, Well 5 has data missing at the bottom of Nahr Umr. Depth reference is flattened on Nahr Umr Formation. Distance from well 2 to 5 is 2952 m. Well locations are shown in the small map, which is the Shuaiba surface as shown in (Figure 2.1).

The Shuaiba is more prolific than the Kharaib Formation, and they are stratigraphically separated by a thin layer of shale known as Hawar Shale member (Masse et al., 1998). Top Shuaiba reflector can be picked relatively easier in seismic section compared to Kharaib Formation, due to progradational clinoforms terminating the continuity of the upper Kahmah layers (Figure 2.7). Therefore, the top Kharaib surface map is generated by adding the Shuaiba map to the thickness difference between the two reservoirs deduced from the well tops. Faults cut through strata from the bottom part of Nahr Umr down until the top of Ara Salt (Not shown in (Figure 2.7)), below which they cannot be traced any further in seismic section, (Figure 2.7).

The Mid-Cretaceous Wasia Group unconformably overlies the Kahmah Group in central Oman, and it consists of the shale unit of Nahr Umr in the lower part and the carbonate Natih Formation in the upper part (Alsharhan, 1991), (Figure 2.5). The upper contact is a significant unconformity eroding almost half of Natih members, A, B, C, and partially D, in this field. The erosion is due to the emplacement of allochthonous Semail Ophiolite and Hawasina sediments on top of the continental crust in North Oman. This led to a foreland bulge in central Oman. Natih is one of the major oil-producing reservoirs in the whole of the Middle East, but Nahr Umr is a seal rock to the underlying Shuaiba Formation in Oman and UAE. This is in contrast to Iraq, Kuwait, and northern Saudi Arabia, where it is also a producing reservoir rock. Although being a shale rock, it is not a source rock for the Shuaiba or the Natih.

2.2.1 Nahr Umr Formation

The Albian Nahr Umr Formation is deposited in a shallow marine to deep shelf environment in the Northern Arabian Peninsula. Sand content increases westward via the inclusion of a higher percentage of interbedded sandstone lenses moving from Bahrain to Iraq, where the Formation is a reservoir rock (Al-Dabbas et al., 2013; AL-Muftah et al., 2019).

In Oman and UAE, the Nahr Umr Formation is mainly comprised of mudstone and siltstone. The lower part of the Formation in this Field contains a thin limestone bed having high radioactivity and very distinct in gamma-ray logs (well 6 of Figure 2.6). It has a fairly constant thickness of 130 m throughout the field except for the area around the central graben structure, where it becomes $\sim 20m$ thinner. Its large uniform isopach makes it an ideal cap rock for the underlying Shauiba Formation, (Figure 2.8). Although being a shale rock, its organic content is only a maximum of 0.5%, making it a poor source rock. The Nahr Umr presents drilling challenges such as circulation loss and well-bore stability due to the existence of abundant clay lamination and microfractures (Nguyen et al., 2009). Lamination and the existence of unidirectional natural microfractures will probably create strong velocity anisotropy and thus shear wave splitting. Internal reflections within Nahr Umr exhibit hummocky seismic facies. Figure 2.7.

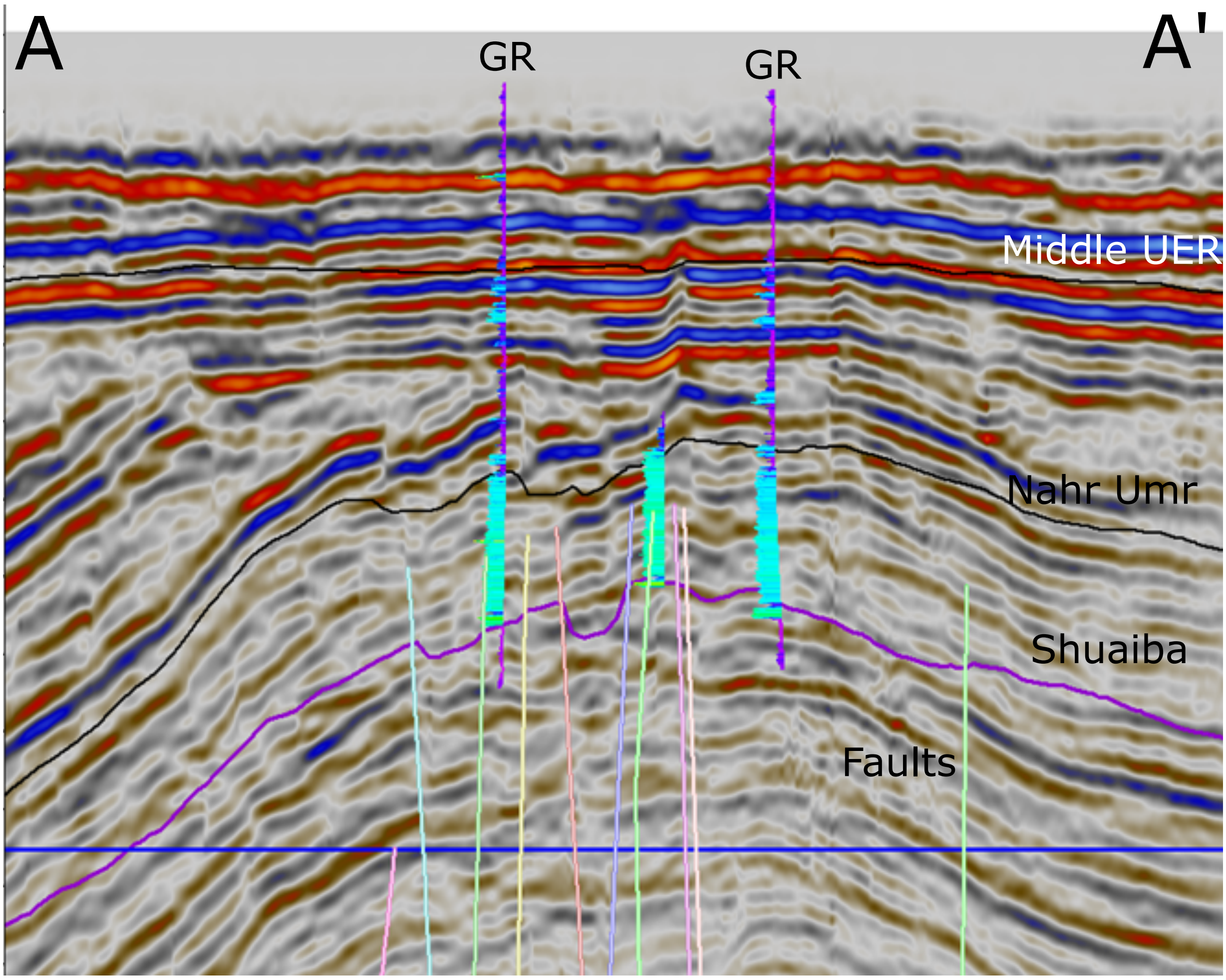

FIGURE 2.7. Seismic section perpendicular to the main graben structure-oriented NW-SE. High angle normal faults extend from the Ara Salt (not visible here) up to the lower part of the Nahr Umr. The main graben structure is located at the center of the section. The faults throw is higher at Shuaiba level than Nahr Umr. The blue colored horizontal line is pre-injection oil-water contact. The outline of this cross-section is shown in (Figure 2.1), (Figure courtesy of PDO).

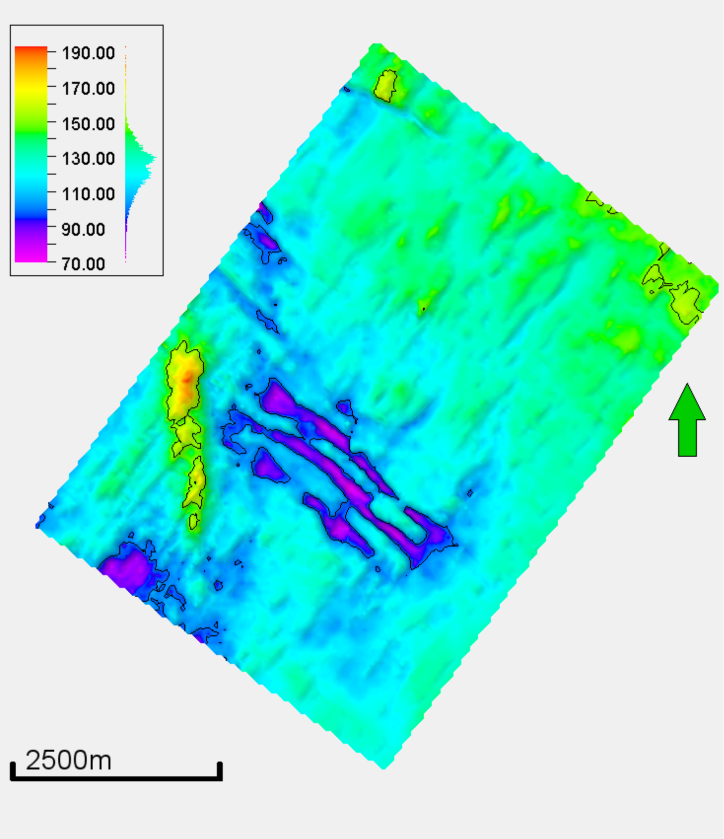

FIGURE 2.8. Isopach map of Nahr Umr. The thickness is approximately constant at 130 m with ±20 m variation around central graben structure and the western steep flank. Thickness histogram is shown to the right of the color-bar.

2.2.2 Shuaiba Formation

The Aptian carbonate Shuaiba Formation constitutes the upper part of the Kahmah Group. It is separated from the underlying Kharaib Formation by a conformably lying thin bed known as the Hawar Member. The latter is correlatable in the subsurface across North Oman and is easily distinguishable through its relative high gamma-ray characteristics (Clarke, 1988; Droste, 2010; Litsey et al., 1986). Well log interpreters usually mark this thin unit as top Kharaib (Figure 2.6).

The thick Nahr Umr shale is the seal rock for the Shuaiba over all of central Oman and most parts of the Arab Gulf countries. However, due to the complex nature of post ophiolite obduction (Forming forebulge and the associated foreland basin in which Aruma Group is deposited) and salt halokinesis, certain areas in Oman have Shuaiba overlain by rocks other than the Nahr Umr. For example, in a Lekhwair field, Shuaiba is overlain by clastic rocks of the Shammar Formation (the Hadhramut Group), whereas in the Huqf-Haushi Highs, it is overlain by the younger Rus or UER Formations. In all case cases, the younger overlaying units act as seal rocks, though not always of the same quality as the Nahr Umr. The exception is at long piercing salt domes of the Ghaba Salt Basin, elevating strata to a very shallow depth and thus breaching seal rock. In Field X, the contact between the Nahr Umr and the Shuaiba is the late Aptian unconformity (Figure 2.5). Further south, deeper layers of the Kahmah Group are also eroded, as shown in (Figure 2.9).

Sedimentologically, core samples studies show that the Shuaiba Formation consists of a complex variable composition of laterally extensive algal wackestone to boundstones in the lower part. The upper part consists of chalky oolitic carbonates rich in organic matter and grainstones to rudstones (Droste, 2010; Litsey et al., 1986). Chalk content increases westward toward the Bab basin in UAE, developing more homogeneity and creating a high percentage vuggy porosity (Alsharham, 1985). Facies analysis of core samples shows that the Formation has experienced post-deposition diagenesis, and part of the Formation was dolomitized with the degree of dolomitization increasing downward (Al-Awar and Humphery, 2012; Sena et al., 2014). The dolomitization was resulted from fluid percolation through deep-seated fault planes. It is believed that dolomitization has helped to slightly improve matrix porosity, particularly in the vicinity of fault planes. Progradational clinoforms patterns are apparent in the seismic section as discontinuous inclined reflections within the Formation (Al-Salmi et al., 2019).

The regional thickness of Shuaiba in Oman is quite variable, with a maximum of 140 m in the Safah field close to the border with the UAE. It thins to both the east and the south for two reasons: 1) Uplift due to salt dome, particularly affecting the Huqf area in the west, and 2) Forebulge uplift caused by ophiolite emplacement, truncating the entire Kahmah Group in both west and south directions. However, in Field X, the thickness of Shuaiba is relatively constant (30 ± 5 m). Small local variations in thickness are attributed to differences in precipitation rate of calcite during deposition and chemical compaction after deposition.

Wireline logs of gamma-ray intensity show similar characteristics throughout the field (Figure 2.6). The bottom of Shuaiba has a relatively high gamma-ray reading associated with dense Hawar Member. In the Shuaiba zone, gamma-ray logs show a funnel-shaped indicative of a change in depositional environment from drowned platform to more active platform ramp at the top of Shuaiba (shoaling-up).

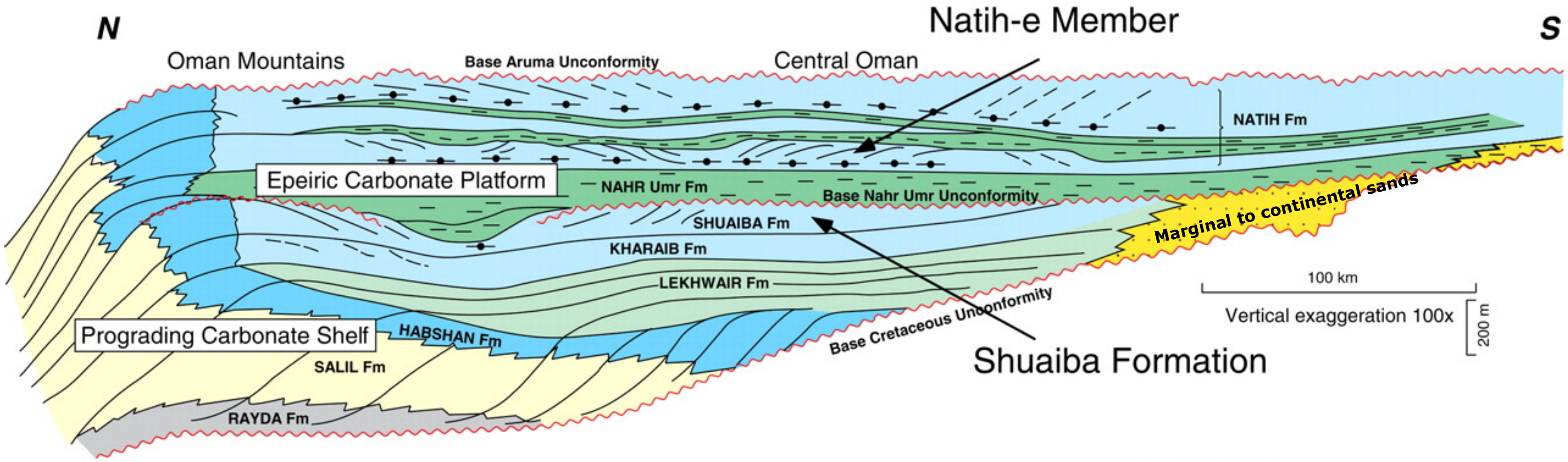

FIGURE 2.9. Geologic cross-section across the Wasia and the Kahmah Groups of the Cretaceous rocks from north to south of Oman irrespective of tectonic activities. Two major uniformities exist within the Wasia and Kahmah groups; the base Aruma and the base Nahr Umr unconformity. The first erodes most of the Natih units up to Natih-E member, and the latter truncates the upper part of Shuaiba in Field X. Adopted from Droste (2010).

2.2.3 Kharaib Formation

The Late Barremian to Early Aptian Kharaib Formation is the second reservoir unit in Field X. It conformably lies on top of the Lekhwair Formation. It represents a transgressive system tract made up of several fifth or fourth-order aggradational and progradational stacked parasequences, capped by the dense Hawar Member (upper part of Kharaib). The Hawar member marks maximum flooding surface (Ehrenberg and Wu, 2019; Strohmenger et al., 2004; van Buchem et al., 2002). It is hard to clearly identify Hawar Member in the surface outcrops at Jabel Akdhar mountains or outcrops of the Adam foothills of the Salakh Arch (Figure 2.2). However, in wireline logs, it is easily distinguishable by a relatively higher gamma-ray intensity and density than the lower unit of Kharaib, (Figure 2.6). Petrophysical reservoir qualities of the Kharaib are somehow more inferior than the Shuaiba Formation (Jeong et al., 2017). In general, both reservoirs developed higher porosity and permeability upward from flanks toward the crest. On a regional scale, reservoir qualities improve westwards and deteriorate northward due to loading and compaction exerted by the ophiolite slab, decreasing their porosity and matrix permeability in Jabel Akhdhar below 0.1 and 5 mD, respectively. Borehole core analysis shows the development of a secondary porosity, indicating leaching due to subareal exposure.

Sedimentological facies of the Kharaib vary regionally based on the depositional system of the carbonate platform. Deposition in moderate energy inner ramp developed a heterogeneous composition of rudstones and floatstones sediments, whereas, in the proximal and distal mid-ramp platform, orbitolina-rich burrowed packstone and wackestone are more abundant (Strohmenger et al., 2004). The presence of post-depositional stylolites (parallel to layer bedding) could have hindered the initial phase of hydrocarbon infilling and possibly acts as barriers to fluid flow (Ehrenberg et al., 2016; Heap et al., 2014).

The thickness of Kharaib in field X is smaller compared to its thickness in the north and the west of Oman. Its thickness in Field X is quite uniform, measuring an average value of 50 m, Figure 2.10. Picking Kharaib top reflection in 2D or 3d seismic data is challenging because impedance contrast along the interface with Shauiba is low. Therefore, Kharaib is usually mapped by isopach stacking of Shuaiba seismically generated surface map with thickness map of Shuaiba generated from well tops. Consequently, the Kharaib surface map looks identical to Shuaiba's map.

Petrophysical properties of both the reservoir units are similar in Field X. Additionally, being intensely fractured might have helped homogenizing fluid interaction between different facies units within the same Formations or across them. Table 2.1 summarizes average reservoir properties for both Formations in Field X. An interesting observation in the table is that the reservoir units have good porosity, but the matrix permeability is very low. This fact, combined with the high viscosity of oil, made the field an ideal case for the application of TA-GOGD as the chosen development plan as was discussed in section 1.2.3.

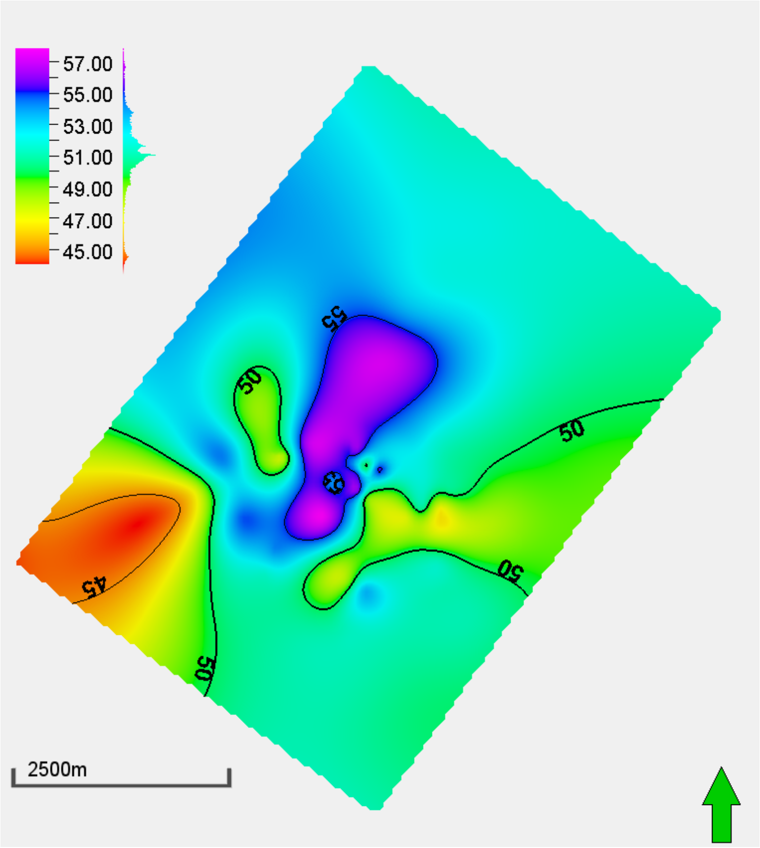

FIGURE 2.10. Isopach map of Kharaib. Thickness of Kharaib is approximately uniform measuring an average value of 50 m. The map is generated via subtraction of top Kharaib from top Lekhwair depths points at well tops and then applying interpolation.

TABLE 2.1. Shuaiba reservoir petrophysical properties.

Reservoir	**Dome-shaped stacked fractured carbonates**
Matrix Porosity	~ 30%
Matrix Permeability	1 - 20 mD
Oil Viscosity	220 cP
Oil Saturation	~ 95%
Gas Oil Ratio	~ 10 sm^3/m^3

2.3 Petroleum system

The trap systems in Oman are generally more complex than what is found in other nearby Middle East countries, ranging from 4-way dome-shaped anticlines and 3-way fault-assisted anticlines to stratigraphic pinch-outs and salt stringers. The first two are common in the North Oman carbonate reservoirs, while the latter types present throughout clastic reservoirs in the South of Oman. Additionally, in recent years due to advances in fracturing technologies, it became possible to target very tight sandstone reservoirs in depths exceeding 3500 m and producing mostly gas.

Source rocks are identified throughout various stratigraphic levels in Oman, ranging from old Proterozoic rocks of the Huqf and the Haima Supergroup to recent Tertiary rocks. Five chemically different types of oil were recognized, namely, Huqf (Shuram Formation), Silurian Safiq Group, Mid-Cretaceous Natih, the Upper Jurassic Diyab Formation, and finally Q-Oil, whose source rock still has not been identified but assumed to be originated from a Formation within the Huqf Supergroup. The Neoproterozoic to Cambrian Huqf and the Q-Oil comprise some of the oldest known source rocks in the world. The Diyab Formation exists in UAE and charged the Cretaceous reservoir units in the Lekhwair, the Dhulaima, and the Safah oil fields located at the border with UAE (Grantham, 1986; Grantham et al., 1990; Terken et al., 2001).

2.3.1 Trap system

The Trap system in field X developed during different tectonic events starting from the deposition of the Huqf Supergroup (Figure 2.3), followed by the Aptian ophiolite obduction, and finally deposition of the Tertiary rocks in a stage of extensional stress regime and eustatic sea-level rise. The most important mechanism during the entire geologic age contributing to the Formation of the 4-way anticline in field X is salt halokinesis creating diapirs, folding upper strata, and forming deep-seated faults. Several oil fields located within the same basin share a similar trap system, particularly those producing from the Shuaiba and the Kharaib reservoir rocks (Al-Kindi and Richard, 2014).

2.3.2 Seal

The Nahr Umr Formation acts as an excellent seal rock for the majority of the Shuaiba Reservoir in the Middle East. Its large thickness and incompetent nature reduce the number of dilational faults to extends and cut into the overlaying shallower layers and hence preserved the trap system even at juxtaposition lines along faults with large throws, e.g., graben structure. These characteristics of the seal helped maintain reservoir pressure during the early stages of production when dissolved gases break out of the solution forming a gas cap which contributed to the reservoir drive mechanism in addition to the aquifer drive.

2.3.3 Source rock maturation and migration

The Shuaiba and the Kharaib were deposited in a hyperoxic environment, then exposed to the surface in Turonian time before being overlain by Nahr Umr (Scott, 1990). These factors led to the disintegration of autochthonous existing organic content. The upper part of the Kahmah Group never reached the oil generation window in Oman except at the foredeep region of the Oman foreland basin system along the margin with Oman North Mountains range. The Shallower unit of Natih Formation is both a reservoir and a source rock which matured and started oil generation since the Late Cretaceous to present days mostly from the deepest part of the kitchen in the foreland basin (Terken, 1999). Source rock that fed the reservoir units of the upper Kahmah Group are located within the Huqf Supergroup (Huqf and Q-Oil) (Figure 2.3).

The deep-seated basement faults acted as conduits for the oil migration (Filbrandt et al., 2006). Oil is believed to be generated from half-mature source rocks after trap formation in late Devonian and undergone slight degradation after migration into the reservoir units, decreasing its API. The amount of hydrocarbon migrated into the reservoir units was dependent on the source maturation level, the existence of traps, and the extent of the faults juxtaposition. Tectonically, the source rocks experienced deep burial in a rifting phase, followed by an uplift with minor subsidence and associated with raised palaeo heat (Grantham et al., 1990; Grosjean et al., 2012; Visser, 1991). Several nearby oil fields produce medium to heavy oil.

2.4 Production challenges

Oil production from the field started in 1975 and peaked after the end of the first year but declined at a rapid rate to a none profitable level at the beginning of the third year. Despite having a vast Stock Tank Oil Initially In Place (STOIIP), oil is mainly produced from the dense fracture network contributing to only about 3% of the STOIIP, whereas the remaining oil in the rock matrix was unrecoverable via the initial main recovery technique of cold gas-oil gravity drainage (GODG). The latter is supported by a secondary gas cap of 30 m occupying the fracture system and a continued aquifer pressure. Gas cap formed after gas injection from several production wells into the fractures within the oil-bearing zone to introduce additional pressure and reduce oil density using the gas lift mechanism. In general, the primary initial oil production mechanism is gravity drainage, subdivided in half between gas-oil and water-oil gravity drainage. The high viscosity of the oil made further seepage of oil from rock matrix via gravity drainage or enhanced GOGD processes of production prolonged and unfavorable.

Pressure build-up tests showed a variation in the permeability of fracture corridors from 10 to 1000 mD based on their proximity to faults, post-depositional cementation, and leaching. On the other hand, matrix permeability was only 5-20 mD. Water breakthrough was measured as high as 90% in some of vertical producing wells at the early stage of the production, which indicates fractures are wide open and continuous throughout oil and water columns, hence resulted in oil being bypassed and the Oil Water Contact (OWC) slightly raised upward before oil was swept entirely. The oil-wet nature of the reservoir played a critical role in oil retention to the rock matrix and posed a challenge to field development. Under these circumstances, it was estimated that without using EOR techniques, only about 5% of STOIIP could be produced within a reasonable timeframe. Therefore, several EOR methods were suggested, including hot water injection, in-situ combustion, and steam injection. The latter was considered more suitable, as was proved by pilot tests, increasing the recovery rate to almost 40%. Pilot tests of TA-GOGD conducted at the crest of the reservoir for an extended time showed that oil viscosity decreased to 20 cP or less. Test results have shown that Field X exhibits wettability reversal from oil-wet to water-wet upon continuous exposure to heating.

The delayed application of EOR techniques is partly due to the high capital cost of full-field scale development using any sophisticated derive mechanism, particularly there were no analog cases to learn from, and the industry in the Middle East has not matured enough to embark full exploitation of heavy oil fields. Nevertheless, field development plans usually take years of building a representative static reservoir model, numerical simulation, and laboratory experiments to understand field's response to different scenarios.

2.5 In-situ stress

(Filbrandt et al., 2006) had made an extensive study on the effect of different tectonic activity on the stress state on north Oman using an integrated approach including various data types such as 3D seismic, surface outcrop measurements, and subsurface formation images logs. In their study, they conclude that Oman has undergone mainly two phases of stress regime, which considerably affected several oil fields' structural and petroleum elements. The first obsolete stress direction is oriented NW-SE, which was active until the Campanian and is related to the collision of the Arabian plate with the Indian plate. This period is dominated by thrusting and oblique strike-slip faults, producing major fault-assisted trap systems like the Fahud and the Natih fields. This event might have allowed the re-migration of hydrocarbon from deep clastic sediments of the Huqf and Haushi to the Hajar Supergroup carbonate rocks (Figure 2.3). Fractures associated with this event are now mainly none-conductive.

Maximum horizontal in-situ stress orientation changed course 180° to the present-day NE-SW trend in Oligocene and Miocene due to the obduction of the Arabian plate underneath the Eurasian plate and the emplacement of Semail ophiolite. Figure 2.11 shows the present-day in-situ stress orientation at Oman Salt Basins. Minor variation in the orientation of the in-situ stress from one locality to another could be attributed to local salt movement post ophiolite obduction.

(Warrlich et al., 2009) made fracture modeling of a nearby field having similar characteristics to the field X using downhole wireline logs of borehole image, resistivity, and sonic. They deduced that open fractures are oriented parallel to the present-day in-situ stress direction. Bedding interfaces of the Formations usually interpret fractures continuation. Figure 2.12 depicts rose diagrams of a) major seismically mappable faults, b) mega open communicating fractures, c) closed none-conductive fractures, and finally d) in-situ stress direction.

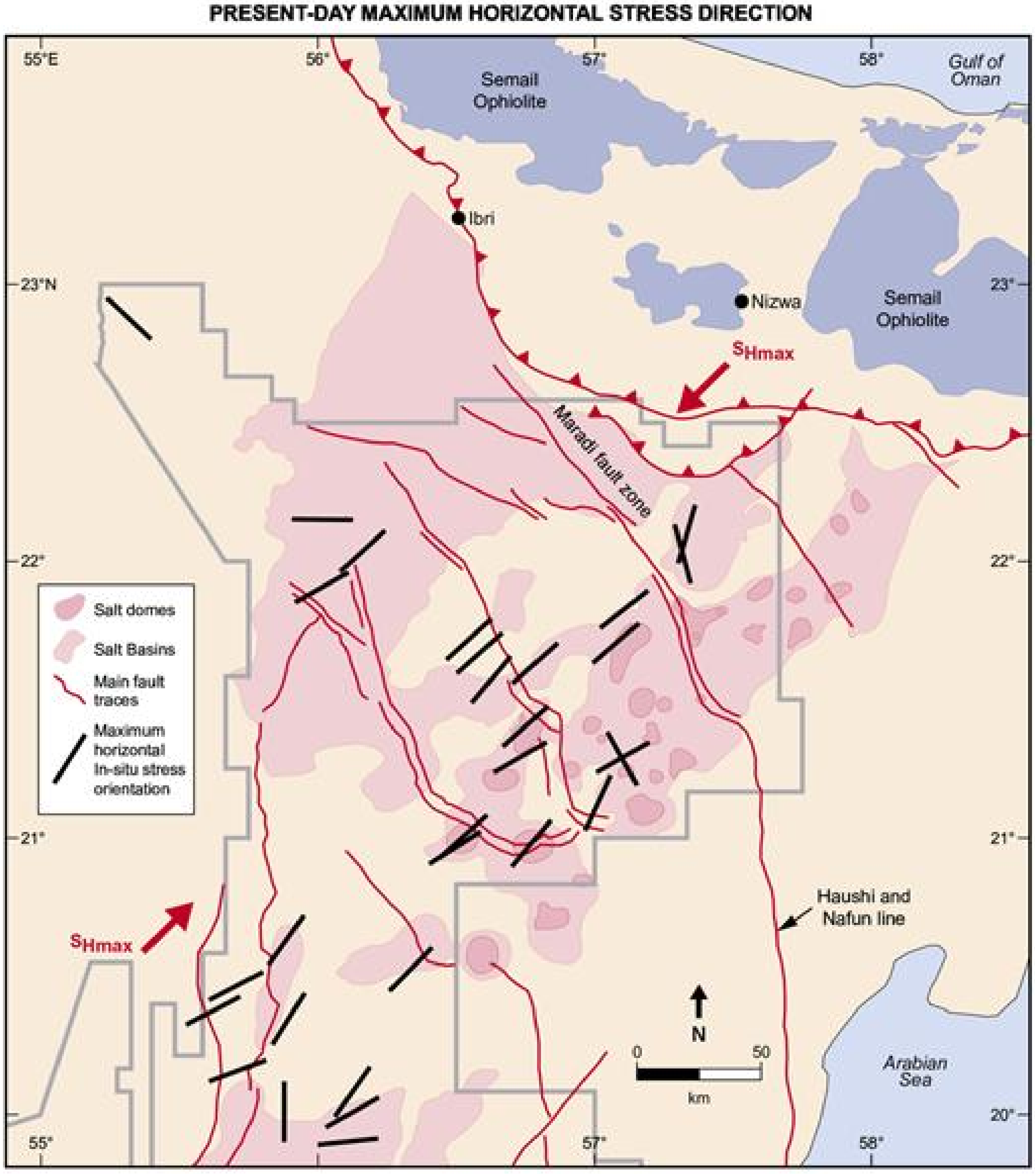

FIGURE 2.11. Present-day insitu stress orientation in Oman Salt Basin. Adapted from Filbrandt et al. (2006)

.

(a) Major seismic faults

(b) Open mega fractures

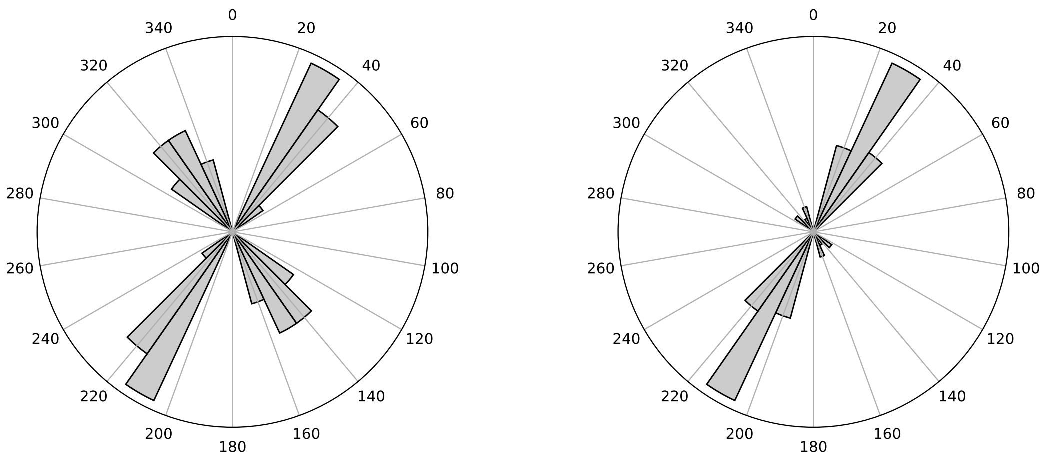

(c) Closed fractures

(d) Maximum horizontal insitu shear stress

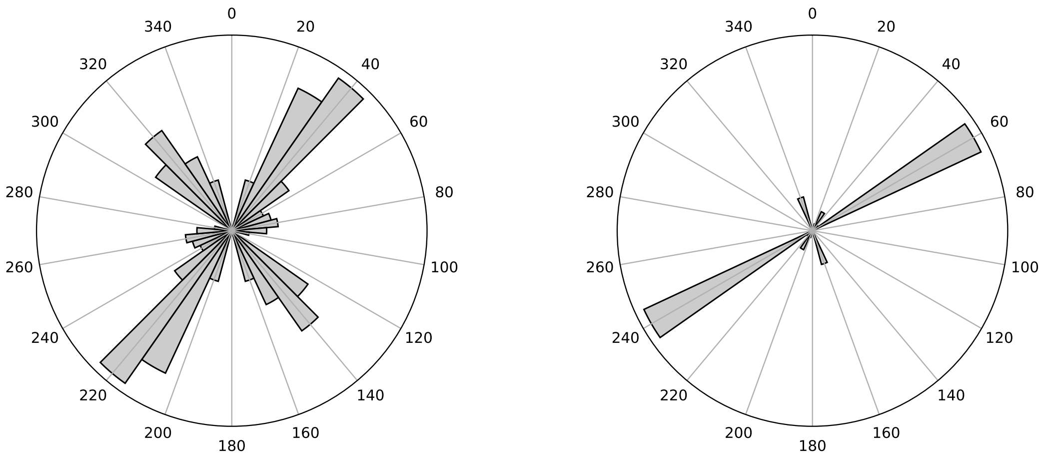

FIGURE 2.12. Rose diagrams of faults, fractures and insitu stress in the subject field. Modified after (Warrlich et al., 2009)

2.6 Fracture characterization from subsurface and outcrop data

2.6.1 Subsurface data

(Rawnsley et al., 2013, 2005) have done a detailed study on the subsurface data for field X. In their study, they created a static model of the reservoir Figure 2.13, incorporating data gathered from several wells and integrating them with 3D seismic data. The objective was to assess the connectivity of the fracture system since it determines the speed of heat conduction into the rock. They found that fractures are mainly oriented NE-SW, and their density increases in the Shuaiba unit. There are also fractures branching out from NW-SE and NE-SW faults system. Their model shows that the main controlling factor of fracture distribution is of structural origin. Fracture density increases toward the existing fault or at close proximity to the field's curvatures. Change in facies has no significant contribution. They claim that fractures are open and highly connected, as indicated by drastic circulation loss upon landing on reservoir crest while drilling. The contribution of 3D seismic to the model building process was limited by the poor quality of the seismic data, and thus borehole image data has the lion share toward understanding fracture characteristics. They believe incorporating higher quality 3D seismic or microseismic data might help to construct a full discrete fracture network and understand the geomechanical behavior of Field X to the steam injection process.

(Warrlich et al., 2009) conducted a similar study to a nearby field producing from heavy oil by TA-GOGD. Although the orientation of the fractures is different, they found that fracture density around faults, their spacing, and permeability characteristics are quite similar. They categorized fracture into three types based on their ability to flow fluid as highly-likey, probable, or possible. This categorization allowed them to create different scenarios for the field development plan. Fractures become none conductive electrically with respect to depth due to an increase in cementation by calcite infilling. These none conductive fractures have a dual-orientation similar to the orientation of the faults (Figure 2.12(b)). Open mega fractures (Figure 2.12()) shows no mechanical hindrance into their electrical conductivity in the Shuaiba reservoir. Breakouts in the Formation wall are aligned with the same orientation as the maximum stress direction. The 3D seismic data is ant tracked (seismic discontinuity) to produce a fracture network system but is constricted by the resolution of the seismic data. Nevertheless, surface time-lapse seismic cannot usually capture the rapid physical changes in rock properties due to steam being injected on a daily basis. The dynamic nature of surface activities and ever-changing infrastructure cannot guarantee good repeatability between the base and repeat 4D seismic surveys (Forgues et al., 2011; Naess, 2006). However, advanced seismic imaging techniques such as Amplitude versus Offset and Azimuth (AVOA) and Quality Factor Versus Offset and Azimuth (QVOA) can characterize fracture properties within a reservoir (Minsley et al., 2004; Vizuett and Davis, 2017).

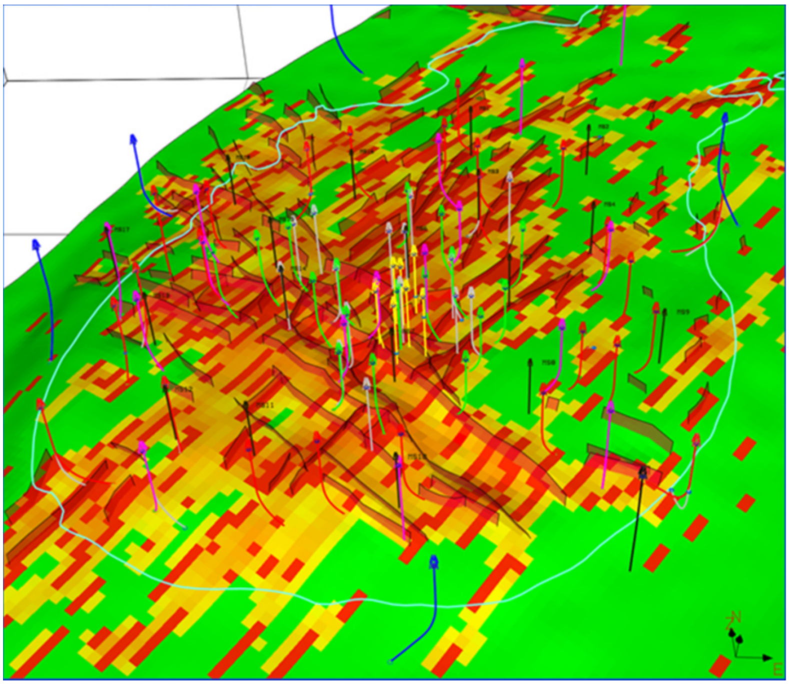

FIGURE 2.13. Reservoir fracture model from integrated study of borehole and 3D seismic data (Ant tracking). Hot colours correspond to closer spacing. Adapted from Rawnsley et al. (2013).

2.6.2 Outcrop data

The best analog outcrops are located at the foothills of Salakh Arch to the north of Field X and the Huqf mountains highs in the south-east (Figure 2.2). Qishn Formation found in the Huqf mountains is time equivalent to Shuaiba Formation (Figures 2.2, 2.5). Bertotti et al. (2005) studied structural features in Qishn Formation and discovered abundant of 1-6 m sub-vertical joints oriented NW-SE and NE-SW. De Keijzer et al. (2007) made a study of one of the five mountains of Salakh Arch. They reported a very similar trend of faults as found in the subsurface. The fracture density is higher upward, and conglomerates into clusters around major faults. They vary a lot in length from a few centimeters to 6 meters. Al-Kindi (2006) made an extensive study on all foothills of Salakh Arch and observed variation in fracture trend from one mountain anticline to another. He concluded that there are three main fracture trends; E-W, NE-SW, and NW-SE. The trend follows the long axes of the anticline, suggesting that local thrusting and uplift have played a role in their Formation. They are also variable in length and opening, measuring at 2-20 meters and an average of 8 mm, respectively.

2.7 Conclusion

In this chapter, I summarized the geologic history of north Oman from the Precambrian to the Cenozoic. The major tectonic events presented in Oman were briefed. It was explained how the tectonic setting of Oman was evolved through time and the controlling factors in the development of major oil fields. Two tectonic events are responsible for the creation of the field's doom shape. The first is salt diapirism, and the second is the Ophiolite obduction. The first contributed to the overall shape of the field, and the latter developed petroleum elements. The field X is comprised of two stacked highly faulted and fractured carbonate rocks. They have a good porosity but a bad matrix permeability. The reservoir is charged by hydrocarbon migrating from the deep Formation located within the Huqf Supergroup through the faults system developed during the emplacement of allochthonous rocks on North Oman. The primary production pumped out oil contained in the fracture system, which has a high permeability. The high viscosity oil initiated the need to deploy EOR technique for long-term field development. The TA-GOGD method after several pilot tests proved to hugely increase the recovery factor and thus is adopted for the development plan. The fracture network plays a critical role in the success of the TA-GOGD techniques as they facilitate heat flow and increase the rate at which oil viscosity is reduced. Several scholars conducted an integrated study incorporating surface and subsurface data to characterize the fractures' properties and understand their heterogeneity. The faults have two orientations, major NW-SE and minor NE-SW. The Fractures are oriented NE-SW parallel to the minor orientation of the faults. They are open, interconnected and their density increases toward major faults.

CHAPTER 3

DATA PROCESSING AND PREPARATION

> *"Advances in science and current production methods are enhancing the output levels of our petroleum resources. As little as ten years ago, tight oil or shale oil, was not even considered a part of a nation's stated reserves. These newer technologies are giving the oil and gas industry a new face."*
>
> — Shawn Barholomae

Any seismic dataset requires a degree of preprocessing to enhance SNR. Ideally, microseismic data are noise-free with sharp impulse phase amplitudes. Furthermore, accurate sensor location and orientation are necessary to locate microseismic events successfully. This chapter first discusses the application of several geophone orientation techniques. PDO provided the event data in a raw format without any preprocessing. Microseismic analysis requires geophone orientation to be known before commencing event location and subsequent source parameter estimation. A new orientation method is developed and compared with several other established techniques to assess its fidelity. The task is to find the orientation of geophone components from 8 vibroseis shots made at the surface per each microseismic well. Five different orientation techniques are tested. In the second section of the chapter, data are filtered using a newly developed multi-notch and a Butterworth bandpass filter to remove random monochromatic and low-frequency noise, respectively.

3.1 Microseismic equipment setup at Field X

Permanent microseismic monitoring has been installed in Field X since 2010 and the actual event detection started by April 2011. The deployment program was completed over the course of six months, from November 2009 till April 2010. A total of 14 microseismic monitoring wells were initially installed at the crest of the field (Figure 3.1). Microseismic wells are numbered from 4 to 17. The first three were discarded from the monitoring program and used for other purposes. A system check had shown poor resistance values for the geophone array in well-13 and thus found to be non-operational. Therefore, in this thesis, the microseismic data are acquired by 13 monitoring wells. The average inter-spacing between the wells is approximately 700-800 meters. The total number of events recorded by the network between the period from 5th of April 2011 until the end of August 2015 is 7201.

There are eight triaxial geophones installed in each monitoring well (Figure 3.2). The geophones are accompanied by two thermistors that record the geophones' temperature continuously. The geophones operating temperature is between $-40\,^{\circ}\mathrm{C}$ to $200\,^{\circ}\mathrm{C}$. These geophones are known as OMNI2400 geophones, have a sensitivity of 86.6 (v/m/s), and record frequencies greater than 15Hz. The spacing between the geophones is 20 meters, and the deepest geophone is 2 meters above the wells' total depth. The geophone axes are gimballed so as the vertical axis is pointing upward and the two horizontal axes are at a right angle (orthogonal) to each other. In chapter 3.2, the orientation of the horizontal components will be determined.

Although the contractor company that worked on the installation of the microseismic system reported in March 2011 that all microseismic sensors are fully operational, I found that some geophones are unserviceable or having at least one component dead (always reading zero amplitude in all events) (Table 3.1). These geophones were excluded from location algorithms since they provide unreliable location and source parameters results. Deeper sensors have a higher rate of failure than shallower ones. An interesting observation is that microseismic wells located at the flanks of the reservoir (e.g., MSW-14 and MSW-16) have more failed sensors than the ones located at the crest of the reservoir (e.g., MSW-4, MSW-7, MSW-9). Deeper geophones also usually have higher SNR than shallower ones for reasons discussed in chapter 3.

All in One (AIO) units record the continuous microseismic waveform data in real-time. The AIO contains a radio transmission and GPS antenna, power supply solar panel, and a junction box, which in turn constitutes the recording system. The recording system executes the typical

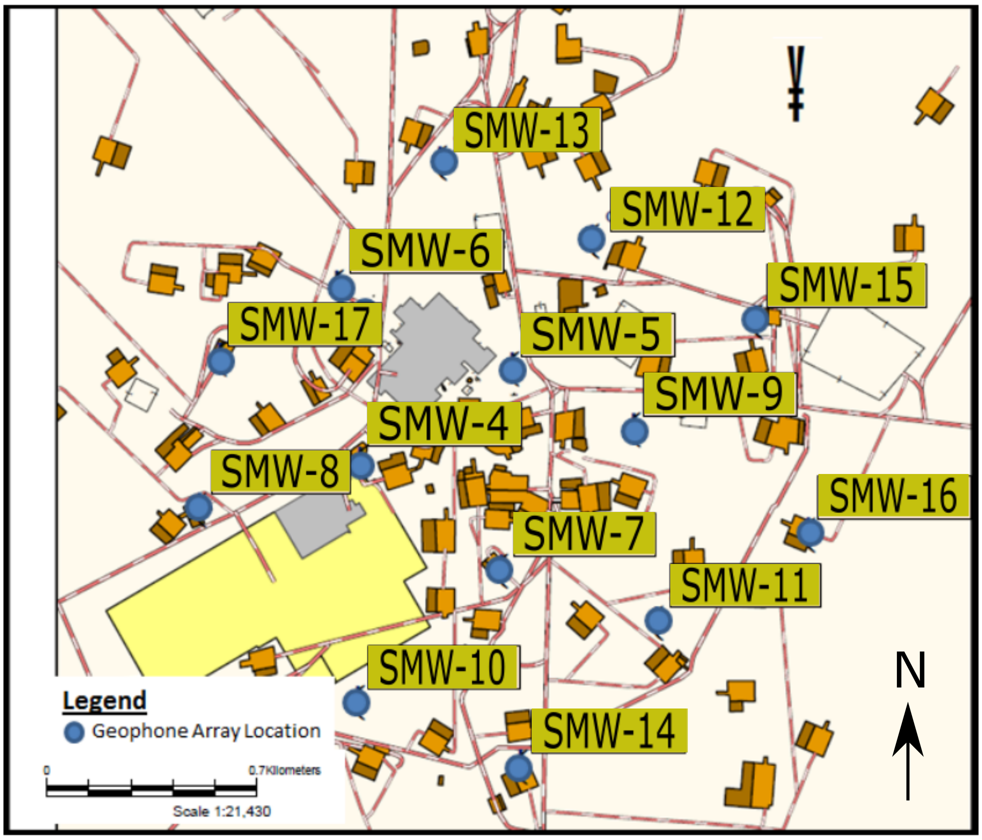

FIGURE 3.1. A surface map of the seismic monitoring wells (SMW) in blue circles. Small rectangular boxes are the drilling rigs. Yellow and gray areas are the field's surface operating infrastructures. SMW are numbered from 3 to 17. SMW numbers 1, 2, 3, and 13 were not provided or have been discarded from the monitoring project. Courtesy of PDO.

seismic acquisition routines such as digitization and amplification. The recording systems are connected to the geophones having a sampling frequency of 4000 Hz. Data transmits from the junction box after amplification to a local computer which auto-triggers events based on amplitude threshold and STA/LTA methods. The triggering system is set so that when an event is triggered in only one monitoring well, two other closest monitoring wells will also record the same event. For example, if an event is triggered in two distant monitoring wells, the total number of wells that record the same event is six. But if these two monitoring wells are close to each other, the total number of wells recording the event could be less than six. A central server located in Oman then receives the triggered events from Field X and other oil fields. This central computer can perform reconnaissance processing of events in near real-time. However, comprehensive analysis,

TABLE 3.1. Operational status of the downhole geophones. Green (Fully operational), yellow (1 componenet dead), brown (2 components dead), red (unserviceable).

	SMW-4	SMW-5	SMW-6	SMW-7	SMW-8	SMW-9	SMW-10	SMW-11	SMW-12	SMW-14	SMW-15	SMW-16	SMW-17
Geophone 1	🟩	🟩	🟩	🟩	🟩	🟩	🟩	🟩	🟩	🟩	🟩	🟫	🟩
Geophone 2	🟩	🟩	🟩	🟩	🟩	🟩	🟩	🟩	🟫	🟩	🟨	🟫	🟩
Geophone 3	🟩	🟩	🟩	🟩	🟩	🟩	🟩	🟩	🟨	🟩	🟫	🟥	🟩
Geophone 4	🟩	🟩	🟨	🟩	🟩	🟩	🟩	🟫	🟩	🟫	🟫	🟫	🟩
Geophone 5	🟨	🟩	🟫	🟩	🟩	🟩	🟨	🟫	🟫	🟫	🟩	🟫	🟩
Geophone 6	🟩	🟩	🟫	🟩	🟩	🟩	🟫	🟫	🟫	🟫	🟫	🟫	🟩
Geophone 7	🟩	🟩	🟫	🟩	🟩	🟨	🟫	🟥	🟩	🟥	🟫	🟫	🟨
Geophone 8	🟩	🟩	🟨	🟩	🟨	🟩	🟩	🟥	🟩	🟥	🟫	🟨	🟫

categorization, and processing of the data are made after they are transmitted to the contractor's headquarter abroad. Figure 3.3 outlines the described recording system and the data flow.

The geophone orientation process requires acquisition or either vibroseis shots made at the surface or controlled perforation shots in the subsurface. In Field X PDO acquired 8 vibrator shots for each monitoring well (Figure 3.4). The proposed layout of the vibrator location is closely resembled by the distribution of vibrator points at seismic well-16. However, due to surface obstacles, the actual layout deviated from the proposed one. One of the advantages of using multiple vibrator shots per monitoring well is the elimination of the uncertainty in the determination of geophone orientation, as will be discussed in chapter 3.

Figure 3.5 combines the geophone locations with the geologic framework and also displays the injection and production well location and configuration. Figure 3.5-(a) shows that no geophone exists in the reservoir units. The gap between the last geophone in the monitoring borehole and the top level of the reservoir is about 40 meters. The steam injectors target the top reservoir unit and drilled from the crest of Field X. The production wells, on the other hand, are drilled from the flanks of the field and enters horizontally into the reservoir zone in the oil rim. Figure 3.5-d is a map view combining the microseismic wells with the production and injection wells.

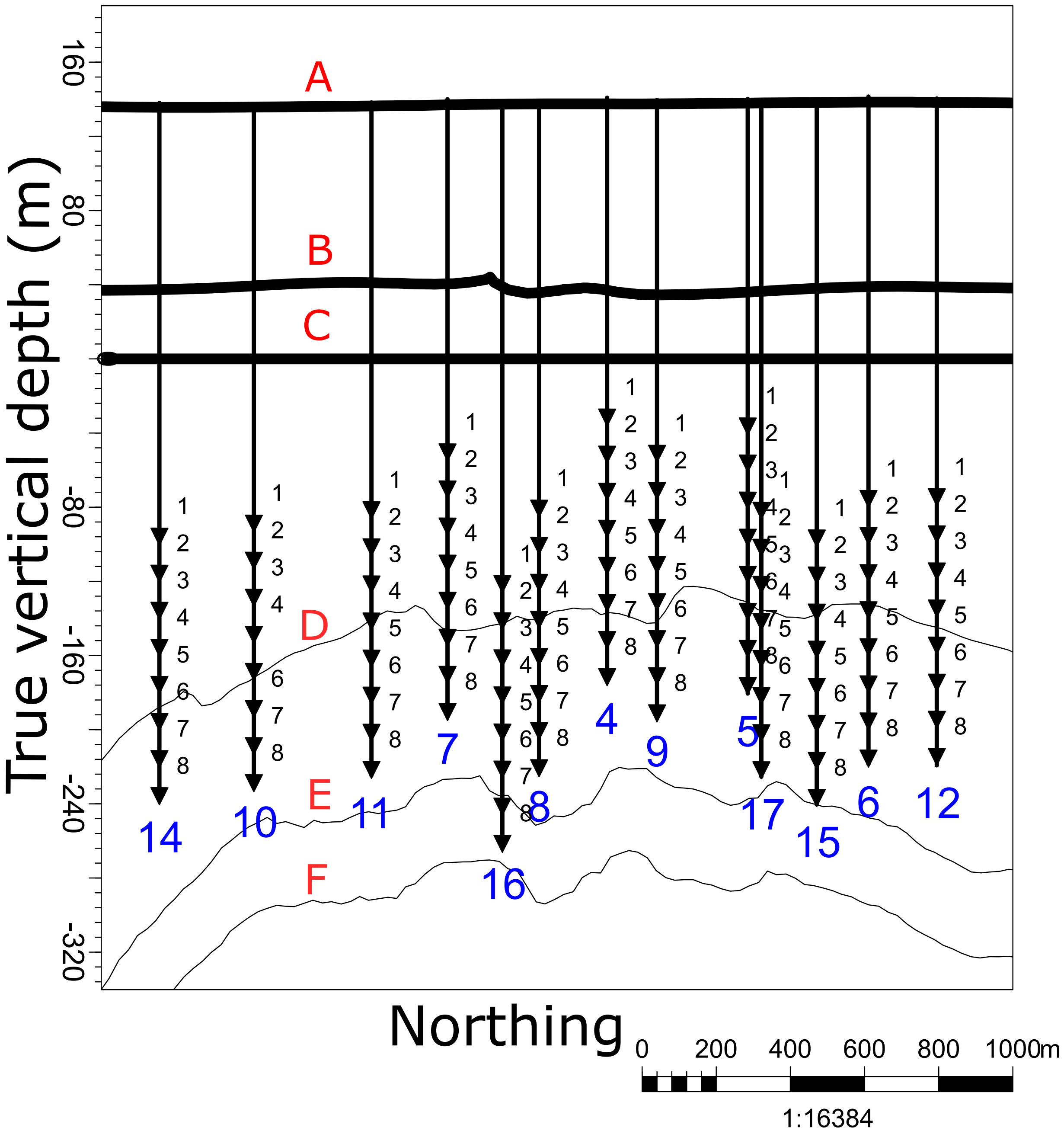

FIGURE 3.2. A cross-sectional illustration of the geophones setup in each microseismic well. The variation in the depth of geophones from one well to another in reference to the mean sea level is related to the dome shape of the field. Somehow a constant distance is maintained from the deepest geophone to the top level of the upper reservoir unit (E-Shuaiba). Therefore, the microseismic well located at the crest of Field X has shallower geophones than microseismic wells drilled along the outer flanks of the field. The north direction increases from left to right. The letters A, B, C, D, E, and F refer to ground surface, UER, mean sea level, Nahr Umr, Shuaiba, and Kharaib Formations, respectively. Small triangles along the well trajectory are the geophones.

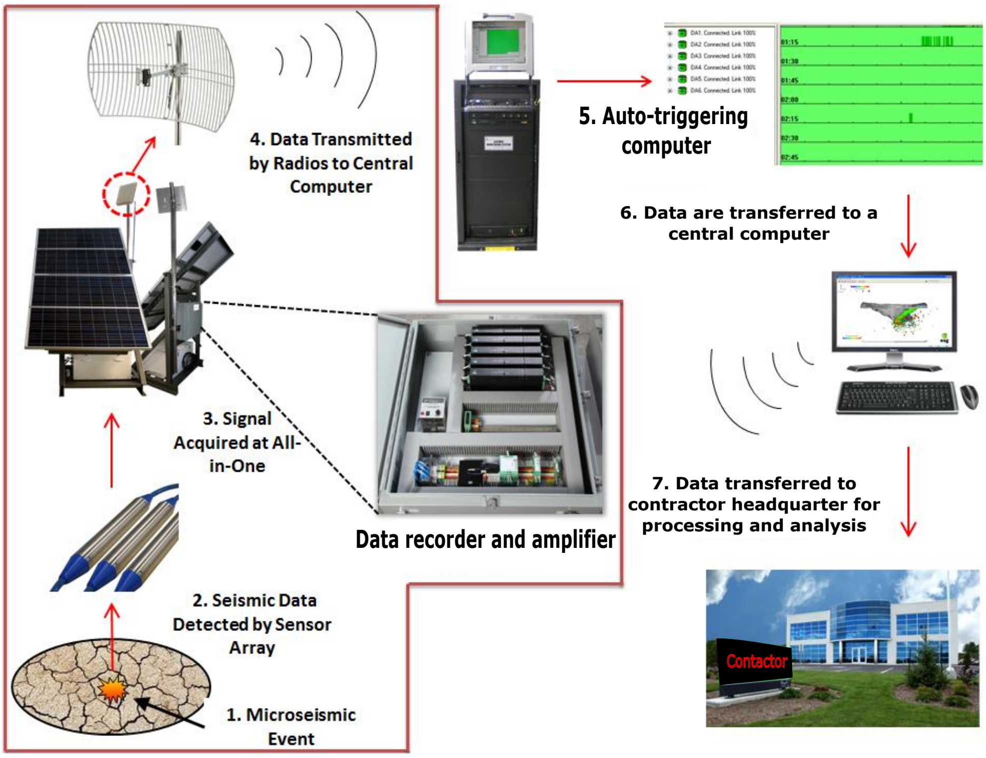

FIGURE 3.3. Microseismic data transmission flow path from subsurface to contractor's headquarter. Courtesy of PDO.

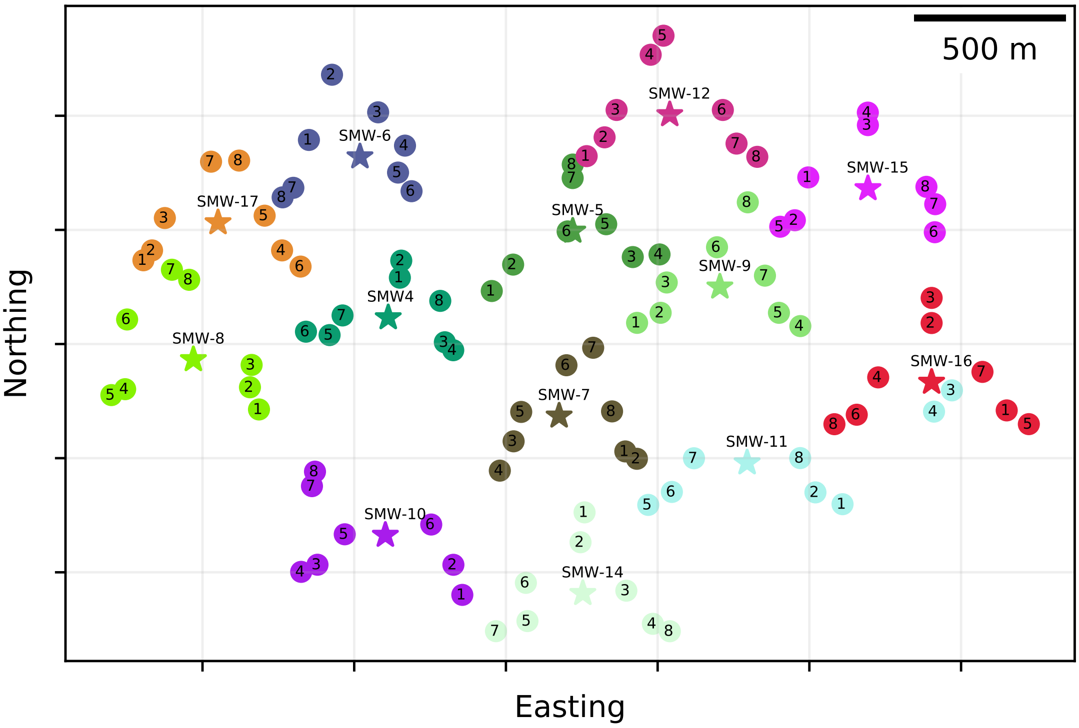

FIGURE 3.4. The layout of the microseismic monitoring wells (star) donated as SMW (seismic monitoring well) and the associated vibrator shots (circle). Vibroseis shots are numbered based on their acquisition date from earliest to latest.

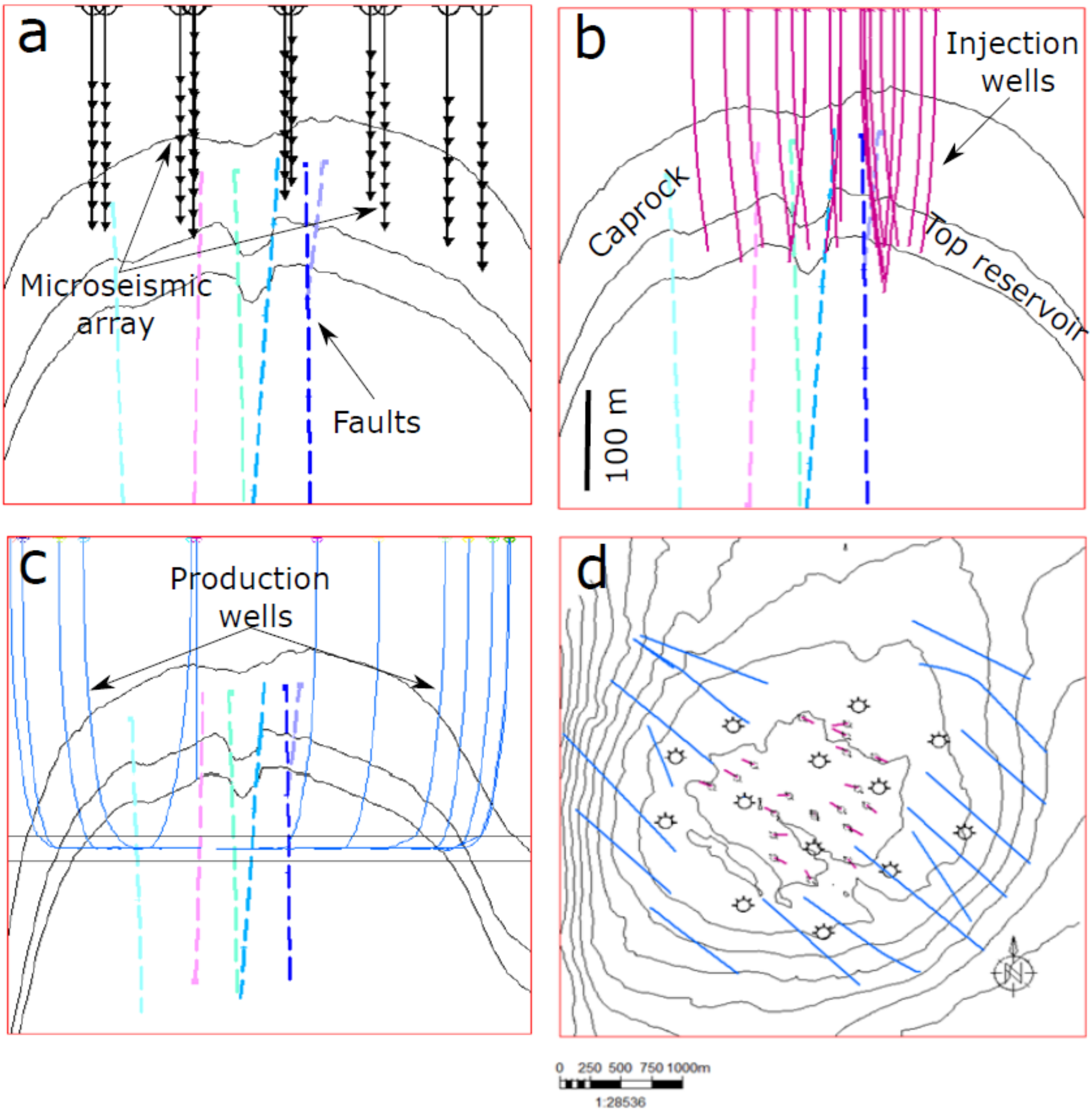

FIGURE 3.5. The layout of the geophones in the monitoring well within the geological framework. The production and injection wells are also displayed. (a), (b) and (c) show the geophone configuration in the subsurface, the injection wells placement, and production well Horizontal path, respectively. Note that in these three cross-sections, the vertical scale is different from the horizontal scale. (d) combines all different well in a map view. The contoured lines (d) belong to the top reservoir depth map. In (c), the two horizontal lines are OWC (deeper) and fracture OWC (shallower).

3.2 Polarization analysis for geophone orientation determination

3.2.1 Introduction

The determination of the orientation of geophone components is a crucial step in the downhole microseismic processing workflow. Sensor axes can freely rotate when deployed in monitoring well (Daley et al., 1988). Auxiliary equipment like an inclinometer, compass, or gyro can indicate the geophone's attitude and bearing (Greenhalgh and Mason, 1995).

Several algorithms have been developed over the last 50 years for polarization analysis of incoming wavefield at a triaxial station. These algorithms mostly analyze particle motion direction within a window having a specific number of samples. In earthquake seismology, the analysis is performed on a sliding window stepping through the whole waveform at a user-specified step size. The window length in time is set so that the window ideally contains one seismic phase (Hendrick and Hearn, 1999; Jepsen and Kennett, 1991). However, different phases within the same window can be distinguished if the analysis is made in the frequency or tau-p domains, provided that phases have distinctive frequency characteristics (Bataille and Chiu, 1991; Greenhalgh and Mason, 1995). Seismic phases can exhibit either rectilinear, planar, or elliptical polarization in the direction of wavefield particle motion. For instance, the P-wave is rectilinearly polarized along particle motion direction, while Rayleigh waves exhibit an elliptical shape (Aki and Richards, 1980; Guevara and Stewart, 1998).

Knowledge of the wave types within a specific time window of the seismic trace and the polarization state of these waves enables seismologists to utilize several established methodologies for various applications. For example, polarization analysis can be used to separate wave types, signal filtering and enhancement, shear wave splitting analysis, source azimuth, and dip inference by measuring the rectilinearity of particle motions. The direction of P-wave linearity in a window around the P-wave first break can be assessed when the data are rotated into the ray-frame coordinate system using the correct source back-azimuth $\theta + 180$ and plunge. Hence, the geophone's components orientation must be known and configured into the processing workflow beforehand. The scenario can be reversed to determine a geophone's components orientation if the source azimuth and plunge from a station are known (e.g., controlled vibrator sweeps at the surface or downhole perforation shots) (Figure 3.6).

Errors in microseismic events locations are usually attributed to uncertainty in the arrival time pickings process and the velocity model used in the location algorithm (Akram, 2014; Smith et al., 2016). However, errors in the defined geophone orientation will also have a severe effect on the accuracy of microseismic locations (Van Dok et al., 2016), particularly when a single well is used to locate microseismic events (Jones et al., 2010). Therefore, considerable efforts should be dedicated toward obtaining reliable geophone orientation before proceeding into subsequent microseismic workflows.

Here, we will investigate several methods for horizontal components orientation determination of gimbaled geophones. A newly developed method is also tested and compared with established technique in term of accuracy, the impact of saturated noise and its performance. The methods are:

1. Covariance matrix analysis (Flinn, 1965; Jurkevics, 1988)
2. Complex covariance matrix (Vidale, 1986)
3. Orthogonal distance regression (Boggs et al., 1987)
4. Energy maximization (DiSiena et al., 1984)
5. Ray-frame rotated P-wave maximum RMS amplitude (the new method)

3.2.2 Theoretical background

Multi-component stations are in mainstream use for earthquake seismology. However, they became commonly used in the exploration seismology in the 1990s. Complex and heterogeneous structural and stratigraphic hydrocarbon trap systems require sophisticated technologies to reveal subsurface reservoir properties. Vertical Seismic Profiling (VSP) and microseismic acquisitions are relatively modern tools utilized in exploration geophysics for a better delineation of subsurface reservoirs. Instead of treating seismic waveforms as a scalar quantity, in conventional surface surveys, the use of multi-component instruments enables incorporating vector wavefield information into the processing routine and, thus, the analysis of seismic phases separately (Gaiser and Strudley, 2005; Hardage et al., 2011). Polarization analysis is a technique applied to multi-component seismic waveforms that determines the geometrical orientation of the vectorized nature of the particle oscillations (Shearer, 2009).

The theoretical background of polarization analysis was originated from electromagnetic theory (Born and Wolf, 1999). It was introduced into earthquake seismology by several scholars using different approaches (Flinn, 1965; Magotra et al., 1987; Montalbetti and Kanasewich, 1970). The method is used in exploration seismology, particularly in VSP and microseismic data analysis, to determine downhole geophone orientation, waveform mode separation, filtering unwanted noise from the signal, locating microseismic events, and shear wave splitting analysis ((Hearn and Hendrick, 1999), and references therein).

Hearn and Hendrick (1999) classify polarization methods into two main categorizations: instantaneous and window-based methods. The window-based methods are further sub-categorized into covariance matrix formulation and iterative optimization of a test function. The latter can be either amplitude aspect ratio or energy maximization. Covariance matrix analysis techniques on three-component data were first introduced by (Flinn, 1965). Others (Jackson et al., 1991; Jurkevics, 1988; Montalbetti and Kanasewich, 1970) subsequently developed several variants. (DiSiena et al., 1984) present a method based on power maximization in a time window following the P-wave first arrival to determine geophone orientation using a calibrated shot at the surface in application to VSP data.

Here I test the covariance matrix method of Flinn (1965), Jurkevics (1988) and Vidale (1986), as well as a modified version of the energy maximization method of Vidale (1986), as defined by Hendrick and Hearn (1999). The latter can be extended for use in deviated wells where all component orientations are unknown. The analysis is also made using the Orthogonal Distance Regression method described by Boggs et al. (1987). The ODRPACK library (Boggs et al., 1989) interface in the SciPy Python package is used in this project. Here I give the mathematical description of each method as implemented for geophone orientation determination, and in the following section demonstrate their application to the Oman dataset.

The first three techniques deploy the singular value decomposition method to a matrix C to find the eigenvalues and eigenvectors. The analysis of these two parameters will determine the rectilinearity and the particle motion's planarity, as will be explained in more detail later. They differ in the way of C matrix formulation. The data fed into the C matrix are the orthogonal east, north, and depth components in a window around the P-wave first break.

3.2.2.1 Flinn's method (Flinn, 1965)

In a window of mean close to zero ($\bar{\boldsymbol{u}} = 0$), the sum of vector outer products $\boldsymbol{u_i u_i^T}, i = 1, 2, \ldots, N$, where N is the number of sample points in a window, gives the sample covariance matrix (R. Lynn Kirlin, 1999). The shape or dimension of the vector for microseismic data is (3, 1). The number 3 refers to a 3-component geophone.

(Flinn, 1965) method calculates the sum of the outer product of the three-component data with itself in the analysis window,

$$C = \sum_{i=\tau_0-\frac{W}{2}}^{\tau_0+\frac{W}{2}} \boldsymbol{u_i u_i^T}, \tag{3.1}$$

in which $\boldsymbol{u_i}$ is a data vector containing the i^{th} components $[z_i \; n_i \; e_i]$, where z, n, and e are the vertical, north and east rotated data, respectively, and i is the sample point of each component. W is window length, T denotes transpose and τ is the start time of the window.

3.2.2.2 Jurkevics's method, (Jurkevics, 1988)

This approach examines the dependency of z (down), n (north), e (east) components in a multivariate statistical manner by the formulation of a covariance matrix described as,

$$C = \begin{bmatrix} S_{zz} & S_{zn} & S_{ze} \\ S_{nz} & S_{nn} & S_{ne} \\ S_{ez} & S_{en} & S_{ee} \end{bmatrix}. \tag{3.2}$$

The covariance matrix elements are auto and cross-covariance of z, n, and e rotated components in the analysis window. For example, the element (row=0, column=0) in the covariance matrix C is the covariance of z components with itself, which is the variance. The matrix C is symmetric since the covariance of e with z component S_{ez} is equal to the covariance of z with e component S_{ze}.

The covariance of, for example, e and n components is mathematically described as,

$$cov_{e,n} = \frac{\sum_{i=1}^{N}(e_i - \bar{e})(n_i - \bar{n})}{N-1}, \tag{3.3}$$

variance of e component is calculated as,

$$\mathrm{Var}_e = \frac{\sum_{i=1}^{N}(e_i - \bar{e})^2}{N-1}, \tag{3.4}$$

where, $\bar{e}$ and $\bar{n}$ are the mean values of the e and n vectors, respectively. N is the number of observations in the analysis window.

3.2.2.3 Vidale's method, (Vidale, 1986)

This method is similar to the previous one except that data are first converted to a complex signal where the real part is the original signal, and the imaginary part is the Hilbert transform of the signal,

$$\begin{aligned} z_i &= z_i + jH\{z_i\} \\ n_i &= n_i + jH\{n_i\} \\ e_i &= e_i + jH\{e_i\}, \end{aligned} \tag{3.5}$$

where j is $\sqrt{-1}$ and i is the sample number in the analysis window. The complex covariance matrix is then built by the dot product of the complex signal with its conjugate,

$$C = \begin{bmatrix} zz^* & zn^* & ze^* \\ nz^* & nn^* & ne^* \\ ez^* & en^* & ee^* \end{bmatrix}, \tag{3.6}$$

where the asterisk represents complex conjugate.

In the three methods described above, the source is the vibrator point at the surface, which has a known azimuth (θ) and a dip (α) (Figure 3.6) with respect to the 3C-geophone. The rectilinear, found from eigenvalue and eigenvector analysis of the singular value decomposition of the matrix C, will be maximized when the z, n, and e of the geophone are oriented correctly. The correct orientation can be found by testing all possible orientations of e and n with an increment of 0.25 degrees. The z component is kept vertical during the test.

To assure that the components are oriented correctly, the calculated θ and α from the eigenvalues and eigenvectors must numerically be close to the known ones from the vibrator shot location.

3.2.2.4 Orthogonal distance regression (ODR) method, (Boggs et al., 1987)

The ordinary least square technique of fitting a model to data allows only one variable to have errors in measurement, and the independent variable is assumed to be fixed. In contrast, the ODR method can handle data where significant uncertainties exist in the explanatory and the response variables (Figure 3.7). The dependent variable y is an approximate function of the independent variable x and an unknown parameter β, where both variables have errors in measurements,

$$y_i \approx f_i\left(x_i + \delta_i; \beta\right) - \varepsilon_i, \tag{3.7}$$

where, ε and δ represent errors in y and x, respectively. The variable y best fits function f when solving a minimization problem which approximates ε by finding its value for the sum of squares of all orthogonal distances from the curve $f(x;\varepsilon)$ to data sample points in the analysis window,

$$\min_{\beta;\delta} \sum_{i=1}^{n} \left(\left[f_i\left(x_i + \delta_i; \beta\right) - y_i \right]^2 + \delta_i^2 \right), \tag{3.8}$$

where n is the total data points in the analysis window. The minimization function is solved iteratively using a trust-region Levenberg-Marquardt method (Moré, 1983). The Fortran routine of the ODRPACK package finds the solution of orthogonal distance regression problem using the quadratic penalty,

$$P\left(\beta,\delta;r_k\right)=\sum_{i=1}^{n}\left(r_k\left[f_i\left(x_i+\delta_i;\beta\right)\right]^T\left[f_i\left(x_i+\delta_i;\beta\right)\right]+\left[\delta_i^T\delta_i\right]\right), \tag{3.9}$$

where r_k is the penalty parameter. The constructed model is a linear function of $y=\beta_x$. The data vectors of x and y components in a window around the P-wave first break will best fit the model when the correct x and y orientations are used to rotate them into east and north coordinate system.

ObsPy (Krischer et al., 2015), a Python framework for seismological data analysis, has a subroutine for each of the methods mentioned above to make window-based polarization analysis for the determination of the source azimuth θ and dip angle α when a station's components orientations are known. I provide a modification to these routines, so the operation is reversed to find the orientation of geophone components when θ and angle α are measured from a known source location (vibroseis).

3.2.2.5 Energy maximization method, (DiSiena et al., 1984)

This method and a variant by Shih et al. (1989) are used quite commonly to orientate geophone's horizontal components in VSP data. Hendrick and Hearn (1999) describe a generalization of the technique for application in 3-components data. The sum of absolute maximum power ratio between dot and cross-product of the data vectors and a unit vector pointing to the direction from geophone to source point over sample points in the analysis window. The unit vector is rotated by scanning all possible ranges of source azimuths θ and plunges α. The function reaches a maximum when the data vector and the unit vector coincide in 3D space.

In geophone orientation determination, since vibrator location is known, the unit vector pointing from geophone to vibroseis shot location is constructed as,

$$\begin{aligned} de &= \sin(\theta) * \cos(\delta) \\ dn &= \cos(\theta) * \cos(\delta) \\ dz &= \sin(\delta) \\ u &= [de \quad dn \quad dz] \end{aligned}, \tag{3.10}$$

where γ is the back-azimuth and α is the source plunge in degrees. Waveform data consisting of vectors x, y and z components are rotated into e, n and z geographic coordinate system where the y component orientation ranges from $(0-360)$ and the x component is set to the orientation of the $y-component+90$. The energy maximization function is defined as,

$$F = \sum_{i=0}^{n} \left| d_i^T \cdot u \right|^2 / \sum_{i=0}^{n} \left| d_i^T xu \right|^2, \tag{3.11}$$

where d represents rotated data vector (e,n,z), T denotes transpose, x is the cross-product operator, and n is the number of sample points in the analysis window. The summation is performed over the sample points in the analysis window.

The true geophone components orientation is determined when the function F is maximized. This happens when the true values of γ and α are inserted into the equation 3.10. Similar to the previous methods, the waveforms of the x and y components are rotated in reference to the geographic coordinate system (e,n) at a step size of 0.25. One of these steps will maximize the F.

3.2.2.6 Ray-frame rotated P-wave maximum RMS amplitude method

Whereas the rotation is performed once for the previous methods, in this algorithm, the data are first rotated into the geographic coordinate system (obtaining n and e from y and x) and then rotated into the ray-frame coordinate system. The P-wave phase's longitudinal component will be at its maximum amplitude with respect to SV and SH phase movement when the correct geophone orientations are used in the rotation process. The ObsPy package provides functions for tri-axial waveform rotation into the geographic and ray-frame coordinate system. Mathematically, this can be described as,

$$\begin{bmatrix} z \\ n \\ e \end{bmatrix} = m^{-1} \begin{bmatrix} v \\ y \\ x \end{bmatrix}, \text{ where } m \text{ is },$$

$$m = \begin{bmatrix} -\sin(\delta_v) & \cos(\theta_v) * \cos(\delta_v) & \sin(\theta_v) * \cos(\delta_v) \\ -\sin(\delta_y) & \cos(\theta_y) * \cos(\delta_y) & \sin(\theta_y) * \cos(\delta_y) \\ -\sin(\delta_x) & \cos(\theta_x) * \cos(\delta_x) & \sin(\theta_x) * \cos(\delta_x) \end{bmatrix} , \qquad (3.12)$$

where α and θ denotes components' dip and azimuth, respectively.

In the case of a vertical well, as the is the with Oman dataset, δ_v and θ_v are set to -90 and zero respectively for an upward pointing vertical component, whereas δ_y and δ_x, are set to zero. θ_y has range between 0 to 360, while θ_x is equal to $\theta_y + 90$, in a circular pattern (e.g., 300 + 90 = 30).

Data can be rotated into the ray-frame coordinate from the geographic coordinate system following (Plesinger et al., 1986) technique,

$$\begin{bmatrix} P \\ SV \\ SH \end{bmatrix} = M \begin{bmatrix} z \\ n \\ e \end{bmatrix}, \text{ where } M \text{ is },$$

$$M = \begin{bmatrix} \cos(\gamma) & -\sin(\gamma) * \sin(\varphi) & -\sin(\gamma) * \cos(\varphi) \\ \cos(\gamma) & \cos(\gamma) * \sin(\varphi) & \cos(\gamma) * \cos(\varphi) \\ 0 & -\sin(\varphi) & \sin(\varphi) \end{bmatrix} , \qquad (3.13)$$

where φ and γ are back-azimuth and incident angle measured up from straight down, respectively. Again, the back-azimuth and incident angle (Figure 3.6) can be calculated from survey data of the vibrators and geophones locations.

Methods of Flinn (1965), Jurkevics (1988) and Vidale (1986), creates a covariance matrix which can be decomposed into the corresponding eigenvalues and eigenvectors using singular value decomposition (Jackson et al., 1991). Purely rectilinear particle motion is dominated by one eigenvalue. The source azimuth, the incident angle and the particle motion rectilinearity are calculated as,

$$\begin{aligned}
\text{azimuth} &= \arctan 2\left((v_1)_1, (v_2)_1\right) \\
\text{incident angle } &= \arctan\left((v_3)_1 / \sqrt{\left((v_1)_1^2 + (v_2)_1^2\right)}\right) \ . \\
\text{rectilinearity} &= 1 - \sqrt{(\lambda_2/\lambda_1)}
\end{aligned} \tag{3.14}$$

where, λ_1 is the largest eigenvalue and λ_3 is the smallest. v_1 and v_3 are the corresponding eigenvectors and the subscript 1 denotes first value of the eigenvector.

3.2.3 Application to Oman dataset

Figure 3.8-a shows the location of 4 microseismic monitoring wells and the associated vibroseis shot points. These are the wells that we will analyze here, but the same procedure is applied to all microseismic wells. There are eight geophones spaced 20 meters apart in each microseismic monitoring well. Figure 3.8-c shows a cross-section of the monitoring wells, illustrating the depth of the geophones. Geophones are gimbaled, so the vertical component is pointing upward. I determine only with the orientation of the two horizontal components X and Y in a left-handed configuration (X is leading Y by 90 degrees).

The P-wave first breaks are manually picked for all vibroseis generated waveforms using a newly developed package in Python. (Figure 3.9) shows one of the shot records at microseismic well-7. These vibrator shots were re-acquired in the April of 2017 following the first acquisition in 2011. The purpose was to gain data of better fidelity with a higher signal to noise ratio. For instance, (Figure 3.10) shows the difference in geophone orientation between the two vibrator acquisitions at one of the microseismic wells. New vibrator shots data also produced higher confidence location results than the old one. The rotation analysis window is set to the 4th zero-crossing of the highest amplitude component following the P-wave onset time pick. Usage of an adaptive window ensures that the window contains at least two cycles but no interference from possible later arrivals. An adaptive window has shown an advantage over fixed time windows resulting in higher P-wave linearity values. The waveform sampling interval of all shot records is 4000 Hz.

The P-wave first breaks are manually picked for all vibroseis generated waveforms using a Python package I developed. Figure 3.9 shows one of the shot records at microseismic well-7. These vibrator shots were re-acquired in the April of 2017, following the first acquisition in 2011. The purpose was to gain data of better fidelity with a higher SNR. For instance, Figure 3.10

```python
def flinn_orient(v, y, x):
  orient = np.arange(0, 360, 0.25)
  result_flinn = []
  for orient_y in orient:
    if 0 <= orient_y < 270:
      orient_x = orient_y + 90
    else:
      orient_x = (orient_y + 90) - 360
    z, n, e = rotate2zne(v, 0, 90, y, orient_y, 0, x, orient_x, 0)
    source_info = particle_motion_flinn(z, n, e)
  result_flinn.append(source_info)
  return result_flinn
```

Listing 3.1: Flinn method implementation in Python.

shows the difference in geophone orientation between the two vibrator acquisitions at one of the microseismic wells. New vibrator shots data also produced higher confidence geophone orientation results than the old one based on the variance calculated from the different shot locations at the same microseismic well. The rotation analysis window is set to the 4^{th} zero-crossing of the highest amplitude component following the P-wave onset time pick. Usage of an adaptive window ensures that the window contains at least two cycles but no interference from possible later arrivals. Tests show that an adaptive window has an advantage over fixed time windows resulting in higher P-wave linearity values.

Python implementation for the covariance method of Flinn (1965) is shown in Listing 3.1, where v, y, and x input positional arguments are the windowed orthogonal 3-components at a geophone for respective axes. Python function **rotate2zne** is described in equation 3.12, which rotates the data to the geographic coordinate system. The function **particle_motion_flinn** is shown in equations 3.1 and 3 3.14. The scan is performed from 0 to 360 at a step size of 0.25. The returned result gives the azimuth θ, dip α, and the P-wave rectilinearity. The index at which the difference between true vibrator azimuth and calculated azimuth is at a minimum will correspond with the components' correct orientation. Python implementation of the newly developed method is shown in Listing 3.2. The function **rotate_zne_lqt** rotates the data from geographic to the ray-frame coordinate system and is shown in equation 3.13. Likewise, other methods follow a similar execution process.

Figure 3.11 shows the y-component orientation plot as deduced from each method using all vibrator shots at microseismic well-7. Circular variance measurements have a range from (0 to 1), and it can be considered as an indication of how robust each method is (Fisher, 1995). All methods

```python
def maximum_amp(v, y, x, vib_azimuth, vib_dip):

  orientation_y = np.arange(0, 360, 0.25)

  max_p = []
  out_put = np.zeros((3, len(x1)))
  for azi in orientation_y:

    if 0 <= azi < 270:
      orientation_x = azi + 90
    else:
      orientation_x = (azi + 90) - 360
    z, n, e = rotate.rotate2zne(v, 0, -90, y, azi, 0, x, orientation_x, 0)
    l, q, t = rotate.rotate_zne_lqt(z, n, e, vib_azimuth, vib_dip + 90)
    maxp = np.sqrt(np.mean(np.square(l)))
    rect = np.corrcoef(e, y=n)[0, 1] / (np.sqrt(np.corrcoef(e) + np.corrcoef(n)))
    out_put[0, :] = l
    out_put[1, :] = q
    out_put[2, :] = t

    max_p.append((maxp, azi, rect, out_put))
  return max_p
```

Listing 3.2: The implementation of the newly developed method in Python.

show very comparable orientation results. Variance statistics are calculated using orientation results for the same geophone from eight vibrators locations. Figure 3.11 shows that the variance is usually below 0.1, indicating good agreement from different shots.

Figure 3.12 shows the variance comparison between different approaches for all vibrator shots at well-7. In this example, Geophone 6 has the highest difference. Data quality (SNR) and clarity of the first break in the waveforms are the main reason for higher differences between different methods.

SNR for each vibrator shot per geophone is plotted in Figure 3.13. Signal windows length is set to be the same as polarization analysis window, and the noise window is selected before P-wave pick onset time. For the covariance matrix methods, rectilinearity is calculated as defined in equation set 3.14. In the energy maximization and the RMS amplitude methods, the rectilinearity is calculated as $n \otimes e / \sqrt{(n \otimes n)(e \otimes e)}$, (Akram, 2014), where $\otimes$ is correlation operator, and n, e are north and east components, respectively. Figure 3.13 also shows The difference in rectilinearity between the covariance matrix and correlation methods. In general, there is a good correlation between SNR and rectilinearity.

The impact of rotation window length on the estimation of component orientation is shown in

Figure 3.9. The Diff subplots show the difference between the mean calculated y-orientation from all methods using a fixed window length of 4_{th} zero-crossing and a varying window length from 10 to 150 ms with an increment of 10 ms. Computation time in seconds per each geophone is plotted in the same Figure (the Time subplot). The optimal rotation window is about two cycles of the waveform around the P-wave first break. Flinn (1965) and the new methods have the fastest calculation time. The ODR has the slowest performance after Vidale (1986) than the rest of the methods.

When placing a vibroseis sweep point close to the well-head, as is the case with vibrator point 6 at microseismic well-5, the retrieved component orientation will not reliability represent the correct orientation, giving rise to high circular variance values as shown in Figure Figure 3.15. Excluding the vibrator number 6 lowers the circular variance (black edge colored bars). When placing the vibrator shot very close to the well-head, the horizontal component receives minimum P-wave energy. Thus, it cannot be helpful to retrieve horizontal geophone orientations confidently.

When only the vertical component is dead (zero amplitude), it is likely that the true horizontal components orientation can still be retrieved but with lower uncertainty than if all sensors are active, particularly for ODR method. Whereas, if more than one component is defunct or it is the one other than the vertical component, the true orientation cannot be determined (Figure 3.16). In fact, a 180° ambiguity rises when only the vertical component is dead. Information from the vertical components is used to reveal ray-vector plunge.

When only the vertical component is dead (zero amplitude), it is likely that the true horizontal component orientations can still be retrieved but with lower uncertainty than if all sensors are active, particularly with the ODR method. Whereas, if more than one component is defunct or it is one other than the vertical component, the true orientation cannot be determined (Figure 3.11). In fact, a 180± ambiguity rises when only the vertical component is dead. Information from the vertical components is used to reveal the ray-vector plunge (Jones et al., 2010).

Table 3.2 presents the y-component orientation due north from all vibrator shots per each geophone (column 2-9). Column 10 is the mean orientation and the last column is the circular variance. The geophone orientations in this table are measured using the newly developed method (RMS amplitude max).

Table 3.2: The y-component orientation due north estimated using the RMS amplitude max for 8 different vibrator shots at one of the monitoring wells. The variance is zero for all geophones.

Geophone	vib-1	vib-2	vib-3	vib-4	vib-5	vib-6	vib-7	vib-8	mean	variance
1	203.5	198.0	198.0	191.5	203.5	182.3	192.5	204.8	196.8	0.0
2	358.0	356.5	356.5	337.8	350.0	346.5	343.0	357.0	350.7	0.0
3	145.3	144.0	142.5	128.8	136.0	138.5	132.0	136.5	137.9	0.0
4	8.8	4.0	0.5	355.3	15.0	6.3	0.0	8.5	5.5	0.0
5	339.3	336.8	336.3	324.8	340.5	335.5	332.0	337.0	335.3	0.0
6	66.0	70.5	74.0	65.8	112.5	90.0	81.0	70.3	78.5	0.0
7	211.0	213.5	213.5	196.5	215.8	215.8	211.8	211.3	211.1	0.0
8	243.3	240.8	240.8	229.8	242.5	241.5	244.0	244.8	240.9	0.0

3.2.4 Conclusion

In this part, we use established techniques for polarization analysis to determine horizontal geophone orientations in vertical microseismic monitoring wells. The tested methods are Flinn (1965), Jurkevics (1988), Vidale (1986), Orthogonal Distance Regression (Boggs et al., 1987), a modified version of energy maximization method (DiSiena et al., 1984). Finally, a newly developed technique (RMS amplitude). The last method rotates the data first to the geographic coordinate and then to the ray-frame coordinate system and determines the horizontal components' orientations, which result in the maximum root mean square amplitude of the longitudinal rotated component within the analysis window. For the covariance matrix and ODR methods, the correct orientations are obtained when the difference between calculated and real source azimuth is minimal. Comparison is made between methods in terms of circular variance calculated from 8 vibroseis sweeps made at each well. The sensitivity of each method to the rotation window length around P-wave first break and SNR is assessed. Results show that the covariance matrix method of Flinn (1965) and Jurkevics (1988) give similar results. Likewise, energy maximization and RMS amplitude are comparable to each other. All methods except ODR are not susceptible to a 180-degree ambiguity in source azimuth. The ODR Boggs et al. (1987) and Vidale (1986) methods take considerable computational time compared to the rest. The advantage of re-implementing these methods in Python over, for example, Montalbetti and Kanasewich (1970) available in the Insite software, is that 180± ambiguity is auto-corrected without the need to inspect each geophone components individually. Insite is the software package I used to locate microseismic events. Insite has a routine to find the orientation of geophone sensors using a known source location. The method applied to Oman dataset is the RMS amplitude technique. It proved to show consistent results between different vibrator shots. It is also the least sensitive to the length of the rotation analysis window and shows fast computational performance. The final component's orientation is the average orientation obtained from all vibrator shots. If a maximum of three vibrators shows an outlier, their deduced orientation is not included in the subsequent processing (e.g., locating events). Also, if particular geophones show a consistent orientation discrepancy between the suite of vibrator shots, they are discarded from the location process.

For future studies, I recommend using one of the two methods; (Flinn, 1965), or the newly developed method. These two methods showed the lowest sensitivity to the noise level. Their computational performance is good, and they are not affected by the 180° degree-ambiguity. In this project, I developed the codes of these techniques for vertical wells. However, the codes can easily be expanded for deviated wells. I also recommend the use a subsurface controlled source (e.g., drill bit noise) as another tool for geophone's sensor orientation analysis in addition to the surface vibrator shots. The eight vibrators are at the same elevation. Thus, the value of α in Figure 3.6 can not be adequately constrained, whereas controlled source points from more than one elevation point would have provided a better assessment on the value of α. Nevertheless, the higher variation in α compared to θ observed for all methods can also be due to ray bending at geological interfaces. The downhole controlled source can also be used for velocity calibration in the velocity building process.

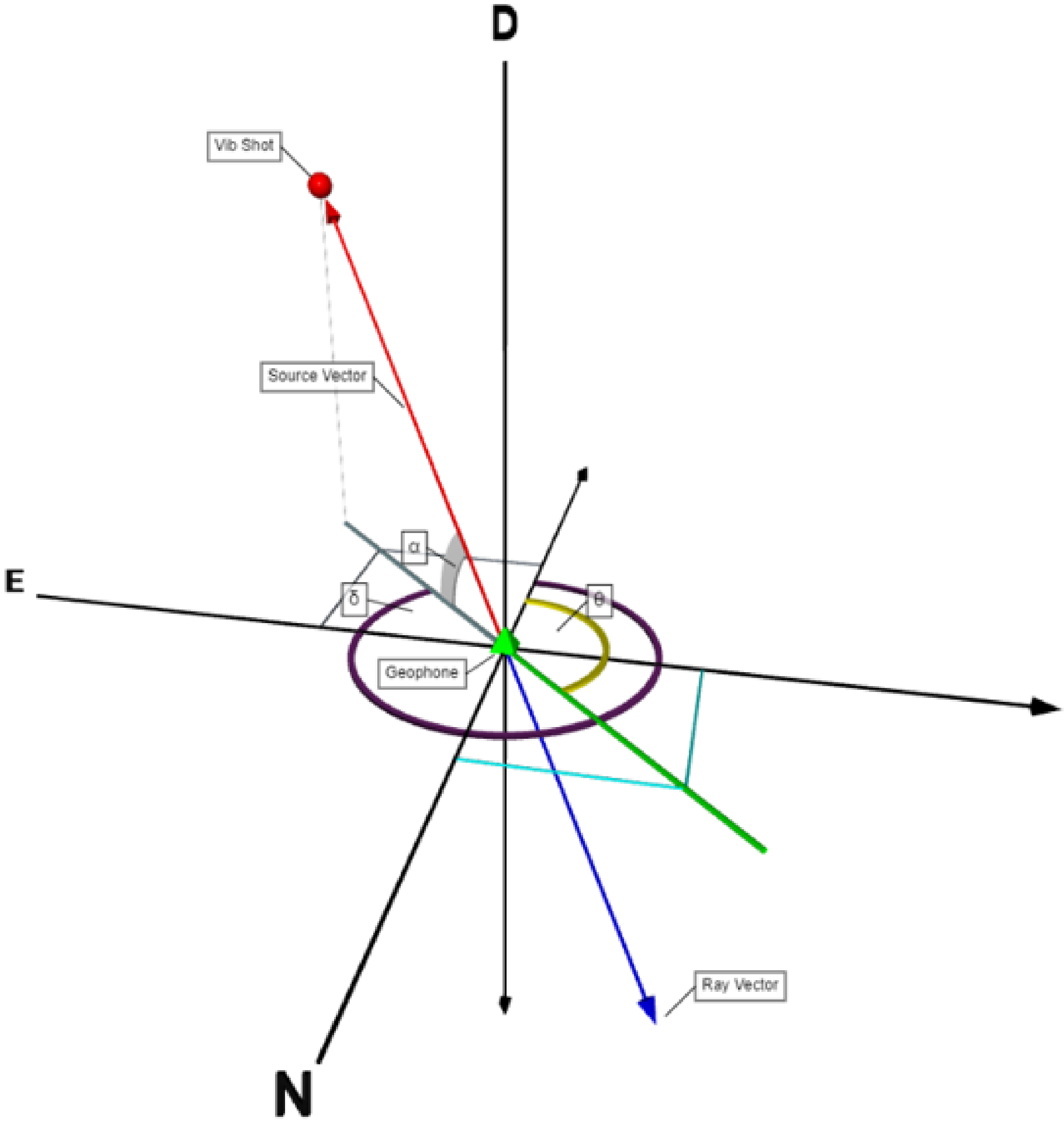

FIGURE 3.6. A schematic view of the ray and the source vectors between a geophone and a vibrator shot. θ is the azimuth measured clockwise from the north, and α is the plunge measured down from the horizontal. α is negative in this figure and it has a range of (0 - $\frac{\pi}{2}$) upward or (0 - $-\frac{\pi}{2}$) downward. The back-azimuth is equal to $\theta + 90$. Geophone orientation can be determined from P-wave particle motion when the vibrator source location is known. The source vector points from source to the geophone location, whereas the ray vector points in the opposite direction. The magnitude of the vector is dependent on waveform amplitudes.

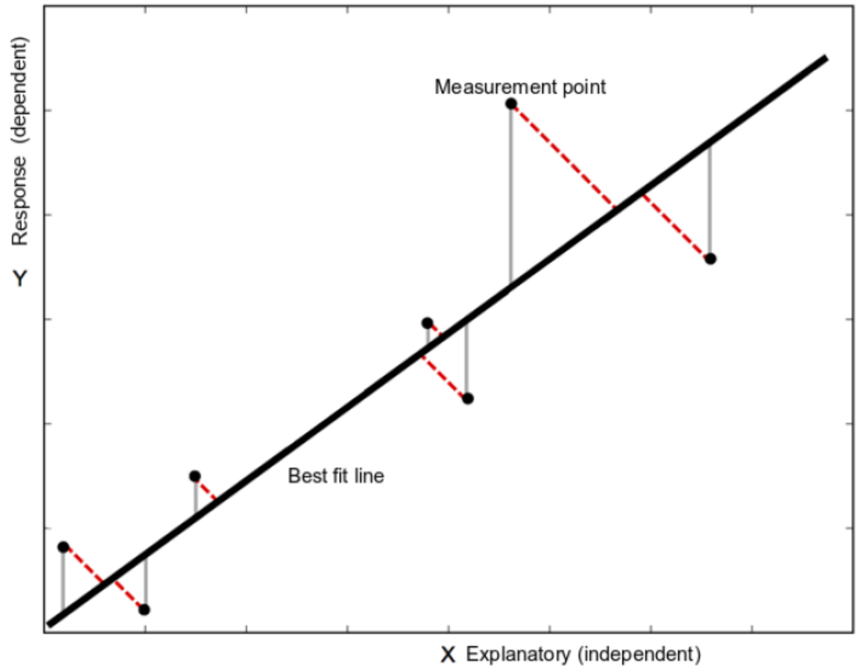

FIGURE 3.7. The difference between ordinary least square and orthogonal distance regression. In orthogonal distance regression, both x and y have errors in measurements (red dashed line).

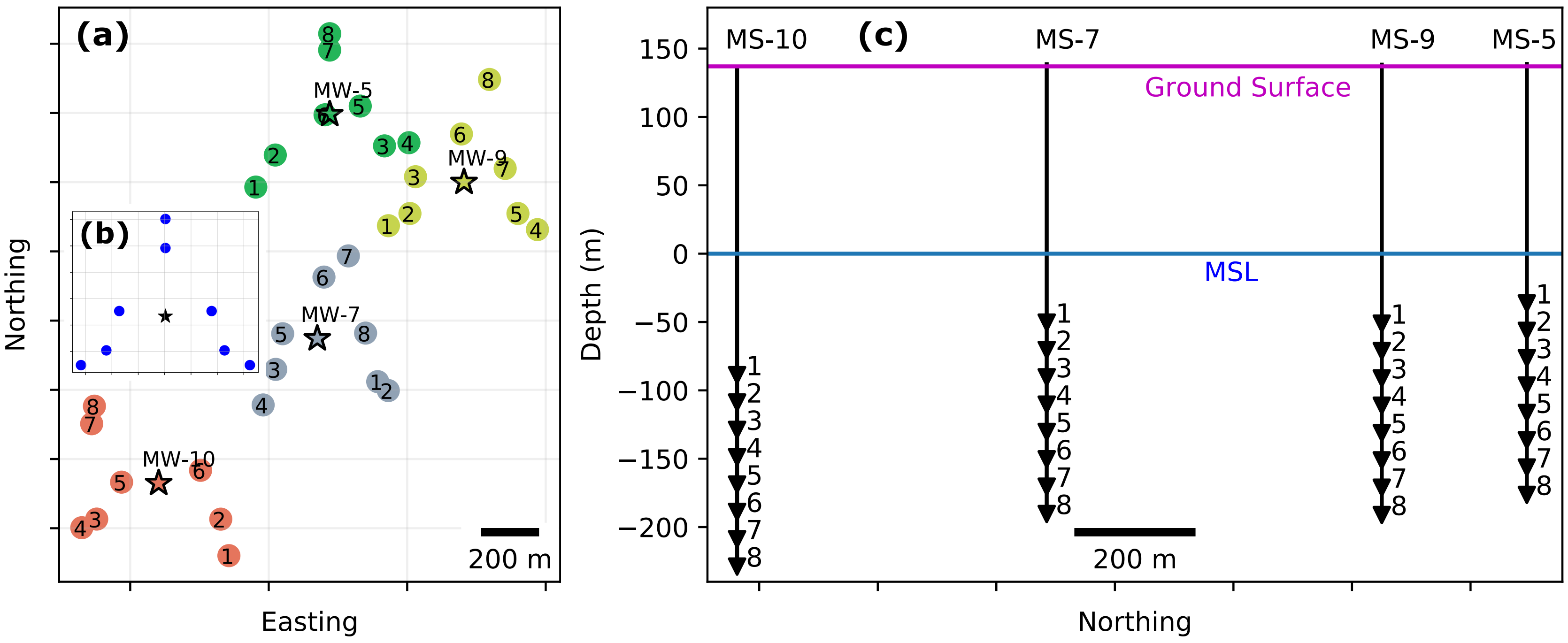

FIGURE 3.8. (a) Microseismic wells (star) and the associated vibroseis locations (circle). Vibrators' locations are numbered according to their acquisition time from earliest to latest. The planned layout of vibrator locations is depicted in sub-figure (b); however, actual layouts are slightly different due to the existence of production and injection facilities on the surface. (c) A cross-section showing depths of geophones from mean sea level for all microseismic wells. Vibrators are shot at ground surface level.

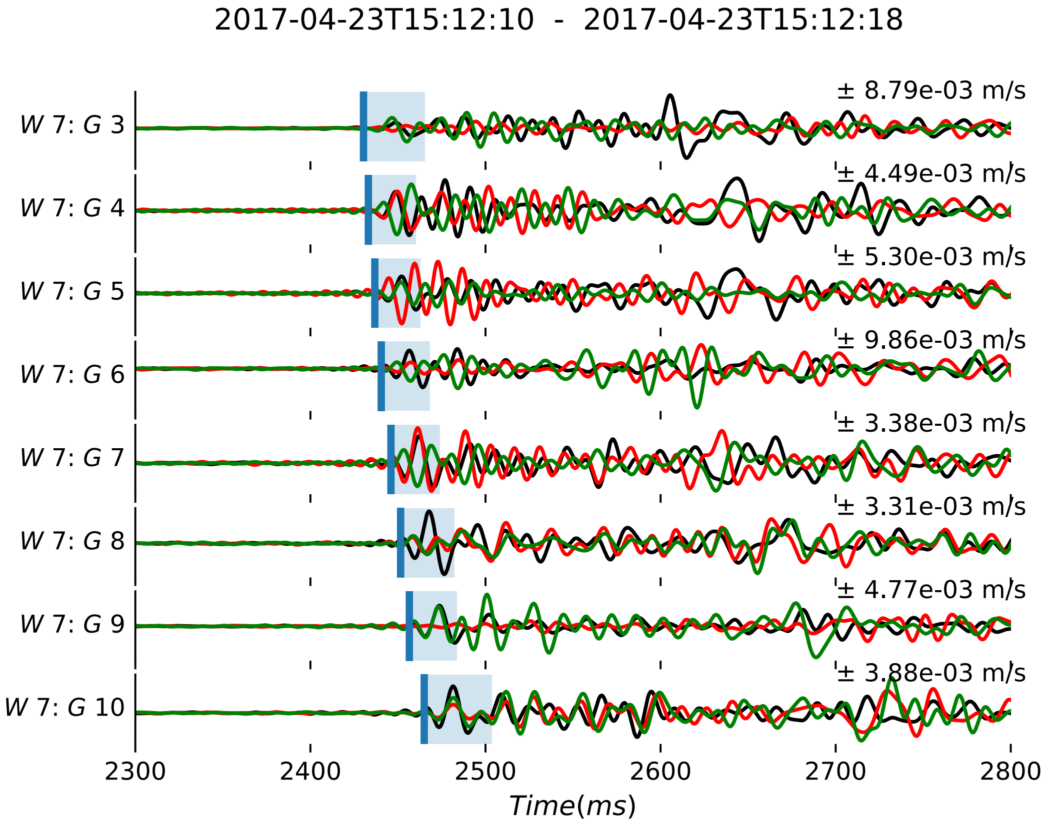

FIGURE 3.9. A Vibroseis waveform is recorded by the microseismic well-7. The window length is set to 4th zero-crossing following the P-wave pick, and it is usually wider for deeper geophone due to intrinsic attenuation of high frequencies with depth. The new acquisition (2017) included two more geophones at the surface, for which the segy events files I received have no records. Therefore, I discarded these two geophones from further analysis.

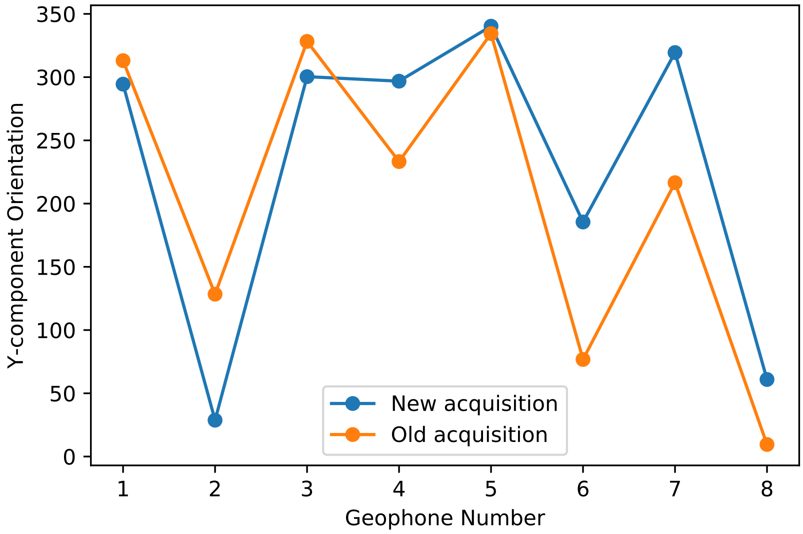

FIGURE 3.10. The orientation difference between new and old vibroseis data acquisition. Maximum root-meas-square error between the two acquisition at well-4 is 69°.

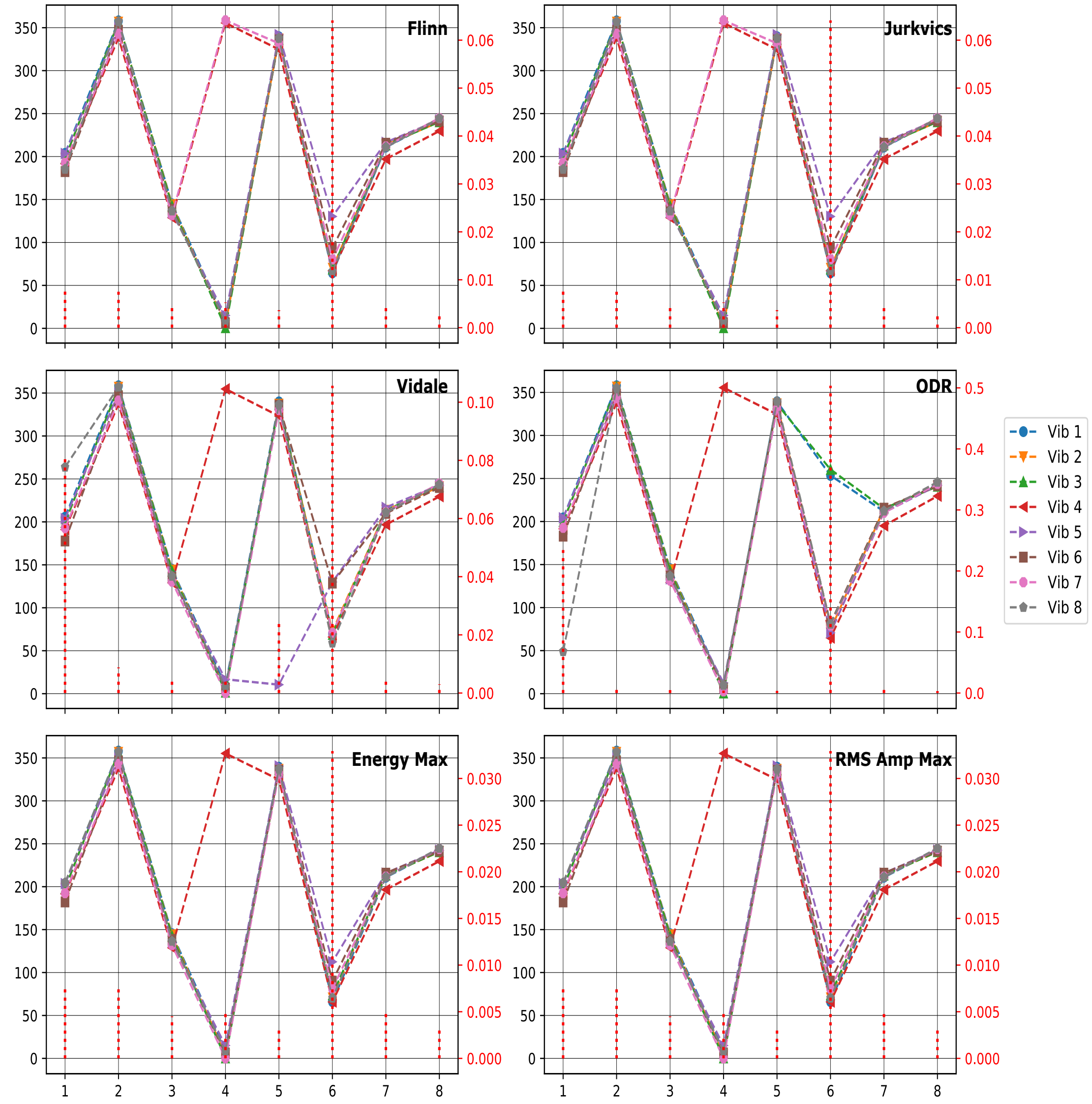

FIGURE 3.11. Orientation result for each method from all eight vibroseis. The x-axis represents geophone number, where geophone 1 is the shallowest and geophone 8 is the deepest. The left y-axis is the orientation of the y-component from the north, whereas the right y-axis is circular variance plotted as dotted vertical lines. The x-component is equal to $y - component + 90$

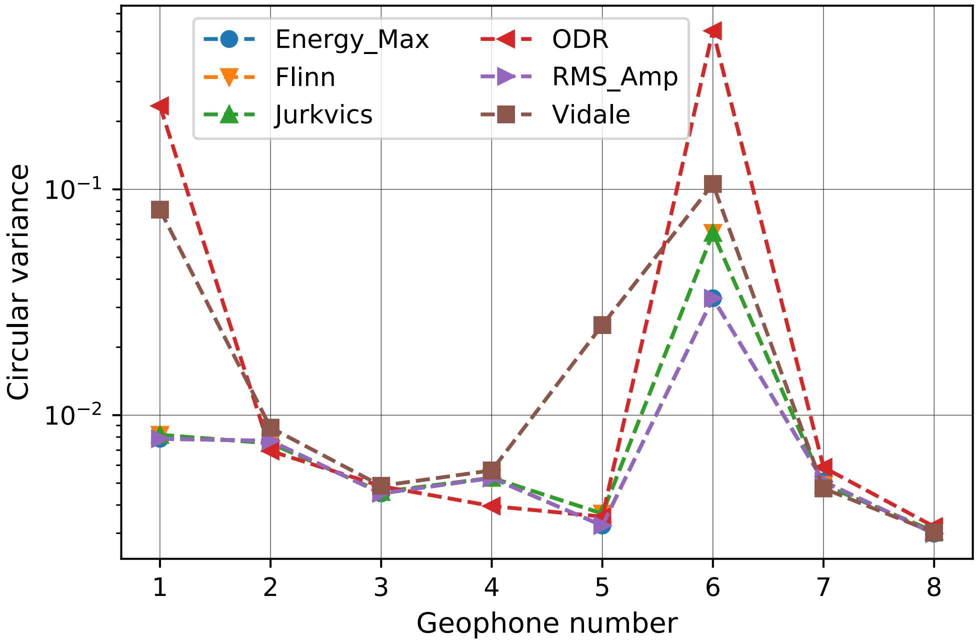

FIGURE 3.12. Circular variance in the y-component orientation per each polarization method at MSW-7. The maximum variance is 0.9 reported from ODR method at geophone 6. The variance is the highest for ODR and Vidale (1986) methods, particularly at geophones 1 and 6.

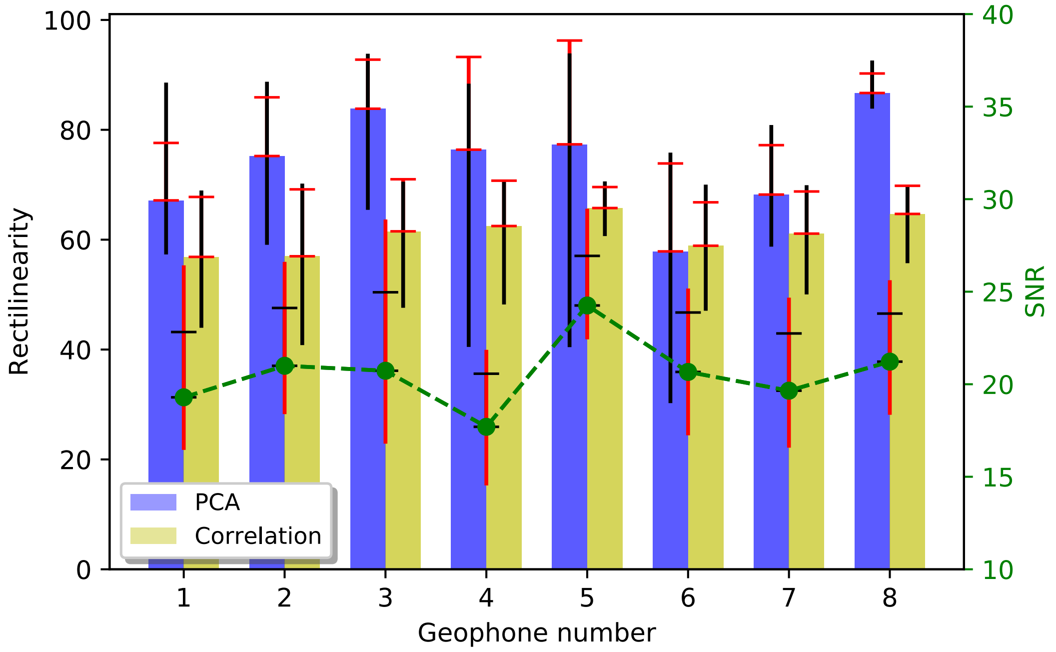

FIGURE 3.13. Bar plots (left y-axis) represent mean rectilinearity obtained using principal component analysis method (covariance matrix) (blue) and correlation method (Energy maximization and RMS amplitude) (yellow). Green line plot (right y-axis) is the mean SNR in dB. Error bars represents maximum and minimum values from all geophone and the cap on the upper error bar represents the standard deviation.

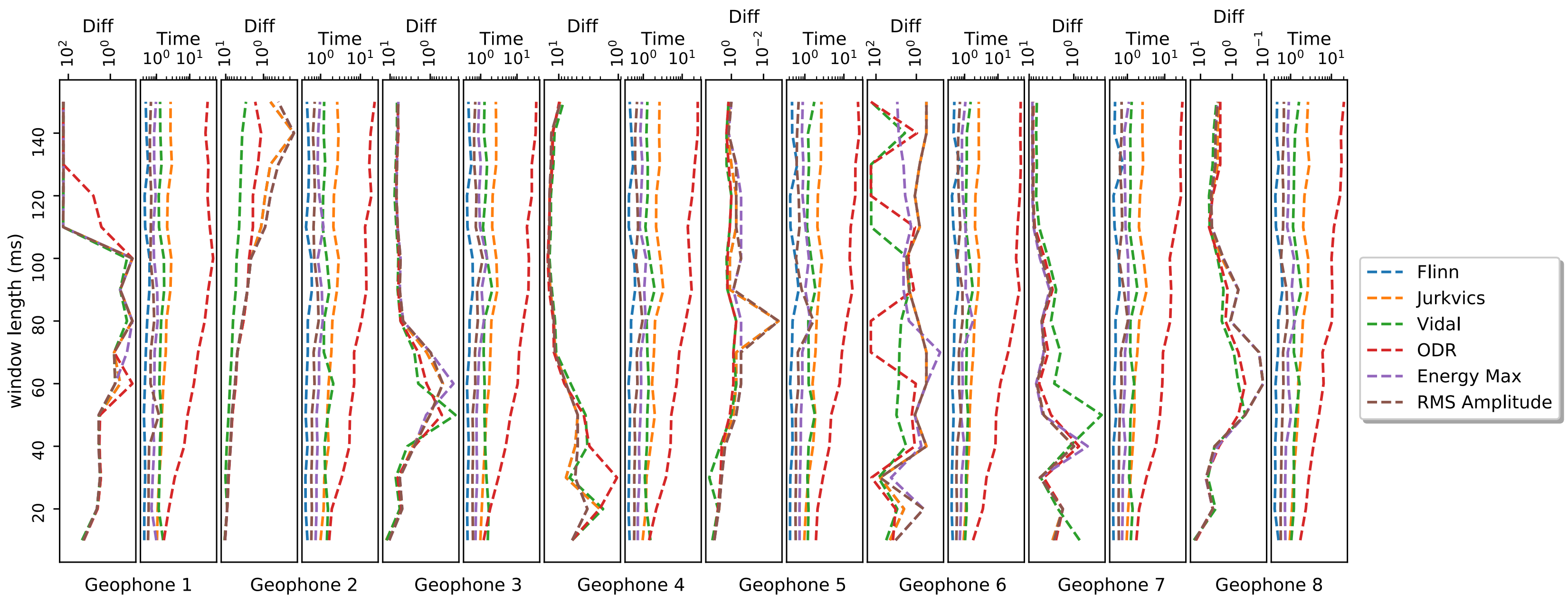

FIGURE 3.14. Impact of rotation window (Diff subplot) representing difference between mean calculated orientation using a fixed window length and a variable window length. Computation time is plotted in subplot (Time) in the unit of ms . (Diff) subplot increases from right to left while Time subplot increases from left to right.

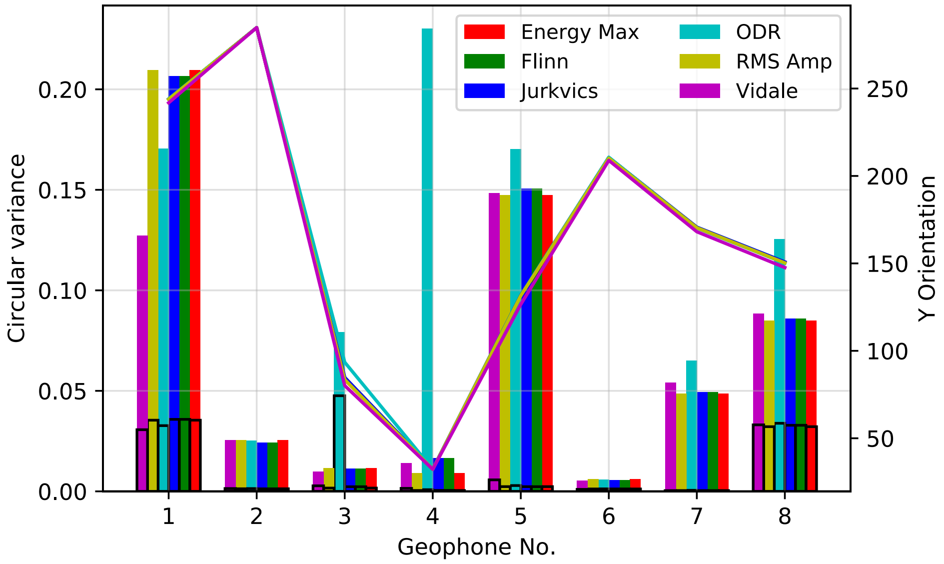

FIGURE 3.15. Effect of placing vibrator shot at a close proximity to well-head on orientation circular variance. Orientation results will be unreliable for vibrator shots placed very close to microseismic well-head..

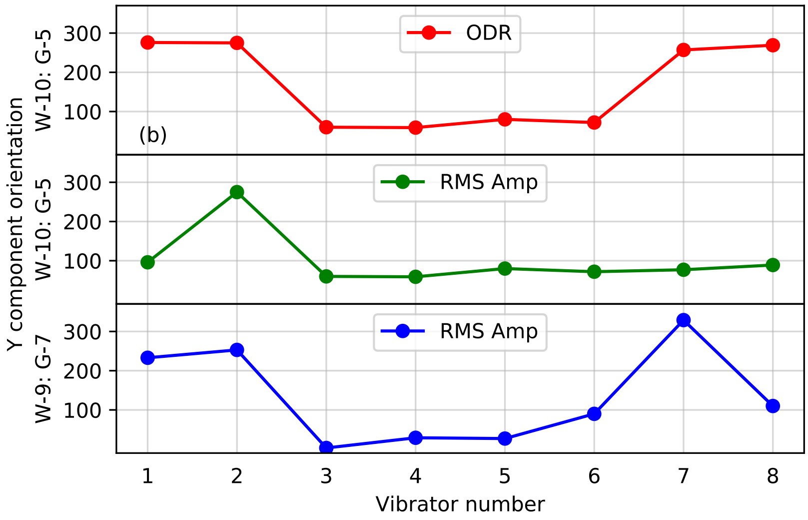

FIGURE 3.16. Impact of dead component on geophone orientation. There is 180° ambiguity when only the vertical component is dead. The true orientation cannot be determined when more than one component is dead.

3.3 Waveform Filtering for Noise Reduction

3.3.1 Introduction

A crucial step in microseismic data analysis is the removal of unwanted noise from the signal. Saturation of seismic signal with noise can happen for various reason including but not limited to:

1. Powerline noise occurring at 50 Hz.
2. Field operation noise.
3. External distal earthquake events.
4. Inherent equipment noise.

The same noise types that happen in surface seismic data can also appear in microseismic data. However, elimination of noises in surface seismic data is facilitated by the stacking process (Yilmaz, 2001), as usually surface seismic data are acquired with hundreds of channels per one common mid-point. Common mid-point stacking, which can enhance data quality, cannot easily be expanded to microseismic data. In the microseismic method, there is usually a limited number of sensors and an uncontrolled source location. Surface microseismic data, acquired by sensors placed at ground level or very shallow boreholes, are commonly noisier than downhole microseismic data (Maxwell, 2014). Maxwell (2014) argues that among other benefits, using a combination of surface and downhole microseismic monitoring arrays can help in distinguishing noise properties from downhole arrays and then applying the same filtering techniques to surface data if the source of the noise is the same in both arrays.

Noise can be categorized into two types: coherent and random. For example, powerline noise is a type of coherent noise because it has a known characteristic and is consistently contaminating the signal as long as the powerline is live. Random noises (field operation and cultural noise) often are more challenging to suppress than coherent noises since their exact occurrence time and frequency content are unknown.

Unlike surface seismic data, filtering microseismic or earthquake data requires special care and treatment. For instance, routine application of surface seismic data after prepossessing are horizon and faults picking, relative amplitude extraction, and advanced techniques of amplitude versus offset analysis or seismic inversion. These operations are usually not very sensitive to amplitude variation, and therefore, true amplitude processing is not a high priority. In contrast, the microseismic workflow of first break picking, source parameter calculation, shear wave splitting, and moment tensor analysis can only be successfully performed when the true waveform amplitude is preserved during the processing flow (Havskov and Ottemoller, 2010; Maxwell, 2014).

Recent strategies put efforts toward acquiring noise-free data as much as possible and configuring the acquisition array, and designing its parameters in a way such that there is minimum noise interference (Kovaleva et al., 2018). This is to avoid the hassle of filtering the noise and introducing processing artifacts into the dataset. Recording only the background noise might provide insight into its characteristics and thus help in constructing optimum filters. Additionally, oilfield operators might ask for a temporary cease of surface operation during the microseismic acquisition period, especially if the microseismic program is a few days in length. In the case of Field X, however, stopping production and injection activities even for a day is not possible owing to the severe economic consequences it might bring to PDO. Hence, the data acquired are highly contaminated with different noise types.

3.3.2 Oman dataset quality

Figure 3.17 displays background noise level on waveforms recorded during equipment testing and event triggering parameter setting prior to the microseismic monitoring program. Noise level is actually within the same amplitude as the signal before any filter application, giving SNR values as low as 2. (Figure 3.18) displays a waveform of an event recorded by three microseismic wells. The reason behind recording the microseismic event by geophones of three wells is explained in section 3.1 of chapter 1. It is clear that picking the first breaks is hardly possible without applying any signal enhancement filter type. Well-15 has more than one geophone having at least one component dead. Well-4 has the highest SNR, and most of its components are operational except geophone number four, which has a defunct component (H1). Deeper Geophones have higher SNR than shallower for two reasons. First, deeper geophones are closer to reservoir units and the earliest to receive the seismic energy before it decays due to intrinsic attenuation and geometric spreading. Secondly, they are further away from surface cultural noises.

(Figure 3.19) shows the P-wave, the S-wave and noise frequency content. Noise window is selected before P-wave onset time. The whole waveform shows a strong noise level at frequencies below 50 Hz (Figure 3.20), which displays a sonogram of frequency versus time. The frequency content of the signal varies between different events. Nevertheless, for the majority of events, the signal is contained between 40 to 500 Hz. The dominant P-wave frequency is between 150-200 Hz, whereas the S-wave dominant frequency is about 80-100 Hz. S-wave frequency range has some interference with the noise level. Notice the strong amplitude at 50 Hz in (Figure 3.19), which is related to powerline noise. This monochromatic frequency noise is dominant across the majority events at 50 Hz but is randomly occurring also at other frequency values with a slightly lower amplitude. Events recorded by microseismic wells 15 and 16 do not contain the 50 Hz powerline noise. Random cyclic noises can be related to Field X electric machines operating at certain frequencies and active during specific periods.

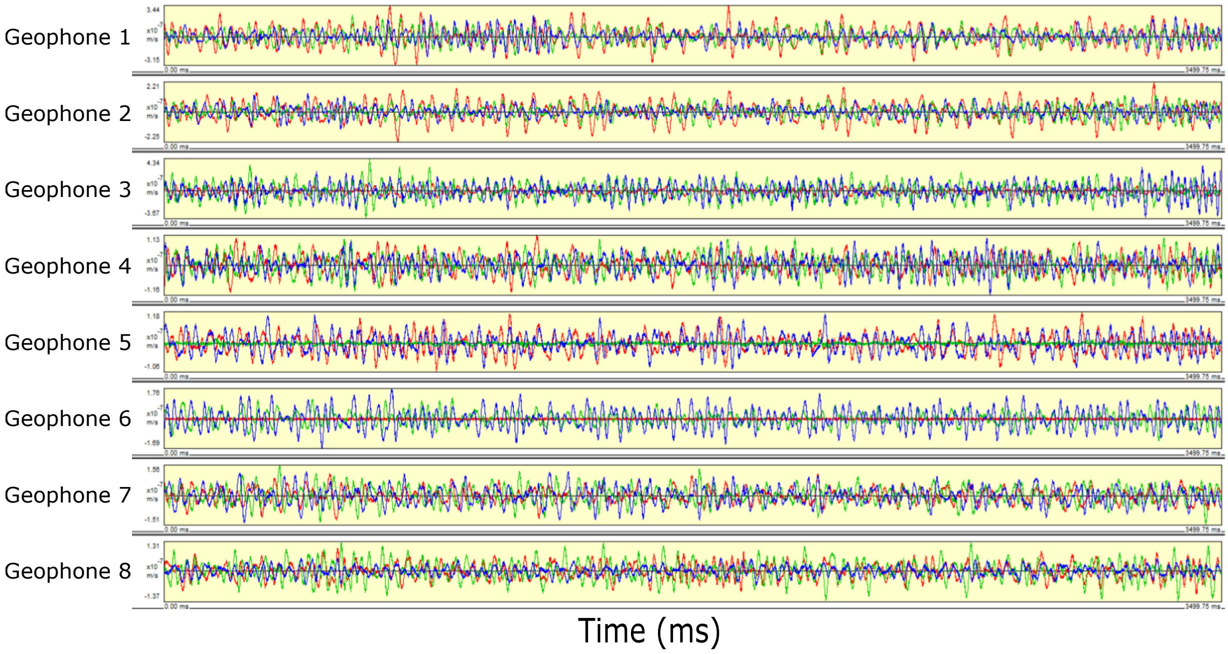

FIGURE 3.17. Background noise level of a waveform recorded during equipment testing and event triggering parameter setting. Courtesy of PDO.

3.3.3 Filters design

After analyzing and understanding the frequency content of both the signal and the noise, several filtering approaches were tested to observe their effectiveness in removing the unwanted noise without modifying the signal's amplitude spectra. Removal of low-frequency noise below 50 Hz can be accomplished using a Butterworth bandpass filter. A 4th order bandpass filter of corner

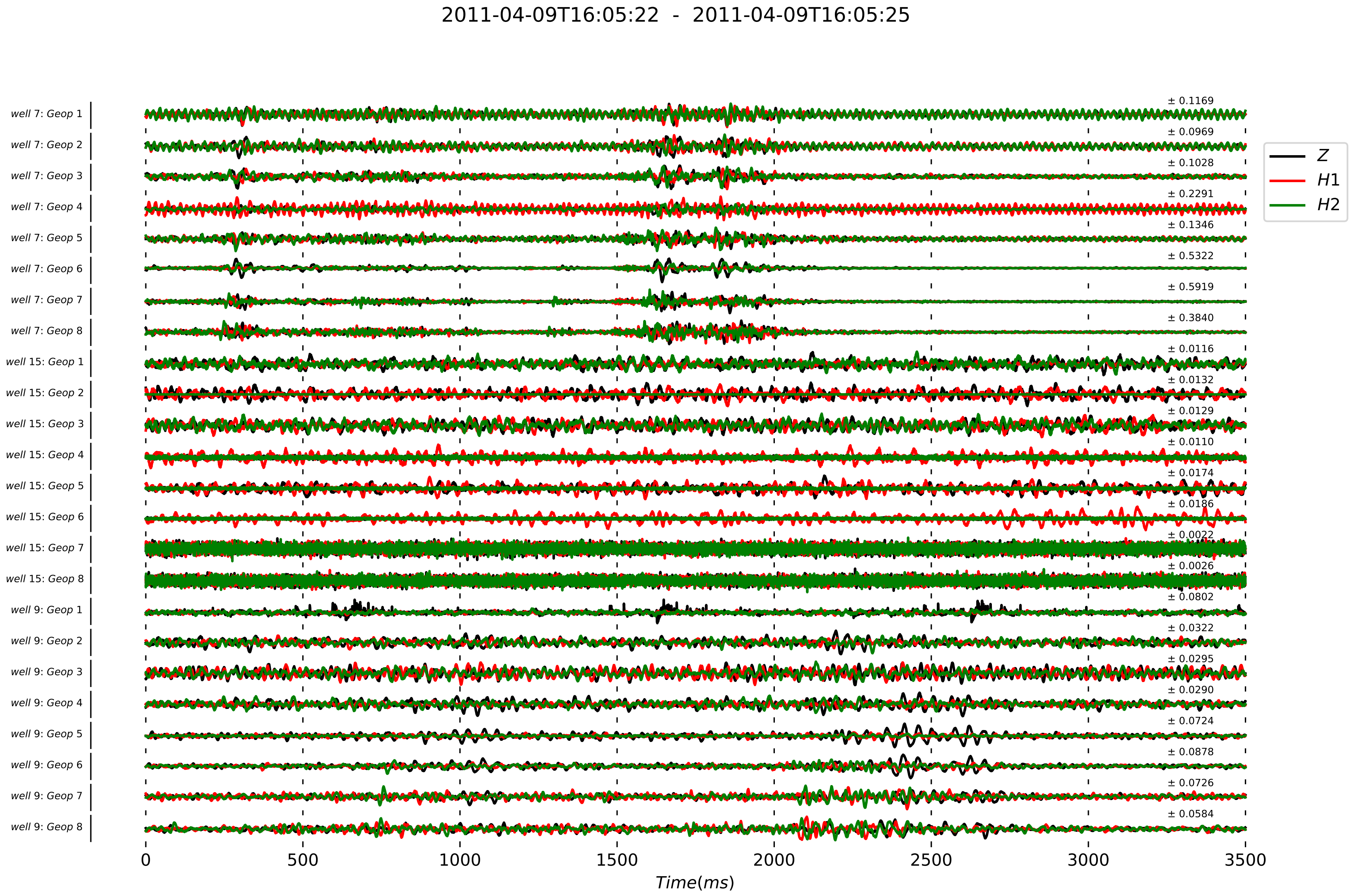

FIGURE 3.18. An example of a microseismic event waveform recorded by three wells before application filtering.

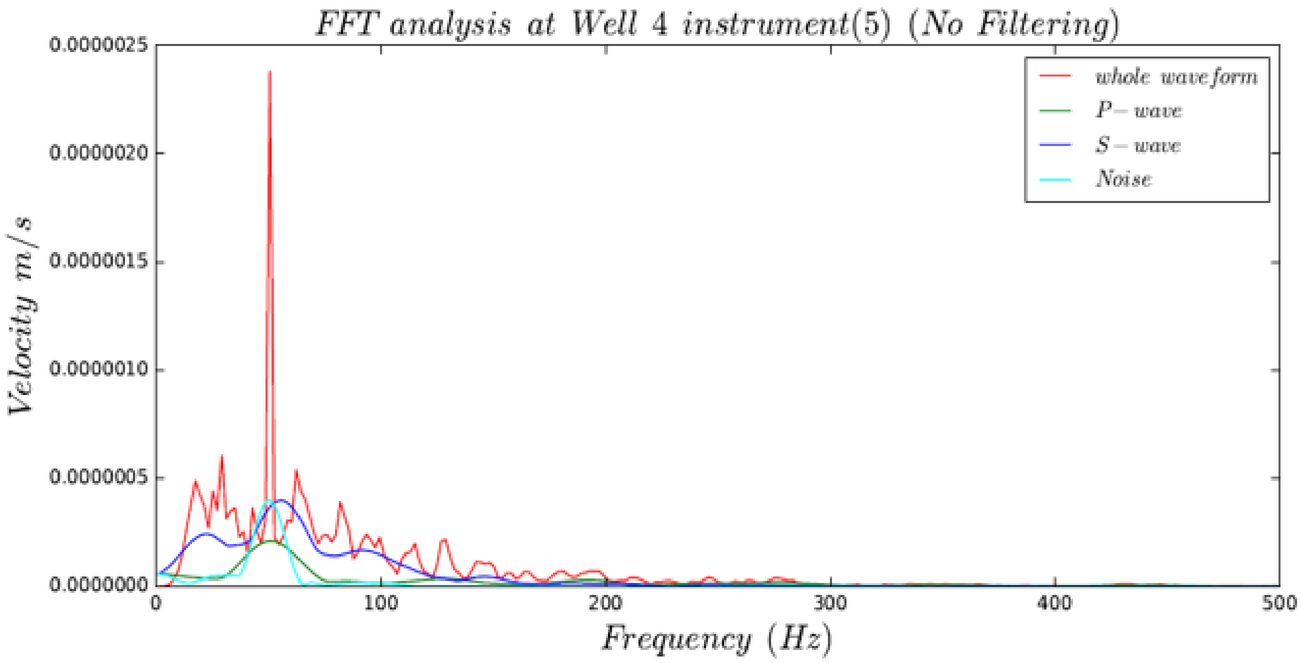

FIGURE 3.19. Frequency content of the P, S-wave and noise at an event waveform.

frequencies 40, 500 Hz is applied to all events. Bandpass filtering is achieved using the signal processing subroutine available in Obspy Python packages (Krischer et al., 2015). Infinite impulse response (IIR) method (Mitra and Kaiser, 1993; Winder, 2002) is used to design the filter, and then the cascaded second-order sections approach (Jenkins and Nayeri, 1986) is used to apply the filter. After the bandpass filter application, SNR increased by about 5% on average.

Most of the notch filter application methods available in literature expect the user to input the notch value(s) into the filtering workflow (Joshi and Dutta Roy, 1997; Xia and Miller, 1998; Yu et al., 1990). The data in Field X suffers from unpredictable monochromatic frequency noises. Therefore, using a direct method of notch filter application is not feasible. Wuestefeld et al. (2010) advised an adaptive multi-notch filter by applying autocorrelation on a noise window in the frequency domain. The window is selected before the P-wave onset time. The notch filter F is designed as described in equation 3.15 by normalizing the noise autocorrelogram S_{Noise}. The filtered signal is the inverse Fourier transform of the multiplication of F with the original trace as shown in equation 3.16,

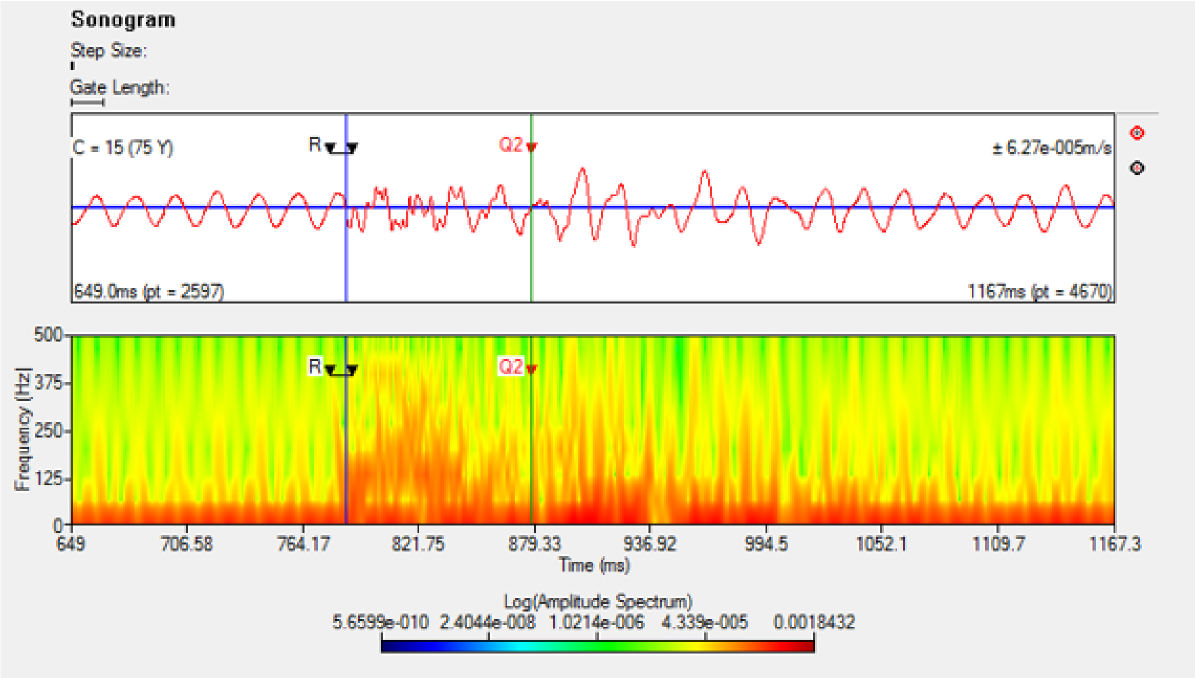

FIGURE 3.20. A Sonogram (Spectrogram) plot of frequency versus time for a raw waveform.

$$F = 1 - (S_{Noise}/\max(S_{Noise})) \tag{3.15}$$

$$T = ifft(S_{Seis} \times F). \tag{3.16}$$

The adaptive notch filter proposed by Wuestefeld et al. (2010) assumes that the noise before P-wave pick does not contain any frequencies that might also exist in the signal. Furthermore, it almost zero-out the frequencies on and around the notch filtered values, which is not a desirable outcome. (Figure 3.21) shows the application of this adaptive multi-notch filter on a waveform. In the amplitude spectrum, we notice that the cyclic noise is not at 50 Hz. A drawback of this filter is that it kills some frequency content at and around the cyclic noise levels instead of flattening (interpolating) the frequency spectrum around the multiple notch frequencies. Another disadvantage is the requirement to select a window before the P-wave pick, which in some cases in the Oman dataset occurs at the early stage of the event waveform.

Although the adaptive notch filter of Wuestefeld et al. (2010) proved adequate on some waveforms, it fails if the cyclic noises are not contained in the P-wave pick (Figure 3.22). Therefore,

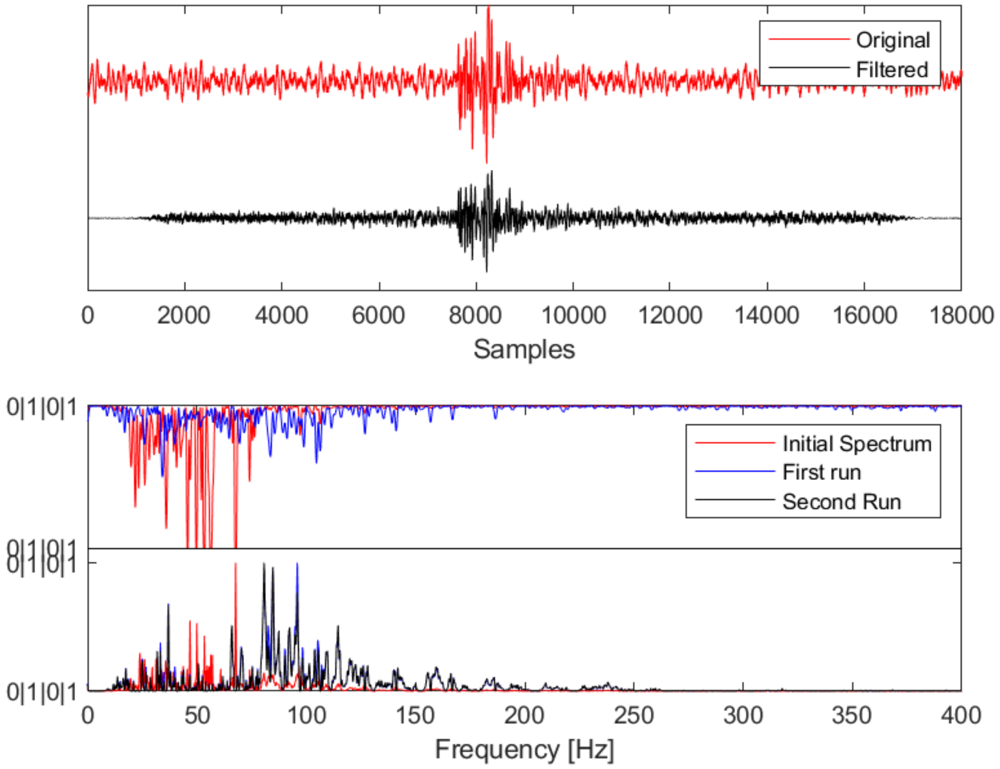

FIGURE 3.21. Application of an adaptive notch filter developed by Wuestefeld et al. (2010). Notice that the frequency of cyclic noise is not at 50 Hz. The upper diagram is the original and the filtered waveforms from one component. The lower figure contains the notch filter spectrum F (upper part) and waveform spectrum (lower part).

I developed a novice adaptive multi-notch filter and found it to be superior in removing the cyclic noises without creating side effects to signal amplitudes. This new filter works in two stages. First, the waveform frequency spectrum is scanned, and high amplitude cyclic noises are detected using peak detection techniques. Secondly, either interpolation is applied to the few frequency samples around the notch frequencie(s), or a second-order IIR notch filter is designed and applied on the identified cyclic noises. If choosing the first approach, an inverse Fourier transform is applied to recover the filtered waveform. The user input required for the first option is the number of frequency samples to be removed and subsequently interpolated at both sides of the frequency spectrum using cubic spline interpolation (Marsden, 1974). On the other hand, if preferring the second option, a data-dependent quality factor has to be determined in order not to create depressions (excess filtering) on the amplitude spectrum around the filtered notch frequencies or under-filter the notches. A data-driven method is established whereby the quality factor is different for each notch frequency and appropriately eliminates them without over or under-filtering.

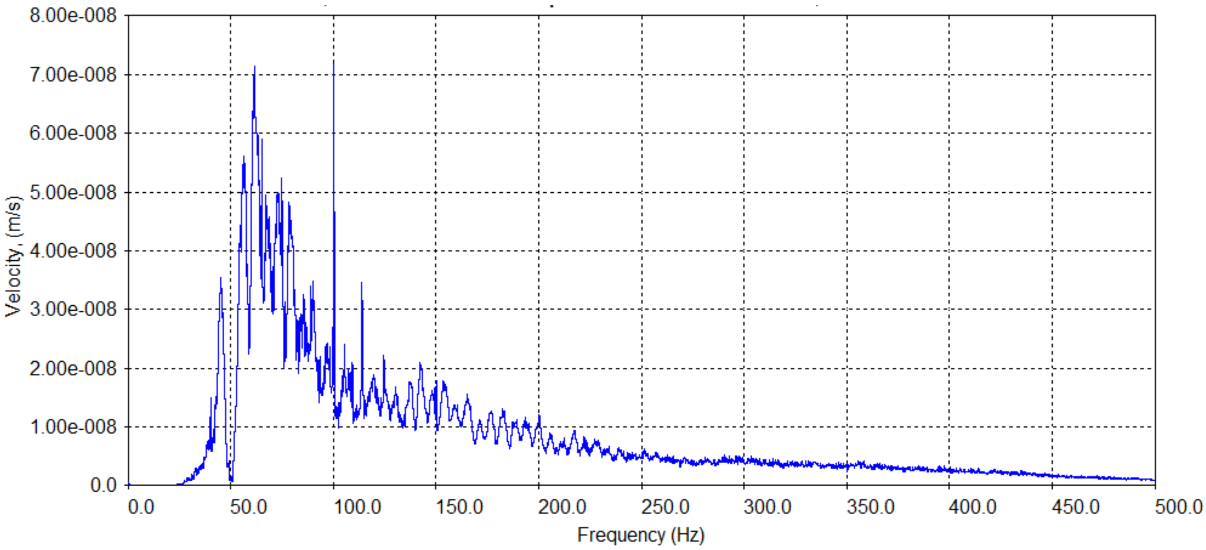

FIGURE 3.22. FFT amplitude spectrum of a wavefrom filtered by the adaptive notch filter of Wuestefeld et al. (2010). Notice that frequencies are muted at 50 Hz. Additionally, two cyclic noises are apparent at about 100 Hz and 115 Hz.

The peak detection method used here is described in Du et al. (2006) by incorporating continuous wavelet transform (CWT). The CWT mathematically described by Daubechies (1992) as follows,

$$C(a,b) = \int_R s(t)\psi_{a,b}(t)\mathrm{d}t, \psi_{a,b}(t) = \frac{1}{\sqrt{a}}\psi\left(\frac{t-b}{a}\right), a \in R^+ - \{0\}, b \in R, \tag{3.17}$$

where $s(t)$ is the original waveform, a is the amplitude at the translated time b of $\psi(t)$ which is the mother wavelet(ricker), $\psi_{a,b}(t)$ is the amplitude of translated wavelet and C is the 2D matrix of wavelet coefficients.

Using the CWT approach, peak-detection can be applied without the need to preprocess the raw data. In equation 3.18, $P_{\text{raw}}(t)$ represents a peak region in the original waveform, $P(t)$ is the real peak and $B(t)$ is the baseline function having zero mean,

$$P_{\text{raw}}(t) = P(t) + B(t) + C, t \in [t_1, t_2]. \tag{3.18}$$

The CWT coefficients of the peak $P(t)$ can be calculated as,

$$C(a,b) = \int_R P(t)\psi_{a,b}(t)\mathrm{d}t + \int_R B(t)\psi_{a,b}(t)\mathrm{d}t + \int_R C\psi_{a,b}(t)\mathrm{d}t. \tag{3.19}$$

Figure 3.23 shows an example of peak detection on a frequency spectrum. In this example, the highest notch appears at about 41 Hz. When two peaks are adjacent to each other within a defined threshold, only the largest one will be selected. A Gaussian filter (red curve) is used to limit the number of detected peaks and select the real notches. The Gaussian is described in equation 3.20 where σ is the standard deviation, and n is the number of samples in the Gaussian window. The window is convoluted with the frequency spectrum of the waveform to apply the Gaussian filter.

$$w(n) = e^{-\frac{1}{2}\left(\frac{n}{\sigma}\right)^2}. \tag{3.20}$$

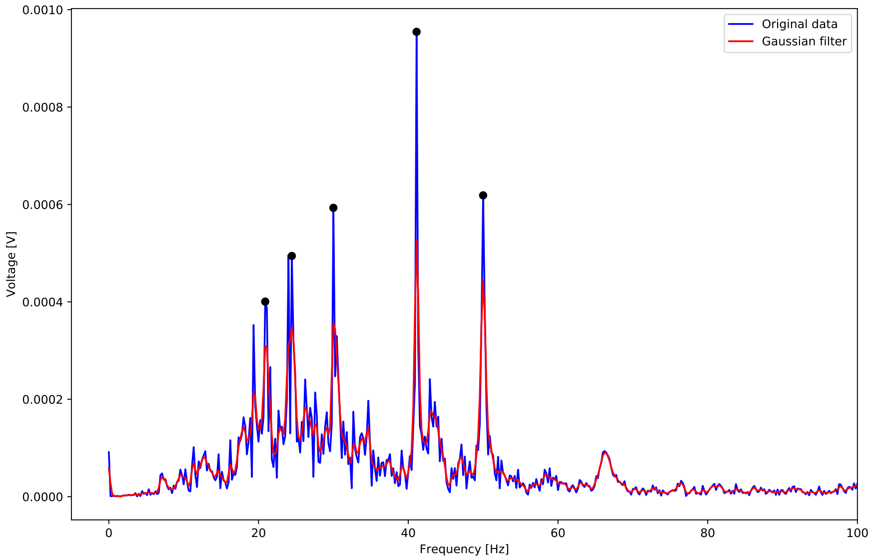

FIGURE 3.23. Peak detection of notch frequencies on a frequency spectrum. P-wave and S-wave are marked as blue and green vertical line respectively.

The calculation of an appropriate Q factor is based on the amplitude difference between each possible notch frequency and the baseline amplitude in the frequency domain. This difference also acts as quality control to determine if the selected frequency notches are valid cyclic noises and thus reject notches that do not satisfy a user-defined threshold. The threshold selected for Oman data is 2-time of baseline frequency value.

A more straightforward implementation of the new multi-notch filter is by removing and then interpolating few frequency samples around notch frequencies. The advantage this method has over IIR notch filter is that it does not require a Q factor and hence there is no concern of over or under filtering.

3.3.4 Filter application

Both methods of IIR and spline interpolation proved to work well in removing the cyclic noises. Here, results obtained by spline interpolation techniques will be shown. Overall, an increase of about 30% in SNR is observed throughout the waveform of events for which P-wave and S-wave can be picked. Those waveforms are usually from wells that first were triggered. For example, in (Figure 3.18) SNR drastically increased for well-7 but has shown no considerable improvement in the other two wells. The event first triggered Well-7, and well-15 and 9 recorded it since they were the closest to well-7.

Figures 3.24, 3.25 and 3.26 display the multi-notch in combination with bandpass filter application on an example waveform. Figure 3.24 shows the unfiltered waveform. Figure 3.25 depicts the filtered output, while Figure 3.26 is the difference between filtered and unfiltered data. In all these three figures, the first row is the waveform, the frequency spectrum in the second row, the phase spectrum in the third row, and the last row shows a spectrogram. P-wave and S-wave signal boost after filter application. P-wave is dominant around 150-200 Hz, while S-wave has lower frequency content. Phase spectrum is not distorted after filtering, particularly at P- and S-wave coda. The difference frequency spectrum (row 2) and the sonogram (row 4) plots (Figure 3.26) demonstrate that the frequency removed are cyclic and low-frequency noises below 50 Hz.

Figures 3.27 and 3.28 are another example of the same filter applied on a different waveform. The number of detected notches is fewer than the first example. There is also cyclic noise at 100 Hz which could be an overtone of the fundamental 50 Hz noise. Due to excessive noise level at this event, filtering could not help autopicking algorithms to pick first arrivals at the first three shallow geophones successfully.

Figure 3.29 shows three histograms (A, B, C) of SNR before and after applying first only Bandpass filter (B), then Bandpass plus adaptive notch filters (C). Bandpass filter increased the mean SNR about from a mean of 2 (Figure 3.29-A) to 17. The application of adaptive notch filter the Bandpass filtered data further increased SNR to a mean value of 31. The analysis is made on a sample of 100 traces selected randomly from microseismic wells for which the P- and S-wave can be picked confidently.

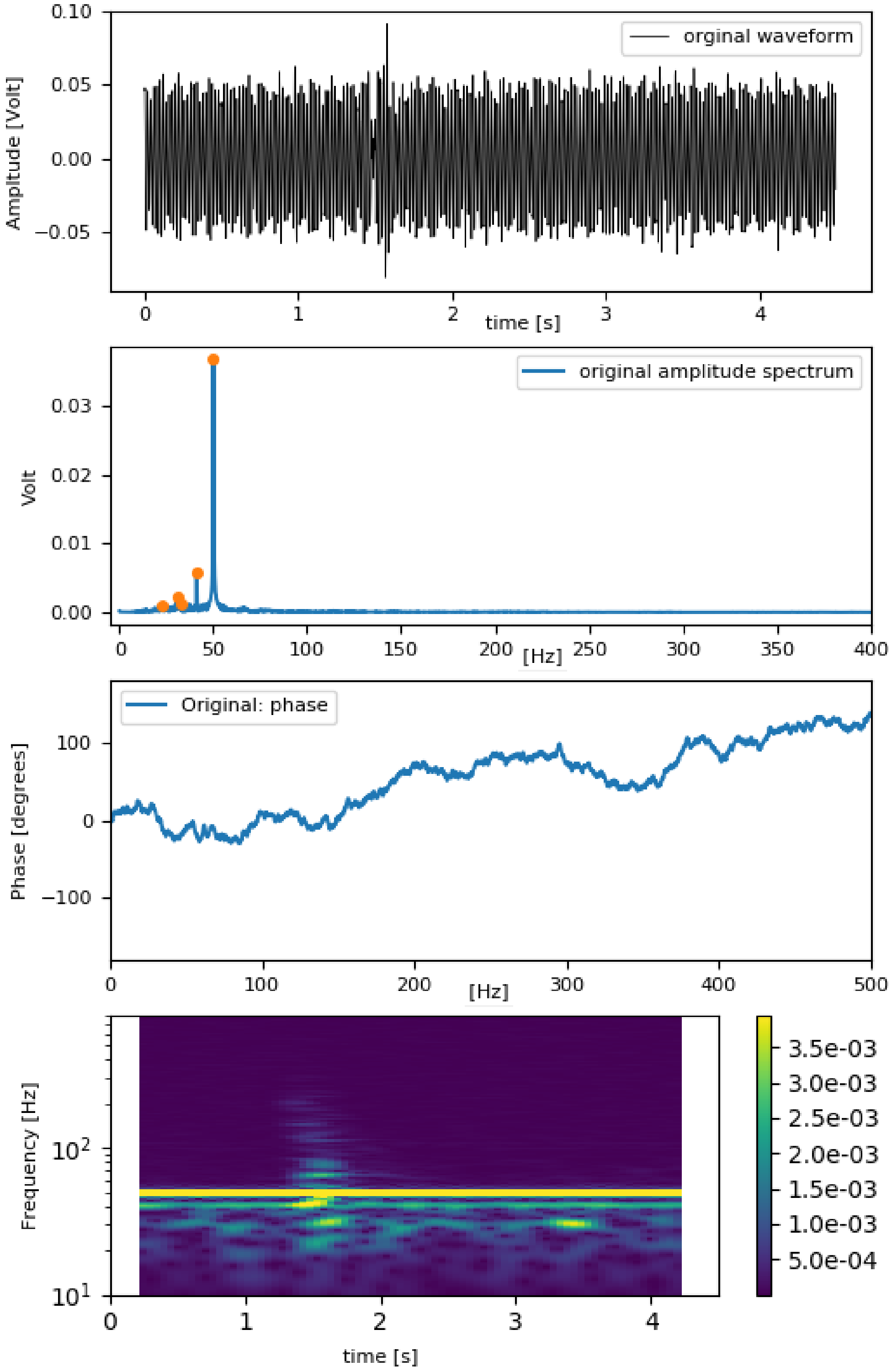

FIGURE 3.24. The rows show from top to bottom waveform in the time domain, the frequency spectrum of the waveform, phase spectrum, and finally, a sonogram of frequency versus time. This figure shows the data before filter application.

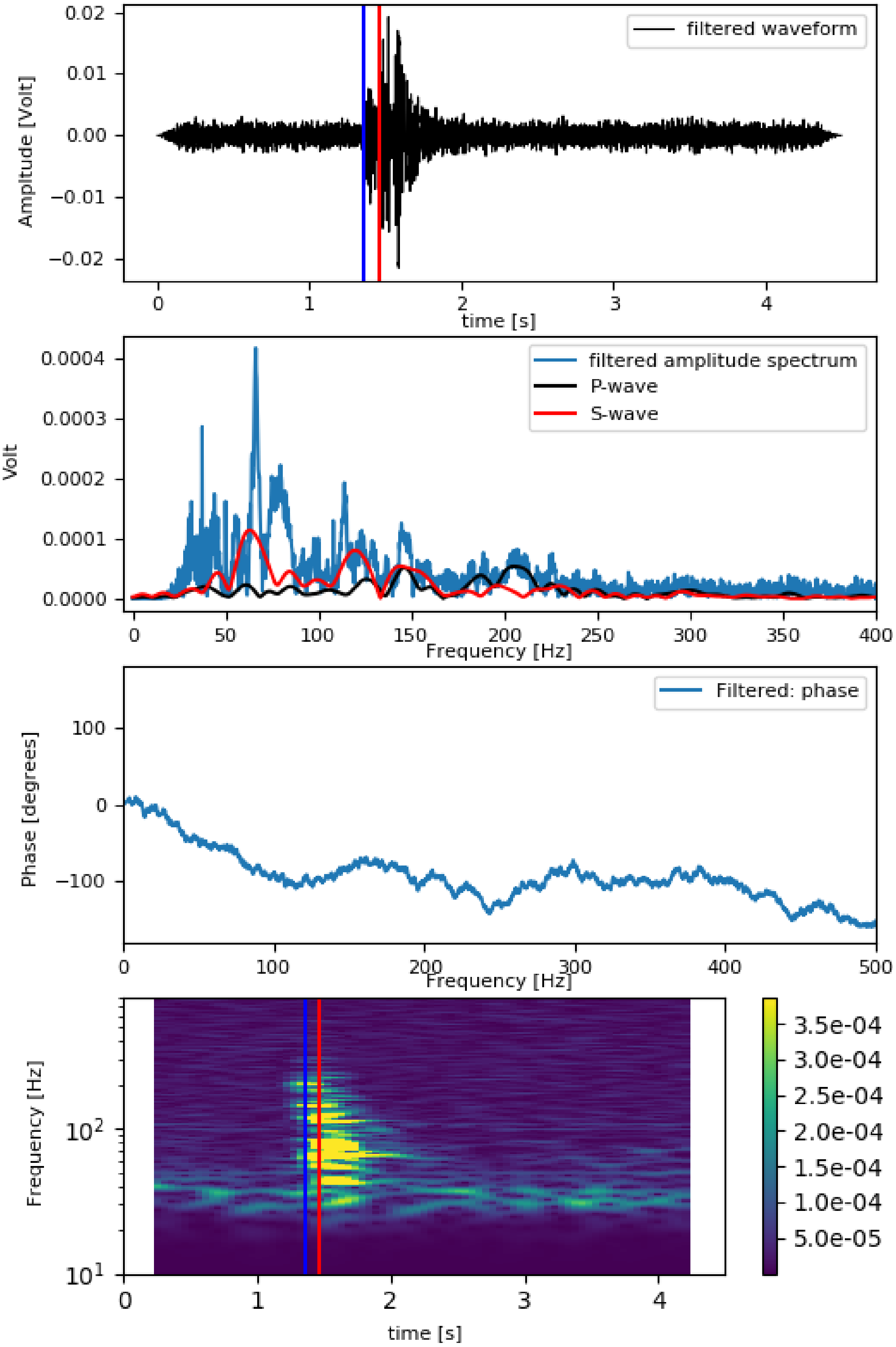

FIGURE 3.25. The rows show from top to bottom waveform in the time domain, the frequency spectrum of the waveform, phase spectrum, and finally, a sonogram of frequency versus time. This figure shows the data after filter application.

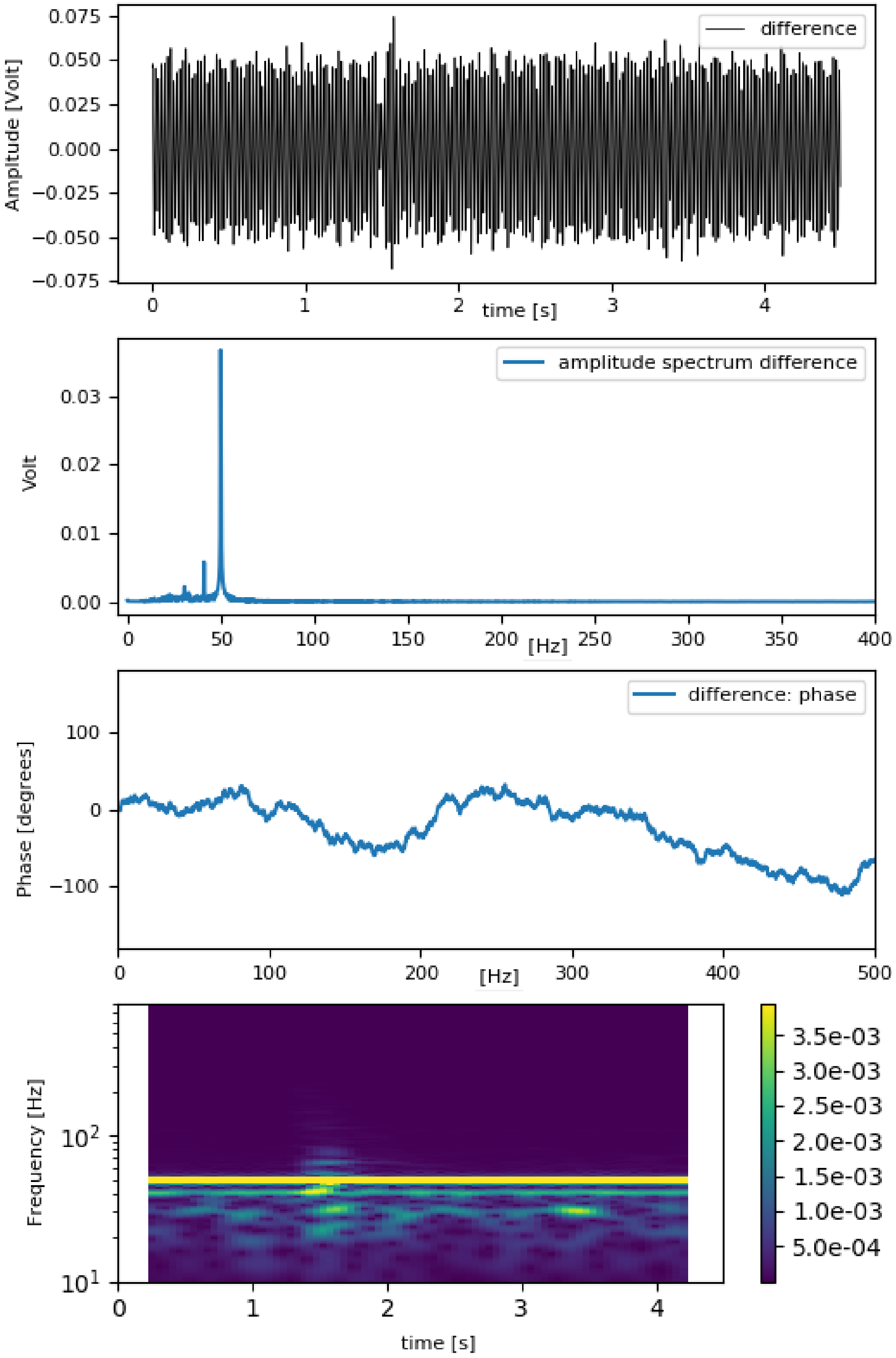

FIGURE 3.26. The rows show from top to bottom waveform in the time domain, the frequency spectrum of the waveform, phase spectrum, and finally, a sonogram of frequency versus time. This figure shows the difference between the filtered (Figure 3.25) and the original (Figure 3.24) data.

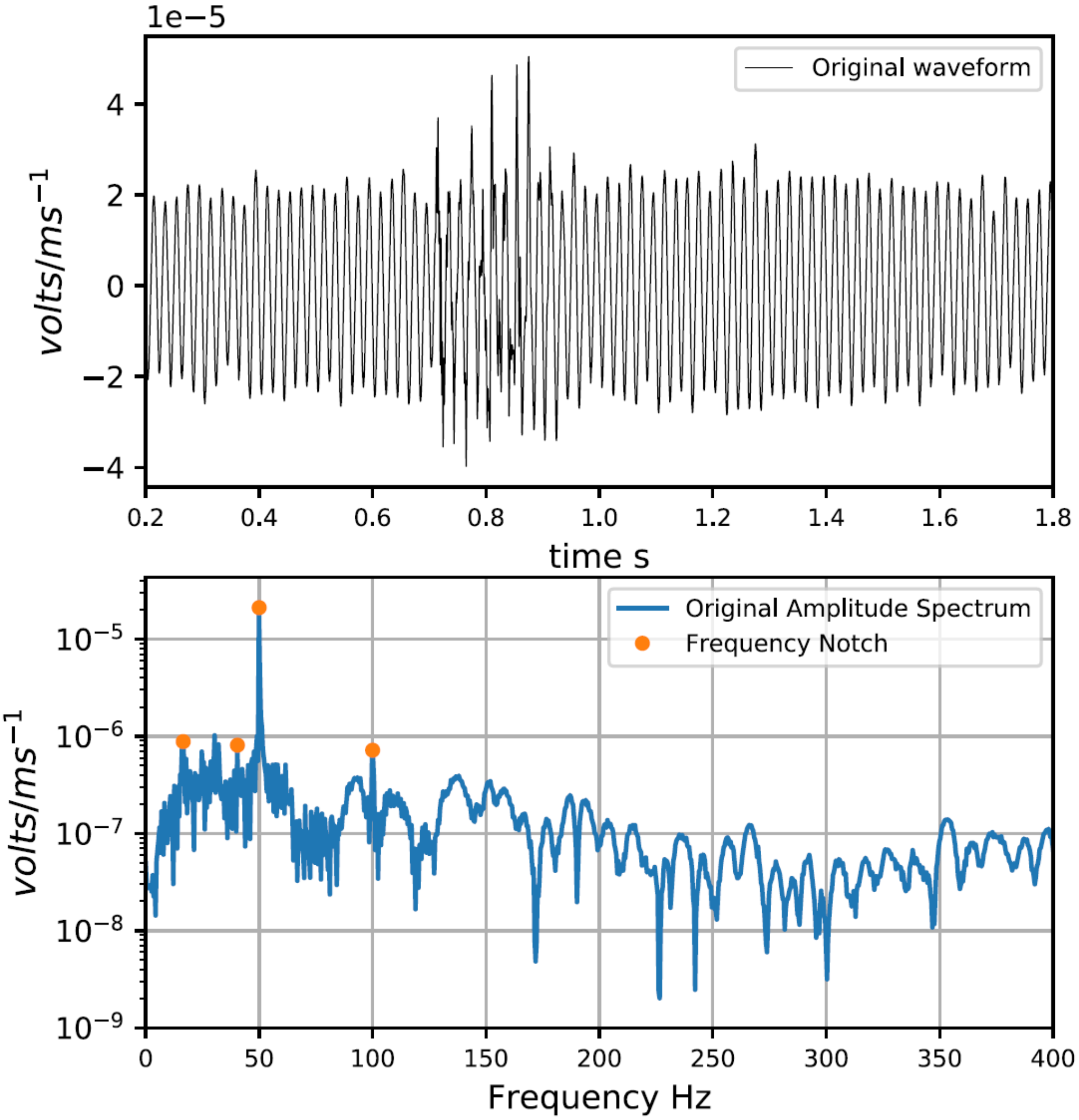

FIGURE 3.27. An example of a waveform before the application of bandpass and adaptive multi-notch filter. The top figure is the waveform while the lower figure is the frequency spectrum of the waveform. At this event the powerline noise at 50 Hz is very dominant as seen in the frequency spectrum.

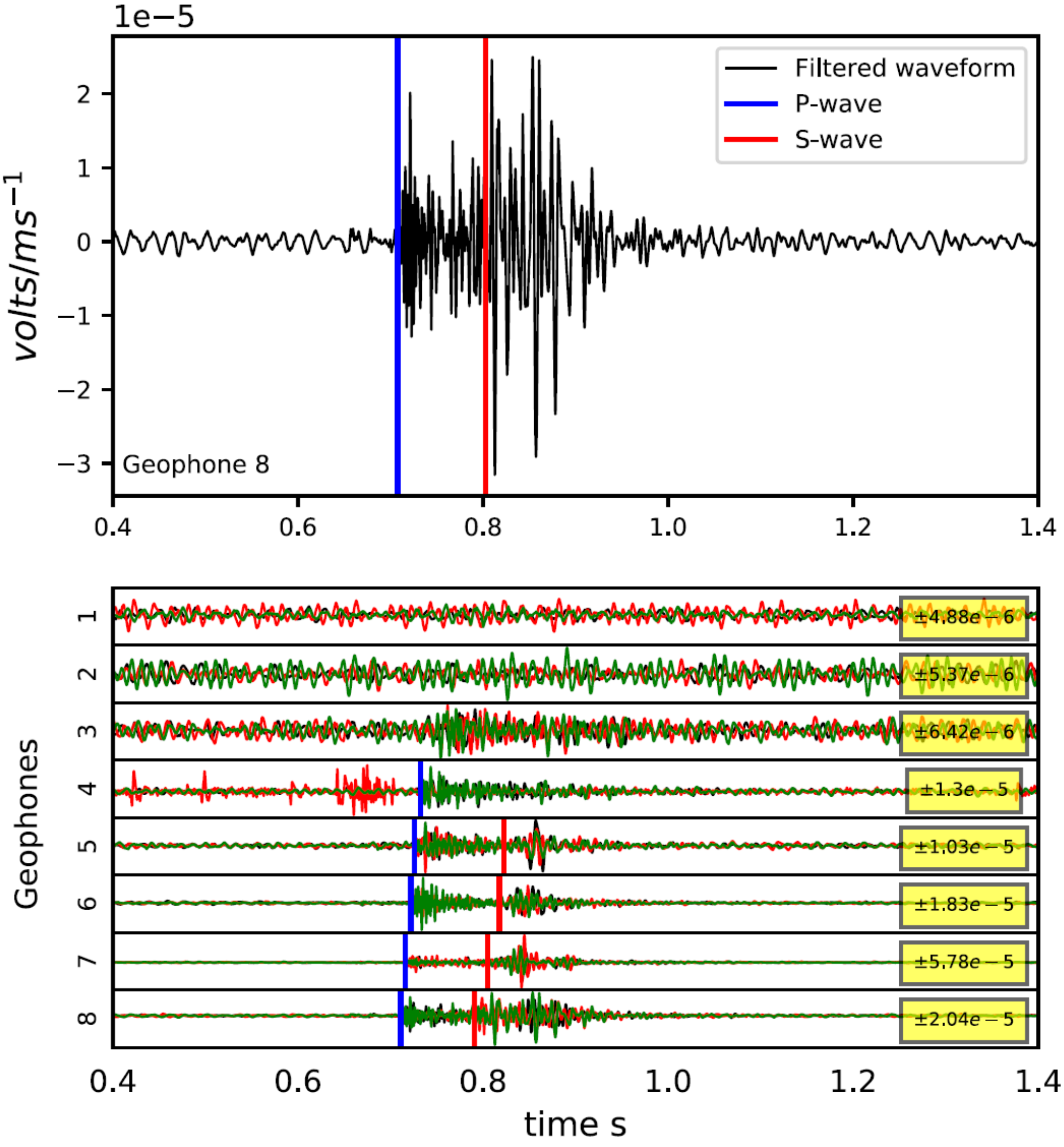

FIGURE 3.28. Bandpass and adaptive multi-notch filter application. The same waveform as in Figure 3.27 but after the application of bandpass and adaptive multi-notch filter. The top figure shows the a single waveform while the lower figure shows three waveforms for each geophone. Move-out display of the waveforms (lower figure) indicates that shallow events are very noisy and the filtering could not help improve the SNR for first break picking.

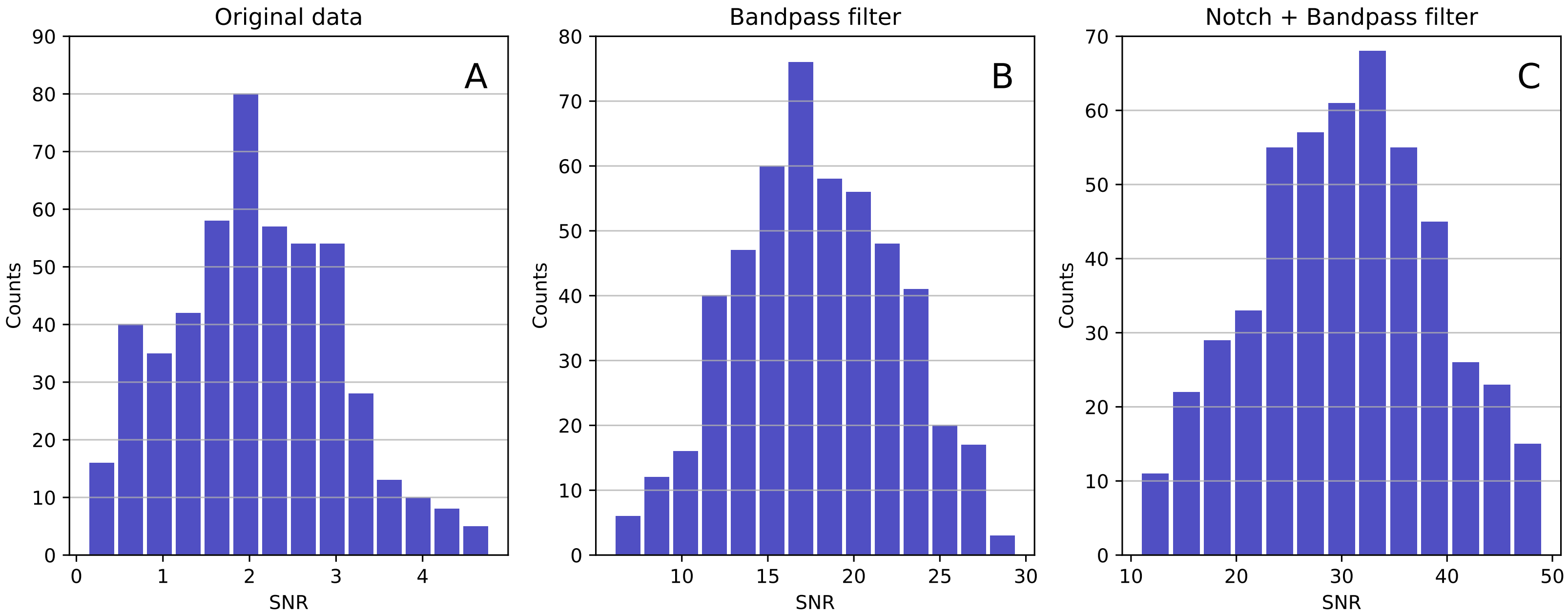

FIGURE 3.29. Histogram of SNR before and after application of notch and Bandpass filters. A is the distribution of SNR for the original data. B shows the histogram of SNR after only Bandpass filter. C is rge SNR of a combination of Bandpass filter and adaprive notch filter.

3.4 Conclusion

I start the Chapter by describing the equipment setup used in Field X. 13 microseismic wells equipped with 3C-component geophones continuously monitor induced fracture and faults.

In this chapter, I oriented geophones components using a newly developed technique. The technique is compared with other established algorithms to assess its effectiveness in finding true geophone orientation correctly. Results obtained from different methods are consistent with each other. The new method and the re-implementation of other methods in Python resolve the 180° inherent ambiguity, which arises when the events are recorded by one vertical well. The optimal rotation window is two cycles after the P-wave onset time. I Flinn (1965) and the new method show the best calculation performance, whereas ODR performs very slowly.

In the second section of the chapter, I introduced a data-driven novice multi-notch filter. Random cyclic noises dominated most of the waveform but almost always existed on 50 Hz (powerline noise). Application of this filter combined with a Butterworth bandpass filter increased the SNR to 30 from as low as 2. The filter has a minimum effect on the P- and S-wave signal amplitude and phase spectrum. Preserving amplitude spectrum of P- and S-wave allows obtaining accurate event source parameters.

CHAPTER 4

TRAVEL TIME PICKING AND VELOCITY ANALYSIS

> *"It takes an earthquake to remind us that we walk on the crust of an unfinished earth."*
>
> — Charles Kuralt

Arival time picking and velocity model building are the two main inputs into the micro-seismic location algorithm. In this chapter, I discuss the arrival time picking methods used to obtain P- and S-wave first arrivals. In the second part of the chapter, the steps followed to estimate 1- and 3-dimension velocity models will be discussed.

4.1 Travel time picking

4.1.1 Introduction

The process of picking is almost always a necessity in all seismic methods. For instance, in the seismic refraction technique, the geophysicist often picks the first arrival time of direct and refracted waves to build a subsurface model of the ground (Mooney et al., 1985). In active seismic data processing, the static correction requires picking of first arrivals to eliminate the effect of the weathered layer and topographic variations (Cox, 1999; Höcker and Fehmers, 2002). Seismic common mid-point stacking and migration demand picking of semblance power in the velocity analysis process (Yilmaz, 2001). Multichannel analysis of surface waves (MASW) needs picking of dispersion curves before obtaining the S-wave velocity profile of the subsurface (Park et al., 1999). Seismic interpreters spend a considerable time picking subsurface layers reflection times in 2D and 3D active seismic data for structural modeling (Höcker and Fehmers, 2002). One of the main steps in the microseismic data processing is also the arrival time picking of the P- and S-wave. The uncertainty in the microseismic location accuracy is a function of many parameters, but the impact of arrival times is very crucial. In recent years the number of channels deployed in microseismic data acquisition has seen a tremendous increase. Therefore, Manual picking of arrival time is a tedious and time-consuming process. Manual picking is prone to human errors, and the perception of everyone to the first arrival time is different. Hence, the geophysical scientific community has introduced various automatic arrival time picking techniques.

In the domain of microseismic processing, the interest is on the detection of the events from continuous records and arrival time picking. The most common technique is the classic STA/LTA for both event detection and arrival time picking (Allen, 1978; Sharma et al., 2010). Several variants of the classic STA/LTA method exist. They include recursive, delayed, carl STA/LTA, and z-detect (Trnkoczy, 1999; Withers et al., 1998). Other methods also exist that depend on different seismic data attributes such as polarization methods which use particle motion direction to isolate a certain phase from others and thus enhance phase-detection criterion (Amoroso et al., 2012; Reading et al., 2001), wavelet transform (Anant and Dowla, 1997; Karamzadeh et al., 2012), Akaike information criterion (Sleeman and Van Eck, 1999; Takanami and Kitagawa, 1991), variation produced from fractal dimension calculation (Boschetti et al., 1996; Jiao and Moon, 2000), neural network learning algorithms (McCormack et al., 1993; Murat and Rudman, 1992; Zhou et al., 2019), and a high-order statistics approach of kurtosis and skewness measurements (Küperkoch et al., 2010; Li et al., 2016; Lokajicek and Klima, 2006).

Section 1.4.1 of chapter 1 gave a brief overview of the event detection method. The triggered data had already been detected, and each event is provided in a separate seg-y file. Events detection was made based on two combined techniques of amplitude threshold and STA/LTA. This section focuses on the onset time picking of P- and S-wave arrivals. I will test several methods of automatic arrival picking on a random sample of events of mixed SNR and choose the one which gives the lowest mean difference to the manual picking. Leonard (2000) compared some automatic arrival times with manual picking and concluded that the former method provides comparable results with the latter.

Figure 4.1 shows the recording of signals from the deepest geophone in MSW-7 having a high SNR. On the other hand, Figure 4.2 shows moderate SNR recordings from the same well but geophone number four. Deeper geophones commonly have higher SNR than shallower ones. The left column shows the 3-component seismograms, while the right column displays the respective spectrograms. The red line in the spectrogram is the central frequency of the whole waveform. The dominant frequency of P- and S-wave is in the range of 180 to 240 Hz and 90 to 160 Hz, respectively. First arrival picking for shallow geophones (e.g., geophones 1, 2, and 3) is hard by manual picking for the majority of events. However, picking can be facilitated when the event is plotted in a move-out display (Figure 4.3). MSW-7, MSW-15, and MSW-9 record the event shown in Figure 4.3 but picking first arrivals on wells other than MSW-7 is impossible due to very low SNR. Many events exhibit similar behavior where manual picking is possible only in the waveforms of one well from the array of wells recorded the events. Manual picking is performed using the Python Matplotlib package on 50 selected seg-y files.

4.1.2 P- and S-wave automatic arrival time picking

Automatic arrival time picking of microseismic data processing involves determining the onset times of P- and S-wave. Successfully identifying these two phases highly depends on the SNR of the seismic data. Fifty events of variable SNR are selected to test the robustness of several auto-picking algorithms. Table 4.1 shows the SNR statistics of P- and S-wave phases of picked manually in these events. The SNR is given mathematically as $10\log_{10}\left[\left(\frac{A_{\text{signal}}}{A_{\text{noise}}}\right)^2\right]$ in dB, where A_{signal} and A_{noise} are the RMS amplitude of the P-wave or S-wave, and noise windows, respectively. The window length is set at 100 ms starting from onset time, whereas the noise window is selected before the P-wave. Generally, S-wave has higher SNR, and some waveforms have negative SNR values indicating that the noise level is higher than the signal. Geophones having dead components or unserviceable are excluded from the analysis.

Although the events have been auto-triggered and each event is contained in a single file. I observed that many events might need re-triggering. An example of such an event is shown in Figure 4.4. This waveform shows two possible events. The one that occurs after 3 seconds is most probably the correct event since it shows clear P- and S-wave onset times in the STA/LTA curve (also known as the Characteristic Function curve). Details of the computation methodology are explained below. Such waveforms made the determination of a single P- and S-wave from one seg-y file quite impossible and increased the difference between manual and auto-picking considerably. Carefully inspecting the events occurring after 3 seconds reveals the existence of

TABLE 4.1. SNR statistics of 50 events for P- and S-wave phases picked manually.

Statistics	P-wave SNR (dB)	S-wave SNR (dB)
mean	5.5	12.9
std	6,0	7.0
min	-12.0	-6.7
percentile 25%	1.7	8.2
percentile 50%	4.8	12.7
percentile 75%	9.0	17.5
max	30.7	36.2

three peaks. The first is associated with the P-wave. The remaining two peaks are related to the orthogonal SV- and SH-waves generated due to splitting in an anisotropic media. In this project, I pick only the earliest of the splitting S-wave arrivals.

For some other seg-y files, the waveforms show a train of successive events having similar characteristics indicating that they are probably occurring from the same source point but having varying amplitudes (Figure 4.5).

4.1.2.1 STA/LTA

The STA/LTA technique is one of the most common approaches for arrival time picking. Several variants of this technique exist. The difference between them is the calculation of the characteristic function (CF). The CF can be the power of the signal ((Allen, 1978)), the absolute value ((Swindell and Snell, 1977)) or an envelope function ((Earle and Shearer, 1994)). The method can be considered as a measure of noise level where STA keeps track of the signal amplitude level, and the LTA measures the background noise level ((Vaezi and Van der Baan, 2015)). Here I use two of the methods developed by ((Trnkoczy, 1999; Withers et al., 1998)). The two formulated variants of the technique are Classic and Recursive STA/LTA.

The classic STA/LTA is described as

$$\mathrm{STA}_i = \frac{x_i^2 - x_{i-\mathrm{Nsta}}^2}{N\mathrm{sta}} + \mathrm{STA}_{i-1} \tag{4.1}$$

$$\mathrm{LTA}_i = \frac{x_{i-Nsta-1}^2 - x_{i-Nsta-Nlta}^2}{Nlta} + \mathrm{LTA}_{i-1}, \tag{4.2}$$

where N donates number of sample in the respective STA and LTA windows, x is the waveform and i is the sample number in the waveform. In the definition of STA/LTA shown in equations 4.1 and 4.2, no overlap between windows is made and the STA starts right after LTA. The However, when introducing a short delay between the two windows, the technique will be called delayed STA/LTA ((Ruud and Husebye, 1992)). This delay ensures better statistical independency between STA and LTA. The recursive STA/LTA produces an impulse response which is exponentially decaying rather than rectangular as is the case with the classic one. The recursive STA/LTA is defined as

$$\mathrm{STA}_i = Cx_i + (1 - C)\,\mathrm{STA_{i-1}}\mathrm{LTA}_{i-1} \tag{4.3}$$

$$C = 1 - e^{-S/T}, \tag{4.4}$$

where S is the sampling interval, and T is the characteristic decay time. The value of C used in this project is 1/Nsta and 1/Nlta for STA and LTA, respectively. The calculation of LTA is the same as equation 4.3.

There are two inputs needed to calculate the STA/LTA and then detect the first arrivals. The first is the determination of the window size for STA and LTA separately. Making the LTA window very long obscures strong arrivals and boosts weak signals arriving after the main onset times. On the other hand, making the STA window very short results in high fluctuations in STA/LTA curves and hence, the detection of many small peaks. Figure 4.6 shows the effect of the window size on the retrieved STA/LTA curves. For the classic method, testing proved that choosing a window length equal to 1 and 0.05 times frequency sampling for LTA and STA, respectively, results in STA/LTA curves that are smooth but clearly distinguish the onset arrival times. Contrarily, the recursive method produces the best STA/LTA curves when the window lengths are 80 and 2000 sample points for STA and LTA, respectively. The STA/LTA peak curves have sharper right edges for the recursive method than the classic method, enabling better arrival time detection (Figure 4.7).

The other input parameter is the threshold. This parameter determines at what value of the STA/LTA the arrival times should be placed. Usually, This parameter is split into two in order to encapsulate the coda wave instead of only the first onset. These two parameters are trigger-on and trigger-off. Determination of the threshold in this project for STA/LTA methods is omitted since the value is data-dependent. Using a constant threshold determination produces first arrivals, which are way off from the manually picked arrival times. Instead, I use a detection technique described below:

1. Obtain the STA/LTA values using the classic and recursive methods.
2. Apply a Gaussian smoothing to the STA/LTA curve using equation $g(x) = \frac{1}{\sqrt{2\pi \cdot \sigma}} \cdot e^{-\frac{x^2}{2\sigma^2}}$, where σ is the standard deviation and x is the STA/LTA.
3. Find peak values in the gaussian-filtered curve using a continuous wavelet transform technique developed by Du et al. (2006).
4. Compute the gradient along the curve.
5. Find zero-crossing along the gradient curve.
6. Determine the index of the sample point of the zero-crossing for only the two largest peak values found in step 3. The smallest and the largest of these indexes are the P- and S-wave travel times.

4.1.2.2 Phase arrival identification-Kurtosis

The kurtosis is a higher statistical distribution measurement characterizing the tailedness of the probability of a random variable (Baillard et al., 2013; Saragiotis et al., 2002). (Baillard et al., 2013) defines the kurtosis mathematically as,

$$K \equiv \frac{E\left[(X-\mu)^4\right]}{\left\{E\left[(X-\mu)^2\right]\right\}^2} = \frac{m_4}{\sigma^4}, \tag{4.5}$$

where X is the random variable, E is the expected value, μ is the mean, m_4 is the fourth central moment, and σ is the standard deviation. For sampled seismic data, the equation 4.5 becomes,

$$K = \frac{\frac{1}{n}\sum_{i=1}^{n+1}(x_i - \bar{x})^4}{\left[\frac{1}{n}\sum_{i=1}^{n+1}(x_i - \bar{x})^2\right]^2}. \tag{4.6}$$

Similar to STA/LTA methods, it requires a moving window to calculate the kurtosis and a threshold value to determine first breaks arrival times. I used a moving window length of 0.2 seconds. Contrary to the constant value defined in the classic and recursive STA/LTA methods, the threshold is a dynamic value. The application is based on the Python module developed by (Chen and Holland, 2016). Generally, for high SNR data, the picks produced from this method are good. This method is more sensitive to the window length than STA/LTA method.

4.1.2.3 Modified transient energy method

The method is developed by Lomax et al. (2012), which applies an octave filter to create various frequency bands to the analyzed waveform. The number of total bands starts from the first central frequency defined by a user-input and doubles each time until the high corner of the last band exceeds the Nyquist frequency (Chen and Holland, 2016). The method is mathematically defined as,

$$E_n[i] = BF_n[i]^2, \tag{4.7}$$

where $BF_n[i]$ is the Bandpass filtered data of each produced band. The CF is calculated as,

$$\mathrm{CF}_n^{\mathrm{rms}}[i] = \frac{E_n[i]}{\mathrm{rms}(E_n[i-1-l:i-1])}, \tag{4.8}$$

where l is the window length. The threshold here is also a dynamic floating value calculated by multiplying the RMS of the moving window with an input value. The input parameters I used for the moving window to calculate the CF for the Bandpass filtered data and the moving average window for dynamic threshold are 0.5 and 1 seconds, respectively.

4.1.2.4 Akaike Information Criterion (AIC)

The AIC method is very well known for its wide use for arrival time picking, particularly P-wave. The method conventionally works by searching the global minimum of an auto-regressive model. However, different variants exist (Leonard and Kennett, 1999; Sleeman and Van Eck, 1999; Zhang et al., 2003). Sleeman and Van Eck (1999) describes AIR function as a division of two segments (observed and stationary)

$$\mathrm{AIC}(P) = (P-M)\log\left(\sigma^2_{1,\max}\right) + (N-M-P)\log\left(\sigma^2_{2\max}\right) + Constant, \tag{4.9}$$

where P is the division point, N represents the number of sample points in the data M is the order of the auto-regressive model, and $\sigma^2_{1,2\max}$ is the variance of the two segments of the waveform. The method used here does not incorporate the auto-regressive model Maeda (1985) and is expressed as

$$\mathrm{AIC}(P) = P\log\{\mathrm{var}(x[1,P])\} + (N - P - 1)\log\{\mathrm{var}(x[P+1,N])\}, \tag{4.10}$$

where the division point covers all the data points of the seismogram x. This method is the only one from the mentioned one above which does not require an analysis window. The only needed parameter is the length of the moving average window for the adaptive threshold. A value of 0.05 seconds is used for this window.

Insite software provides a routine for the AIC picking method, but I used the Python implementation of the method developed by Chen and Holland (2016) since it allows to have more control on the input and output seg-y files management via Obspy package.

4.1.3 Discussion on the performance of the methods

All the methods mentioned above are applied to seismograms on a trace by trace basis. The arrival time for each geophone is selected as the mean value of the auto-picked arrival times from the waveforms of the three components. I only selected seg-y files that show one clear event. Figure 4.8 shows the characteristic function for each method on a good SNR waveform. The approach I developed to obtain the picks from the CF of STA/LTA methods always produces picks even if there exist no real arrival times. However, for good quality data, this approach performs better than using a constant threshold for STA/LTA methods, and the retrieved arrival times show lower differences to the manually picked ones.

Classic and recursive STA/LTA methods produce quite similar CF. The peak curves for the recursive STA/LTA are sharper and narrower when using a similar window size. The phase arrival identification-Kurtosis method gives very sharp left edge CF at the pick location when an optimum analysis window is used, but the number of peaks in the CF is sensitive to the selection of the window length. Notice that the CF is zeroed out at the beginning of the trace with a length equal to the sliding window size (Phase arrival identification-Kurtosis and Modified energy ratio) or STA size IN STA/LTA method in seconds. Since about half of the events have a total length below 2 seconds, these four methods become unusable. Therefore, to overcome this shortcoming, I padded the beginning of all traces with a Gaussian noise having a length equal to the sample size of the analysis window. The Gaussian noise level is set equal to the first few samples from the original waveform before padding. The extra added time is later subtracted from the auto-detected arrival times.

The adaptive threshold makes the identification of both P- and S-wave arrival quite close to the manually picked one in the modified energy ratio and Kurtosis method. The threshold level increases above small peaks produced after the P- and S-wave arrival times. AIC method picks the P-wave very accurately even for noisy data but does not perform similarly for the S-wave. However, in general, AIC provides the lowest error for both P- and S-wave than other methods. In this project, I selected the AIC method but did a manual review of all waveforms and cleaned up the pickings or manually picked the arrival times for shallow geophones when AIC failed. A contact company to PDO also provided arrival time picks. The main issues with the provided picks are slightly off S-wave arrivals and wrong identification of both the P- and S-wave when multiple possible events exist in the same seg-y file.

Table 4.2 provides a statistical description of the difference between the manually picked and auto-picked arrival times for all the methods. The RMS increases considerably when including seg-y files showing multiple probable events. The geophones with the highest error are usually the shallow ones.

TABLE 4.2. P- and S-wave statistics describing the difference between manual and auto-picking methods.

	P-wave				
	Classic STA/LTA	Recursive STA/LTA	Kurtosis	Transient energy	AIC
RMS error (s)	0.060	0.055	0.033	0.048	0.032
min (s)	-0.0120	0.0022	0.0050	-0.0050	-0.0022
max (s)	0.131	0.203	0.069	0.079	0.055
	S-wave				
	Classic STA/LTA	Recursive STA/LTA	Kurtosis	Transient energy	AIC
RMS error (s)	0.090	0.081	0.054	0.072	0.053
min (s)	0.0163	-0.0097	-0.0036	0.0065	0.0113
max (s)	-0.216	0.171	0.099	0.281	-0.316

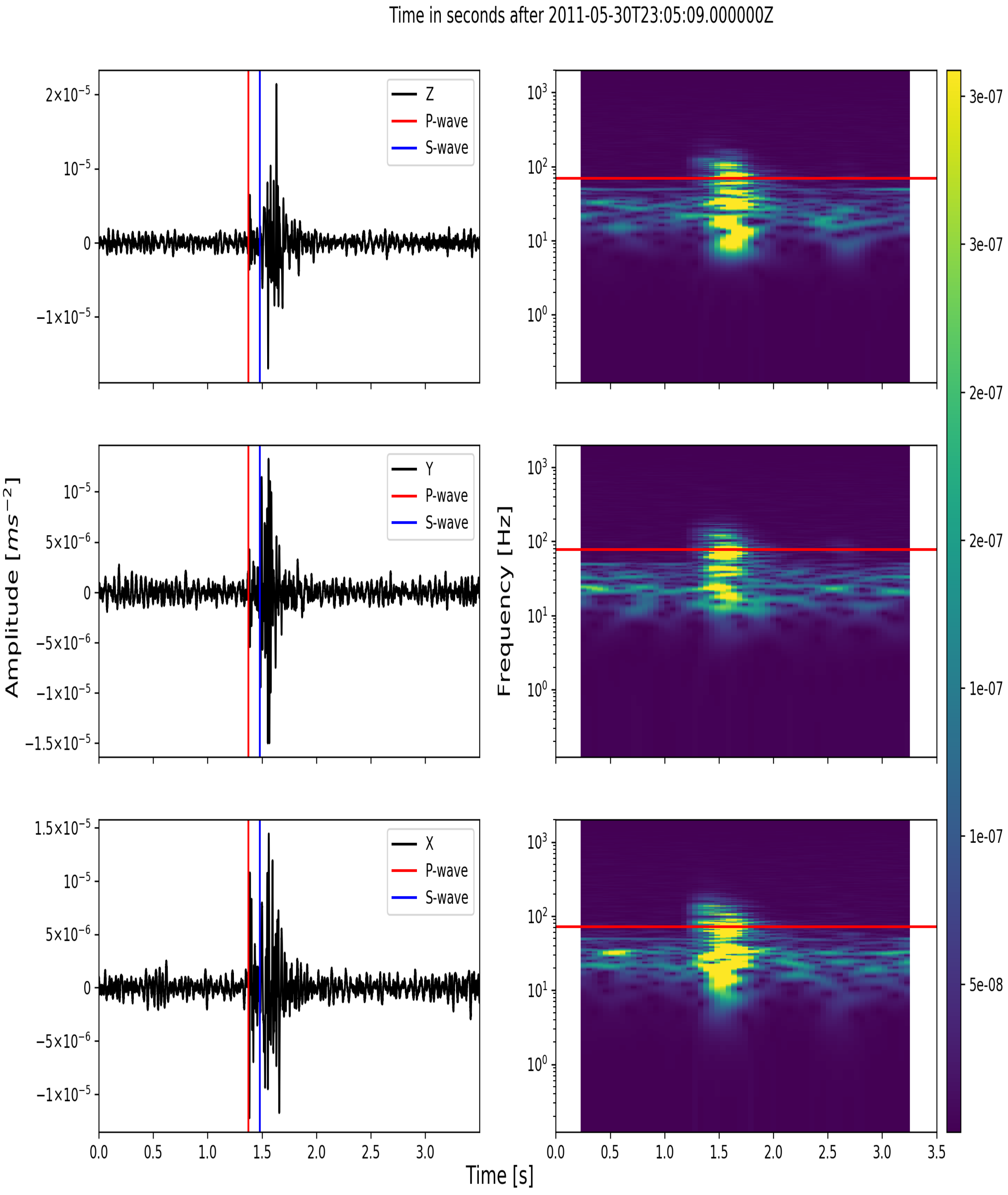

FIGURE 4.1. An example of manual picking in a high SNR waveforms. The left column shows the respective Z, Y, and X components. The red vertical line the P-wave pick and the blue vertical line is the S-wave pick. The right column shows the respective spectrogram for each component. The red horizontal line the central frequency for the whole waveform.

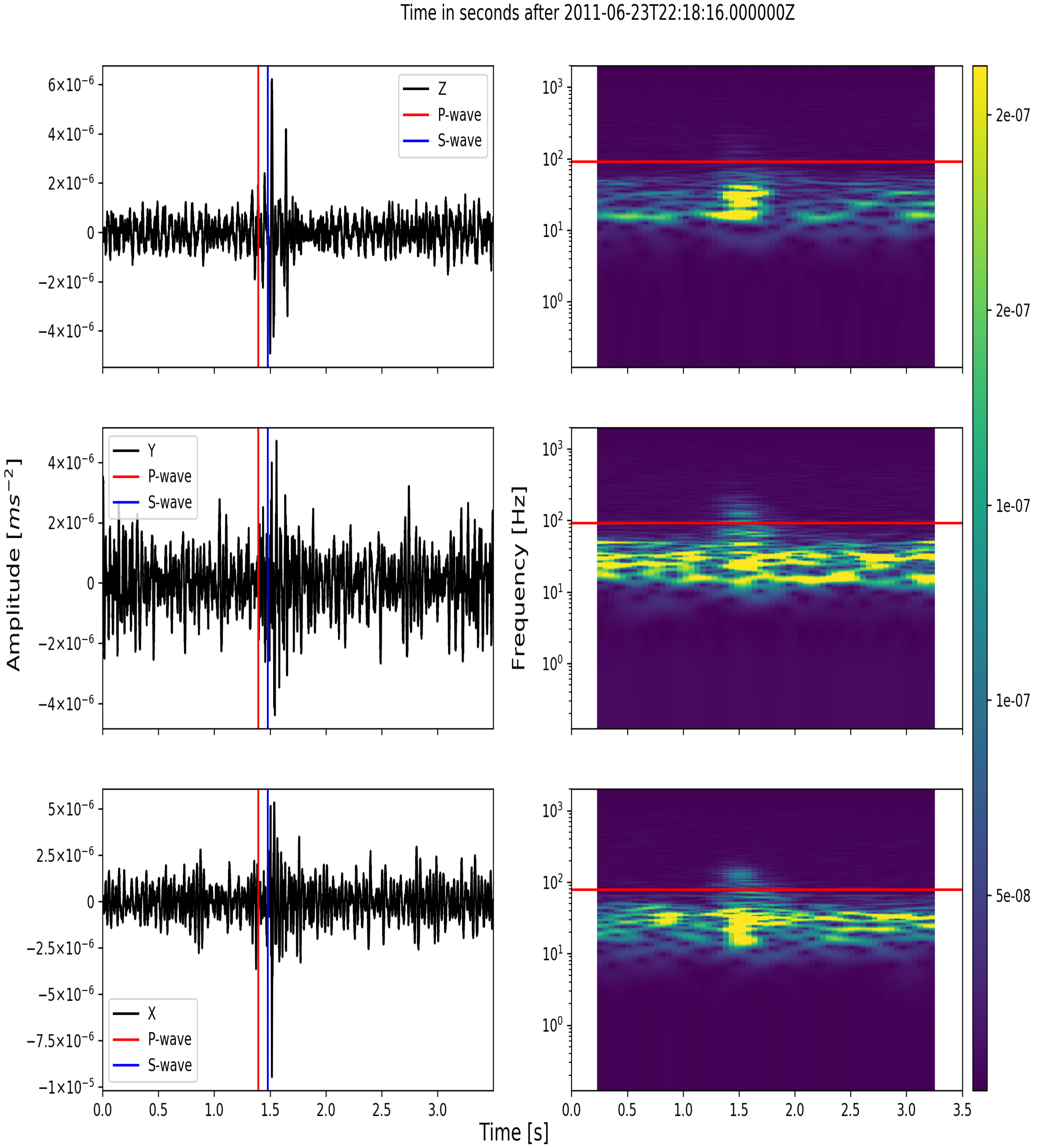

FIGURE 4.2. An example of manual picking in an average SNR waveforms. Refer to Figure 4.1 for more details.

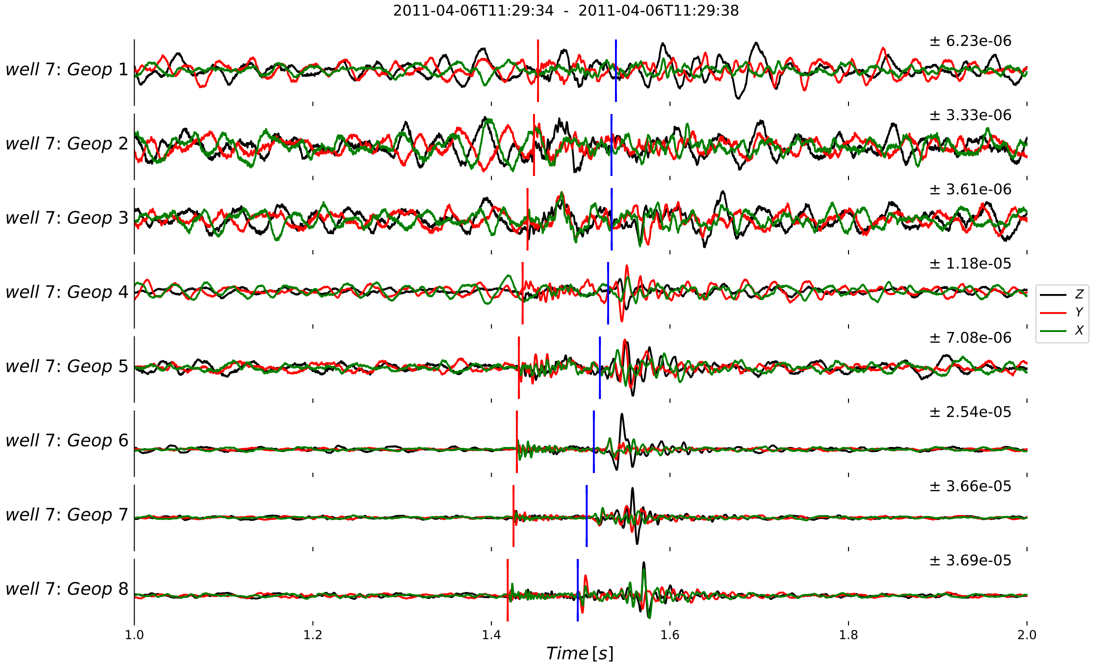

FIGURE 4.3. A move-out display of a moderate SNR event in one well. Geop is an abbreviation for geophone number. Noise level increases from deeper to shallower geopones. Manual picking of arrival times one shallow geophone is hard but can be aided using the observed move-out trend.

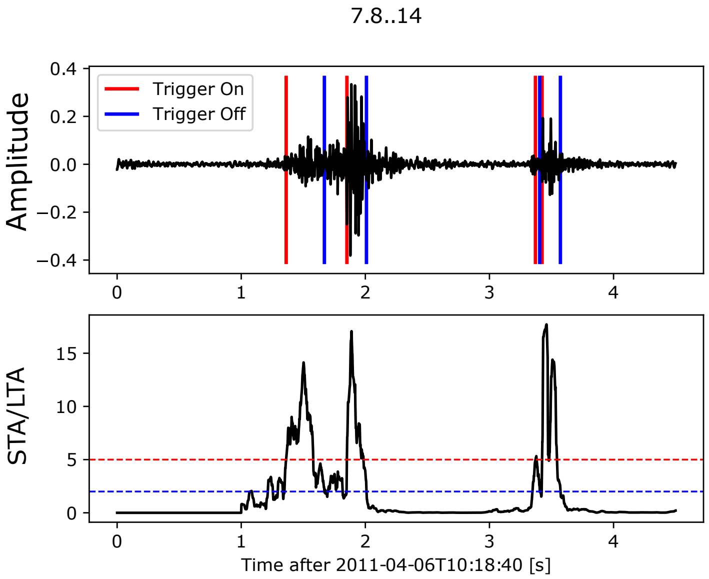

FIGURE 4.4. A waveform from a single seg-y file showing two possible events. The upper plot is the waveform amplitude, and the lower plot is the characteristic function (CF) computed using STA/LTA. The red and the blue lines are the trigger start and end values, respectively. The title of the figure provides information about the recording MSW (7) and the geophone number (8). Fourteen means that the component that recorded this waveform is the X-component. The Z-component and the Y-component are donated as 12, 13, respectively. This notation is used for component naming to simplify saving this information as integer values in seg-y trace headers. A close inspection at the STA/LTA curve for the event after 3 seconds reveals that there are three peaks. These peaks are associated with P-, SV- and SH-waves.

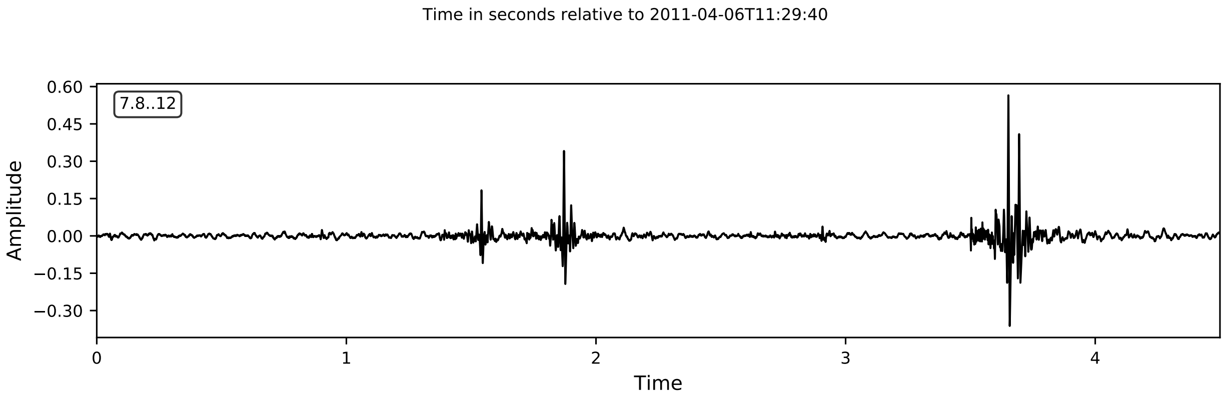

FIGURE 4.5. A waveform containing three possible events. Close inspection shows that they have similar characteristic indicating the possibility of being originated from source location close to each other.

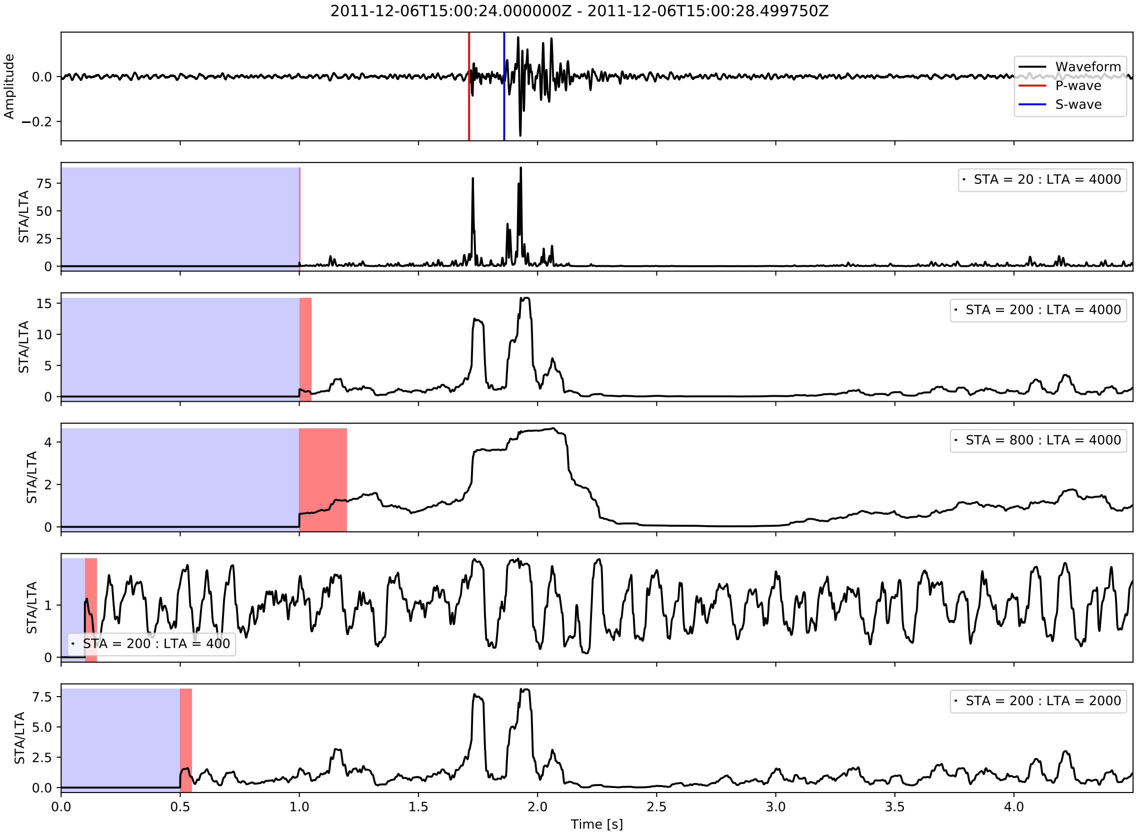

FIGURE 4.6. The effect of STA and LTA windows size on the STA/LTA curve. STA and LTA windows in the figure legend represent the number of sample points. The blue and blue regions are the LTA and STA windows in seconds, respectively. The STA/LTA curves are calculated using the classic method. Manual picking of P- and S-wave is shown in the waveform plot.

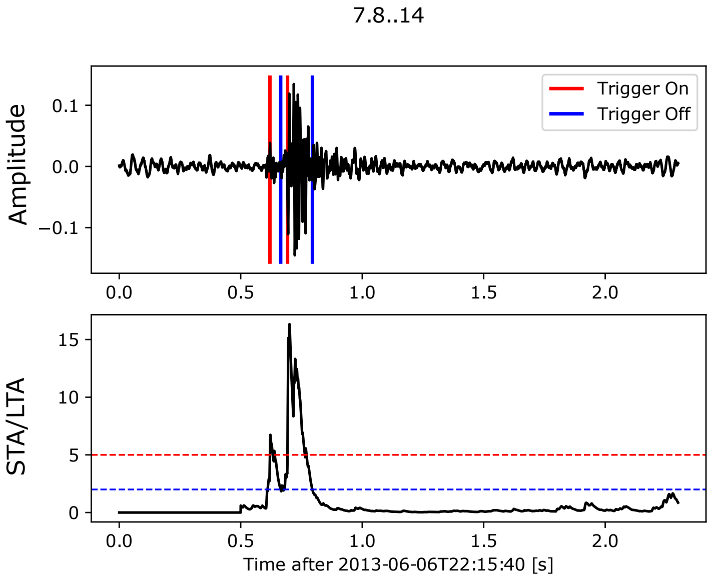

FIGURE 4.7. STA/LTA curve produced using recursive method on a good SNR waveform. The right sharp peak curve edge allows more precise detection of the arrival times than classic method.

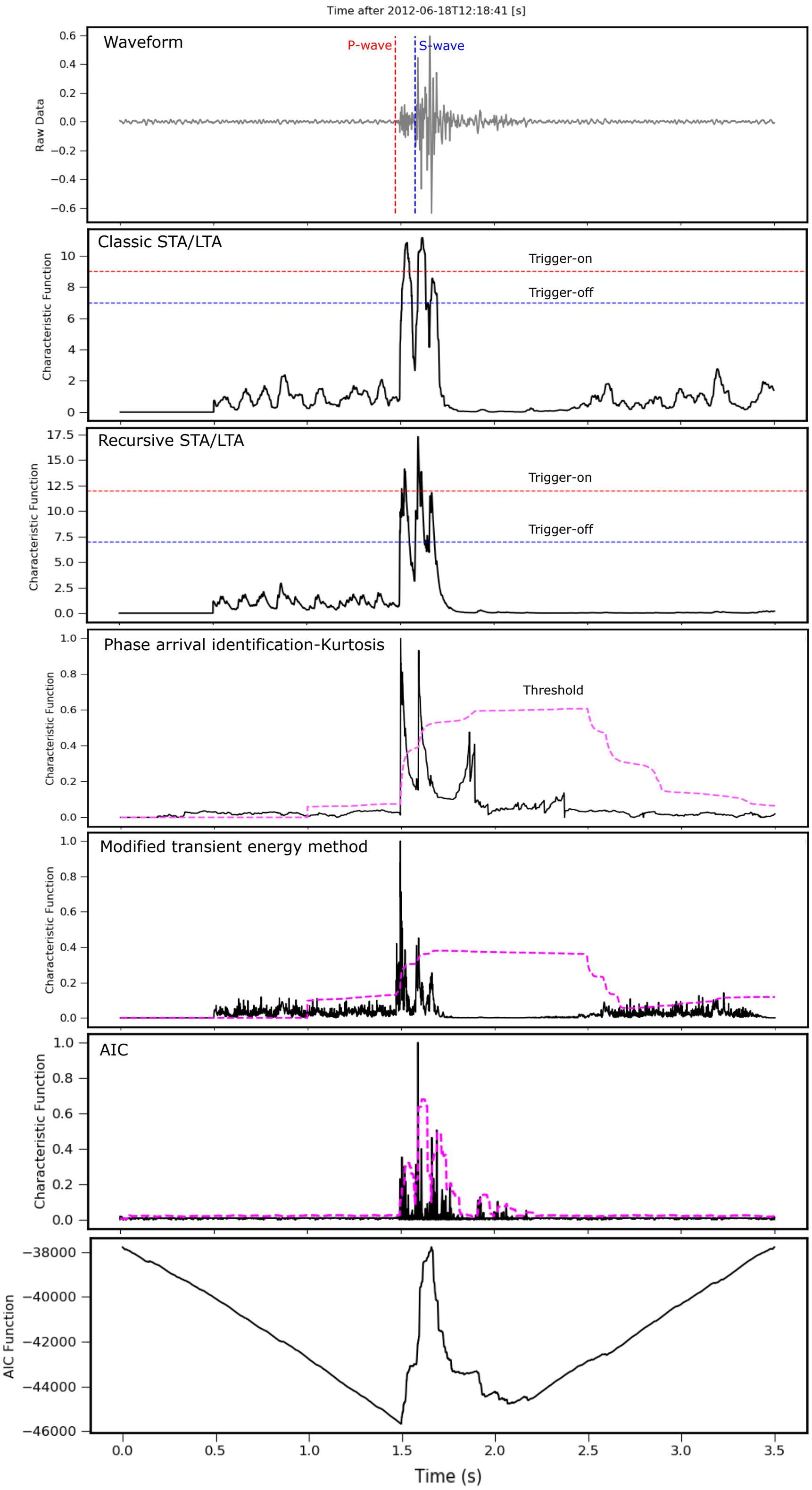

FIGURE 4.8. CF functions for all auto-picking methods produced from a high quality signal.

4.2 Velcity model building

4.2.1 Introduction

Velocity modeling is one of the most challenging aspects of the microseismic data processing workflow. The challenge is brought by the fact that assessing the uncertainty in the location errors due to the subsurface velocity structure cannot easily be quantified using a Gaussian distribution error in contrast to the travel time picks. This limits the uncertainty analysis on location results to deterministic methods. However, very complex geologic structures require probabilistic approaches (Iooss, 1998). Small errors in the travel times or the velocity model can lead to large dislocations of the events (Jones et al., 2014). Stork et al. (2014) assessed the uncertainty in the location results using a deterministic approach whereby they created 3 different velocity models to observe how the microseismic locations varies. Zhang et al. (2018) used the Bayesian inference framework to simultaneously invert for both the microseismic locations and the velocity model. However, such simultaneous inversion techniques also depend on an initial velocity model and are known to be slow in performance, particularly when inverting for a 3-dimensional velocity model.

Zhang et al. (2015) discuss many methods to build a velocity model for application in the microseismic data location process. They state that the velocity model is not actually a static property of the reservoir but ever-changing since the injection of fluids into the reservoir, and hence it needs to be regularly updated using controlled calibration shots or waveform tomography. The latter is quite difficult to use in passive seismic data since the source function and onset time are not known. Another challenge in the process of building a velocity model is the scarcity of data from which a representative model can be built. Subsurface velocity models can be built using different data types such as perforation shots, checkshots, VSP, seismic reflection stacking velocities, seismic refraction surveys and sonic logs. The sonic logs provide a high-resolution 1D velocity profile along the well path. The acquisition of sonic logs is usually restricted to the reservoir zone for cost-saving. Also, often only P-wave sonic logs are acquired since their main use is in the porosity determination through petrophysical analysis, and the compressional velocity does suffice for this purpose. However, in microcosmic processing, the inclusion of both the P- and S-wave produces more accurate microseismic location results. Thus, empirical relationships exist to predict the S-wave from the P-wave velocity (Sabrian et al., 2018) or the S-wave from the porosity, effective pressure, and clay content (Eberhart-Phillips et al., 1989). These types of relationships differ based on rock lithology and mechanical properties, and the S-wave has higher sensitivity to these properties than the P-wave (Ayres and Theilen, 1999).

In microseismic and earthquake studies, the velocity model often used in the locations inversion process is a 1-dimensional model obtained from calibration shots or sonic logs. However, strong lateral elastic variation in the geology produces systematic errors in the microseismic event location. In a complex geologic framework, a 3-dimensional velocity model will likely produce more accurate locations of events. Matrullo et al. (2011) found that using a 3-dimensional velocity model resulted in the relocation of earthquakes in the Campania-Lucania region (Southern Italy) initially produced by a 1-dimensional velocity model. In their study the 3-dimensional velocity model produced lower residuals of P- and S-wave onset times than a 1-dimensional velocity model.

In this section, I demonstrate the processes adapted to built both 1- and 3-dimensional velocity models. The input data are sonic logs from wells having good spatial distribution on the surface of the field. S-wave exists for only two wells and thus was predicted for the rest of the well using a neural network technique.

4.2.2 Sonic log data

Figure 4.9 shows the location of the 12 wells (black color), with respect to seismic monitoring wells (blue color), used to build the 3-dimensional velocity model. The locations of Wells 10 and 12 exactly coincide with the location of MSW-10 and MSW-12, respectively (Figure 3.1). Actually, these two wells had been replaced by the operator to microseismic wells. Well 5 and 23 are away from the MSW cluster, but 5 was included in the velocity modeling process since its sonic log is quite long (covering reservoir and overburden layers), whereas well 23 has deep reading for P- and S-wave logs. These two wells are also within the region of the maximum reservoir closure (dashed black line). Furthermore, initial trials of the microseismic location results using a homogeneous constant velocity had shown a clustering of events at this region. The velocity modeling process I used is a statistical method. Hence the more is the redundancy, the number, and spatial distribution of the wells, the more accurate representation of the true 3-dimensional subsurface velocity is produced from the modeling process.

Figure 4.10 shows the well-section diagram of these 12 wells. Wells 23, 12, 77, 84, and 10 have both P- and S-wave sonic logs available. The reference level of the well-section is at zero True Vertical Depth SubsSea (SSTVD). The length of the sonic logs is variable, and for some wells, the extend of the logs does not reach the reservoir units. The dashed lines indicate the top Formation levels (Nahr Umr, Shuaiba, and Kharaib). The SSTVD value at the marked top surface-level changes from one well to another. The top surface marks are shallower for the wells drilled at the crest of the field compared to the flank. The caprock Nahr Umr has quite flat low sonic logs readings, whereas the Kharaib formation has the highest velocity readings with a fluctuating nature. Wells numbers 5, 77, and 84 have the longest sonic log intervals; however, well 5 does not have S-wave measurements. Surface markers are correlatable from one well to another, and the thickness of the layers is conformable. The carbonate rocks of Natih units overlaying the Nahr Umr, and UER formation have high-velocity measurements. The zone of interest ranges from Natih Units down to 500 hundred below Kharaib Formation since the shallowest geophone is located close to the top marker of the Natih unconformity surface.

4.2.3 Sonic log data smoothing and blocking

The log data contain spurious spikes related to the wellbore condition and the existence of washouts (Ugborugbo et al., 2009). To eliminate the spikes from the log readings, a Gaussian despiking filter is applied where the filter has a standard deviation of 0.7 and a length of 10 sample points. The filter works by removing outlier values outside the given number of the standard deviation, calculated over the given window length. The removed points are then interpolated using the spline interpolation technique. The filter works as a smoothing operator, whereby the degree of the smoothing is directly proportional to the filter length and inversely proportional to the standard deviation. Figure 4.11 shows the application of the filter on two wells (84 and 77). The black and the red curves are the original and filtered logs, respectively. Smoothing the log data is necessary to make the 3-dimensional velocity model have smoothly varying boundaries across different layers. The ray-tracing process will fail to generate the calculated travel times table when there are highly variable velocity zones in the 3-dimensional velocity model.

For the 1-dimensional velocity model to be used in the location algorithms (next chapter) that require only 1-dimensional instead of a 3-dimensional velocity model, smoothing is not required. The log data instead are blocked within each major Formation zone using the Harmonic mean

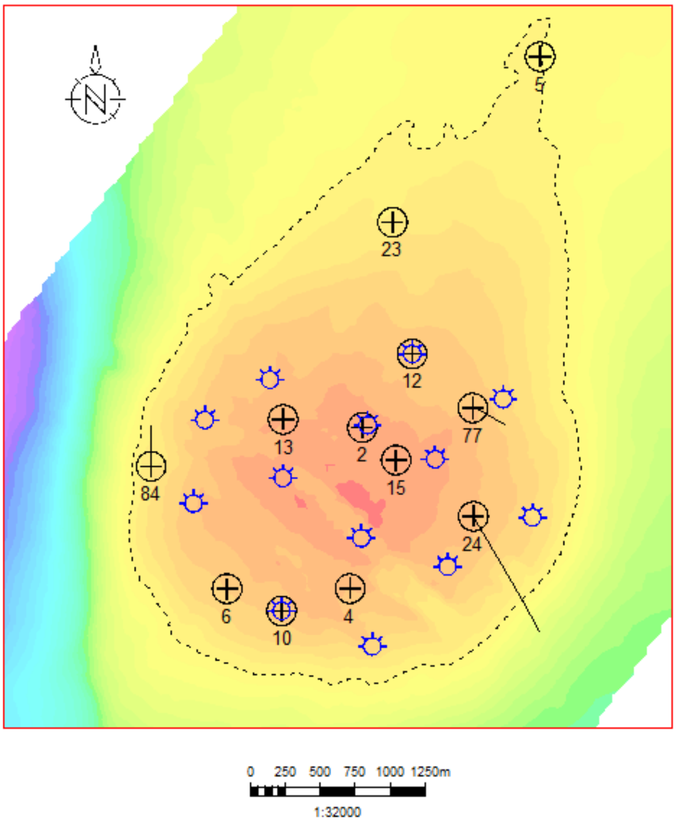

FIGURE 4.9. Location of the wells (black color), used to build the 3-dimensional velocity model, with respect to MSW (blue color). The surface map is the structural map of the Shauiba. The dashed contour is the spill point (the lowest contour of the reservoir closure at the Shuaiba level). Notice that wells 84, 77, and 24 have deviations.

value,

$$H = \frac{n}{\frac{1}{x_1} + \frac{1}{x_2} + \cdots + \frac{1}{x_n}} = \frac{n}{\sum_{i=1}^{n} \frac{1}{x_i}} = \left(\frac{\sum_{i=1}^{n} x_i^{-1}}{n} \right)^{-1}, \tag{4.11}$$

in which n is the number of sample and x sample value. I created the 1-dimensional from only wells 77 and 84, since they have both P- and S-wave logs, and their coverage is quite long. The two velocity values obtained from these two wells for each zone are averaged using harmonic mean (equation 4.11). The boundaries of the 1-dimensional velocity model are later adjusted to be consistent with the Formation boundaries found at the crest of the field. Figure 4.12 displays the sonic log data for the well 77 before and after the application averaging (blocking).

The generated 1-dimensional model is complex and contains zones that are very thin (above

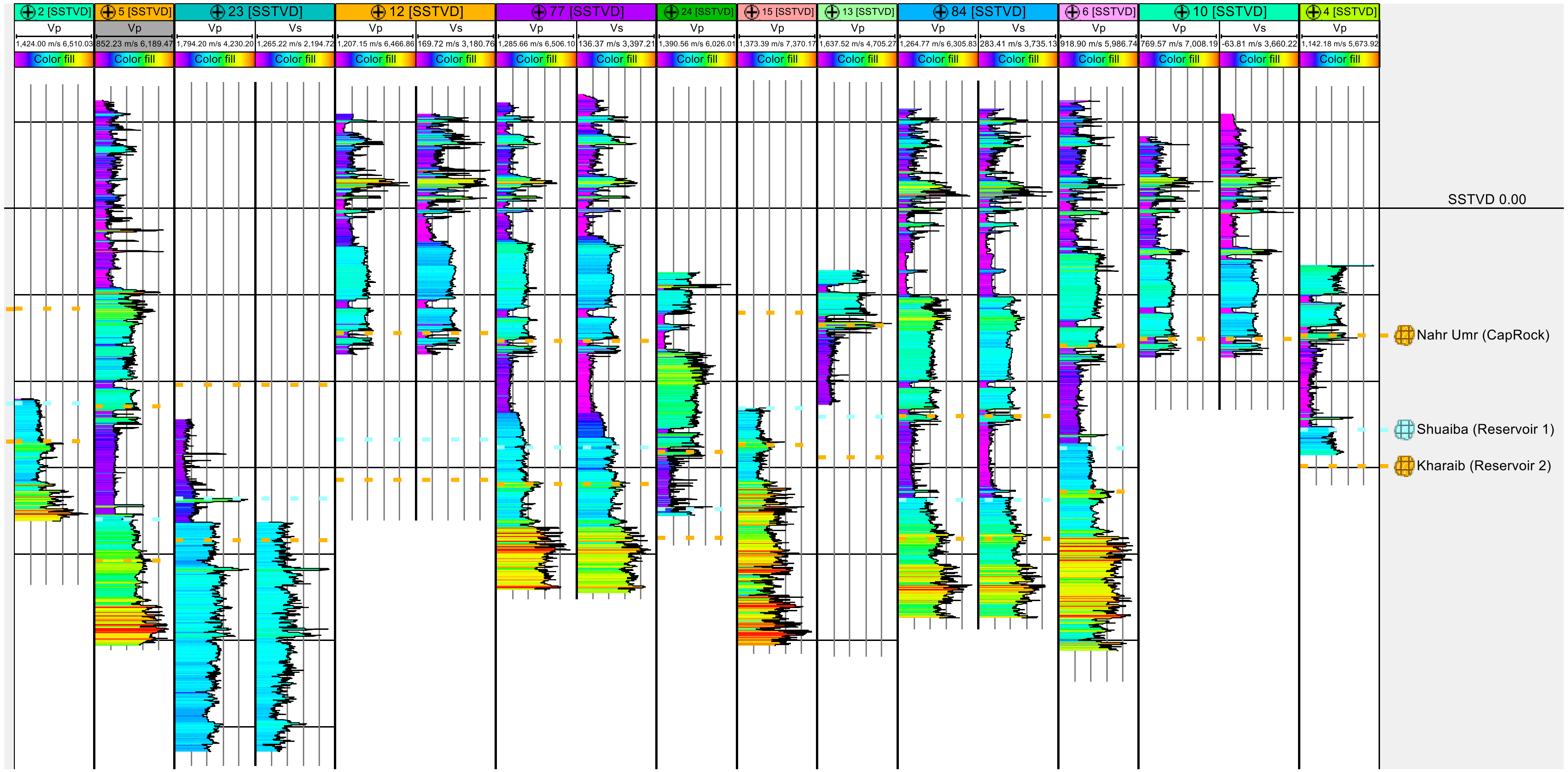

FIGURE 4.10. Well-section view of the wells from which P- and S-wave sonic logs are used to build the velocity models. Logs readings increase from left to right. The well-section is flattened at a SSTVD zero. The dashed lines are the geologic horizons.

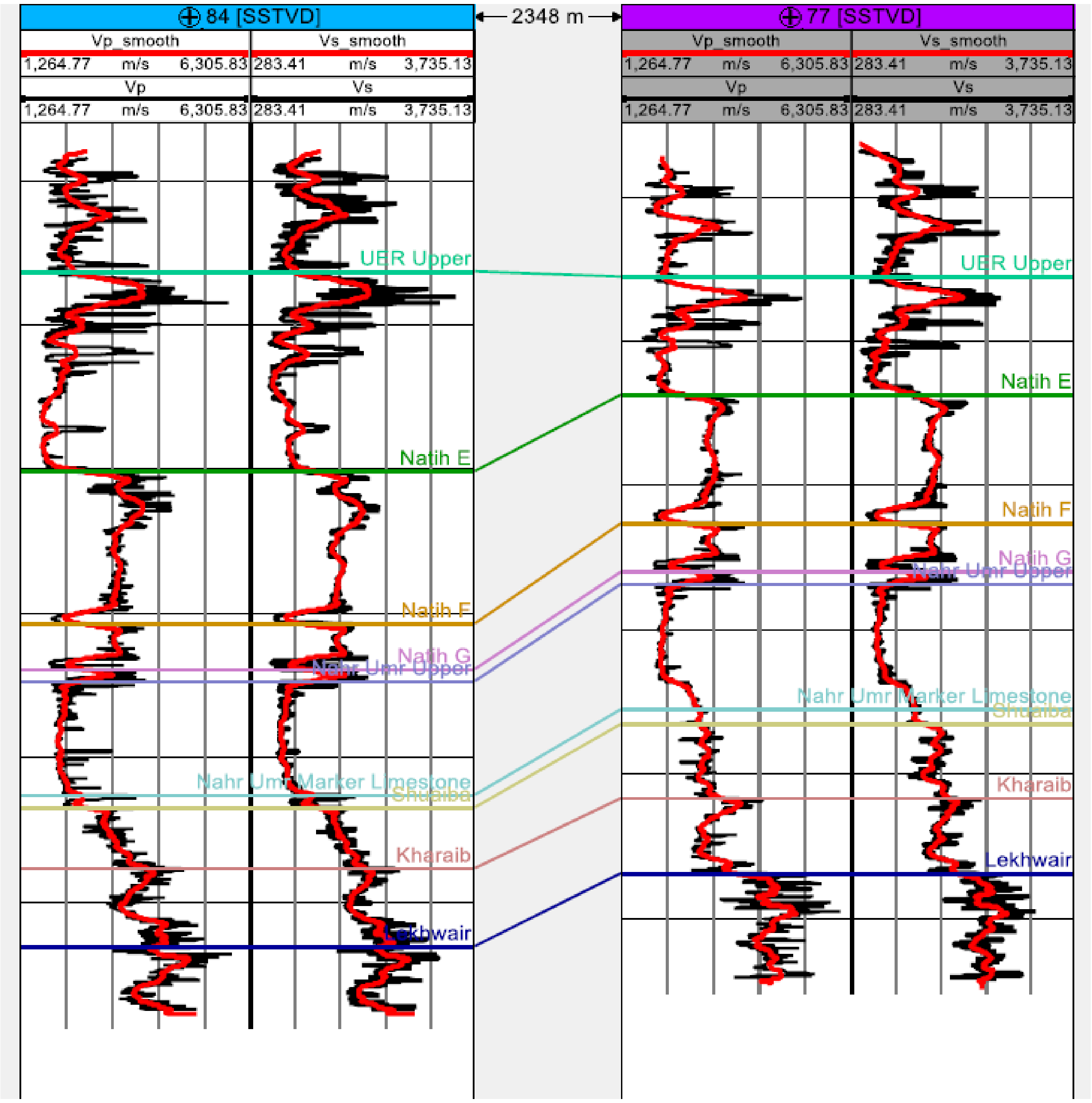

FIGURE 4.11. The filter also smooths abrupt fluctuations. The horizontal colored lines are the Formation tops.

Nahr Umr). Some of the 1-dimensional location algorithms require that the vertical location grid is less than half of the velocity layers. Decreasing the location grid to a very small number makes the performance of the location process very slow. Therefore, The number of velocity layers is minimized to five (Figure 4.13). The Nahr Umr, Shuaiba, and Kharaib zones are retained, but

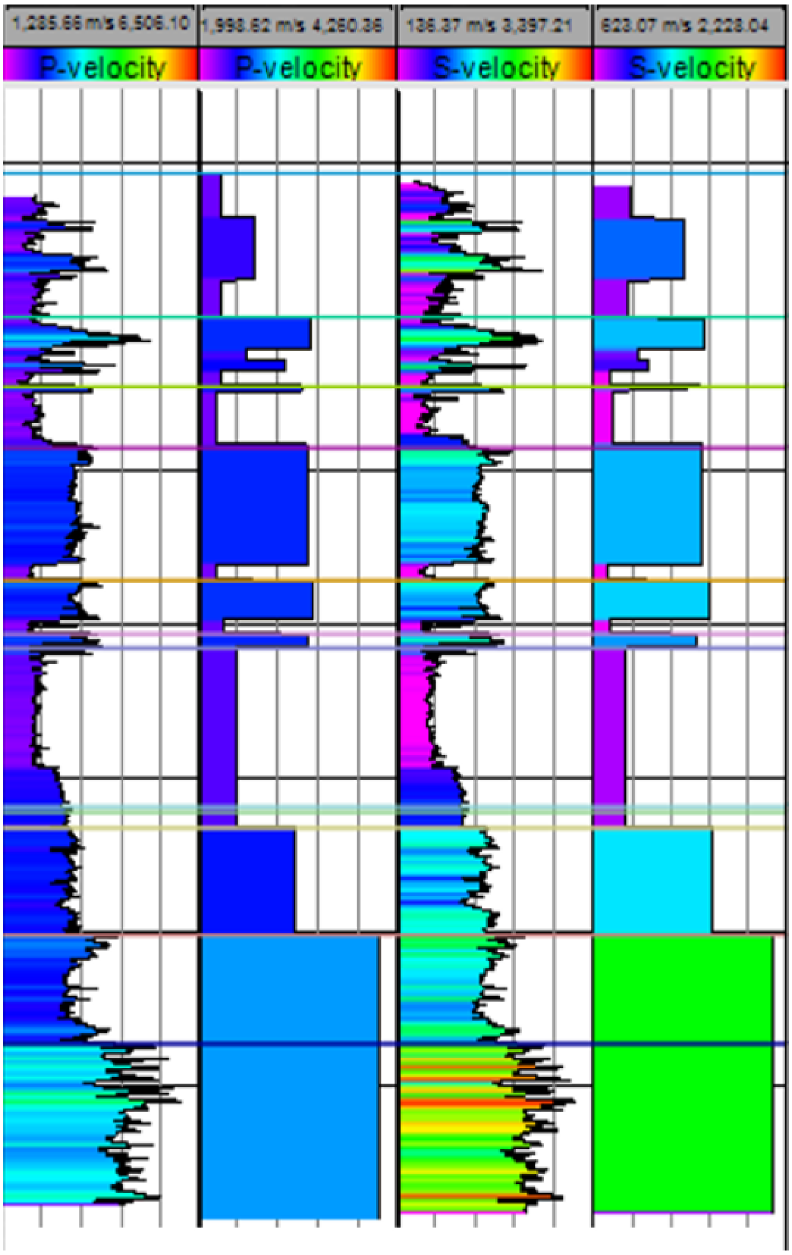

FIGURE 4.12. Averaging (blocking) the sonic logs reading within each major formation. The well shown here is 77, and the horizontal lines are the same Formation tops found in Figure 4.11.

small shaley zones in the Natih units are discarded. The model encompasses all geophones at microseismic monitoring wells.

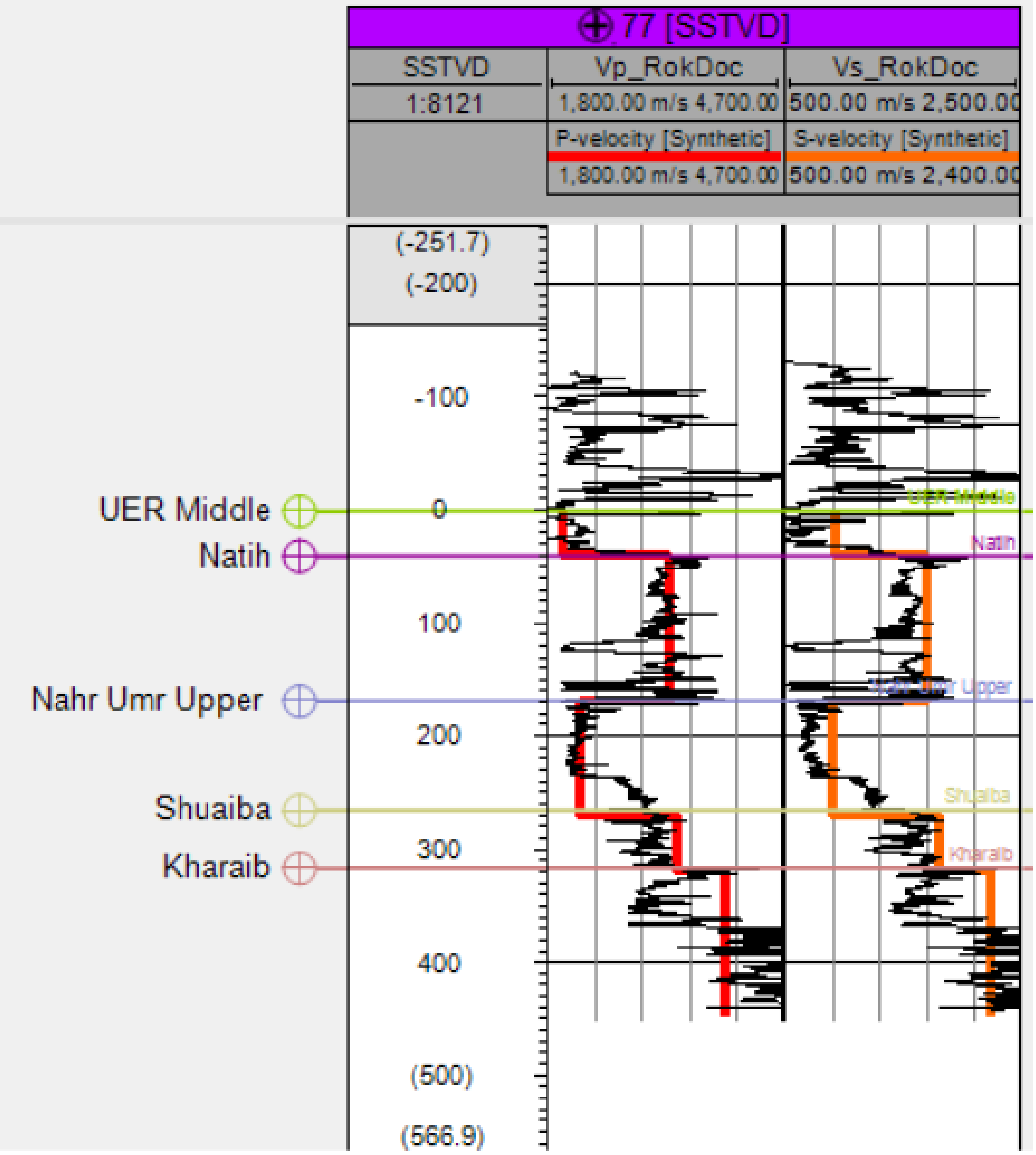

FIGURE 4.13. The final number of velocity zones in the 1-dimensional velocity model. The left panel shows the P-wave velocity (red color), whereas the right panel shows the S-wave velocity (orange color). The black curves are the original velocity logs.

4.2.4 S-wave velocity derivation using neural network

S-wave logs are only available for two wells (77 and 84). S-wave velocity logs are derived for the rest of the wells using a neural-network estimation algorithm. The training data input-output pairs are the P-wave and density versus S-wave logs at the five wells, where they all exist. These 3 log data have shown a strong positive correlation coefficient (Table 4.3). Cross-validation at a well for which S-wave exits proved that the derived S-wave log data resembles quite closely the original log data. In the cross-validation stage, the S-wave is predicted in a well where it actually exists. Then, The predicted data are compared with the actual one. Figure 4.14 shows side by side the original S-wave (left panel in wells 77 and 84) and the derived S-wave velocity logs (right panel in wells 77 and 84). I correlated the original smoothed S-wave and the derived S-wave at both wells 77 and 84 as shown in Figure 4.15. The cross-plot shows a high correlation coefficient of about 0.86. Aleardi (2015) compared the derivation of seismic velocity missing well logs between various methods, including neural network. They conclude that, among others, the neural network method is robust when there is a non-linear relationship between various well logs. The technique of estimating velocity logs or models using neural network methods has proved promising by many scholars (Fabien-Ouellet and Sarkar, 2020; Iturrarán-Viveros et al., 2021; Spichak and Goidina, 2016). Using empirical relationships between various well logs or adapting artificial intelligence techniques to derive the S-wave velocity well log from other logs might be reliable to some extend. However, for complex geological settings, these methods might prove not capable of bringing dependable results (Maleki et al., 2014).

TABLE 4.3. Cross-correlation between P-wave, S-wave (existing) and density logs at wells 77 and 84. The cross-correlation coefficient is higher between P- and S-wave than between velocity and density logs.

	Vp	**Density**	**Vs**
Vp	1	0.73	0.93
Density	0.73	1	0.71
Vs	0.93	0.71	1

4.2.5 3-dimensional velocity modeling

A 3D cuboid mesh of grid spacing 5 meters in the x, y and z directions is built encapsulating all geophones locations and extending 300 meters below the highest point at the crest of the Kharaib reservoir unit. Velocity logs are populated into the grid cell volume using the sequential Gaussian simulation technique (SGS) (Dimitrakopoulos and Luo, 2004; Journel, 1974; Verly, 1993). The specification of the 3D grid cell is (x = 50m, y = 50m, z = 10m). The modeling is applied per zone within the grid cell volume, and the zones were defined based on general velocity trends found in the velocity logs (Figure 4.12).

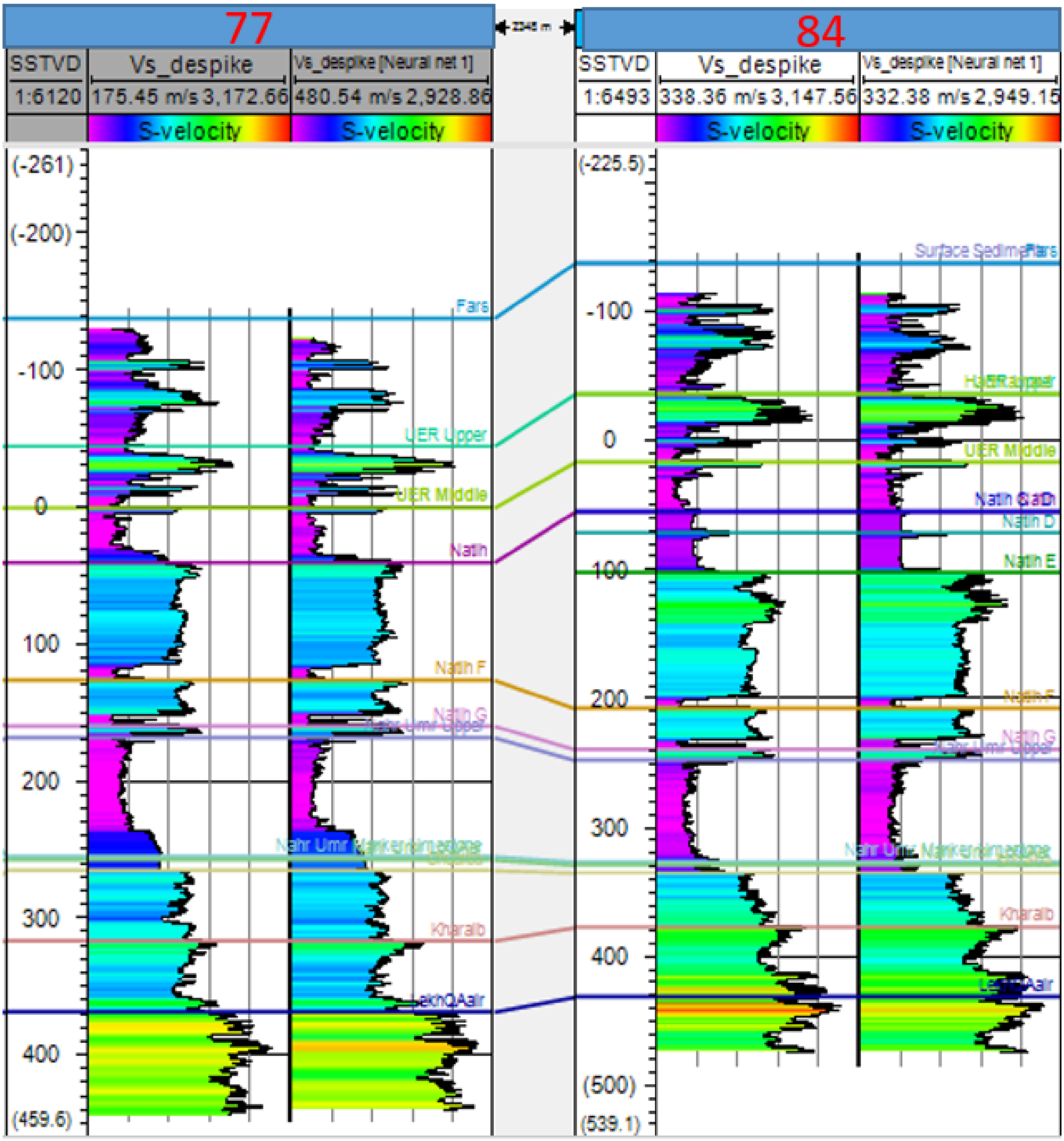

FIGURE 4.14. Derived S-wave cross-validation at wells 77 (left) and 84 (right). The first panel (left) in both wells show the despiked (smoothed) original S-wave log, whereas the second panel (right) shows the derived S-wave.

SGS is a stochastic geostatistical method for data modeling based on Kriging estimator (Cressie, 1990; Krige, 1951; Olea, 2006; Oliver and Webster, 1990). The main difference between

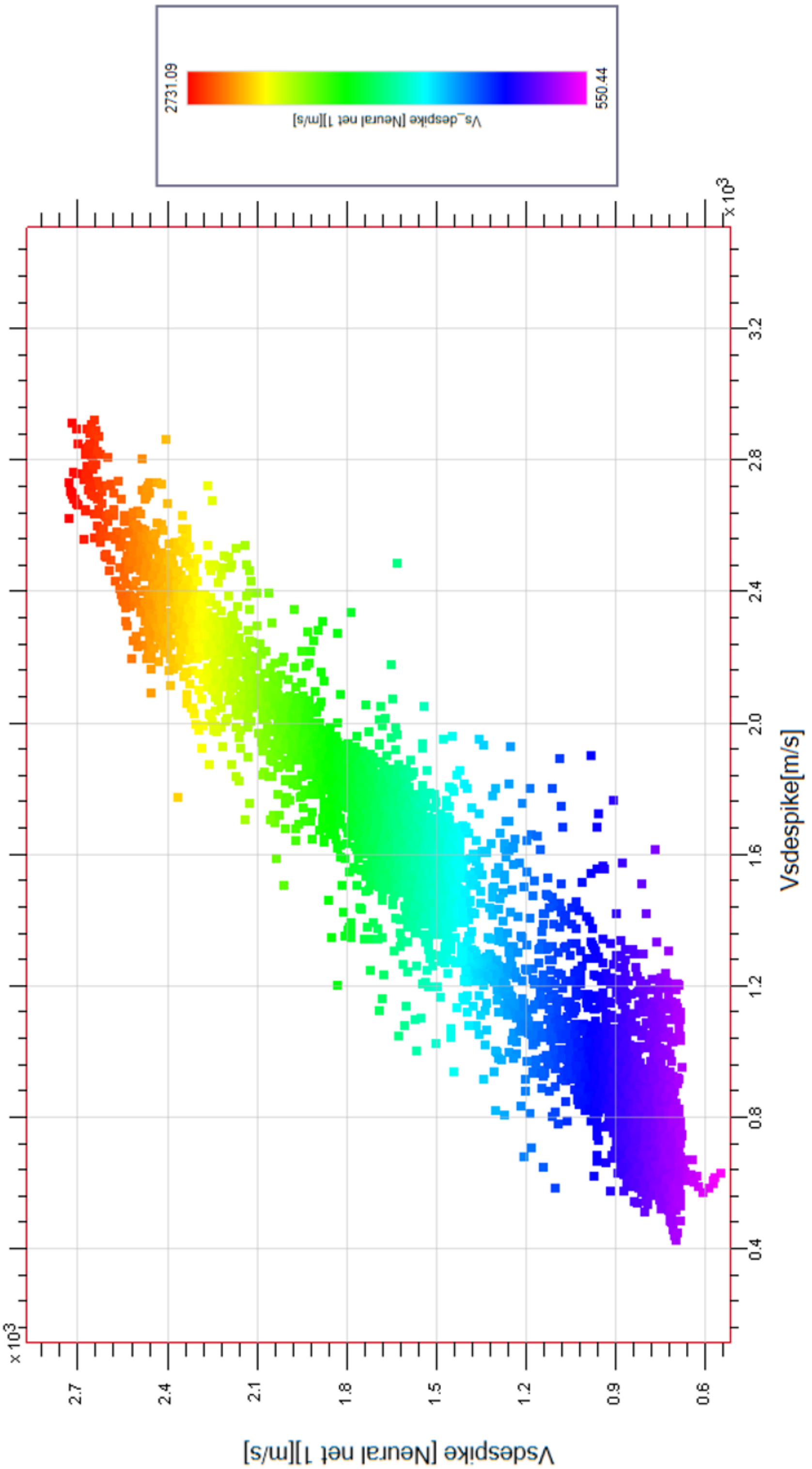

FIGURE 4.15. A cross-plot between smoothed S-wave velocity and the derived one at wells 77 and 84. The scatter points are color-coded on the derived S-wave velocity. The colorbar is shown to the right of the cross-plot.

the two is that the first takes the modeled values into account when modeling for the next cell value, whereas the the second does not. SGS produces models of the subsurface properties (e.g., porosity, water saturation, velocity, etc.) that honor their distribution and spatial variability. The mathematical description of SGS is,

$$Z(\boldsymbol{u}_i) = \sum_{j=1}^{i-1} \lambda_j(\boldsymbol{u}_i) Z\left(\boldsymbol{u}_j\right) + \sigma_E(\boldsymbol{u}_i) U(\boldsymbol{u}_i), \quad \forall i = 1, \ldots, n, \tag{4.12}$$

where U is a standard Gaussian vector used to randomly sample the variable Z, that will be modeled at a location u_i using the available data at locations u_j. λ_j is the kriging weight and $\sigma_E(\boldsymbol{u}_i)$ is the variance error from previsly simulated cell (Nussbaumer et al., 2018). The first term ($\sum_{j=1}^{i-1} \lambda_j(\boldsymbol{u}_i) Z\left(\boldsymbol{u}_j\right)$) in equation 4.12 is the Kriging estimator.

The random path along which cell nodes are simulated will generate a different realization. These realization are equally probable and they together enable global uncertainty analysis of the modeled property. Kriging requires analysis of variograms in horizontal and vertical directions to estimate the kriging weight λ_j in equation 4.12. Variogram is a measure of variability between data points in space as a function of distance (Bohling, 2005; Omre, 1984), and is expressed mathematically as,

$$\gamma(\boldsymbol{h}) = \frac{1}{2N(\boldsymbol{h})} \sum_{\alpha=1}^{N(\boldsymbol{h})} \left(\boldsymbol{z}(\boldsymbol{u}_\alpha) - \boldsymbol{z}(\boldsymbol{u}_\alpha + \boldsymbol{h})\right)^2, \tag{4.13}$$

where $\boldsymbol{z}(\boldsymbol{u}_\alpha)$ is the sample value at a location $\boldsymbol{u}_\alpha$, $\boldsymbol{z}(\boldsymbol{u}_\alpha + \boldsymbol{h})$ is the value of another sample at a distance $\boldsymbol{u}_\alpha + \boldsymbol{h}$, and $N(\boldsymbol{h})$ is the total number of pairs within the lag distance $\boldsymbol{h}$. To ensure unbiasned results the total kriging weight is equated to 1, and the kriging weights are found as,

$$\sum_{j=1}^{n} \lambda_j \boldsymbol{C}\left(\boldsymbol{u}_i, \boldsymbol{u}_j\right) = \boldsymbol{C}(\boldsymbol{u}, \boldsymbol{u}_i), \quad \boldsymbol{i} = 1, \ldots, \boldsymbol{n}, \tag{4.14}$$

where $\boldsymbol{C}\left(\boldsymbol{u}_i, \boldsymbol{u}_j\right)$ is the covariance between the existing data points at the corresponding lag distance $\boldsymbol{C}(\boldsymbol{u}, \boldsymbol{u}_i)$. The relationship between covariance and the variogram is $\boldsymbol{C}(\boldsymbol{h}) = \boldsymbol{C}(0) - \gamma(\boldsymbol{h})$, where $\boldsymbol{C}(0)$ is the covariance at the maximum lag (Sill) (Figure 4.16).

The approach I adapted to create the velocity model using SGS is detailed below:

1. Discretize the volume of interest into cells

2. The velocity logs are transformed to a Gaussian distribution using normal score (Figure 4.17) transformation. This is achieved by ranking the data from minimum to maximum values and then matching them to an equivalent one generated from a normal distribution
3. Upscale velocity logs in the cells cut through the well trajectory
4. Create variogram of velocity well logs in the horizontal and vertical direction
5. Obtain the kriging weights for every cell location within each zone
6. Run the SGS algorithm equation 4.12
7. Transform the data using inverse normal score transformation
8. Repeat the process for all zones
9. Smooth the velocity models using a moving average filter. Stabilization of some location algorithms require a smoothly varying velocity model

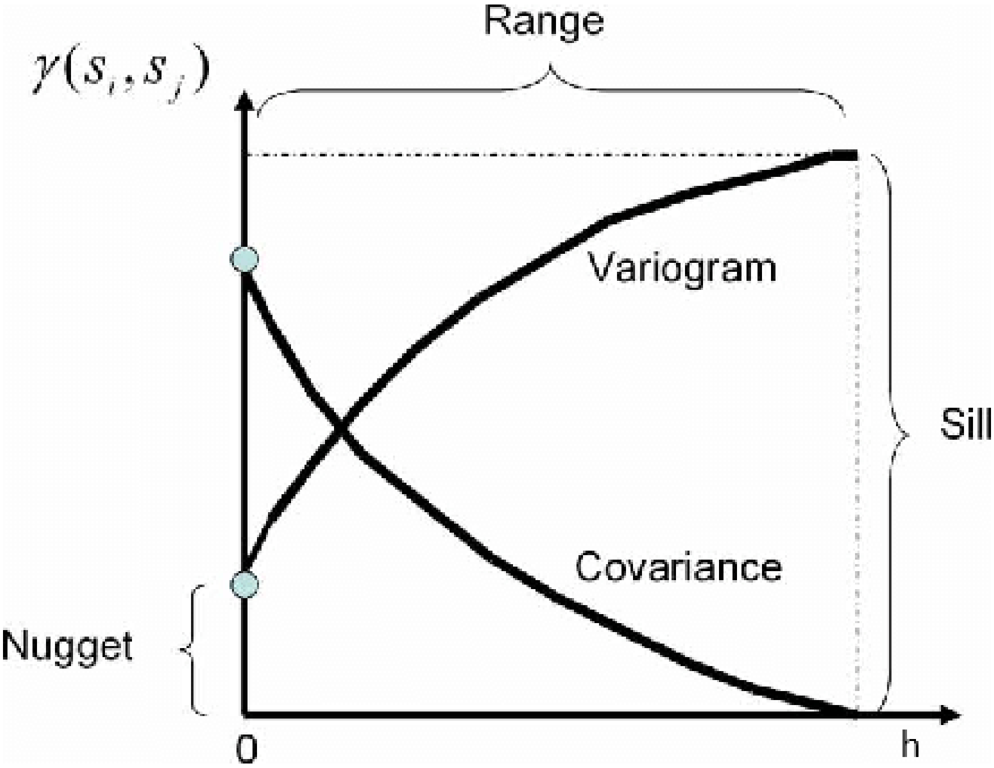

FIGURE 4.16. The relationship between variogram and covariance (Negreiros et al., 2010).

Figure 4.18 shows the derived P-wave velocity at a vertical slice and along the top surface of the lower reservoir unit. P- and S-wave velocities are lower in the shale (caprock) than the carbonates, and they are lower in the upper reservoir unit than the lower reservoir unit. The

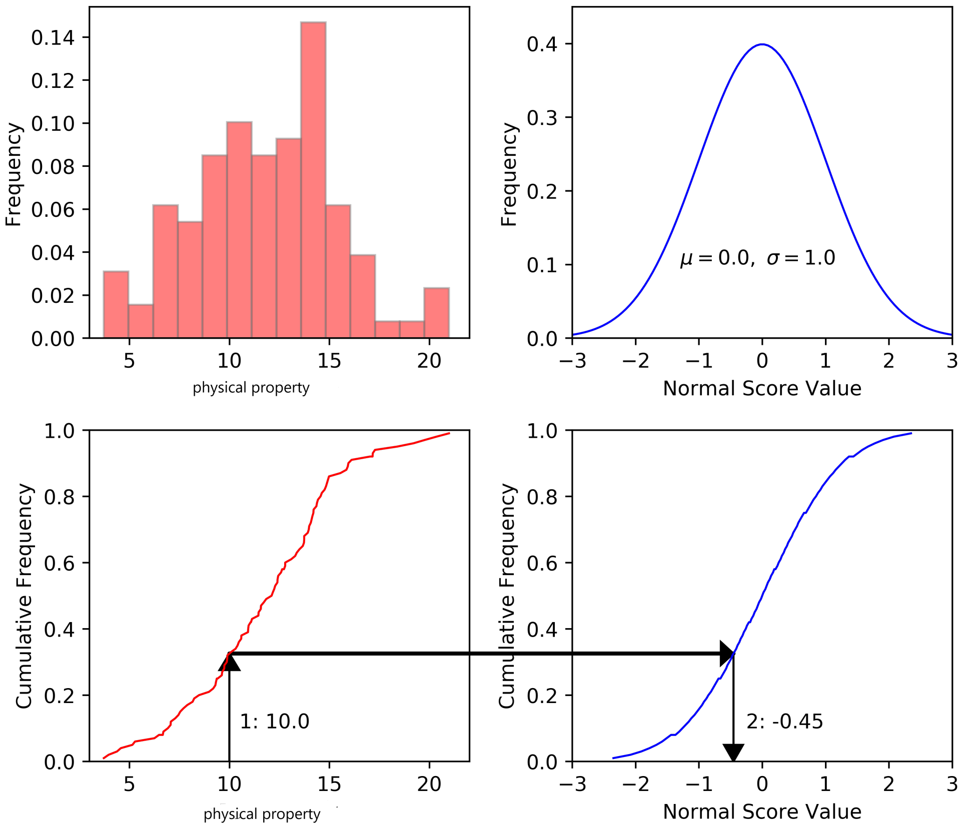

FIGURE 4.17. The procedure of normal score transformation. Adapted from Pyrcz and Deutsch (2018).

variation in velocity values within carbonate rocks is attributed to the existence of shale stringers, the fluid type occupying the pore space, and variation in the lithology. Figure 4.19 is the S-wave velocity model. The velocity model in Figures 4.12 is used to locate microseismic events using algorithms that require 1D velocity model. Another technique of location algorithm is known as FSM, that requires 3D velcoity models. The stabilization of this method requires smoothly varying velocity models. Therefore, the P- and S-wave velocity models are smoothed as shown in Figure 4.20.

4.2.6 Uncertainties in the velocity model

Accurate velocity modeling will result in reliable microseismic event location. Velocity models can be built using many different data types including but not limited to sonic log, checkshot, VSP, stacking velocities, perforation shots and core measurements (Maxwell et al., 2010a). Errors

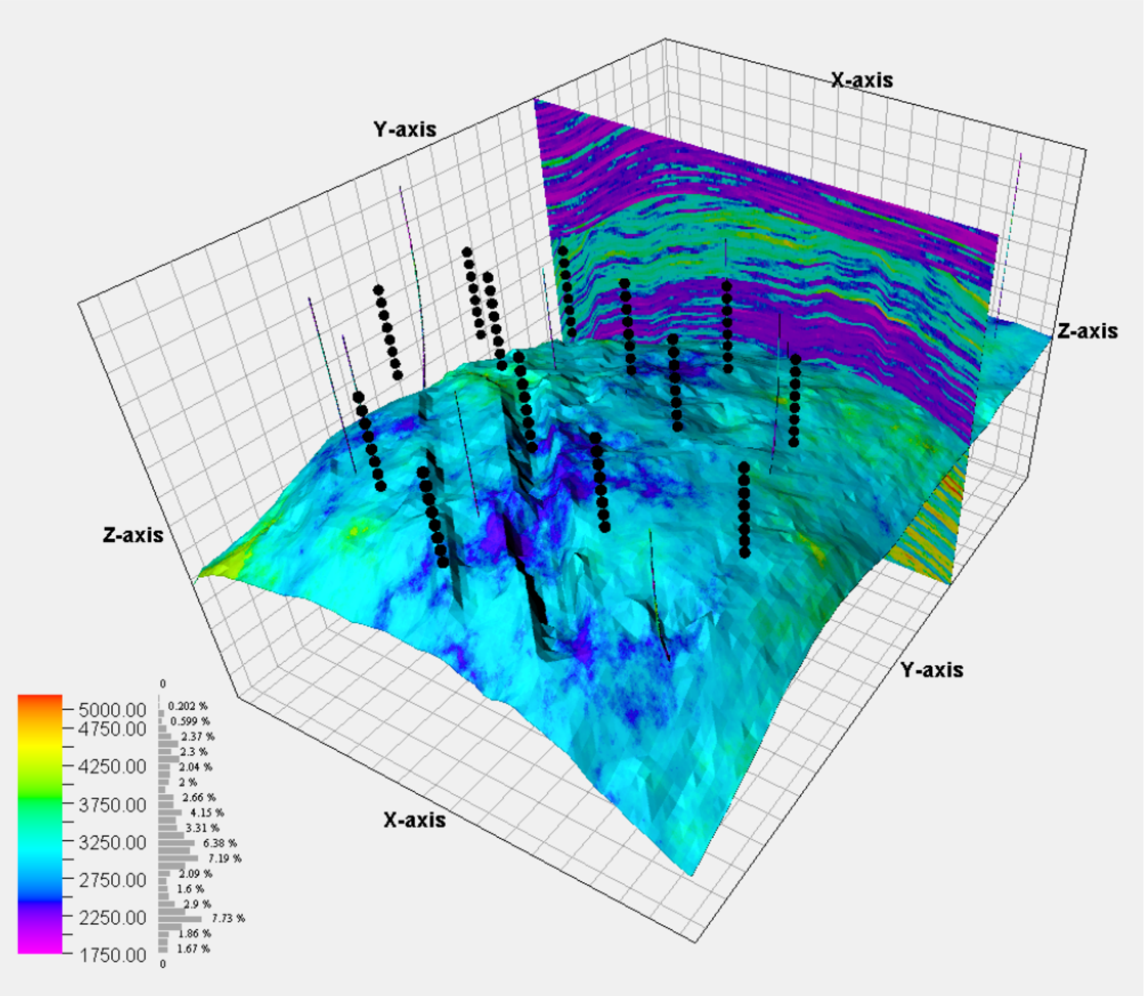

FIGURE 4.18. Estimated P-wave velocities at the top of the lower reservoir unit and in a cross-section are also shown. Black dots indicate the downhole 3C-geophones in microseismic monitoring wells.

in velocity estimation can bring significant dislocation of microseismic events which cannot be ignored (Usher et al., 2013). However, obtaining very accurate velocity models of the subsurface is a challenging task for several reasons. First of all, there is a often lack of necessary data to fully capture the heterogeneity of the reservoir model. For example, sonic logs measurement are limited in the reservoir zone but the source location and the geophones might not be located in the same zone. Secondly, often S-wave sonic is not measured for cost-saving reason. However, accurate estimation of the source location requires existence of both P- and S-wave velocities. For example, Kuang et al. (2013) found that using only S-wave travel time and velocity model will

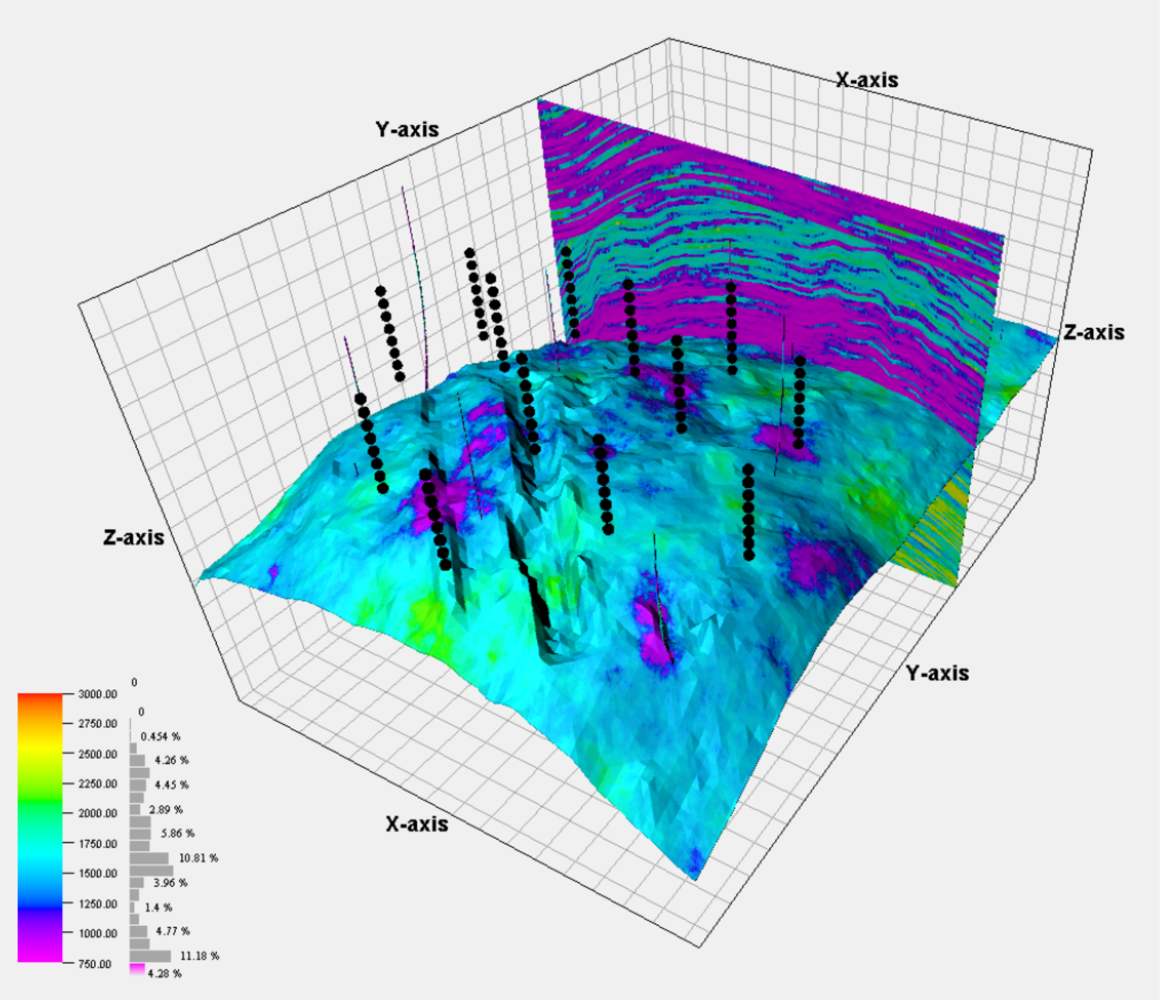

FIGURE 4.19. Estimated S-wave velocities at the top of the lower reservoir unit and in a cross-section are also shown. Black dots indicate the downhole 3C-geophones in microseismic monitoring wells.

produce inaccurate location results, but can be improved if source incident angle is included in the location algorithm.

Another technical challenge is either the use of 1D or 3D velocity model. Theoretically, the earth is 3D and having properties that vary spatially in all direction. Therefore, intuitively 3D velocity models will result into lower uncertainty in location results (Matrullo et al., 2011). Building a 3D velocity model is a daunting task, and algorithms that use 3D velocity models to locate microseismic events are computationally very intensive, leveraging most computer resources. Additionally, there is the question of resolution, that must be addressed by discretizing

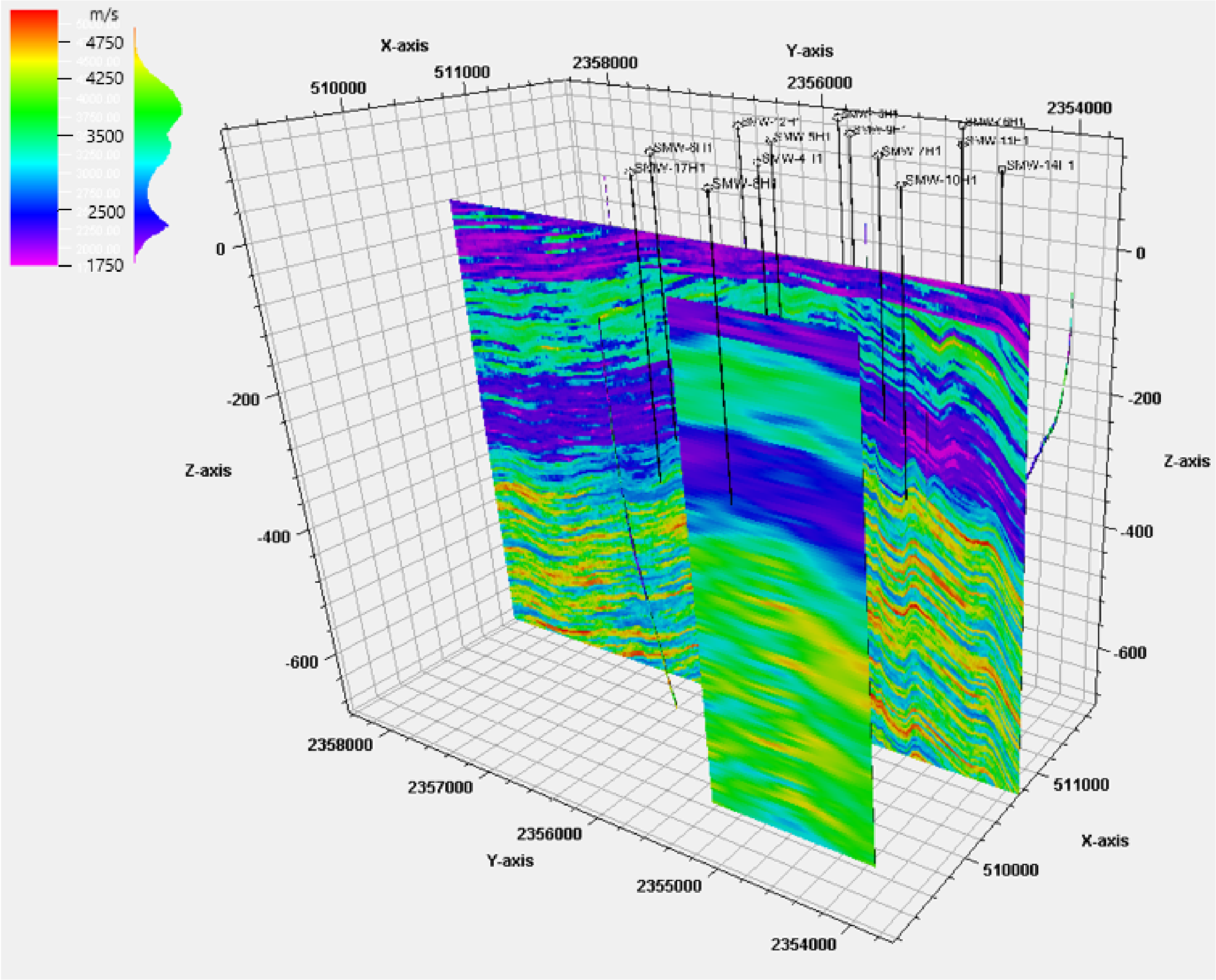

FIGURE 4.20. Smoothing the 3D velocity models for the stabilization of the FSM. The small panel in the front is the smoothed P-wave model shown in the back panel.

the subsurface into small cells, where each is assigned with one property value (P- and S-wave). The smaller the cell volume the more the processing time with an exponential relationship. Accurately locating microseismic events needs a cell volume that truly captures the heterogeneous and anisotropic nature of the seismic velocities (Peng and Wang, 2019; Warpinski et al., 2009; Zhang et al., 2015).

Fractures affect the velocity model of the subsurface and create anisotropic behavior in seismic velocities. S-wave experiences splitting in fractured media. When generating velocity models from log data, we assume the well trajectory intersects the fracture system. But, this is not always true. Therefore, the final velocity model might not be an accurate representation of the true velocity (Anderson et al., 1974; Boadu and Long, 1996; Kahraman, 2002; Pyrak-Nolte et al., 1990).

Field X undergoes continuous injection of steam and production of hydrocarbon, changing the reservoir temperature and pore pressure. Variation in these properties with respect to time will cause the seismic velocities to change too (Martinez et al., 2012). Some of the well logs in Field X are acquired before the start of steam injection program as is inferred from log files header information. Changes in velocity measured from sonic log data can be characterized if the sonic log data are reacquired multiple times through out the life of the field.

4.3 Conclusion

In this chapter, I studied different techniques for first arrival picking of P- and S-wave. These are classic and recursive STA/LTA, phase arrival identification-Kurtosis, modified transient energy method, and Akaike information criterion. All the techniques perform quite well in high-quality waveforms but might produce false arrival times when the signal level is low, or the waveforms contain possible multiple events. The existence of multiple possible events in the same seg-y event file is due to several factors, but most importantly, poor event detection result or contamination of microseismic data from events of none geological nature (e.g., noise). Compared to other methods, AIC does not require an analysis window and provides travel time with the lowest error to the manually picked values. Despite adapting the AIC technique, erroneous or no picks were reported on many events (especially waveforms of shallow geophones), and I reverted to manual picking by reviewing each seg-y event one by one.

In the second part of the chapter, I have shown the approaches followed for the estimation of the 1-dimensional and 3-dimensional velocity models. The former is the average velocity within each zone defined by the main geologic layers. Sonic log data from two wells are used to build the 1-dimensional velocity model. The 3-dimensional is built using the geostatistical modeling method known as sequential Gaussian simulation. The travel times and velocity information will be used in the next chapter to locate microseismic events. The reason to create the 1-dimensional and 3-dimensional velocity models are to test various location algorithms available in Insite software.

CHAPTER 5

MICROSEISMIC LOCATION

> *"The most time-consuming and important process in microseismic processing is obtaining reliable event locations. The subsequent processes of source parameter, focal mechanism, and shear wave splitting analysis, and their validity depend on the event location results."*
>
> — Khalil Al Hooti

This Chapter discusses the source location theories and methods that are used for microseismic events in Field X. The Chapter presents an overview of the principles of source location algorithms and a detailed analysis of several principal approaches, including iterative and grid search methods. I tested five different event location algorithms. These are the methods available in the Insite software, which is a commercial package licensed by Itasca Consulting Limited and is dedicated to microseismic data processing. The first two methods are the Geiger and Simplex that are categorized under iterative approaches. The grid search methods are the Tian ray tracing and FSM. These methods' implementation differs in Insite than, for example, similar methods found elsewhere, particularly by the nature of the velocity model used in the location algorithms.

The second section of the Chapter characterizes the event locations to identify what are the causes of microseismicity. The events cluster are correlated with the existing faults system mapped from active 3-dimensional seismic data. The alignment of events along these faults might suggest that steam is lubricating fault planes; thus, the increased pressure results in their reactivation. I analyze how far microseismicity happens from the injection points in the reservoir units.

5.1 Microseismic event location algorithms

5.1.1 Seismic source location definition

The determination of the accurate location of a seismic source radiating energy is a crucial step in seismology. The principles of various techniques developed in earthquake seismology to determine seismic source locations are the same used in microseismic processing. This section summarizes the most common microseismic event location determination methods without an in-depth explanation of the mathematical background. The five methods used for the Oman dataset are explained in the next section in more detail. The microseismic event location is described by its coordinates (x, y, z) and the origin time. The point of the energy release is the initial rapture location at the fault plane. The origin time is the time the rapture started. The rapture dimension depends on the produced fault or fracture size and is usually termed as fracture radius. The event coordinates and origin time is determined using the seismic phase arrival times (usually the P- and S-waves), a velocity model, and the source vector back-azimuth.

5.1.1.1 Single geophone location method

Practically, the location of an event can be calculated using only one station, provided that it contains three orthogonal sensors. The polarization of the P-wave is along the direction connecting the source and the receiver. The back-azimuth is the angle measured clockwise from north to the direction of the P-wave polarization vector pointing from the source to the event. Equation 3.14 provides the calculation of the azimuth (from which the back-azimuth can be inferred) and the incident angle. The knowledge of these two parameters provides an idea about two possible directions of the source location. The 180 ambiguity arises from the fact that the polarity of the P-wave is either negative or positive in the geophone three components. In the case of a gimbaled geophone, the amplitude of the vertical component is concerned. The distance to the source location is determined using the difference in travel times of the P- and S-wave. In the case of a homogeneous velocity, the distance is,

$$D = \left(t_s - t_p\right)\frac{v_p \cdot v_s}{v_p - v_s}, \tag{5.1}$$

where, $v_{p,s}$ is the P- and S-wave velocities, $t_{p,s}$ is the respective travel times. The origin time is then calculated as, $t_0 = t_p - D/v_p$.

5.1.1.2 Manual location using multiple geophone

The surface location of the event (epicenter) can be determined when at least three geophones exist at the surface. This method is more practical in the determination of an earthquake location than a microseismic event. The method works by manually drawing circles of radius equal to D (equation 5.1) centered at the station location (Figure 5.1). The size of the intersection area of the circles reflects errors in the travel time picking or the velocity model, which is an isotropic homogeneous velocity for both P- and S-wave velocities.

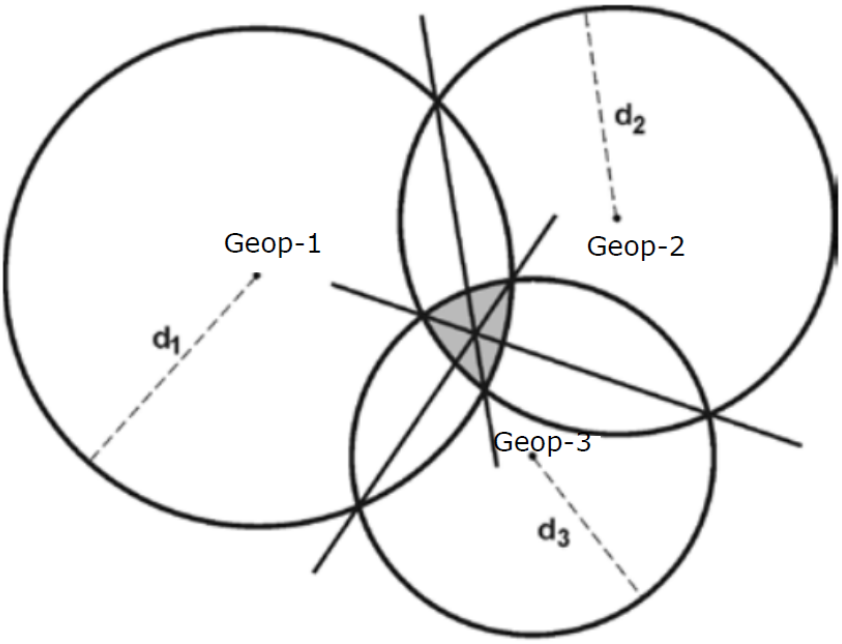

FIGURE 5.1. Epicentral location of an earthquake determined graphically using the "circle and chord" method. The velocity model for this technique is an isotropic, homogeneous velocity for both P- and S-wave velocities.

The calculation of the origin time proceeds by drawing the Wadati diagram (Wadati and Oki, 1933), which is a plot of the P-wave travel times versus the difference between P- and S-wave travel times (Figure 5.2). The origin time is determined when the travel time difference $t_p - t_s$ equals zero. Additionally, the plot provides v_p/v_s from the slope, $(v_p/v_s - 1)$ of the best fitting line. Outliers in this plot might indicate errors in travel time picking. However, this is only applicable when assuming a homogeneous velocity of the subsurface, which is seldom true.

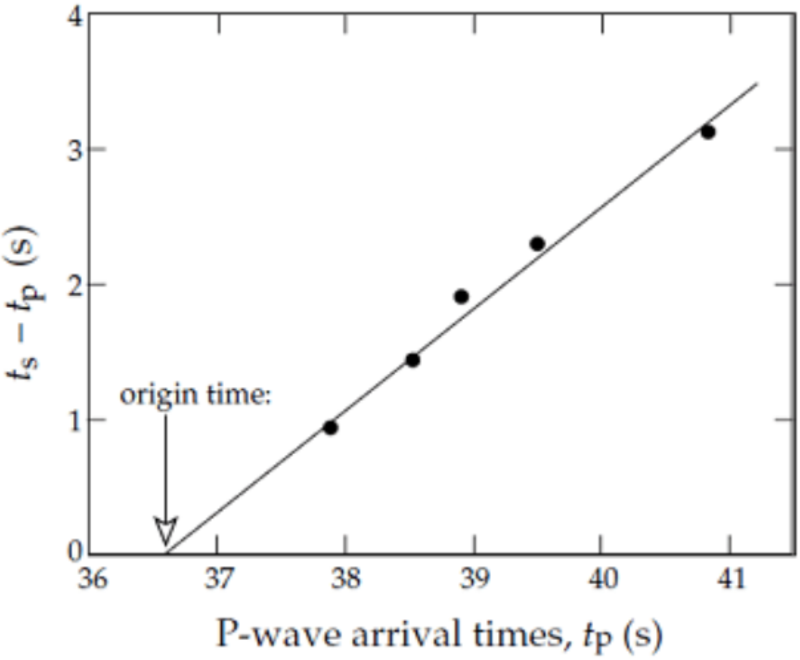

FIGURE 5.2. An example of the Wadati diagram. Interception of the best fitting line with the x-axis defines the origin time.

5.1.1.3 Computer techniques

Since the early days of computer inception, earthquake and microseismic location algorithms have been computerized. In recent years, earthquake early warning system has gained much attention from the public and governments. This required immediate and accurate reporting of earthquake locations, which is made possible by the availability of powerful computers nowadays. In this regard, assuming tens or hundreds of stations, the computed arrival time is,

$$t_i^c = T\left(x_i, y_{i,z_i}, x_0, y_0, z_0\right) + t_0, \tag{5.2}$$

in which t_i^c is the observed time at station i and T is the travel time function which depends on the locations of the source and the receiver. The equation has the source location and the origin time as the unknowns, and a similar number of such equations are needed to solve the system in an over-determined manner. The best solution is reported by the minimization of the difference between the calculated t_i^c and the observed t_i^o travel times,

$$r_i = t_i^o - t_i^c. \tag{5.3}$$

The complexity of the system of equations comes from the non-linearity nature of the relationship between observed time and the source locations,

$$\mathrm{t_i} = \frac{\sqrt{(\mathrm{x}-\mathrm{x_i})^2 + (\mathrm{y}-\mathrm{y_i})^2 + (\mathrm{z}-\mathrm{z_i})^2}}{\mathrm{v}}, \tag{5.4}$$

where, v is the velocity of the medium.

5.1.1.4 Iterative methods of error minimization

Many algorithms exist in the category of iterative methods, and they are fundamentally based on the linearization of an inverse problem. An initial guess of the the event locationis made, which might be the center of the geophones array or a point in space nearby the probable event location (steam injection point or the geophone with the earliest arrival). The assumption here is that the error between observed and calculated arrival time is caused by an inaccurate guess and the method makes a new guess to minimize the residual function,

$$r_i = (\partial \mathrm{T}/\partial \mathrm{x_i}) * \Delta \mathrm{x} + (\partial \mathrm{T}/\partial \mathrm{y_i}) * \Delta \mathrm{y} + (\partial \mathrm{T}/\partial \mathrm{z_i}) * \Delta \mathrm{z} + \Delta \mathrm{t}, \tag{5.5}$$

where, $\Delta x, \Delta y, \Delta z$, and Δt are the correction values that will make the error space zero. The iterative process continues until a predefined minimum error, or the maximum number of iterations reached. The convergence is rapid unless the initial guess is far away from the true location. However, sometimes the method converges to a local minima instead of the global one. An example of this method is the Geiger (1912).

5.1.1.5 Grid search methods

Increases in computer performance allow calculating the travel times to all possible locations in the velocity model. A collapsing grid search technique searches the 3D velocity volume to increase the method's efficiency. In the collapsing grid search, the initial search grid volume is large, but it shrinks by a user-defined factor around the lowest residual error. Another efficient grid search method is the fast neighborhood algorithm developed by Sambridge and Kennett (2001). The point in the velocity model which gives the lowest travel time error is defined as the event location. Example of this technique are Tian ray tracing (Yue and Xiao-Fei, 2005) and FSM (Tsai et al., 2003). In the case of multiple receivers, a measure of best agreement between solutions from all receivers is required, which can be achieved in the least square solution manner.

Other methods that exist which are not categorized under either grid search or iterative methods are relative location (Yang et al., 2002), full-waveform inversion (Yang et al., 2002), double-difference (Waldhauser and Ellsworth, 2000), and amplitude stacking and semblance (Staněk et al., 2015; Zhang et al., 2019).

The relative location method performs best when the master event location is accurately known, and the other events are assumed to happen close to the master event, and the velocity medium between the sources and the stations is the same. The full-waveform inversion provides the best results when the data quality is high, but it is computationally very intensive, making it unsuitable in real-time analysis and when the events number is large. The double difference optimally relocates seismic events when there are measurement errors and earth model uncertainty. The iterative least-squares procedure relates observed and calculated residual time difference for pairs of earthquakes observed at some stations.The vector connecting the two events location changes through the partial derivatives of the travel times for each event with respect to the unknown.

5.1.2 Location methods used in the Oman dataset

I used five different location algorithms to locate the Oman dataset. The objective is to assess their accuracy through the reported time residual and the location errors. These methods are tested on a sample of 545 events recorded by the microseismic well array (4, 11, 7). The arrival times manual and autopicking of the P- and S-wave onset times, however, were only possible on the waveforms recorded by MSW-4. This section describes each of these methods and shows their application on the sample events in the next section.

5.1.2.1 Geiger algorithm (Geiger, 1912)

This method obtains the source location (x_0, y_0, z_0) and the origin time t_0, by minimizing the sum of square residuals between observed and calculated arrival times. The method converges towards the true location using the magnitudes of the time derivatives.

The algorithm uses Singular Value Decomposition inversion from P- and/or S-wave arrival times. The method is an inverse least squares (L_2 norm). The source location is defined by four parameters, $\theta = (t_0, x_0, y_0, z_0)$, of x, y, z, and the origin time t_0, the residual is calculated as, $r_i = t_i - t_0 - T_i$, where T_i is the calculated arrival time, t_i is the observed one, and t_0 is the origin time. The linearization of the function which relates the arrival times and the location is defined as, $\theta = \theta^* + \Delta\theta$, where θ^* is an estimation of the source location near the correct location, and $\Delta\theta$ is a small perturbation. The representation of the observed times uses Taylor series expansion.

$$t_i = t_0^* + \delta t_0 + T_i\left(h^*\right) + \frac{\partial T_i}{\partial h}\Delta h. \tag{5.6}$$

The residual is defined as,

$$r_i\left(h^*\right) = t_i - t_0^* - T_i\left(h^*\right) \tag{5.7}$$

from the above equations, the residual is,

$$r_i\left(h^*\right) = \Delta t_0 + \frac{\partial T_i}{\partial h}\Delta h r_i\left(h^*\right) = \frac{\partial T_i}{\partial \theta}\Delta\theta, \tag{5.8}$$

which in matrix notation is represented as $r = A \cdot \Delta\theta$. The last equation is a system of linear equations.

5.1.2.2 The Simplex algorithm (Falls, 1993)

The Downhill Simplex Method is also categorized under the iterative procedure, which searches the error space for a minimum (Nelder and Mead, 1965). The method is represented by a geometrical shape termed a simplex, which in three dimensions is a tetrahedron having many vertexes (x, y, z) at each corner F (Figure 5.3). Based on the value of the error space at each vertex, the Simplex deflate. The process is repeated until it settles into a minima.

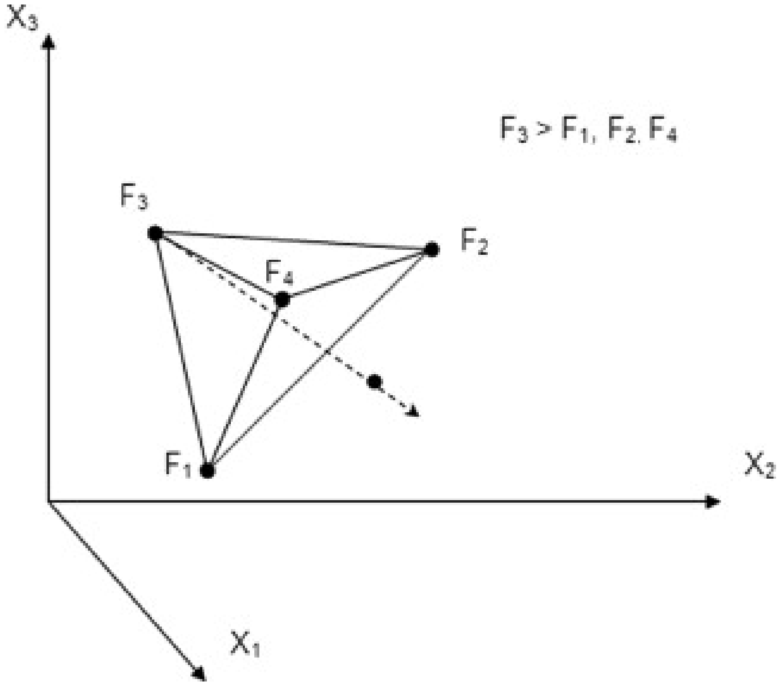

FIGURE 5.3. Simplex is a tetrahedron defined by four vertices F in 3D space. The minimization of the residual is carried out at every vertex. A perpendicular mirrored lines is drown toward the opposite plain segment from the vertex having the highest residual (F_3) (Ouria and Toufigh, 2009).

Chow (1992) and Falls (1993) introduced its application in seismic studies. The error (the sum of the traveltime residuals) for each arrival time of the P- and S-wave is calculated. The error in any Simplex vertex is the mean from all geophones.

5.1.2.3 Tian ray tracing (Yue and Xiao-Fei, 2005)

This algorithm calculates travel times using a two-point ray tracing for a layer-cake velocity model. The algorithm is developed by Yue and Xiao-Fei (2005).

The algorithm iterates through all grid points, defined by the user, within the search volume computing the raypaths connecting to each station. The algorithm searches iteratively for the ray parameter p that solves the location equation,

$$\Delta = p \sum_{k=1}^{L} \frac{\bar{h}_k v_k}{\sqrt{1 - p^2 v_k^2}}, \tag{5.9}$$

where L is the number of layers, $\bar{h}_k$ is the thickness and v_k is the velocity of the phase. The solution ray parameter p is constant for the ray path and provides the take-off angle at each layer zone.

5.1.2.4 Wavefront construction (WFC) (Vinje et al., 1993)

The method uses a two-dimensional adaptive WFC ray-tracing technique (Vinje et al., 1993). The concept is to produce a grid of 2D travel times across the velocity model volume. The nodes of the wavefront are at equal travel times, and the direction of the wavefront is at an equal take-off angle. The time nodes are constructed in two-dimension (source versus depth), propagating away from the source at a user-specified time interval.

5.1.2.5 Bristol University Microseismicity ProjectS (BUMPS)

BUMPS are a set of MatLab codes written by Dr. James Verdon at Bristol University. The software has many capabilities of analyzing and visualizing microseismic borehole data. Bland and Hogan (2005) developed the location algorithm used here, which is a Fast Marching Method (FMM) eikonal equation solver following Sethian and Popovici (1999). The implementation I used is for a 1D velocity model. BUMPS has difficulty locating events recorded by geophones placed in multiple wells. I compare the result of BUMPS with FSM in section 5.2. It worth mentioning that BUMPS is highly configurable to use other location methods than the one developed by Bland and Hogan (2005). Some of these methods are the ones available in NonLinLoc software by Lomax et al. (2000), and Madagascar software package for eikonal equation solver Li et al. (2013).

5.1.2.6 Fast sweeping method FSM (Tsai et al., 2003)

The isotropic version of FSM calculates the travel times by solving Eikonal equation for a 3D heterogeneous isotropic velocity model. The Eikonal equation belongs to the static Hamilton-Jacobi equations. In geophysics, it is derived from the full elastic wave equation with the high frequency approximation as,

$$\left|\nabla T(x)^2\right| = \frac{1}{c^2(x)}, x \in \Omega \setminus \Gamma, \tag{5.10}$$

with boundary condition,

$$T(x_s) = g(x_s), x_s \in \Gamma, \tag{5.11}$$

(Osher, 1993) describes a method to convert a static Hamilton-Jacobi equation to a time-dependent state with the level set method. The time-dependent Hamilton-Jacobi equations can be solved by discretizing the Eikonal Equation as a stationary boundary value problem and tracks the wavefront by following the causality of wave propagation (Rouy and Tourin, 1992). The fast marching method has a similar working principle (Sethian, 1996). FSM (Tsai et al., 2003; Zhao, 2005) uses Gauss-Seidel iterations and alternating sweeping orders such that each sweeping direction covers a class of wave propagation directions. The gradient of misfit function of direct and reflected arrivals is then derived using the adjoint method. Here the method is applied using a three-dimensional velocity medium.

5.1.3 Application to a sample dataset

I apply the methods described above to a subset of the dataset containing 545 events from one of the microseismic well arrays. Figures 5.4 to 5.7 show the location results from the Geiger, Simplex, Tian ray tracing, WFC, and FSM, respectively. The left plot is a cross-section view in these figures, while the right plot is a map view. The three horizontally running lines are the Nahr Umr, Shuaiba and Kharaib Formations. The grey-colored polygons in the right plot are preexisting fault planes shown in the left plot as dashed lines. The event locations are color-coded based on their depth.

The velocity model for the Geiger and Simplex methods is the average P- and S-wave velocity in the Shuaiba zone. Geiger method only locates 37 events. This method does not use source polarization information and thus cannot locate events recorded in only one vertical well. The Simplex method locates 268 events. However, since it uses a homogeneous velocity, an evident 180± ambiguity oriented (NW-SE) presents in the location results. The Tian ray-tracing method displaces events that have an incident angle of more than 70±. Notice scarcity of events close to the MSW-4 wellhead. The events also converge along velocity boundaries. The WFC method locates only 61 events. This method requires that the location grid spacing is half of the lowest thickness zone in the velocity model (Shuaiba Formation). Ensuring this parameter makes the calculation time extremely slow (Locating one event in about 15-20 minutes)

The FSM locates the highest number of events. The events do not exhibit 180± ambiguity. Their clustering is aligned along preexisting faults and mostly concentrated in the reservoir zones. I find the results from the FSM more reliable and geological acceptable, as is further detailed in section 5.2.

Table 5.1 provides some characteristic about each location method described. The maximum residual I defined to the geophone for the events to not be discarded from the location process is 50 ms. The time RMS residual is calculated as,

$$\Delta T_{RMS} = 0.5\left(\sqrt{\frac{\sum_{i=1}^{N^p} \Delta T_i^p}{N^P}} + \sqrt{\frac{\sum_{i=1}^{i} \Delta T_i^S}{N^S}}\right), \tag{5.12}$$

where N^P is the number of P-wave arrivals over the wells array and T_i^P, T_i^S are the difference between the observed and P- and S-wave arrival times, respectively. The location RMS error is calculated as,

$$E_{RMS} = 0.5\left(\sqrt{\frac{\sum_{i=1}^{i=N^P} \Delta T_i^P}{N^P}}\, v_p + \sqrt{\frac{\sum_{i=1}^{i=N^s} \Delta T_i^S}{N^S}}\, v_S\right) \tag{5.13}$$

in which the P- and S-wave velocities are the medium velocities at the source location.

The location process will fail to produce a result if the time residual or location error are higher than a certain threshold. For Field X, I set the time residual threshold to 0.1 ms. Also, a minimum number of four geophones must have a time residual less than 0.1 ms for the location process to proceed.

Table 5.1: Summary of tested location methods.

Method	**Velocity**	**Uses polarization**	**Total events located**	**Mean RMS travel time residual (ms)**	**Mean location error (m)**
Geiger method	homogeneous	No	37	46	115
Simplex method	homogeneous	Yes	2	22	32
Tian ray-tracing	1D	Yes	268	35	22
WFC	1D	Yes	61	40	51
FSM	3D	Yes	530	15	8

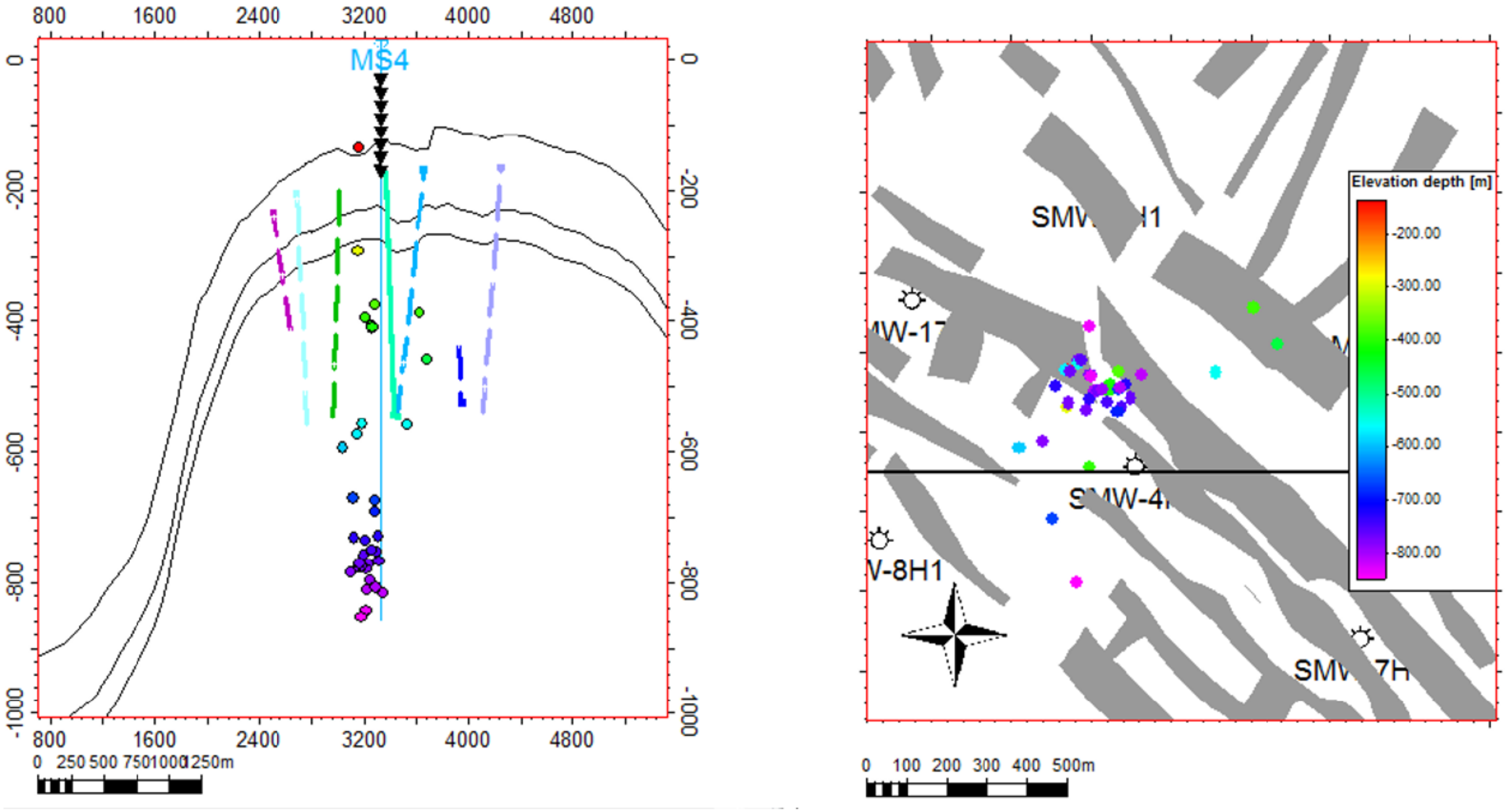

FIGURE 5.4. Location results from Geiger (1912) method. The velocity used are the P and S-wave average velocities from Shuaiba. A total of 37 events are located. The left plot is a cross-section of the black solid line shown in the right plot (map view). events are color coded based on their depth. The gray color polygons in the right plot are the faults planes, which are shown as dashed lines the cross-section plot.

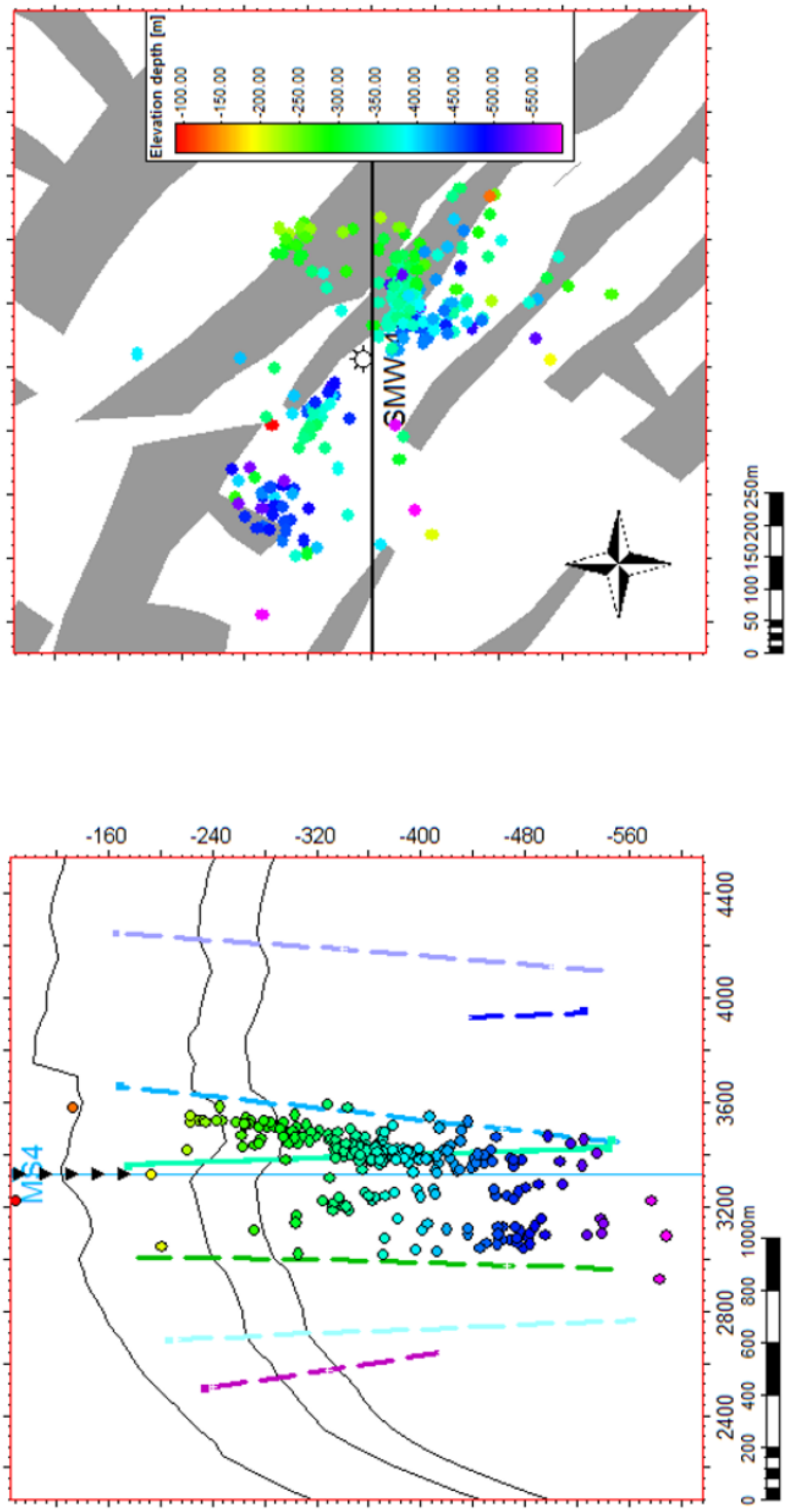

FIGURE 5.5. Location results from Falls (1995) method. The velocity used are the P and S-wave average velocities from Shuaiba. A total of 268 events are located.

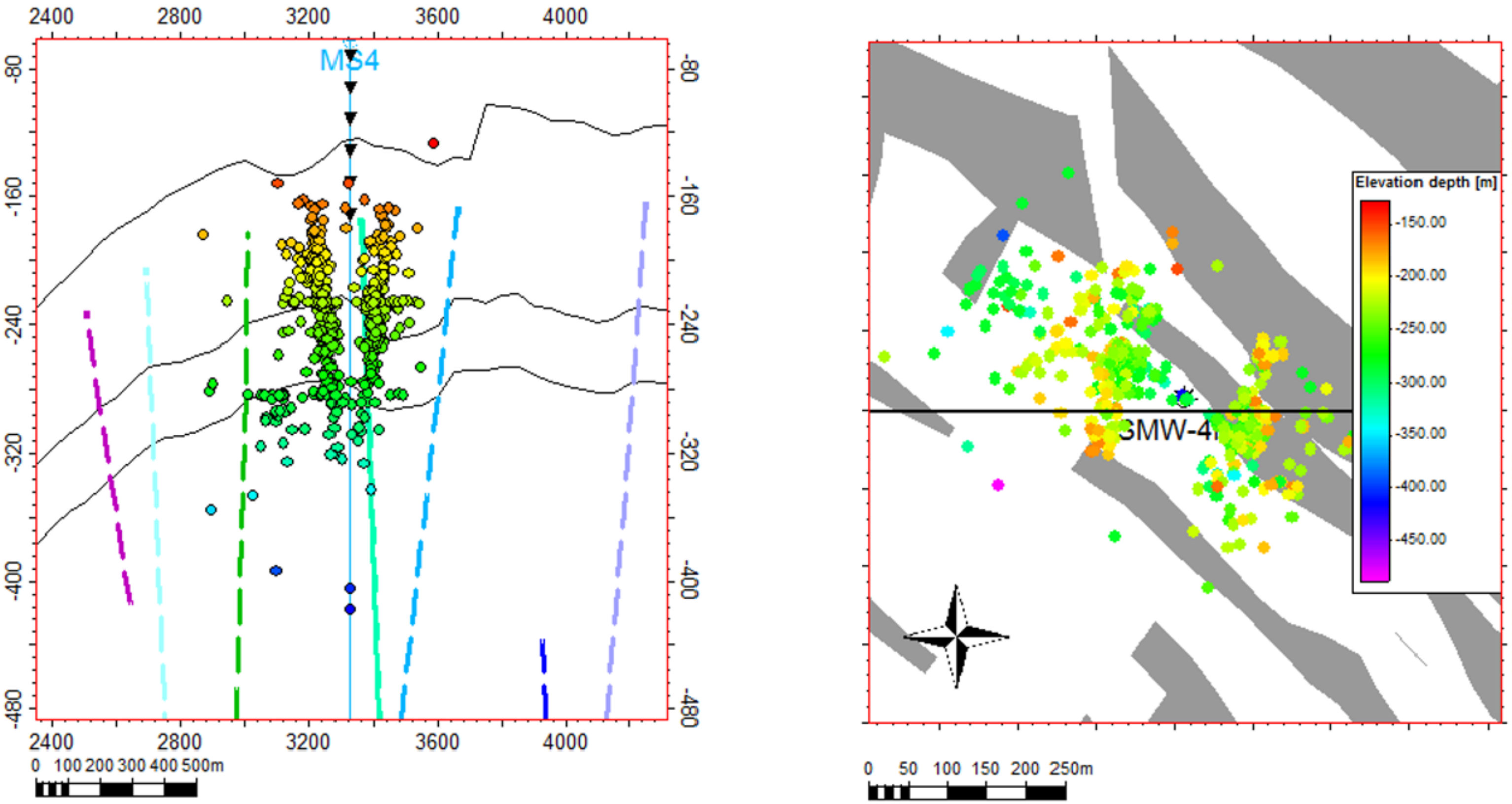

FIGURE 5.6. Location results from Yue and Xiao-Fei (2005) method. The velocity used is shown in Figure 4.13. A total of 465 events are located.

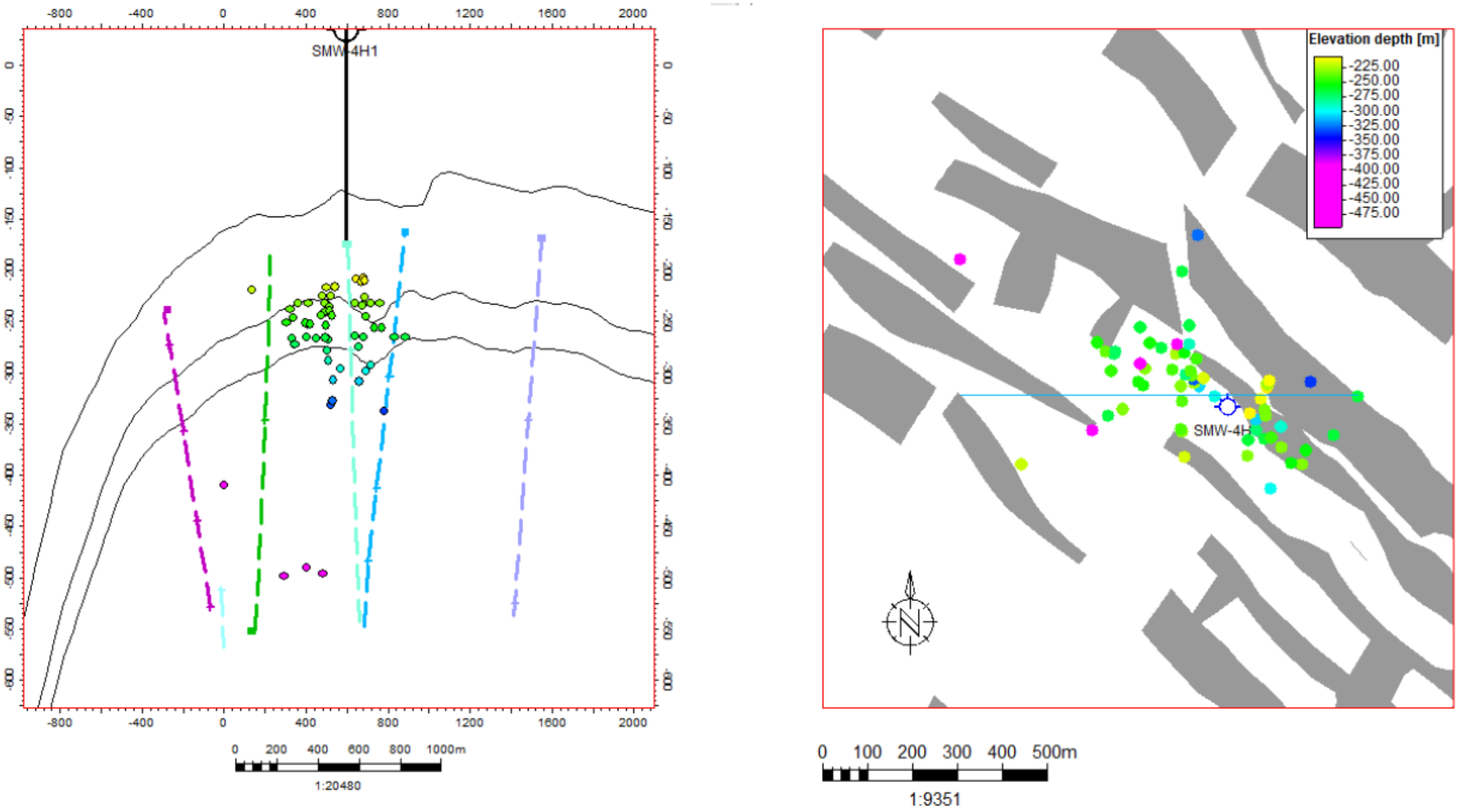

FIGURE 5.7. Location results from Vinje et al. (1993) method. The velocity used is shown in Figure 4.13. A total of 61 events are located.

5.2 Testing location algorithms using a 1D velocity model

In this section, I apply a 1D velocity model at the well array [4, 8, 17]. The velocity model is made of four velocity zones as shown in Figure 5.8-right. The zones from top to bottom are Natih, Nahr Umr, Shuaiba and Kharaib. The velocity of the Nahr Umr shale zone is the lowest, while Kharaib carbonate (lower reservoir unit) has the highest velocity. The purpose of this analysis to test the accuracy of location methods described above to locate a subset of events detected by the well array [4, 8, 17]. The first two methods (Geiger and Simplex) are not included since they accept only a single homogeneous velocity model. The rest of the methods (Tian ray-tracing, WFC, BUM) use 1D velocity model. Here, the same velocity model is supplied to each of these location algorithms. Figures 5.8-left, 5.9 show the travel time grid from WFC method, BUMPS and FSM, respectively. Insite software package directly outputs the travel time grid file when using the Tian ray-tracing method. Therefore, the travel time grid from Tian ray-tracing technique is not plotted here.

I compare the location results from Tian ray-tracing (Figures 5.13), WFC (Figure 5.12) and BUMPS (Figure 5.11) with FSM. In these three figures, the left side panel is a map view, whereas the right-hand side is a cross-sectional view from the black horizontal line shown in the map view. BUMPS software locates events away from MSW-4 that recorded most of the events from the well array [4, 8, 17]. BUMPS fails to locate events when recorded by more than one well. On the other hand, location results from FSM are clustered around the well that detected most events. The inner part trending NE-SW has a low number of events due to the existence of a sequence of horst-graben structures. The events from FSM are concentrated in the reservoir zones and are in close vicinity to injections well. Location results from WFC and Tian ray-tracing are somehow coincident with FSM. However, they suffer from convergent along strong velocity boundaries, as is the case between Nahr Umr and Shuaiba or Nahr Umr and upper Natih units. Figure 5.15 shows the depth range of the events calculated by all methods. Notice, the aggregation of events along the velocity boundary for the Tian ray-tracing and WFC methods. Figure 5.14 displays the difference in location results for 7 selected event. WFC and Tian ray-tracing method results are close to FSM. However, BUMPS software has the event cluster about 200 meters away from MSW-4. Therefore, I decided to use FSM to locate the remaining events.

Figure 5.16 shows the uncertainty in the location error (equation 5.13) for FSM. The location results are color-coded based on the location error for all directions (north, east and depth). The maximum location error is 16 meters. Errors in the depth domain are the lowest. This is due to the fact that only MSW-4 records the majority of the events from the microseismic well array [4, 8, 17]. Also, location results are more constrained in the depth domain for events detected by vertical wells. A histogram of the average location errors is shown in Figure 5.17-bottom. Figure 5.17-top displays the time residual (equation 5.12) for FSM.

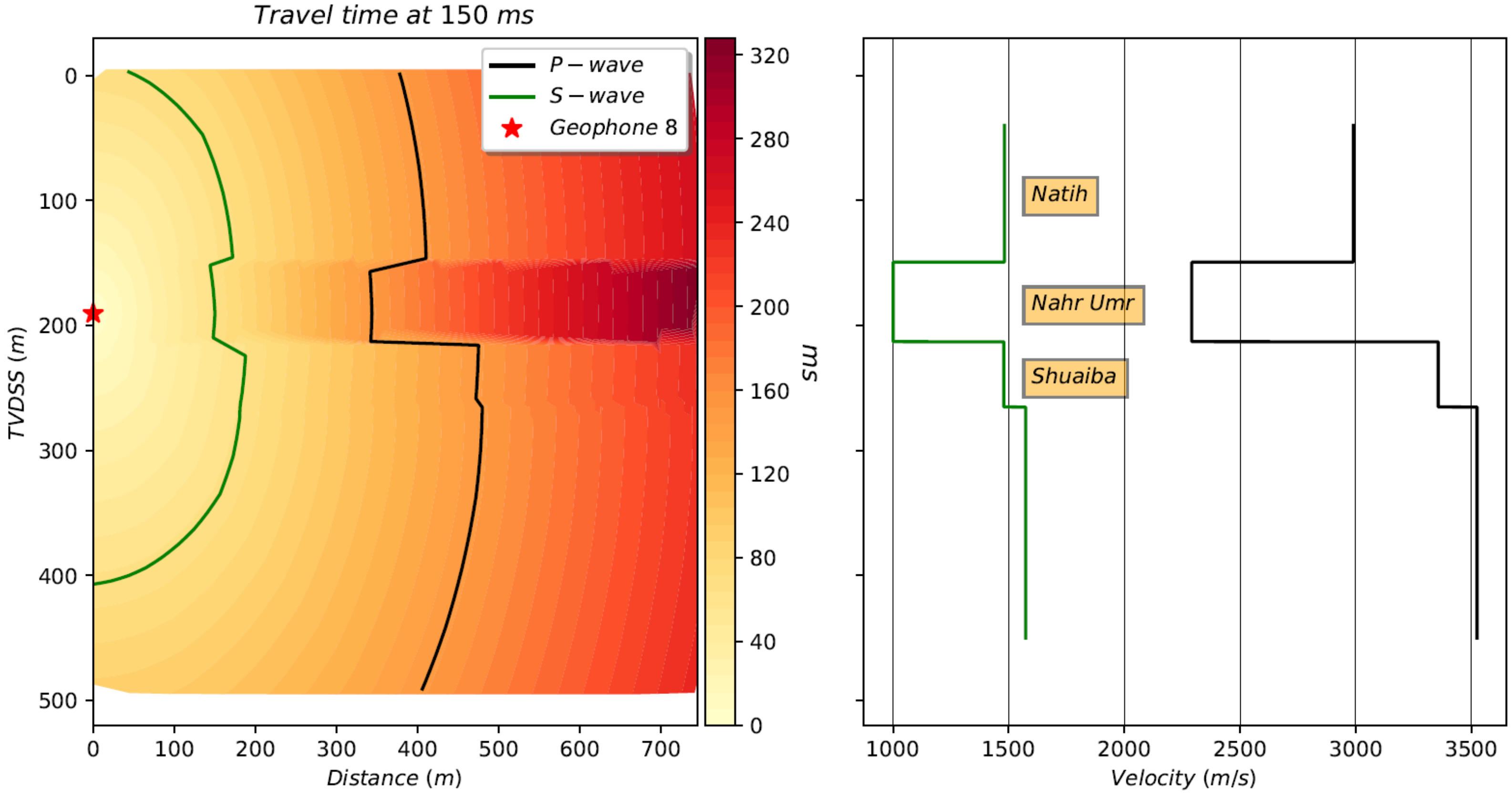

FIGURE 5.8. Four zones velocity model (right). The travel time curves from geophone 8 (left) from the WFC method. The P-wave and the S-wave are shown as black and green curves, respectively, at a time equal to 150 ms.

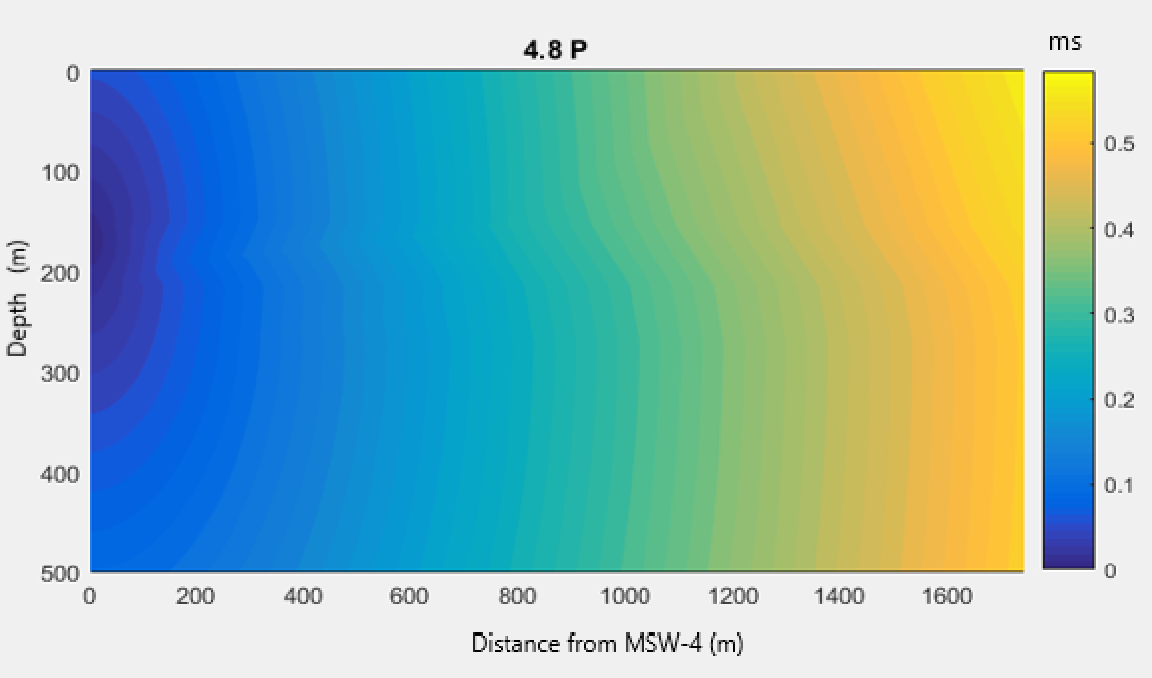

FIGURE 5.9. Travel time grid using BUMPS software by FMM.

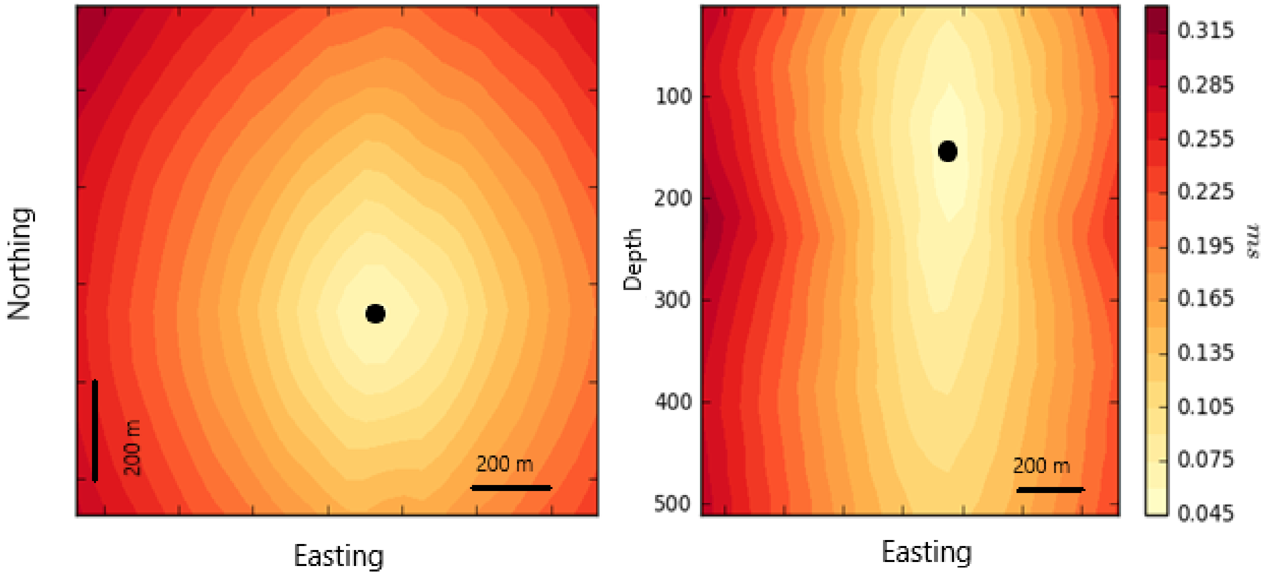

FIGURE 5.10. Travel time grid using FSM in Insite software package. Left figure is x-y cross section at a depth of 200 m, and the right figure is a vertical slice along the y-axis. The black dot is the geophone 8 location from MSW-4.

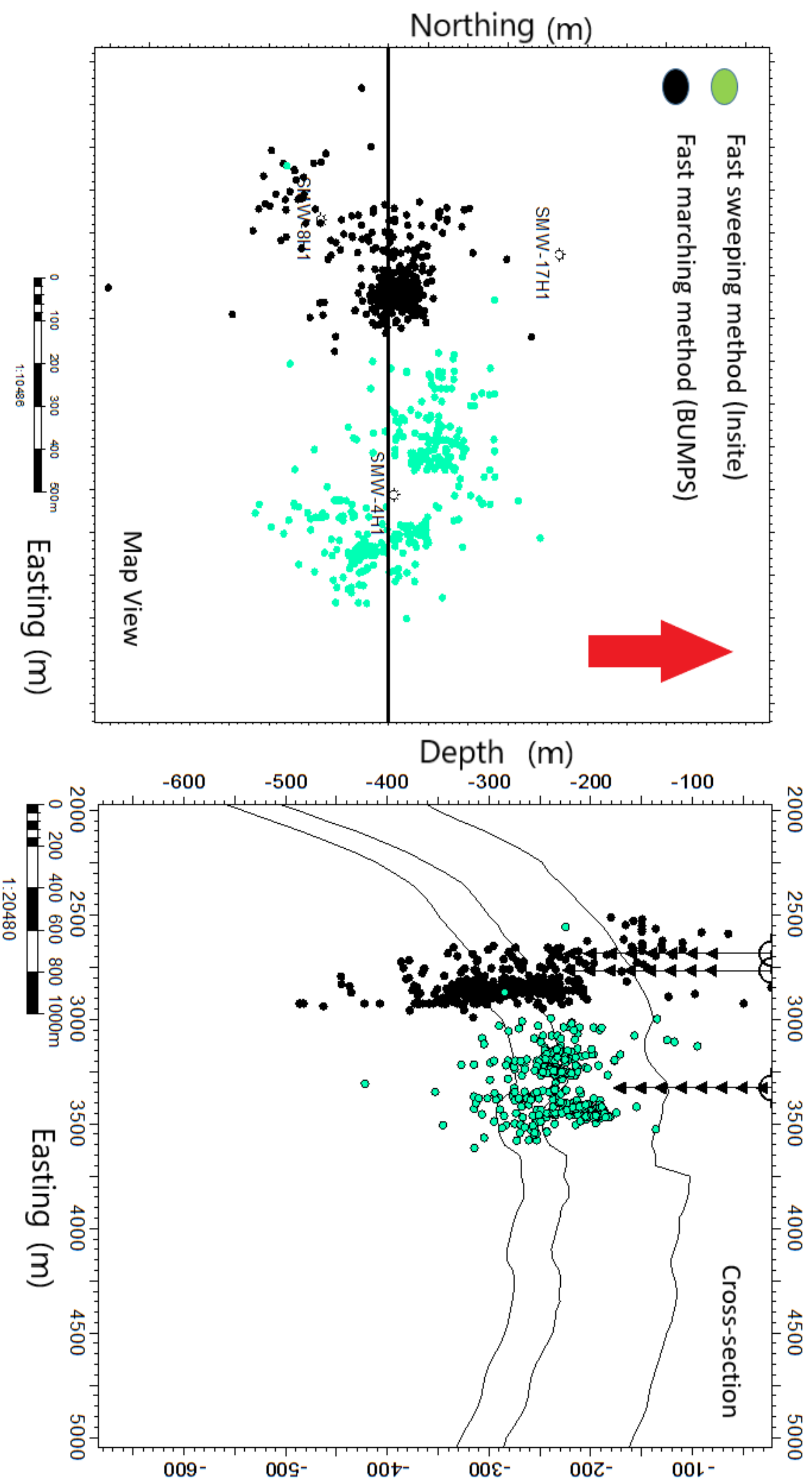

Figure 5.11. Comparison of location result between FSM and BUMPS.

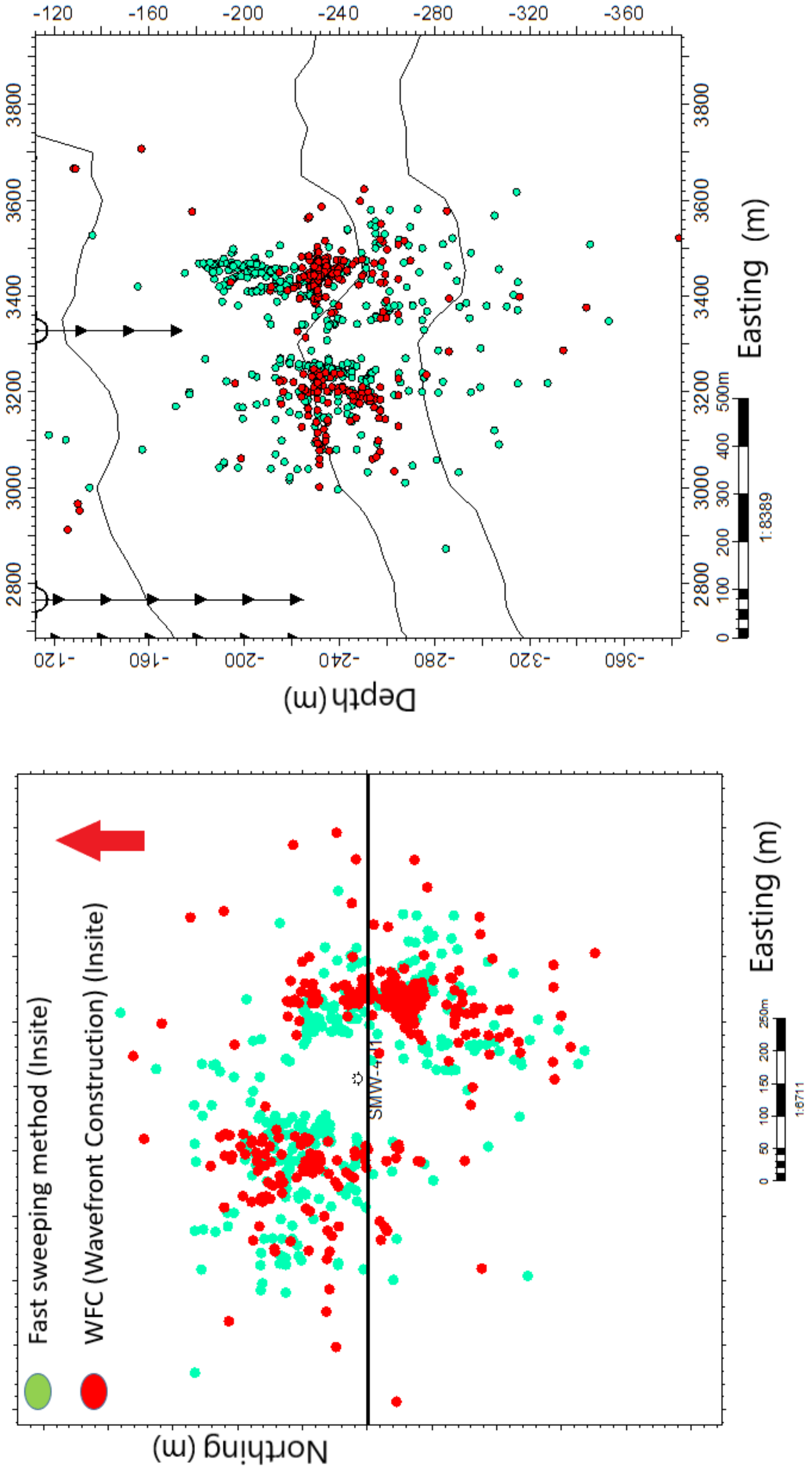

FIGURE 5.12. Comparison of location result between FSM and WFC.

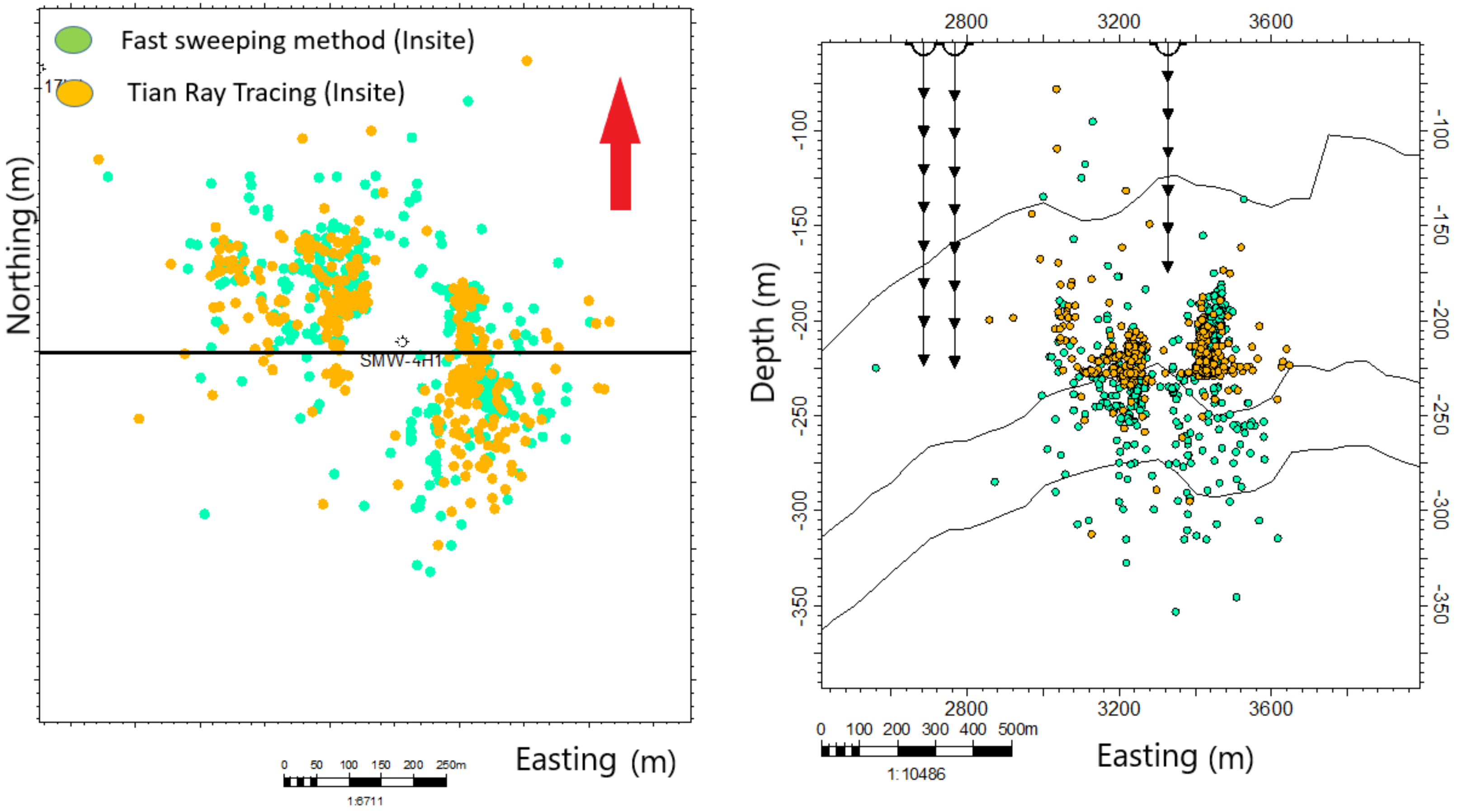

FIGURE 5.13. Comparison of location result between FSM and Tian ray-tracing.

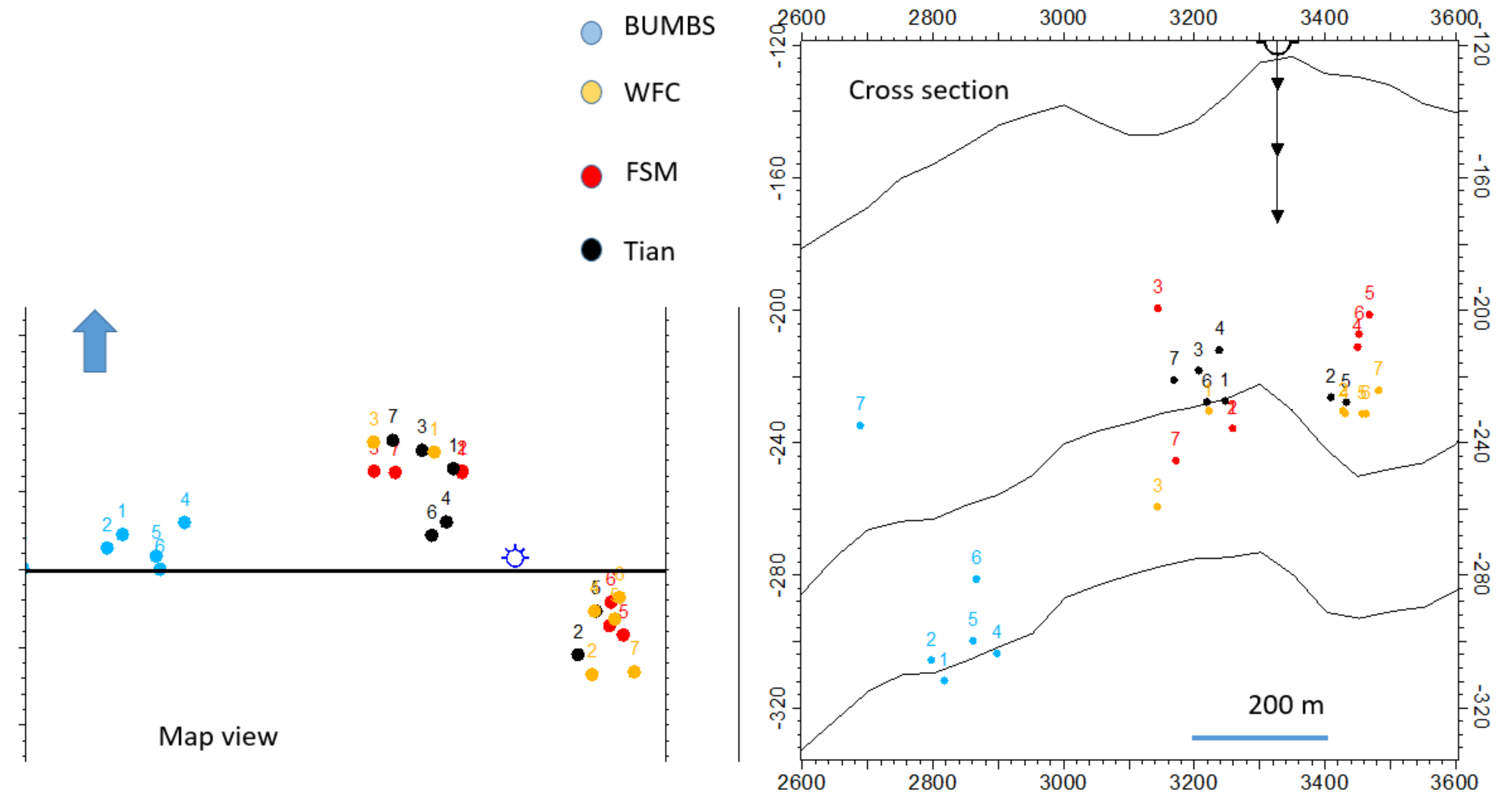

FIGURE 5.14. Difference in location results for 7 selected event. The blue start in the map view is the MSW-4. The same well is shown in the cross-section.

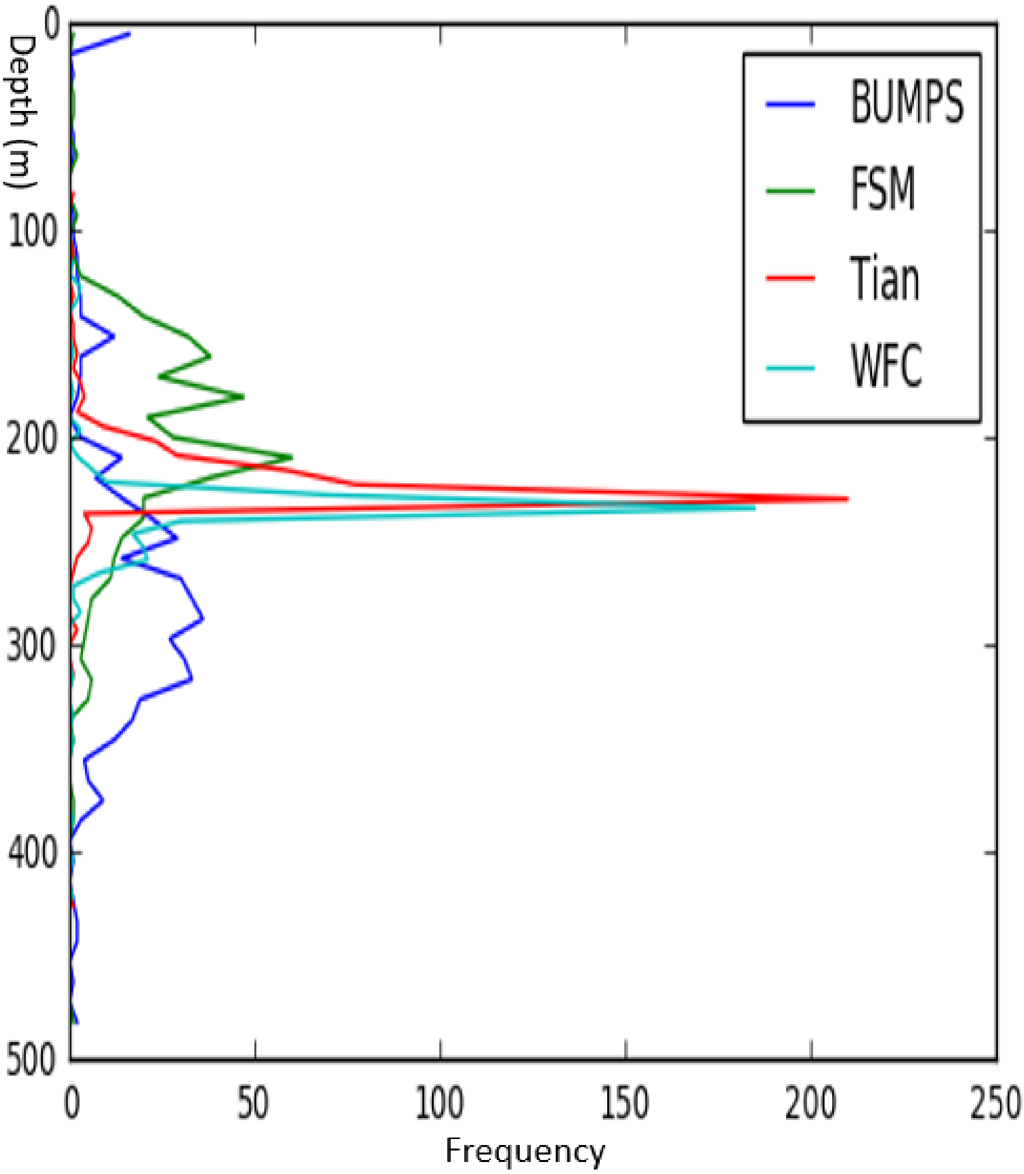

FIGURE 5.15. Depth range of of events calculated by all four method.

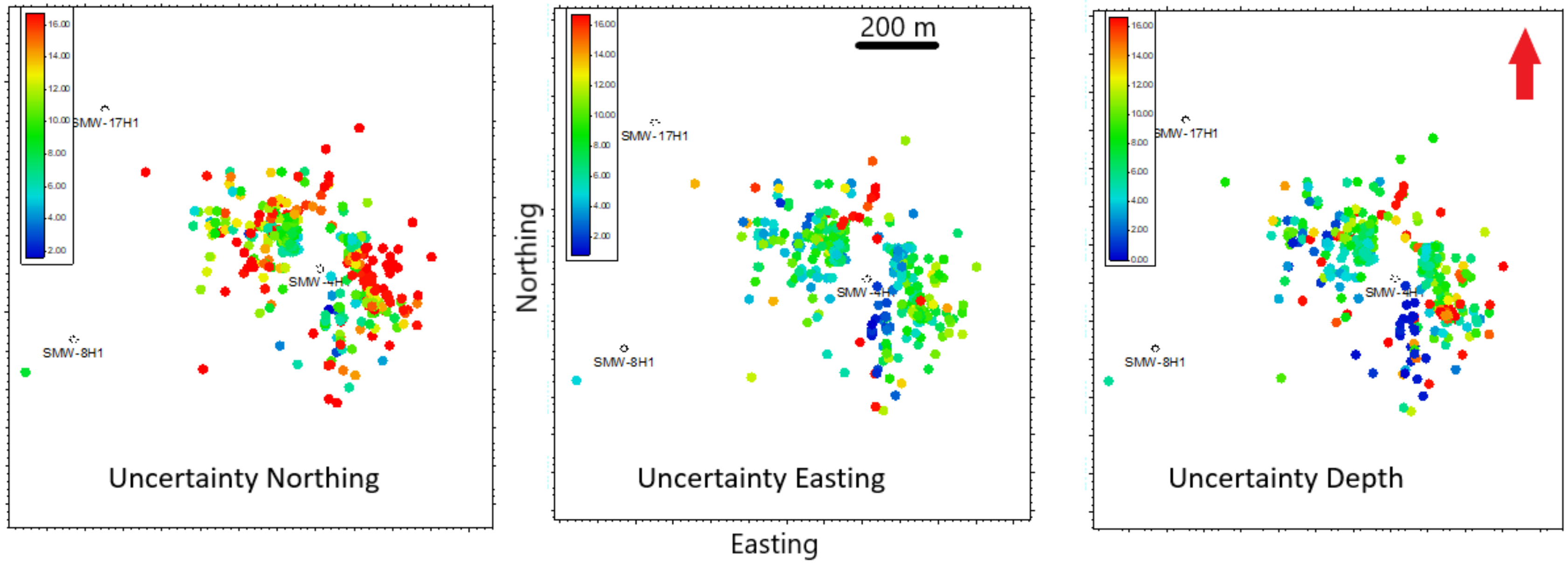

FIGURE 5.16. Location error from FSM. The figure from left to right are uncertainty in north, east and depth domain, respectively.

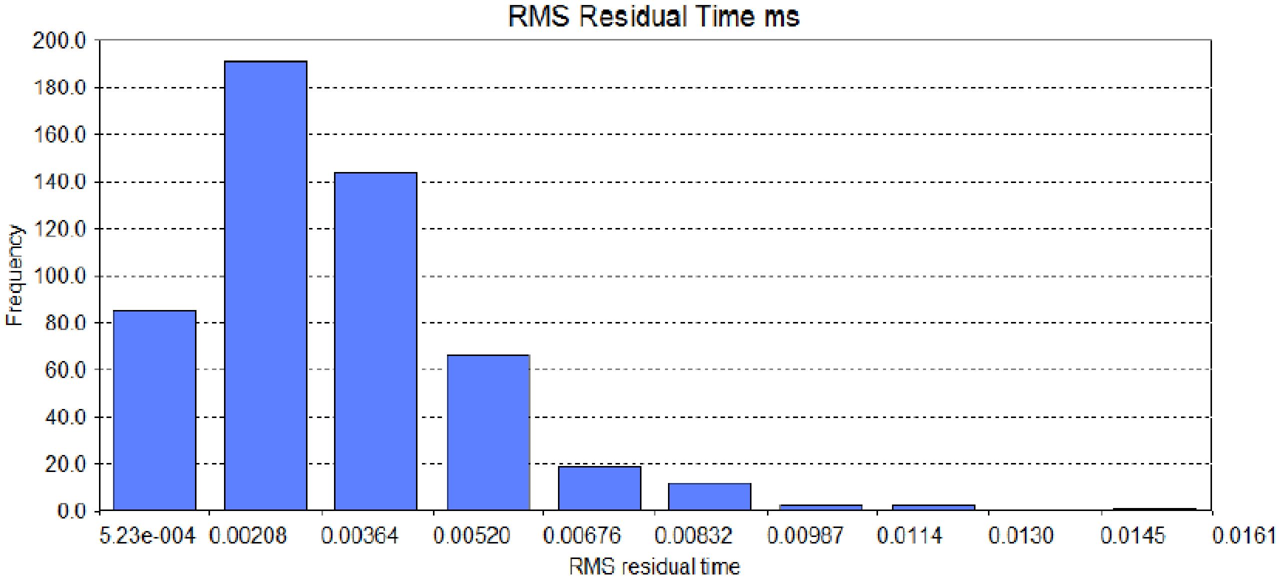

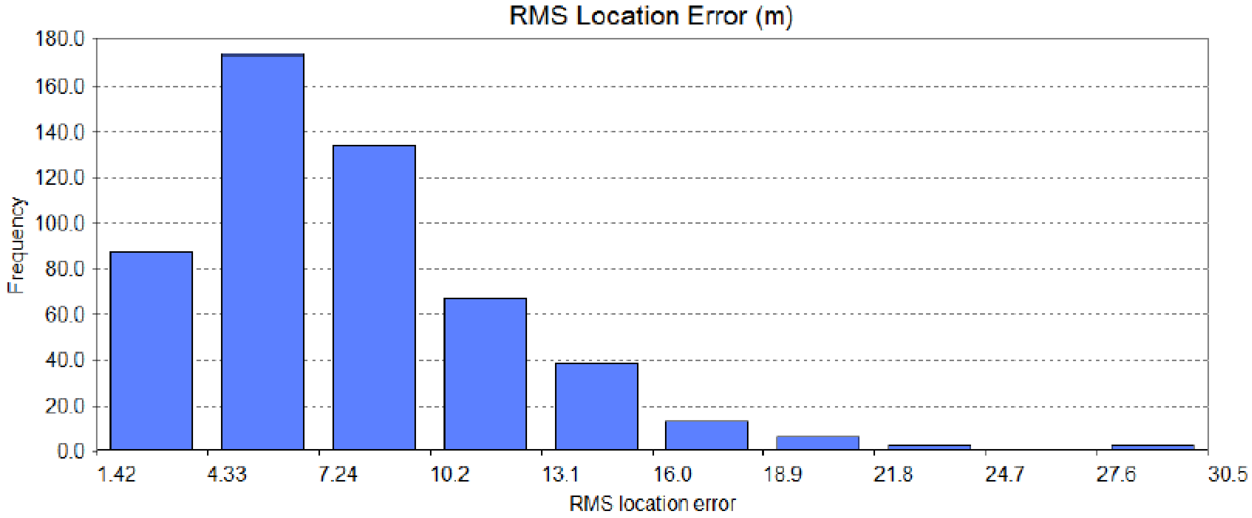

FIGURE 5.17. Time residual (top) and location errors (bottom) from FSM.

5.3 Conclusion

In this Chapter, I tested many different location algorithms to assess their success in locating a subset of events from Field X. The location algorithms tested here are Geiger, Simplex, Tian ray-tracing, wavefront construction, BUMPS software and FSM. Some of these location algorithms require an isotropic homogeneous single velocity value (Geiger and Simplex), whereas for others, the velocity input is a 1D model (Tian ray-tracing, wavefront construction, and BUMPS). The velocity for these three methods is a 1D having four zones of isotropic homogeneous velocities. FSM requires a heterogeneous 3D velocity model. Testing proved that FSM provides location results which do not converge along velocity boundaries, as is the case with Tian ray-tracing and WFC methods. BUMPS software results in event locations far away from where injection wells exist.

CHAPTER 6

CHARACTERIZATION OF MICROSEISMIC LOCATION RESULTS

> *"Microseismic analysis is best performed when integrated with other geological and petroleum engineering data."*
>
> — Khalil Al Hooti

This Chapter discusses the location results obtained from FSM for the whole Field X. I also discuss the correlation of surface surveillance data with microseismic events. Finally, I calculate events source parameters and discuss what objective the project achieved for a sustainable TA-GOGD.

6.1 Event locations characterization

The monthly frequency of events is shown in Figure 6.1. At the start of the monitoring program, the microseismic array detected a low number of events (from May-2011 to November-2011). The first injection program has started in late 2011, during which an abrupt increase in seismicity is observed. This is followed by an injection shut down period to assess the effectiveness of the injection program and start producing oil that is escaping from the rock matrix into the fracture system due to thermal expansion. Many of these events are not related to changes in the reservoir units but originated from drilling noises. The FSM location algorithm did not locate these events because they are not occurring in the reservoir zone since the velocity model encompasses only the volume containing the reservoir zones and the upper Nahr Umr shale unit.

Figure 6.2 shows the seismic activity as a function of time for located events (green) and total events (red). Notice that the events which are not located are related to no injection activities (Drilling process or surface noise).

Having established that FSM is the optimum method among the other tested methods in this project. I located the remaining events using the FSM. Figures 6.3 and 6.5 shows a map view and a cross-section, respectively, displaying all located events (5700 from 7200). The events are aligned along major faults trending NW-SE and NE-SW. There is a scarcity of events in the central graben structure trending parallel to the orientation of the main faults. The ones displayed inside actually are their projection from the deeper areas of the fault planes. The events are mostly concentrated in the reservoir zones. The Shuaiba has about 33% of the events while the percentage of events occurring below Kharaib is 59. The abrupt limit of the events in the middle cluster is a fault, which has not been mapped in active seismic sections. These three clusters are close to the injection locations. The events which are not exactly aligned with the major faults are related to induced fractures occurring close to these major faults. Chronologically, events below MSW-9 occur at an earlier stage than events elsewhere. This might be due to the injection process is taking place at an earlier stage in this region.

A 3D plot (Figure 6.5) of events around well array [7, 11, 4] show preferential orientation of events along existing fault structures.

Structural analysis is performed on the located events around the well array [4, 8, 17] using the three-point method. The method works by drawing a triangular shape connecting a group of every three located events to create a planner feature per group. The maximum inter-spacing between events is chosen to be 400 meters. The preferential orientation of located events is represented by a density plot of the planner features on lower hemisphere stereographic plot (Figure 6.6).

Three main planner features can be discerned from the stereonet plot.

Feature A (Figure 6.7) is oriented NW-SE and having a dip angle of about 45 degrees toward NE. It is parallel to the main fault system creating the apparent graben structure.

B and C (Figure 6.8) are orientated NE-SW opposite to feature A. Both are having a dip angle of about 60 degrees put dipping in opposite directions. They are parallel to the secondary fault system of the field and the fracture system as mapped by geologic data e.g. formation micro imager.

D clustering is some events just above OWC allowed to be grouped into horizontal planes. They are probably attributed to the production process happening at just below Fracture OWC.

The development of events chronologically is depicted in Figures 6.9, 6.10 and 6.11. The events initiate along the sub-vertical features coinciding with major fault trends oriented NE-SW and NW-SE. Three main scatter can be observed. They are concentrated around microseismic monitoring well MSW-4, MSW-7, and MSW-9. These are the wells that detected about 85% of events. Initially, the microseismic events happen parallel to major faults orientation. Starting from mid-2012, thermal expansion diffuses the clustering of events where the steam injection is taking place.

The D-value is a statistical value that characterizes fractal dimensions of hypocenters location. D is equal to 0 for a point, 1 for a line, 2 for a plane, and 3 for a sphere (Grob and van der Baan, 2011). The calculation of D-value follows spatial correlation integral method (Grassberger and Procaccia, 2004),

$$C(r) = \frac{2}{N(N-1)N(R<r)}, \tag{6.1}$$

where N is the number of events in a closed region of a maximum distance R from the center and r is inter-spacing between pairs of events. For fractal distribution of events in space, D-value is found as,

$$C(r) \propto r^D \tag{6.2}$$

The uncertainty in D-value comes from the way the group of events is selected, particularly if mistakenly, events from different geologic features are grouped together, which is quite common. In this project, the analysis is made in Insite software, and the group of events is selected visually by drawing spheres around various events clustered together. The calculated D-values range between 1 and 2. Whenever the D-value is close to 1, the corresponding events are related to injection activity. On the other hand, values close to 2 are related to planner features corresponding to fractures or faults.

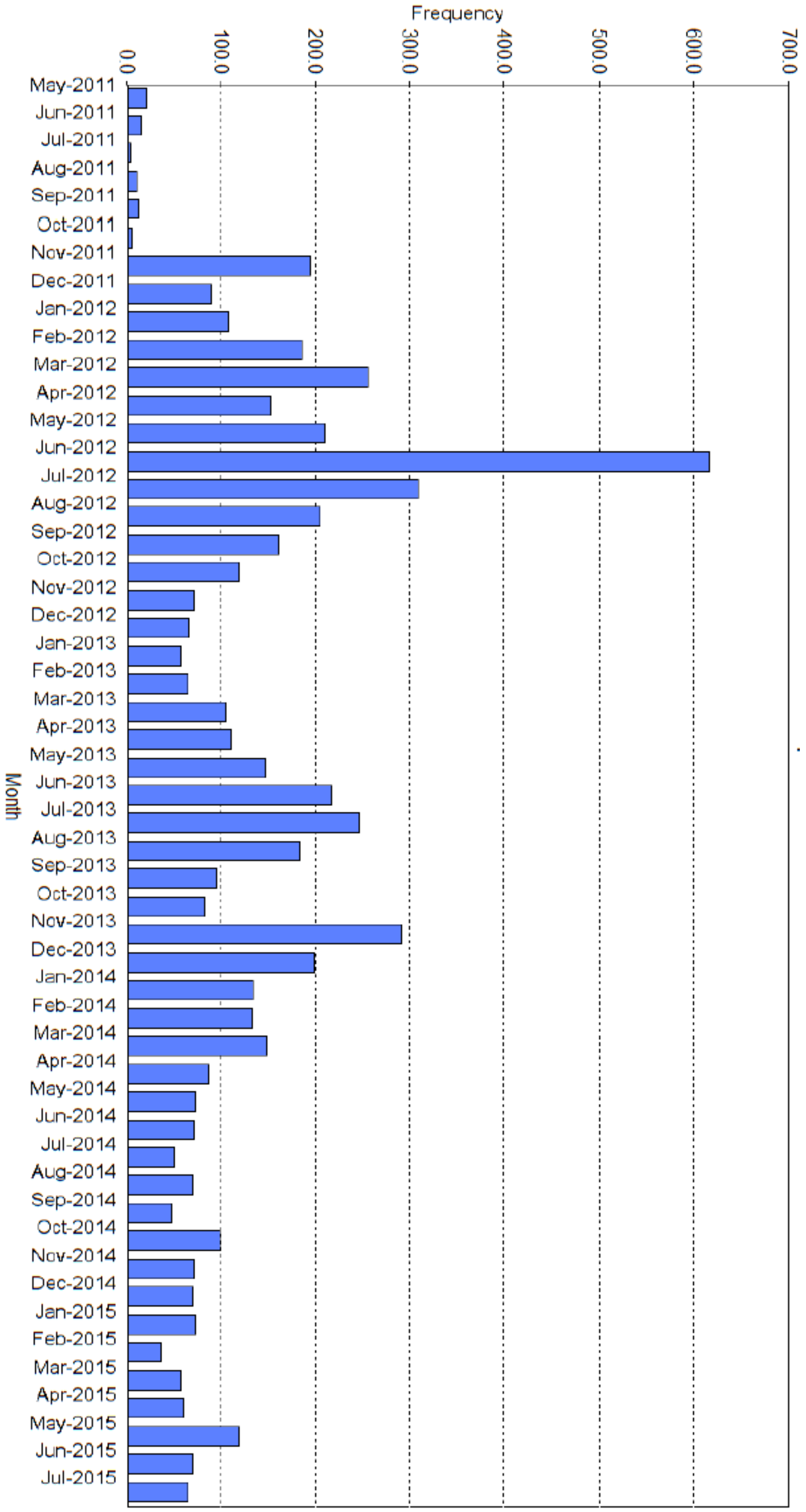

FIGURE 6.1. Monthly event frequency chart.

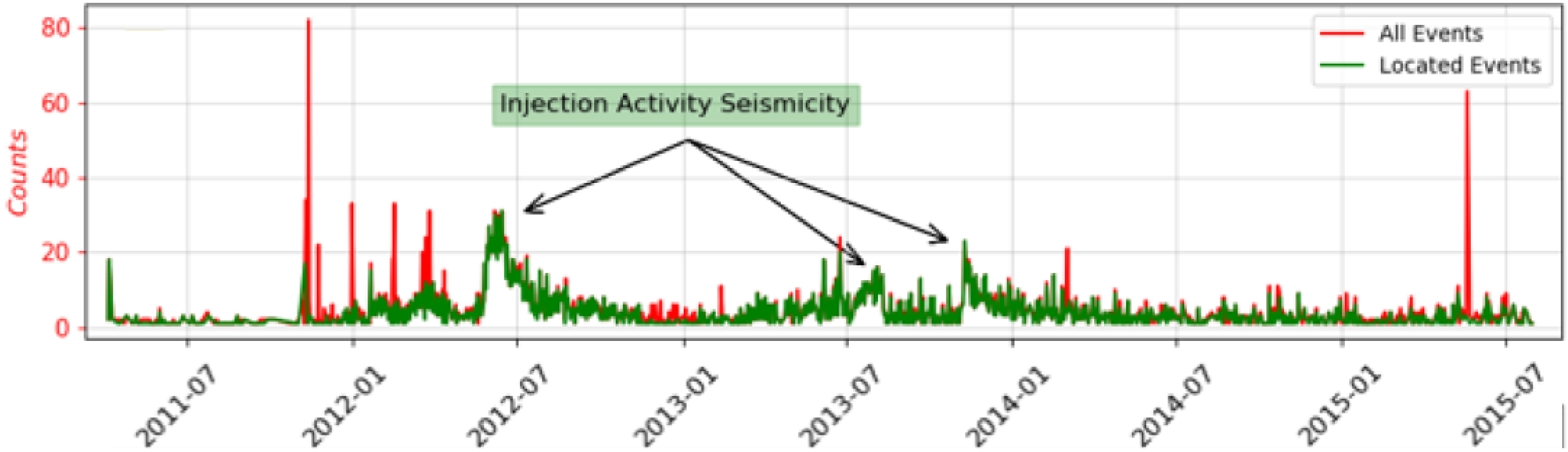

FIGURE 6.2. Histogram of event frequency and correlation with injection times. Other spikes in seismicity are associated with surface activity or drilling.

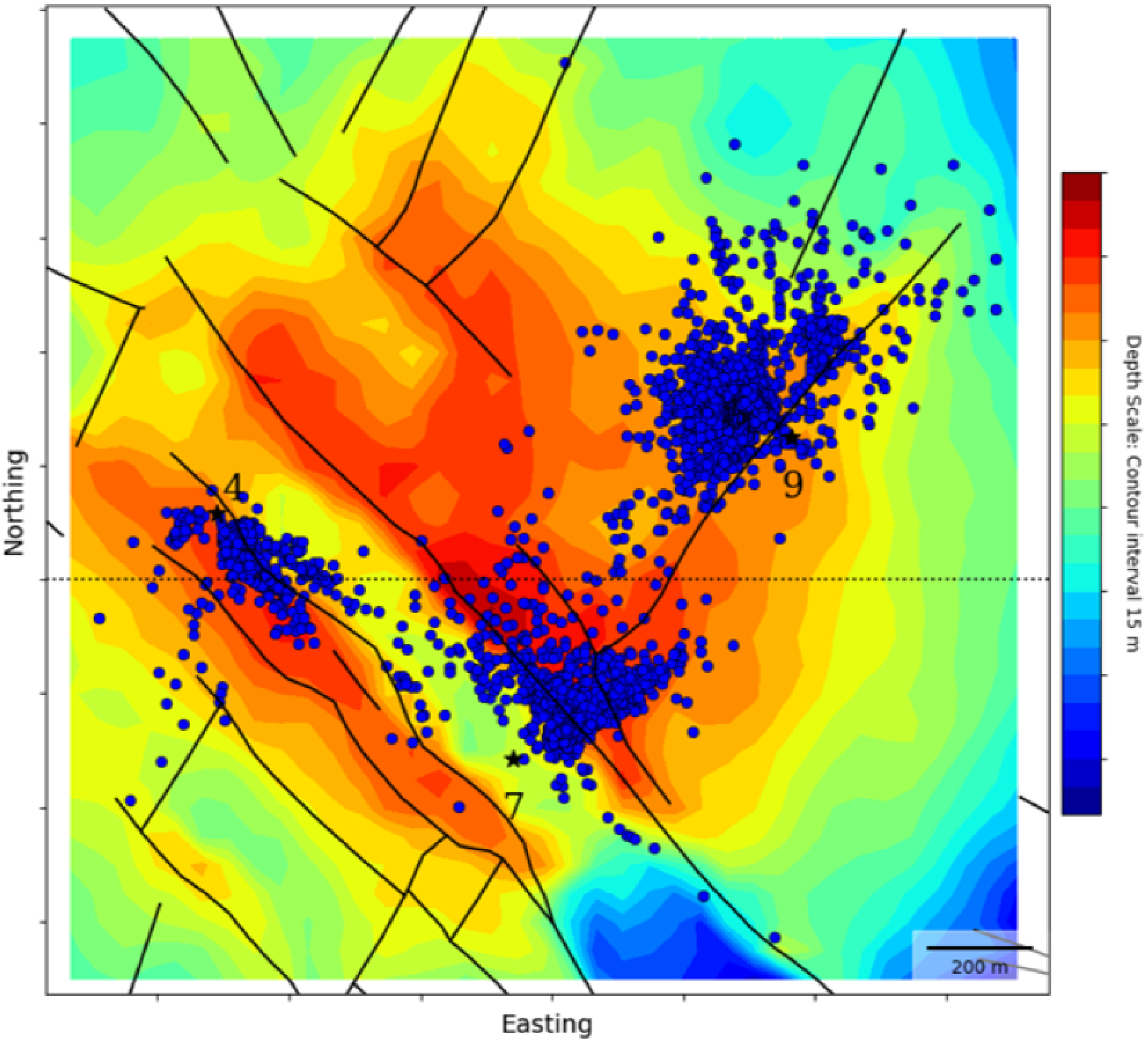

FIGURE 6.3. Map view of the located microseismic events displayed on the top surface of the reservoir. They generally follow the trends of existing fault systems. The surface map is the top reservoir Shuaiba unit.

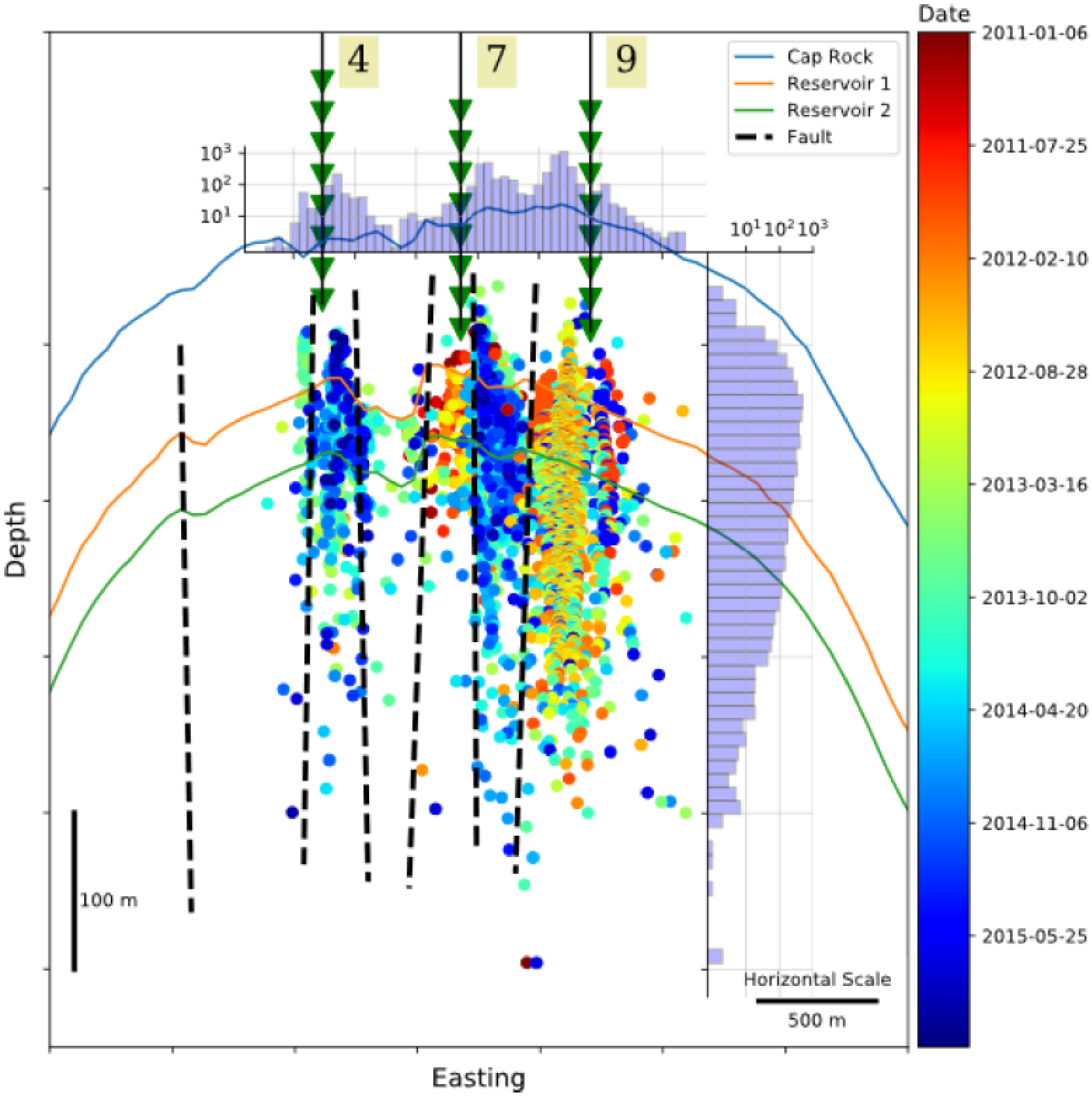

FIGURE 6.4. Events shown in vertical E-W cross section (Figure 6.3) and color coded as a function of time. They align vertically and are generally confined to the complex graben and horst structures.

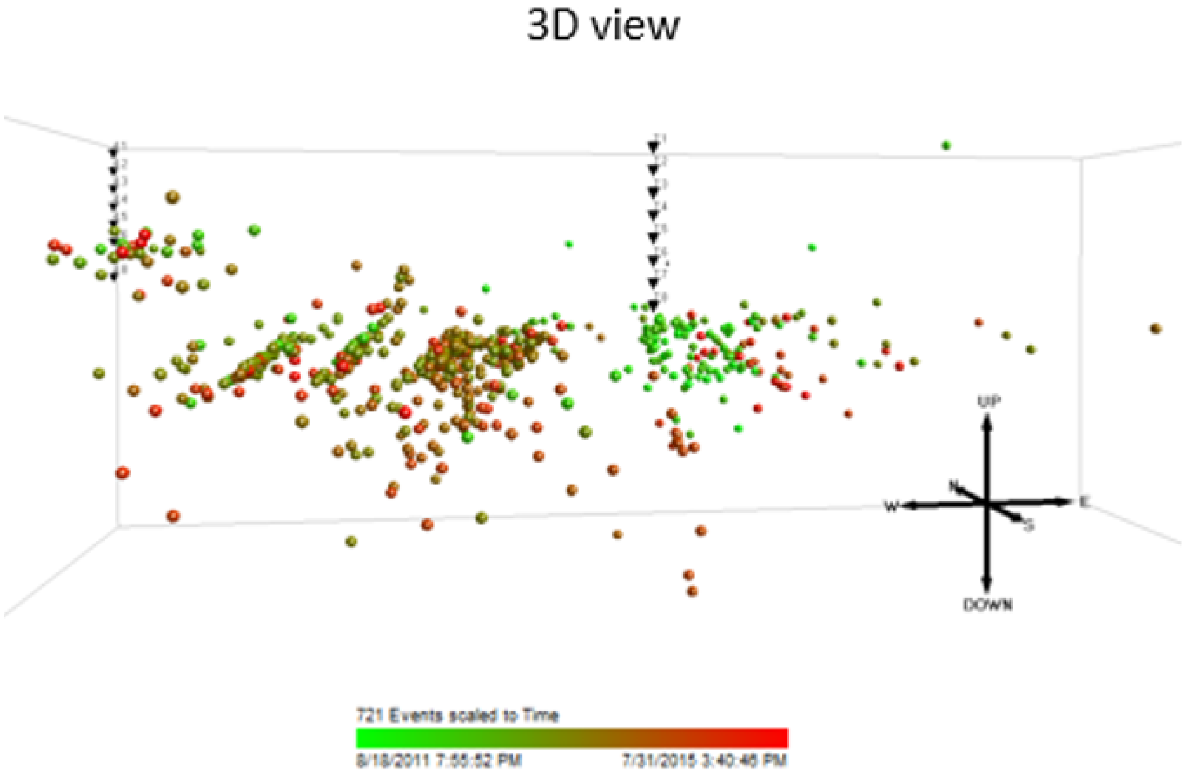

FIGURE 6.5. A 3D view of located events around wells array [7, 11, 4]. Planner concentration of events along preexisting faults is very clear.

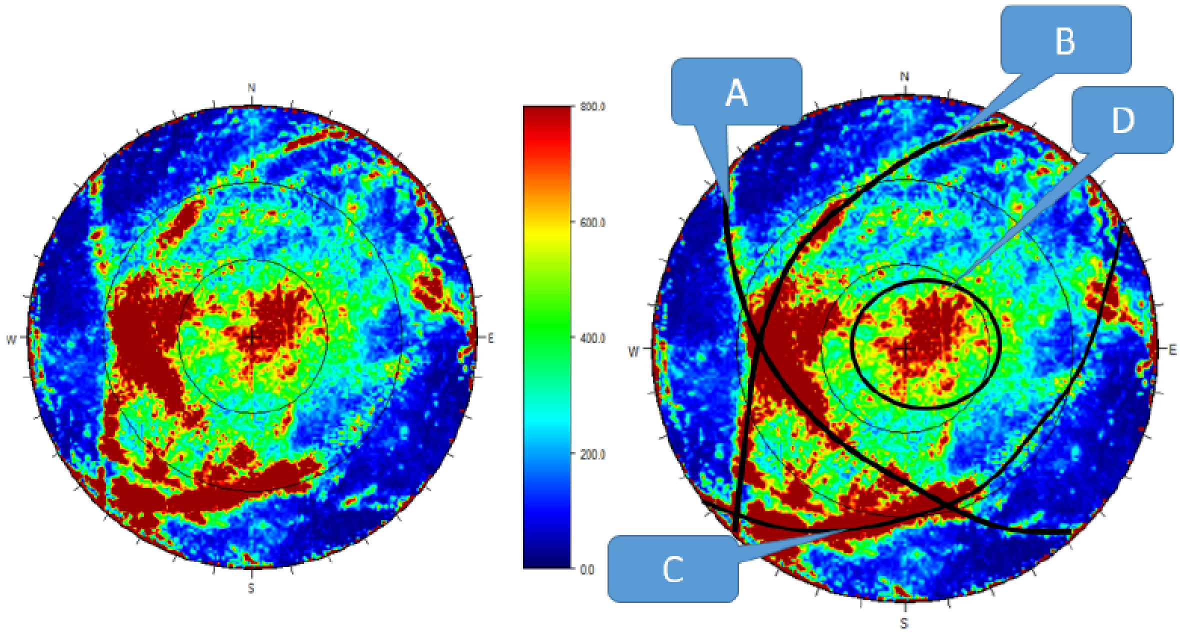

FIGURE 6.6. Structural analysis of events around well array 4, 8, 17. This is a structural stereographic plot showing preferential planes created by event clustering. See Figure 6.7 and 6.8 for the correlation highlighted feature and the microseismic events location.

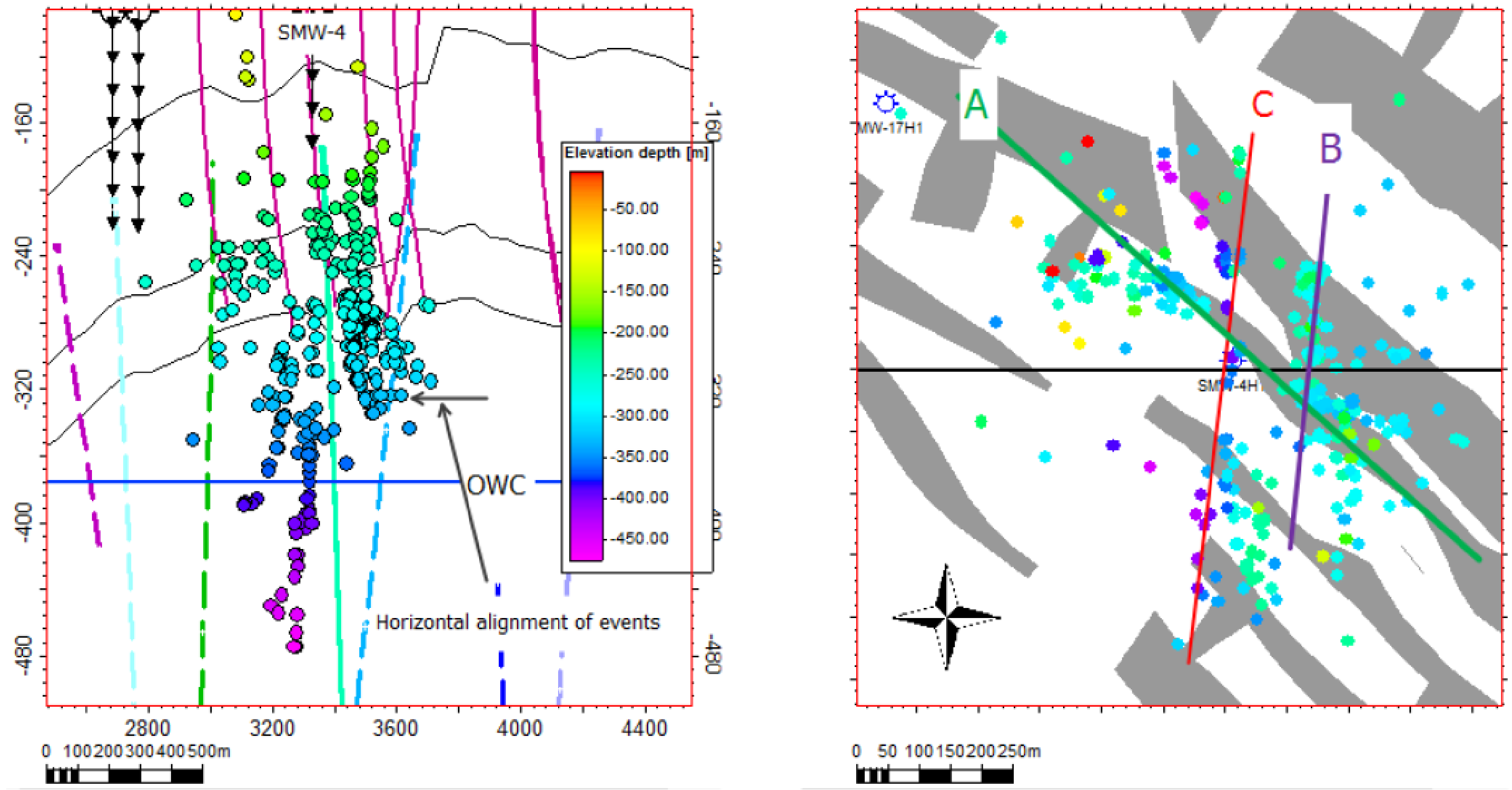

FIGURE 6.7. Left: a plane showing all projected events on the cross-section. Right: a map view of event. clustering of events along planner features A, B, C are highlighted

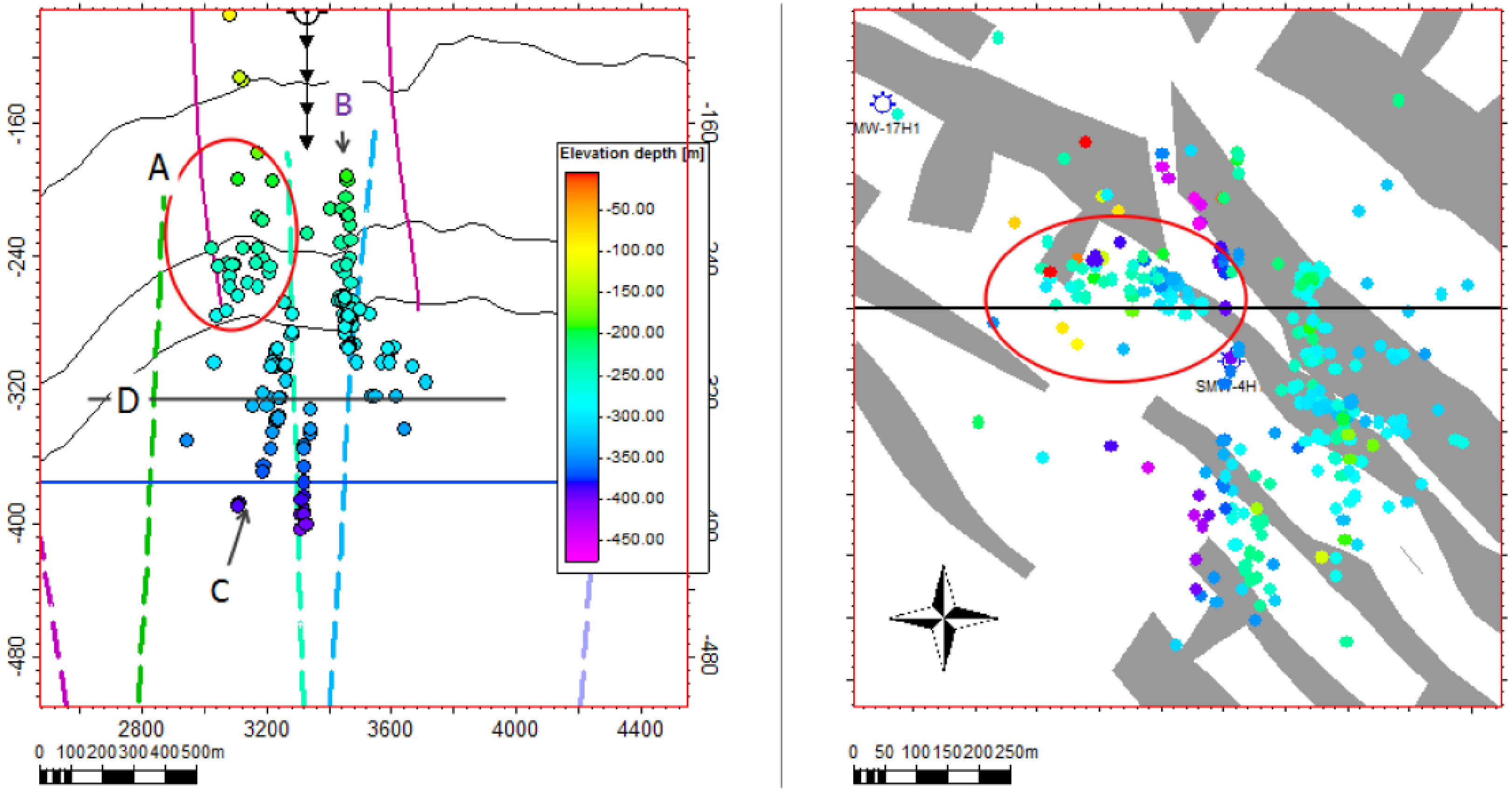

FIGURE 6.8. This is similar to the Figure 6.7 but events are limited to 100 meters from the cross-section line (black line to in the right-side plot). Events belonging to clustering A do not project coherently on this crosssection and hence does not show linear feature. Clustering C is a complex two branching fault system.

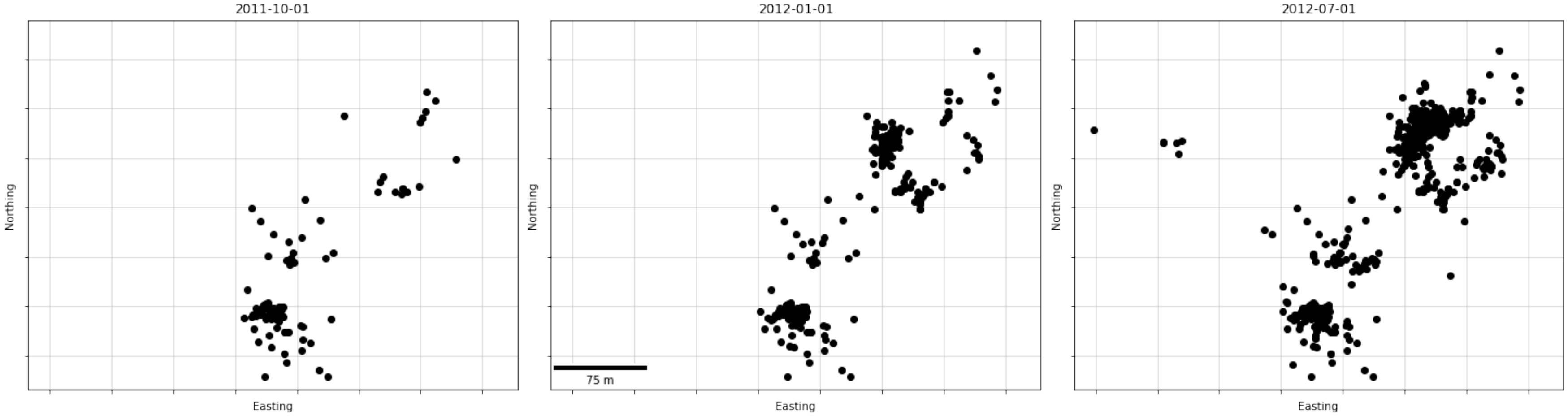

FIGURE 6.9. Development of microseismic events with respect to time at three time-lapses (2011-Oct-1, 2012-Jan-1 and 2012-Jul-1).

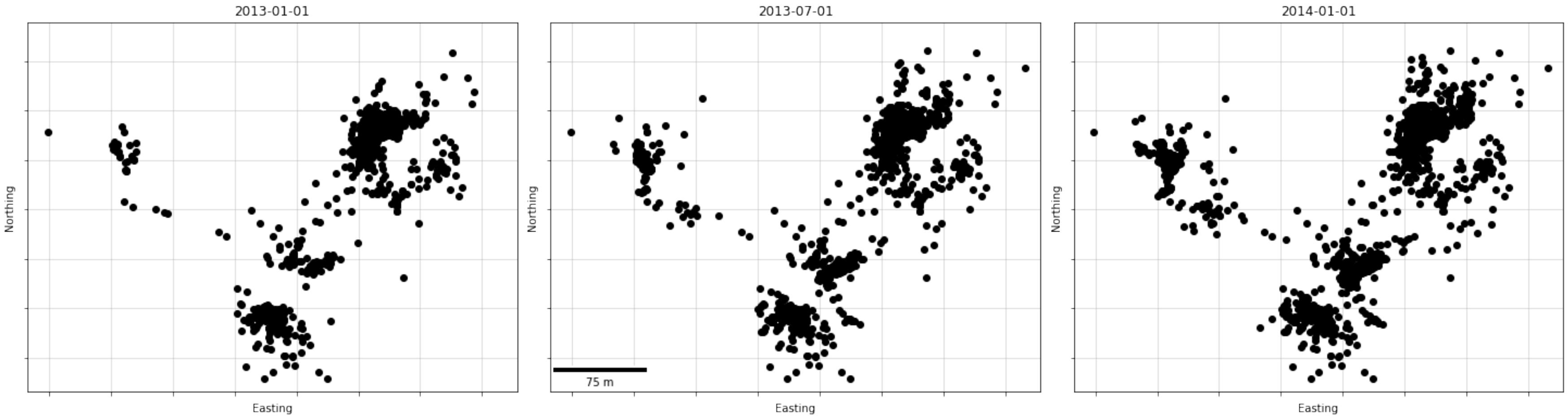

FIGURE 6.10. Development of microseismic events with respect to time at three time-lapses (2013-Jan-1, 2013-Jul-1 and 2014-Jan-1).

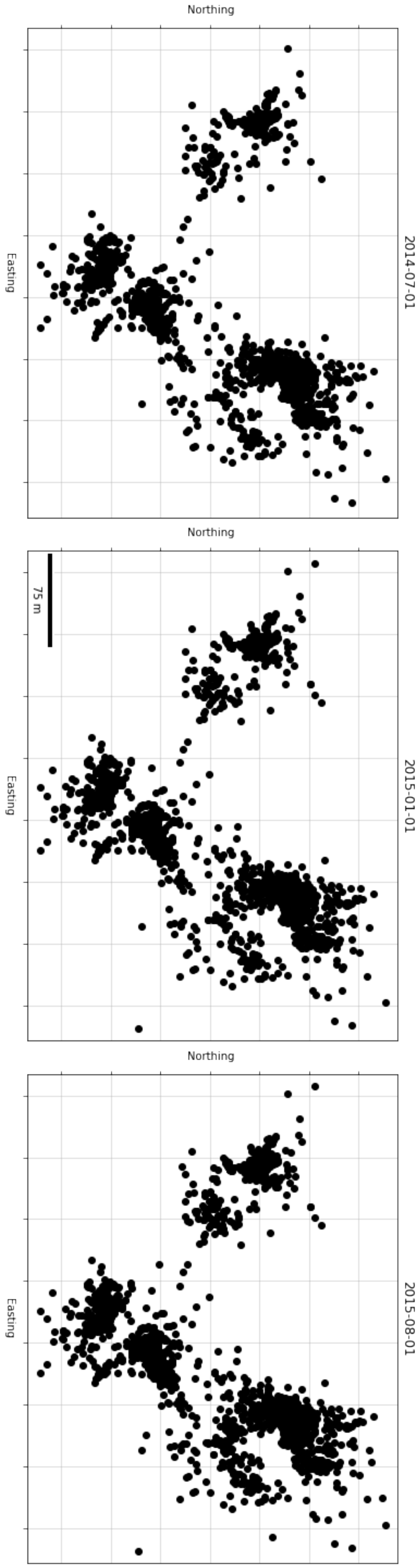

FIGURE 6.11. Development of microseismic events with respect to time at three time-lapses (2014-Jul-1, 2015-Jan-1 and 2015-Aug-1).

6.2 Seismicity correlation with surface surveillance data

Three different surface surveillance measurements are carried out at Field X. These measurements are GPS, optical leveling and InSAR. These measurements are made at different time lapses to find any changes in elevation above the reservoir related to steam injection and oil production.

InSAR is a tool to measure variation in ground attitude between a base and a repeat survey, in which a change in elevation has occurred (Rahmoune et al., 2021). The tool depends on satellite imaging of a large area of the Earth's surface. Satellites send electromagnetic radar signals to the Earth that reflect off the ground to produce an image of the Earth's topography. The interferogram is a map generated by differentiating measurements of SAR data acquired at different time lapses.

RADARSAT-2 satellite captured the InSar data. The radar C-band ground resolution is 5 m (fine beam mode) at horizontal transmitting and horizontal receiving polarization. The nominal incident angle of the collected images is 35○. The repeat orbit happens at 24 days period (Rahmoune et al., 2021).

Measurements of surface surveillance from optical leveling show that there is a slight uplift in the surface level where seismicity is at maximum level. For instance, Figure 6.12 shows that the highest uplift location is in agreement with the high seismic activity observed at those locations.

The same is true for InSAR measurements shown in Figure 6.13. I masked some parts of the figure with white color for confidentiality reasons. The maximum uplift, however, observed with InSAR data is 3 mm. At the northern side of Field X, a surface depression occurred due to production of water from shallow aquifers. The water from shallow aquifers is used for steam generation.

GPS data shows an elevation changes from November 2011 to November 2013 (Figure 6.14). The maximum positive change calculated from GPS data is 25 mm. The normalized injected volume of steam are plotted spatially with circles representing the amount of injected steam in each region of the reservoirs. Steam injection volume is maximum around the flank of the reservoirs. In contrary, the maximum steam expansion happens in the crest of the reservoir. This indicates that steam flows upward direction increasing pore pressure in the upper part of the reservoir. The event locations (black dots) overlie the GPS map. There is a good postive correlation between the uplift and the microseismic events.

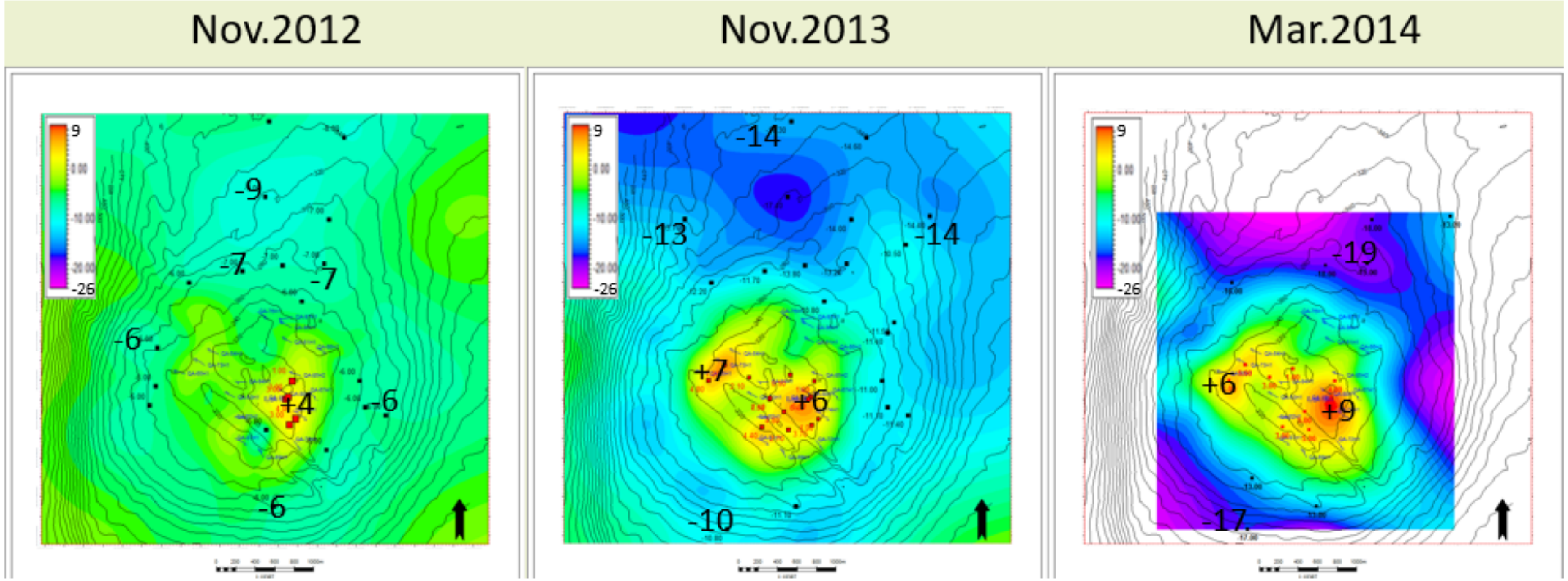

FIGURE 6.12. Optical leveling measurement at three different time periods. The measurements from different periods indicate an uplift of 9 mm observed at the same surface location where the seismic activity is at the highest level. Courtesy of PDO.

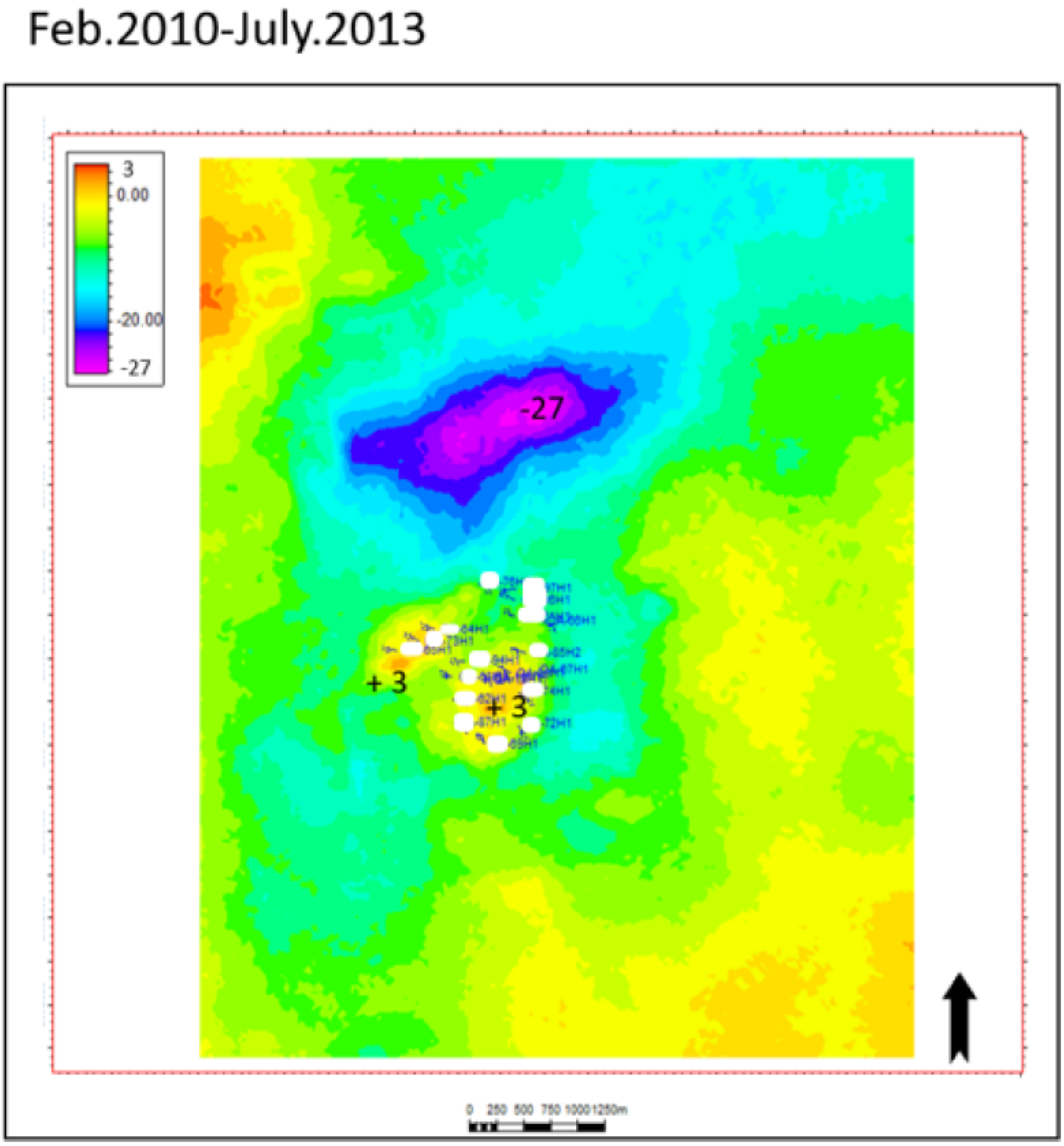

FIGURE 6.13. InSar data shows a slight uplift of 3 mm in the period from February 2010 to July 2013. In the northern area of Field X, a depression occurred due to excessive production of water from the brackish aquifer for steam generation. Well names are masked for confidentiality reasons. Courtesy of PDO.

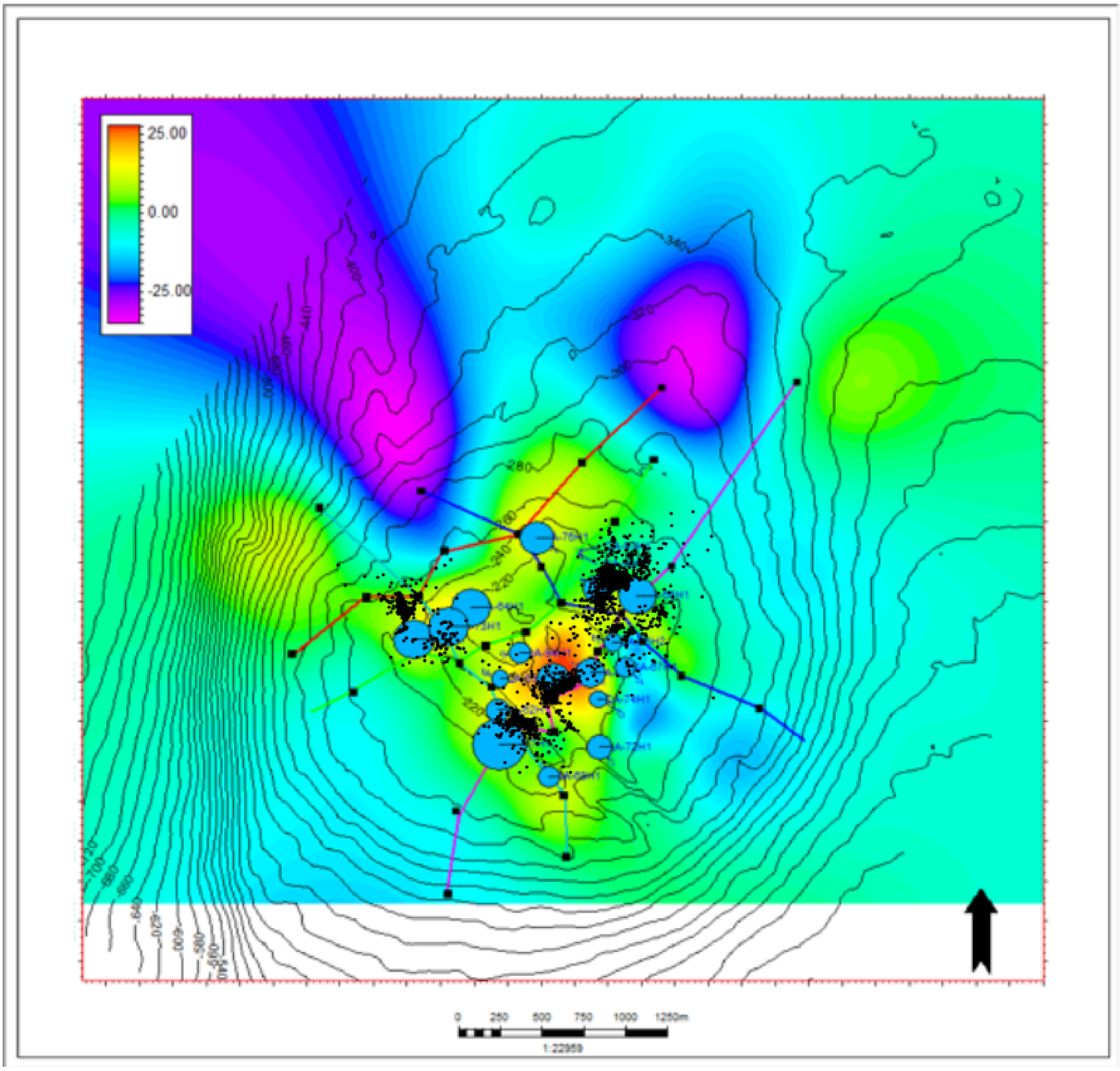

FIGURE 6.14. GPS elevation change between November 2011 to November 2013. The blue circles are normalized injected volume of steam around the flank and the crest of the reservoir. The black dots are the event locations. Courtesy of PDO.

6.3 Source parameters estimation

I calculated the moment magnitude of all the events. Figure 6.15 shows the variation of moment magnitude with respect to time. The mean value is about -1.7 (Figure 6.16), and the plot does not show abnormal values of the moment magnitude. The moment magnitude is calculated as

$$M_w = A \cdot \log_{10}(M_0) + B, \tag{6.3}$$

where A and B are constants, often taken as A =2/3 and B= -6. M_0 is the seismic moment and is calculated as,

$$M_{0_c} = \frac{4\pi\rho V_c^3 r \Omega_{0_c}}{F_c}, \tag{6.4}$$

where is ρ the density, V_c is the arrival velocity, r is the path length between source and receiver, and F_c is the arrival's average radiation coefficient. The radiation coefficient value for P- and S-wave is F_P = 0.52 and F_S = 0.63, respectively. Figure 6.17 shows a map distribution of the moment magnitudes. The map indicates a random spatial distribution of the moment magnitude without the concentration of high values at any specific region. Figure 6.18 shows a distance versus magnitude plot of microseismic events for a selected number of events around the well array [4, 8, 17]. This figure depicts the detectability limit of the microseismic array system. The minimum magnitude recorded by this array is about -1.9.

The estimated b-value is 2.3, which is an indication that the events are related to steam injection Figure 6.19. The b-value is the exponent in the Gutenberg-Richter power law relationship,

$$\log(N(m > M)) = a - bM, \tag{6.5}$$

which relates the number of earthquake N having magnitudes m greater than M. It indicates the number of occurrence of earthquakes of magnitude m in a certain region larger than a magnitude M. A small value might relate the occurrence of large magnitude events, whereas a large value associates with the occurence of small magnitude events in a particular tectonic area (Grob and van der Baan, 2011).

Schorlemmer et al. (2005) suggest that normal earthquakes happen in a region with a b-value grater than 1. A b-value close 1 happens at strike-slip zones, whereas b-value smaller than 1 occur in thrusting zones. Normal faulting is more common than other types of tectonic faults and thus the b-value associated with normal faulting regimes is large. Also, injection process opens up fracture in implosion or explosion manner, increasing the b-value.

The calculation of b-values requires selection of events similar rock failure mechanism, or else the reported value might not be accurate. Additionally, adequate number of events must be included into the calculation process to deem the b-value result valid.

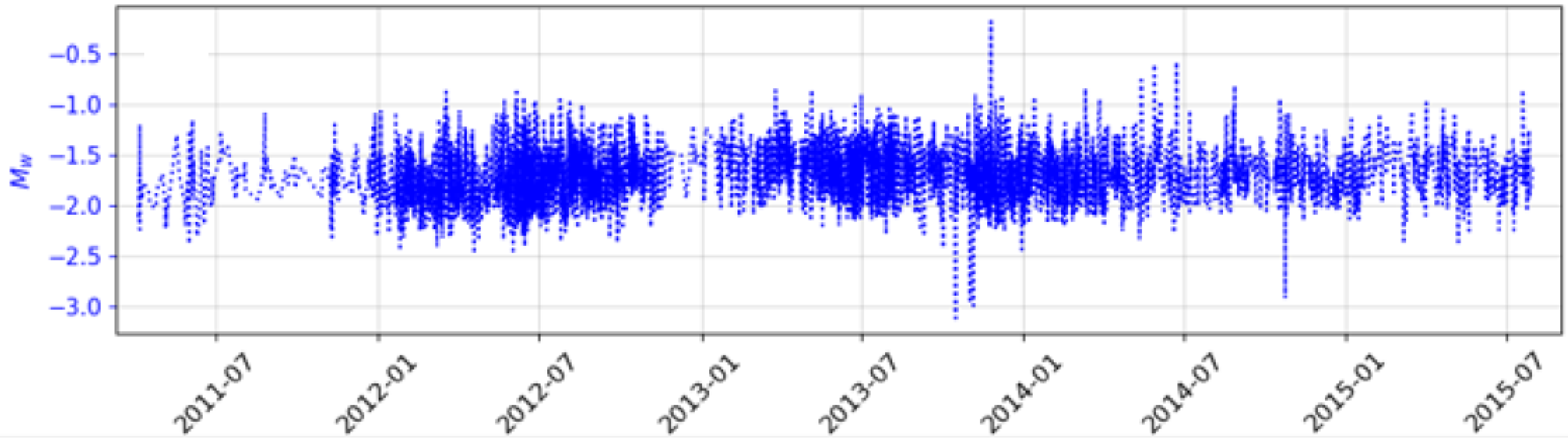

FIGURE 6.15. Mw values as a function of time.

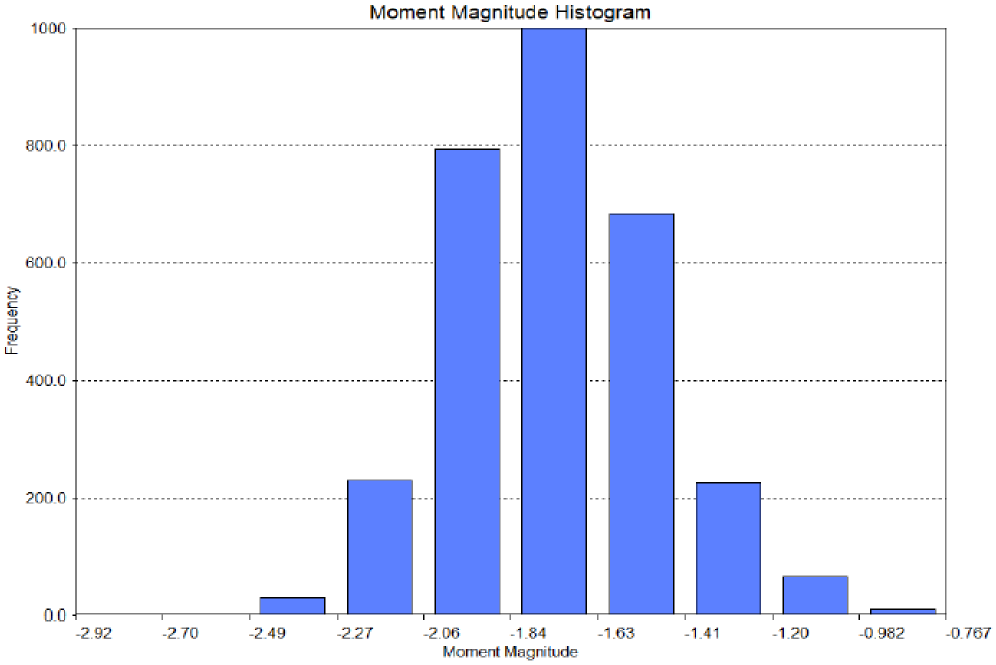

FIGURE 6.16. Moment magnitude histogram. The mean value is about -1.7.

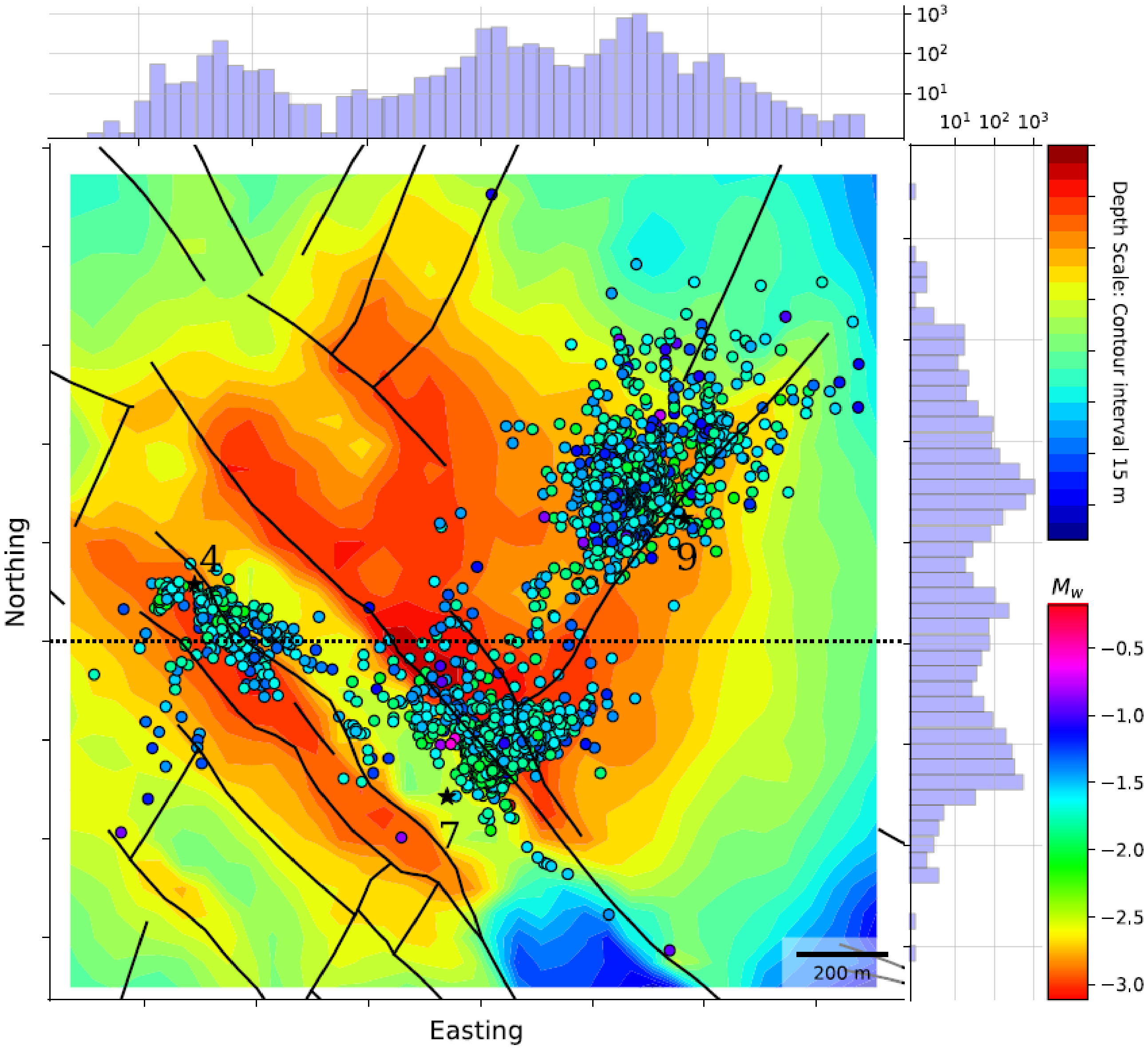

FIGURE 6.17. Moment magnitude spatial distribution. The black curves are fault surface trace. The surface map is the top reservoir horizon (Shuaiba).

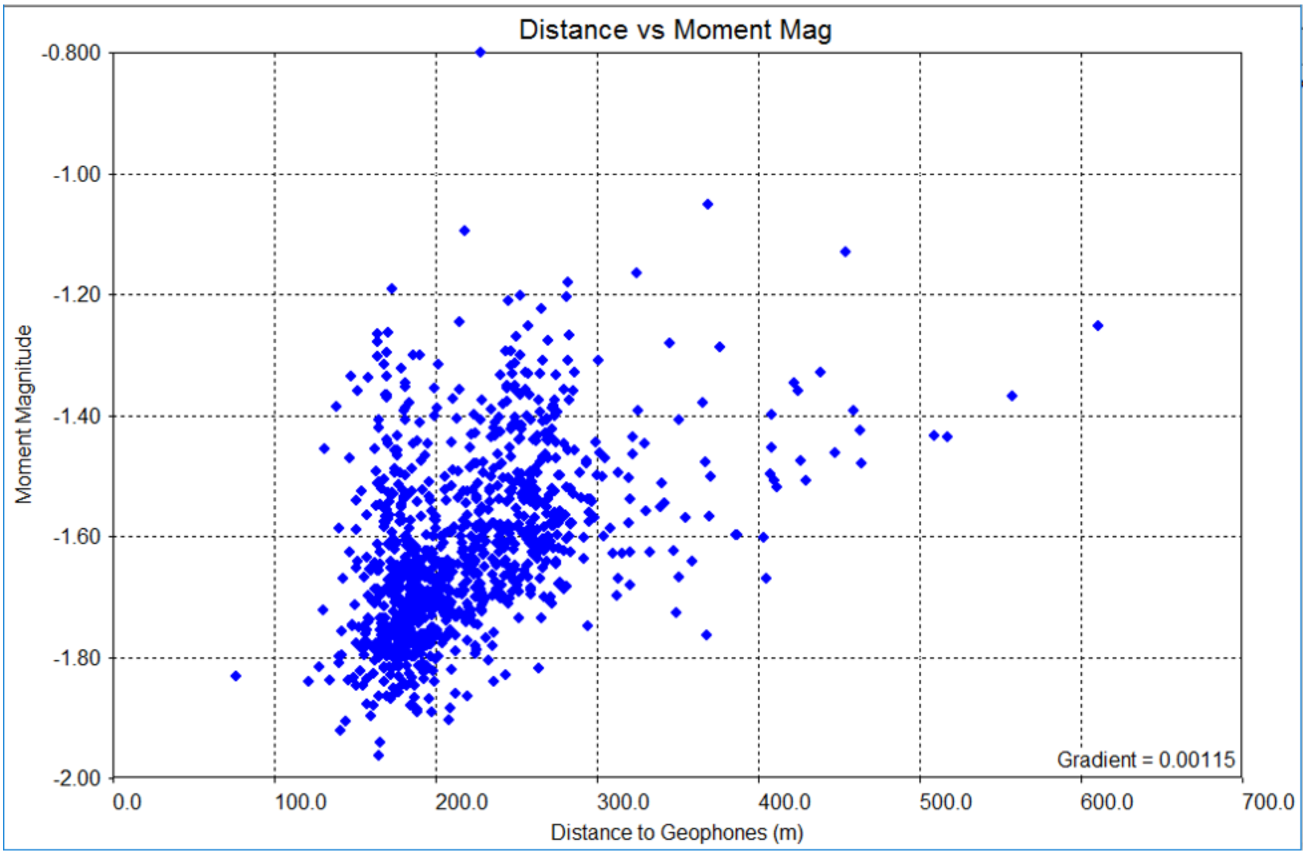

FIGURE 6.18. A plot of magnitude versus distance from the nearest geophones.

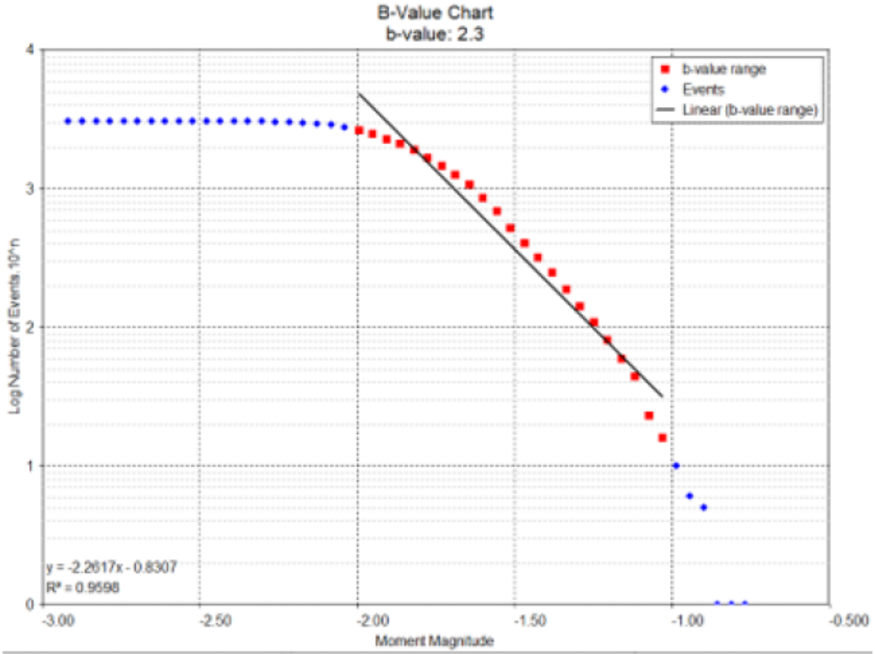

FIGURE 6.19. Calculation of b-value.

6.4 Reflection of results on Field X development

Seismicity activity is attributed to thermal expansion in the upper part of the reservoir units. The maximum stress release is due to the re-activation of preexisting faults or initiation of new fractures. Drilling must be avoided in highly active seismicity zones. Drilling wells in active seismic regions might put them at risk of well failures. Infill injection wells should target areas of low seismicity to heat up the rock and drain the oil out of the rock matrix into the fracture system.

TA-GOGD works by injecting steam in the flanks of the reservoir zones, but the maximum stress because of thermal expansion occurs at the crest of the reservoir units. Steam migrates from the low area flanks into the crest through the fracture network system. It is important to monitor the seismic activity for large events that might cause damage to surface facilities or subsurface wells and pipelines. Microseismic events also should not occur above the seal rock (Nahr Umr) since this will breach the seal integrity and cause the steam to leak into shallower rock layers. It is not feasible to precisely monitor the steam front using microseismic data. However, integration with other geological and petroleum engineering data will help make better decisions on maintaining the steam injection program sustainable and increasing the life span of Field X.

Shear wave splitting and moment tensor inversion results will be useful to quantify and assess TA-GOGD in a broader context. Moment tensor results can help isolate events based on their failure mechanism and provide more valid results for d- and b-values. Fracture orientation can be quantified with shear wave splitting analysis, and fracture direction and intensity can then be correlated with located microseismic events.

It is important to emphasize that risk management is the topmost priority in any oilfield development. Microseismic monitoring of Field X undergoing TA-GOGD will act as traffic light system when to continue, stop or further investigate the steam injection program based on event locations and magnitudes. Additionally, no seismic events are located above the seal rock indicating that no dilational faults are forming outside reservoir zone where the injection takes place.

CHAPTER 7

CONCLUSION AND RECOMMENDATIONS

7.1 Recommendations

The dataset in this project is huge and complex. The microseismic monitoring system covers a large area, and the system contains multiple wells continuously monitoring any seismic activity associated with injection and production activities in Field X. Data analyses and processing, therefore, will be a challenging task. The maximum utilization of microseismic data is accomplished when integrated with geological and engineering data. It is vital to correlate the microseismic results with the geology to consolidate the seismic interpretation.

The field operator must ensure the data collected in a low noisy environment. The contamination of microseismic data with noise can affect the true amplitude of the signal and thus makes the process of first break picking difficult. Also, noisy data can lower the accuracy of source parameter and moment tensor inversion results since they depend on the true amplitude of onset P-wave and S-wave arrivals. Therefore, microseismic data must be carefully processed, preserving the amplitudes.

The raw borehole microseismic data have their sensors orientation unknown. I recommend using more than one controlled source for the orientation determination process. The controlled sources should be from a different location, preferably one on the surface and another from the reservoir zone. Controlled sources from the reservoir zone can calibrate the velocity model.

Automatic travel time picking must be quality controlled with manual picking. Most errors in microseismic location come from either travel time table and/or velocity models. If time permits, it is a good practice to test various auto-picking and choose the one that best suits the dataset.

Earth is heterogeneous and is 3D in nature. Therefore, intuitively location algorithms that use 3D velocity models usually give location results with lower uncertainties. Locating microseismic data is computer-intensive work. It is recommended to use computers with multi-core and also use a location algorithm that is parallel (uses all available computer cores). I advise testing the location algorithm on a small subset of the dataset if the number of events is large or a large number of sensors detects them.

Finally, when interpreting the microseismic location results, integrate them with available geological observations. Characterize events development spatially and temporally to determine stress direction migration or fluid encroachment toward certain paths.

7.2 Future work

I would like to apply moment tensor inversion on the dataset to determine the failure mechanism and correlate that with the cause of microseismic energy radiation. This will differentiate events occurring from fault reactivation from fluid movement.

Shear wave splitting analysis will characterize fracture orientation and density. Correlating shear wave splitting results with microseismic events will clarify ambiguities related to fracture clustering alignment in preferential directions.

Correlating microseismic locations results with changes in reservoir pressure from well testing can answer questions related to an increase or decrease in seismic activity with respect to time and space. I also advise correlating microseismic results with injection and production data. We presume that seismicity is related to the volume of steam injected into the reservoir or the amount of hydrocarbon is pumped. Anomalous seismicity therefore, can easily be distinguished.

I would also want to perform a geomechanical analysis of the microseismic data. This requires input from engineering aspects, particularly pressure and lab studies on core data.

7.3 Assessment of microseismic monitoring for TA-GOGD

TA-GOGD proved a viable option for the development of a carbonate reservoir undergoing steam injection. Various concerns arise when using this EOR method for field development. Among many concerns, seismic activity presents a great risk to the field surface and subsurface infrastructure. It is vital that the field operator monitor TA-GOGD program using microseismic and surface surveillance measurements. Long term success of the program depends on continuous injection of steam in the reservoir zones. Large magnitude events will create or re-activate preexisting faults that can damage field infrastructure. The field operator must maintain the seismic activity and the associated magnitude below an acceptable threshold.

It is also important to map microseismic locations and understand how they develop spatially and temporally and correlate them with other geological data. Faults activation should not breach the seal rock, and the fractures should be constrained in the reservoir zones where the steam is injected to create more fractures that are the key to the success of TA-GOGD program.

7.4 Summary

In this thesis, I analyzed microseismic data to characterize an oilfield in Oman undergoing TA-GOGD. A total of about 7200 microseismic events were recorded from the period April 2011 to August 2015. Field X is made up of high porosity, low permeability carbonate rocks containing heavy oil. The objective is to understand the causes of seismicity during a prolonged period of steam injection and manage Field X operation based on the outcome of fracture development of fault reactivation.

In Chapter One, I gave an overview of the microseismic method and its application in various industries. The microseismic method has recently seen an increase in use, and many different types of oilfields in Oman use the microseismic technique for better field development. TA-GOGD is a process in which steam is injected in the fractured reservoir containing heavy oil to decrease its viscosity and increase the oilfield recovery factor. The Oman microseismic data consist of 13 monitoring wells; each is equipped with eight three-component geophones.

Chapter two describes the tectonic and geologic framework of Northen Oman with an emphasis on the hydrocarbon-bearing formation of Shuaiba and Kharaib. The structural elements of the oilfield in North Oman are dominated by NW-SE and NE-SE trending faults. Fractures mapped by formation image logs indicate a dominant orientation of NE-SW, parallel to the maximum principal stress direction. Deep-seated salt diapirs influenced the shape of Field X, which a domal shape elongated NE-SW.

In Chapter Three, I discussed two important microcosmic pre-processing steps: geophone orientation determination and noise filtering. The provided data are raw data, in which geophone components orientation is unknown. The accurate determination of geophone orientation is crucial to obtain reliable microseismic location results. I developed a new technique based on RMS amplitude maximization of the P-wave. This technique is compared with other established methods to assess its validity. Having eight vibrators shot acquired per microseismic motioning well enabled statistical assessment of the newly developed method. The computational performance of the new development method is on a bar with DiSiena et al. (1984) but butter than other tested methods. The microseismic wells which provide the lowest variance in orientation measurements from different vibrators are MSW-4, 5, 7, 8, and 9. The existence of dead or unserviceable geophones lowered the variance value for other wells. The microseismic continuous monitoring program is conducted in an active field; thus, the data are highly contaminated with various noise levels, but monochromatic frequency noises are dominant, and they randomly happen at different frequency values. However, the powerline noise at 50 Hz is almost always apparent in seismograms. I developed an adaptive notch filter, which removes the monochromatic noises without the need to specify the notch value(s). The SNR increased by 25-35% after applying both the adaptive notch filter and a bandpass filter having corner frequencies 40 and 500 Hz.

In Chapter Four, I perform automatic first arrival picking of P- and S-wave. I tested the classic STA/LTA, recursive STA/LTA, Kurtosis, transient energy ratio, and AIC method. seg-y data appear to have multiple events, but they are provided as triggered events. This made the auto-picking method quite difficult to obtain the true arrival time. However, for seg-y files having a clear event, most of the methods performed well, but AIC and Kurtosis techniques provided arrival time pick with lower residual to the manual picking. Nevertheless, I found that inspecting each event one by one is necessary to correct any wrong picked arrival times.

Chapter Five discusses the location algorithms used in this project. I tested six different techniques. They are the Geiger, Simplex, Tian ray tracing, wavefront construction, BUMPS software, and Fast sweeping method. The last one gives location results that are geologically reasonable compared to other methods.

In Chapter Six, the located events using the FSM gives rise to events clusterings that are in good alignment with preexisting faults. They show two main orientations NW-SE and NE-SW, consistent with the major fault system in Field X. Surface deformation measurements using Insar, optical leveling, and GPS, show an uplift at the surface exactly above the location of the maximum seismicity. Moment magnitudes show no upward trend in measurement through time. The average value is about -1.7.

REFERENCES

Ahmed, U. and Meehan, D. N. (2016). *Unconventional oil and gas resources : exploitation and development*. CRC Press.

Aki, K. and Richards, P. G. (1980). *Quantitative seismology*, volume II. University Science Books.

Akram, J. (2014). *Downhole microseismic monitoring: processing, algorithms and error analysis*. PhD thesis, University of Calgary.

Al-Anboori, A. S. (2005). *Anisotropy, focal mechanisms, and state of stress in an oilfield: passive seismic monitoring in Oman*. PhD thesis, University of Leeds.

Al-Awar, A. A. and Humphery, J. D. (2012). Diagenesis Of The Aptian Shuaiba Formation At Ghaba North Field, Oman. In *Middle East Models of Jurassic/Cretaceous Carbonate System*, pages 173–184. SEPM (Society for Sedimentary Geology).

Al-Dabbas, M. A., Al-Jassim, J. A., and Qaradaghi, A. I. (2013). Siliciclastic deposit of the Nahr Umr Formation, sedimentological and depositional environment studies, central and southern Iraq. *Arabian Journal of Geosciences*, 6(12):4771–4783.

Al-Hadhrami, H. S. and Blunt, M. J. (2001). Thermally Induced Wettability Alteration To Improve Oil Recovery in Fractured Reservoirs. *SPE Reservoir Evaluation & Engineering*, 4(03):179–186.

Al-Harrasi, O., Kendall, J.-M., and Chapman, M. (2011). Fracture characterization using frequency-dependent shear wave anisotropy analysis of microseismic data. *Geophysical Journal International*, 185(2):1059–1070.

Al-Harrasi, O. H. (2010). *Fractured reservoir characterisation using shear-wave splitting in microseismic data: a case study from Oman*. PhD thesis, University of Bristol.

Al Hooti, K., Kendall, M., Al Harrasi, O., Al Azri, S., Al Siyabi, Q., and Verdon, J. (2019). Microseismic Monitoring of Thermally Assisted Gas Oil Gravity Drainage in a Heavy Oil Field in Oman. In *81st EAGE Conference and Exhibition 2019*. EAGE Publications BV.

Al-Kindi, M. (2006). *Structural evolution and fracture pattern of Salakh Arch*. PhD thesis, University of Leeds.

Al-Kindi, M. H. and Richard, P. D. (2014). The main structural styles of the hydrocarbon reservoirs in Oman. *Geological Society, London, Special Publications*, 392(1):409–445.

AL-Muftah, A., Hameed, M., and Mansoor, M. (2019). Reservoir Optimization and Monitoring Challenges in Nahr Umr Reservoirs of Bahrain Field.

Al-Salmi, M., John, C. M., and Hawie, N. (2019). Quantitative controls on the regional geometries and heterogeneities of the Rayda to Shu'aiba formations (Northern Oman) using forward stratigraphic modelling. *Marine and Petroleum Geology*, 99:45–60.

Al-Siyabi, H. A. (2005). Exploration history of the Ara intrasalt carbonate stringers in the South Oman Salt Basin. *GeoArabia*, 10(4):39–72.

Aleardi, M. (2015). Seismic velocity estimation from well log data with genetic algorithms in comparison to neural networks and multilinear approaches. *Journal of Applied Geophysics*, 117:13–22.

Ali, S. (2003). Heavy oil—evermore mobile. *Journal of Petroleum Science and Engineering*, 37(1):5–9. Heavy Oil Recovery: Special issue dedicated to Professor S.M. Farouq Ali on his 65th birthday.

Allen, R. V. (1978). Automatic earthquake recognition and timing from single traces. *Bulletin of the Seismological Society of America*, 68(5):1521–1532.

Alsharham, A. S. (1985). Depositional environment, reservoir units evolution, and hydrocarbon habitat of Shuaiba formation, Lower Cretaceous, Abu Dhabi, United Arab Emirates. *Am. Assoc. Pet. Geol., Bull.*

Alsharhan, A. S. (1991). Sedimentological interpretation of the Albian Nahr Umr Formation in the United Arab Emirates. *Sedimentary Geology*, 73(3-4):317–327.

Amoroso, O., Maercklin, N., and Zollo, A. (2012). S-wave identification by polarization filtering and waveform coherence analyses. *Bulletin of the Seismological Society of America*, 102(2):854–861.

Anant, K. S. and Dowla, F. U. (1997). Wavelet transform methods for phase identification in three-component seismograms. *Bulletin of the Seismological Society of America*, 87(6):1598–1612.

Anderson, D. L., Minster, B., and Cole, D. (1974). The effect of oriented cracks on seismic velocities. *Journal of Geophysical Research*, 79(26):4011–4015.

Arthur, M. A. and Cole, D. R. (2014). Unconventional hydrocarbon resources: Prospects and problems. *Elements*, 10(4):257–264.

Ayres, A. and Theilen, F. (1999). Relationship between P-and S-wave velocities and geological properties of near-surface sediments of the continental slope of the Barents Sea. *Geophysical prospecting*, 47(4):431–441.

Baillard, C., Crawford, W. C., Ballu, V., Hibert, C., and Mangeney, A. (2013). An automatic kurtosis-based P-and S-phase picker designed for local seismic networks. *Bulletin of the Seismological Society of America*, 104(1):394–409.

Baird, A. F., Kendall, J. M., Fisher, Q. J., and Budge, J. (2017). The role of texture, cracks, and fractures in highly anisotropic shales. *Journal of Geophysical Research: Solid Earth*, 122(12):10–341.

Bataille, K. and Chiu, J. M. (1991). Polarization analysis of high-frequency, three-component seismic data. *Bulletin - Seismological Society of America*, 81(2):622–642.

Bertotti, G., Immenhauser, A., and Taal-van Koppen, J. K. J. (2005). Stratigraphic and regional distribution of fractures in Barremian-Aptian carbonate rocks of Eastern Oman: Outcrop data and their extrapolation to Interior Oman hydrocarbon reservoirs. *International Journal of Earth Sciences*, 94(3):447–461.

Bland, H. C. and Hogan, C. (2005). A hypocentre location method for microseismicity in complex regions. Technical report, CREWES Research Report 17.

Boadu, F. K. and Long, L. T. (1996). Effects of fractures on seismic-wave velocity and attenuation. *Geophysical Journal International*, 127(1):86–110.

Boggs, P. T., Byrd, R. H., and Schnabel, R. B. (1987). A stable and efficient algorithm for nonlinear orthogonal distance regression. *SIAM Journal on Scientific and Statistical Computing*, 8(6):1052–1078.

Boggs, P. T., Donaldson, J. R., Schnabel, R. B., and Others (1989). Algorithm 676: ODRPACK: software for weighted orthogonal distance regression. *ACM Transactions on Mathematical Software (TOMS)*, 15(4):348–364.

Bohling, G. (2005). Introduction to geostatistics and variogram analysis. *Kansas geological survey*, 1:1–20.

Bommer, J. J., Oates, S., Cepeda, J. M., Lindholm, C., Bird, J., Torres, R., Marroquín, G., and Rivas, J. (2006). Control of hazard due to seismicity induced by a hot fractured rock geothermal project. *Engineering Geology*, 83(4):287–306.

Born, M. and Wolf, E. (1999). Electromagnetic potentials and polarization. *Principles of Optics*, page 71.

Boschetti, F., Dentith, M. D., and List, R. D. (1996). A fractal-based algorithm for detecting first arrivals on seismic traces. *Geophysics*, 61(4):1095–1102.

Braakman, J. H., Levell, B. K., Martin, J. H., Potter, T. L., and van Vliet, A. (1982). Late Palaeozoic Gondwana glaciation in Oman. *Nature*, 299(5878):48–50.

Briggs, P. J., Baron, P., Fulleylove, R. J., Wright, M. S., et al. (1988). Development of heavy-oil reservoirs. *Journal of petroleum technology*, 40(02):206–214.

Chen, C. and Holland, A. A. (2016). PhasePApy: A robust pure Python package for automatic identification of seismic phases. *Seismological Research Letters*, 87(6):1384–1396.

Chen, Z., Fan, Y., Huang, R., Zeng, B., Walsh, R., Zhou, X., Zoback, M., and Song, Y. (2019). Case study: fault slip induced by hydraulic fracturing and risk assessment of casing deformation in the sichuan basin. In *SPE/AAPG/SEG Asia Pacific Unconventional Resources Technology Conference*. OnePetro.

Chow, T. M. (1992). *Concurrent ultrasonic tomography and acoustic emission in solid materials.* PhD thesis, Department of Geological Sciences, Queen's University, Kingston.

Cipolla, C. L., Mack, M. G., Maxwell, S. C., and Downie, R. C. (2011). A Practical Guide to Interpreting Microseismic Measurements. In *North American Unconventional Gas Conference and Exhibition*. Society of Petroleum Engineers.

Claringbould, J. S., Hyden, B. B., Sarg, J. F., and Trudgill, B. D. (2013). Structural evolution of a salt-cored, domed, reactivated fault complex, Jebel Madar, Oman. *Journal of Structural Geology*, 51:118–131.

Clarke, M. W. (1988). Stratigraphy and Rock Unit Nomenclature in the Oil-Producing Area of Interior Oman. *Journal of Petroleum Geology*, 11(1):5–60.

Cox, M. (1999). *Static corrections for seismic reflection surveys*. Society of Exploration Geophysicists.

Cressie, N. (1990). The origins of kriging. *Mathematical geology*, 22(3):239–252.

Crowell, J. C. (1995). The Ending of the Late Paleozoic Ice Age During the Permian Period. In *The Permian of Northern Pangea*, pages 62–74. Springer Berlin Heidelberg.

Curtis, J. B. (2002). Fractured shale-gas systems. *AAPG bulletin*, 86(11):1921–1938.

Daley, T. M., McEvilly, T. V., and Majer, E. L. (1988). Analysis of P and S wave vertical seismic profile data from the Salton Sea Scientific Drilling Project. *Journal of Geophysical Research*, 93(B11):13025–13036.

Daubechies, I. (1992). *Ten lectures on wavelets. CBMS–NSF lecture notes nr. 61*. SIAM.

De, A., Silin, D. B., and Patzek, T. W. (2000). Waterflood Surveillance and Supervisory Control. In *SPE/DOE Improved Oil Recovery Symposium*. Society of Petroleum Engineers.

De Campos, V. P., Sansone, E. C., and E Silva, G. F. (2018). Hydraulic fracturing proppants. *Ceramica*, 64(370):219–229.

De Keijzer, M., Hillgartner, H., Al Dhahab, S., and Rawnsley, K. (2007). A surface-subsurface study of reservoir-scale fracture heterogeneities in Cretaceous carbonates, North Oman. *Geological Society Special Publication*, 270:227–244.

De Meersman, K., Kendall, J.-M., and Van der Baan, M. (2009). The 1998 valhall microseismic data set: An integrated study of relocated sources, seismic multiplets, and s-wave splitting. *Geophysics*, 74(5):B183–B195.

Deif, A., El-Hussain, I., Al-Jabri, K., Toksoz, N., El-Hady, S., Al-Hashmi, S., Al-Toubi, K., Al-Shijbi, Y., and Al-Saifi, M. (2013). Deterministic seismic hazard assessment for Sultanate of Oman. *Arabian Journal of Geosciences*, 6(12):4947–4960.

Diao, R., Shang, X. M., Xu, H., Sui, Z. Q., and Liu, L. P. (2015). The method of two-step static correction in surface micro-seismic. In *77th EAGE Conference and Exhibition 2015: Earth Science for Energy and Environment*, pages 1826–1830. European Association of Geoscientists and Engineers, EAGE.

Dimitrakopoulos, R. and Luo, X. (2004). Generalized sequential gaussian simulation on group size v and screen-effect approximations for large field simulations. *Mathematical Geology*, 36(5):567–591.

DiSiena, J. P., Gaiser, J. E., Corrigan, D., and Toksöz, M. N. (1984). Horizontal components and shear wave analysis of three-component VSP data. *Vertical Seismic Profiling, Part B: Advanced Concepts edited by M. Nafi Toksoz and Robert R. Stewart*.

Downie, R., Kronenberger, E., and Maxwell, S. C. (2010). Using Microseismic Source Parameters To Evaluate the Influence of Faults on Fracture Treatments: A Geophysical Approach to Interpretation. In *SPE Annual Technical Conference and Exhibition*. Society of Petroleum Engineers.

Dreher, K., Kenyon, D., and Iwere, F. (1986). Heat Flow During Steam Injection Into a Fractured Carbonate Reservoir. In *SPE Enhanced Oil Recovery Symposium*. Society of Petroleum Engineers.

Droste, H. H. J. (1997). Stratigraphy of the lower Paleozoic Haima Supergroup of Oman. *GeoArabia*, 2(4):419–472.

Droste, H. J. (2010). Sequence-stratigraphic framework of the Aptian Shu'aiba Formation in the Sultanate of Oman. *GeoArabia Special Publication 4*, 1:229–283.

Du, P., Kibbe, W. A., and Lin, S. M. (2006). Improved peak detection in mass spectrum by incorporating continuous wavelet transform-based pattern matching. *Bioinformatics*, 22(17):2059–2065.

Duhault, J. L. J., Eaton, D. W., and Pedersen, P. K. (2018). Microseismic Monitoring of a Tight Light Oil Reservoir: A Case History in the Cardium Halo Play, Alberta. *Interpretation*, pages 1–35.

Duncan, P. M. and Eisner, L. (2010). Reservoir characterization using surface microseismic monitoring. *Geophysics*, 75(5).

Earle, P. S. and Shearer, P. M. (1994). Characterization of global seismograms using an automatic-picking algorithm. *Bulletin of the Seismological Society of America*, 84(2):366–376.

Eberhart-Phillips, D., Han, D. H., and Zoback, M. D. (1989). Empirical relationships among seismic velocity, effective pressure, porosity, and clay content in sandstone. *Geophysics*, 54(1):82–89.

Ehrenberg, S. N., Morad, S., Yaxin, L., and Chen, R. (2016). Stylolites and Porosity In A Lower Cretaceous Limestone Reservoir, Onshore Abu Dhabi, U.A.E. *Journal of Sedimentary Research*, 86(10):1228–1247.

Ehrenberg, S. N. and Wu, Q. (2019). Dense Zones of the Kharaib Formation (Lower Cretaceous), United Arab Emirates. *Journal of Sedimentary Research*, 89(4):353–380.

El-Hussain, I., Deif, A., Al-Jabri, K., Toksoz, N., El-Hady, S., Al-Hashmi, S., Al-Toubi, K., Al-Shijbi, Y., Al-Saifi, M., and Kuleli, S. (2012). Probabilistic seismic hazard maps for the sultanate of Oman. *Natural Hazards*, 64(1):173–210.

Eyre, T. S. and van der Baan, M. (2017). The reliability of microseismic moment-tensor solutions: Surface versus borehole monitoring. *Geophysics*, 82(6):KS113–KS125.

Fabien-Ouellet, G. and Sarkar, R. (2020). Seismic velocity estimation: A deep recurrent neural-network approach. *Geophysics*, 85(1):U21–U29.

Fair, D., Scott, G. R., Boone, T. J., Speirs, B. C., Trudell, C. L., et al. (2008). Cold lake heavy oil development-a success story in technology application. In *International Petroleum Technology Conference*. International Petroleum Technology Conference.

Falls, S. (1993). *Ultrasonic imaging and acoustic emission studies of microcrack development in Lac du Bonnet Grey granite*. PhD thesis, Department of Geological Sciences, Queen's University, Kingston.

Falls, S. D. (1995). Ultrasonic imaging and acoustic emission studies of microcrack development in lac du bonnet granite.

Filbrandt, J. B., Al-dhahab, S., Al-habsy, A., Harris, K., Keating, J., Al-mahruqi, S., Ozkaya, S. I., and Richard, P. D. (2006). Kinematic interpretation and structural evolution of North Oman, Block 6, since the Late Cretaceous and implications for timing of hydrocarbon migration into Cretaceous reservoirs. *GeoArabia*, 11(1):97–115.

Flinn, E. A. (1965). Signal Analysis Using Rectilinearity and Direction of Particle Motion. *Proceedings of the IEEE*, 53(12):1874–1876.

Forgues, E., Schisselé, E., and Cotton, J. (2011). Simultaneous active and passive seismic monitoring of steam-assisted heavy oil production. *The Leading Edge*, 30(11):1288–1294.

Freeman, R. F. M. E. D. A. P. A. (2007). Heavy Oil and Natural Bitumen Resources in Geological Basins of the World. Technical report, USGS Open File-Report 2007–1084.

Frost, S. H., Bliefnick, D. M., and Harris, P. M. (1983). Deposition and Porosity Evolution of a Lower Cretaceous Rudist Buildup, Shuaiba Formation of Eastern Arabian Peninsula.

Gaiser, J. and Strudley, A. (2005). Acquisition and application of multicomponent vector wavefields: are they practical? *First Break*, 23(1084).

Ge, M. (2005). Efficient mine microseismic monitoring. *International Journal of Coal Geology*, 64(1-2):44–56.

Geiger, L. (1912). Probability method for the determination of earthquake epicenters from the arrival time only. *Bull. St. Louis Univ*, 8(1):56–71.

Ghosh, G. and Sivakumar, C. (2018). Application of underground microseismic monitoring for ground failure and secure longwall coal mining operation: a case study in an indian mine. *Journal of Applied Geophysics*, 150:21–39.

Glegola, M., Ditmar, P., Vossepoel, F., Arts, R., Al-Kindy, F., and Klees, R. (2015). Gravimetric monitoring of the first field-wide steam injection in a fractured carbonate field in oman–a feasibility study. *Geophysical Prospecting*, 63(5):1256–1271.

Grantham, P. J. (1986). The occurence of unusual C27 and C29 sterane predominances in two types of Oman crude oil. *Organic Geochemistry*, 9(1):1–10.

Grantham, P. J., Lijmbach, G. W. M., and Posthuma, J. (1990). Geochemistry of crude oils in Oman. *Geological Society Special Publication*, 50(50):317–328.

Grassberger, P. and Procaccia, I. (2004). Measuring the strangeness of strange attractors. In *The Theory of Chaotic Attractors*, pages 170–189. Springer.

Greenhalgh, S. A. and Mason, I. M. (1995). Orientation of a downhole triaxial geophone. *Geophysics*, 60(4):1234–1237.

Grob, M. and van der Baan, M. (2011). Inferring in-situ stress changes by statistical analysis of microseismic event characteristics. *The Leading Edge*, 30(11):1296–1301.

Grosjean, E., Love, G. D., Kelly, A. E., Taylor, P. N., and Summons, R. E. (2012). Geochemical evidence for an Early Cambrian origin of the 'Q' oils and some condensates from north Oman. *Organic Geochemistry*, 45:77–90.

Guevara, S. E. and Stewart, R. R. (1998). Multicomponent seismic polarization analysis. *CREWES Research Report*, 10:1–19.

Guglielmi, Y., Cappa, F., Avouac, J. P., Henry, P., and Elsworth, D. (2015). Seismicity triggered by fluid injection-induced aseismic slip. *Science*, 348(6240):1224–1226.

Guo, K., Li, H., and Yu, Z. (2016). In-situ heavy and extra-heavy oil recovery: A review. *Fuel*, 185:886–902.

Haan, E. A., Corbin, S. G., Hughes Clarke, M. W., and Mabillard, J. E. (2008). The Lower Kahmah Group of Oman: the carbonate fill of a marginal shelf basin. *Geological Society, London, Special Publications*, 49(1):109–125.

Hansman, R. J. and Ring, U. (2018). Jabal Hafit anticline (UAE and Oman) formed by décollement folding followed by trishear fault-propagation folding. *Journal of Structural Geology*, 117:168–185.

Hardage, B. A., DeAngelo, M. V., Murray, P. E., and Sava, D. (2011). *Multicomponent Seismic Technology*. Society of Exploration Geophysicists.

Havskov, J. and Ottemoller, L. (2010). *Routine data processing in earthquake seismology: With sample data, exercises and software*. Springer.

Heap, M. J., Baud, P., Reuschlé, T., and Meredith, P. G. (2014). Stylolites in limestones: Barriers to fluid flow? *Geology*, 42(1):51–54.

Hearn, S. and Hendrick, N. (1999). A review of single-station time-domain polarisation analysis techniques. *Journal of Seismic Exploration*, 8(2):181–202.

Hein, F. J. (2006). Heavy oil and oil (tar) sands in North America: An overview & summary of contributions. *Natural Resources Research*, 15(2):67–84.

Hendrick, N. and Hearn, S. (1999). Polarisation analysis: What is it? why do you need it? how do you do it? *Exploration Geophysics*, 30(4):177–190.

Hente, B., Gommlich, G., and Flach, D. (1984). Microseismic monitoring of candidate nuclear waste disposal sites. *Series on Rock and Soil Mechanics*, pages 393–401.

Höcker, C. and Fehmers, G. (2002). Fast structural interpretation with structure-oriented filtering. *The Leading Edge*, 21(3):238–243.

Holland, A. A. (2013). Earthquakes triggered by hydraulic fracturing in south-central Oklahoma. *Bulletin of the Seismological Society of America*, 103(3):1784–1792.

Husseini, M. I. and Husseini, S. I. (1990). Origin of the Infracambrian Salt Basins of the Middle East. *Geological Society, London, Special Publications*.

Iooss, B. (1998). Seismic reflection traveltimes in two-dimensional statistically anisotropic random media. *Geophysical Journal International*, 135(3):999–1010.

Iturrarán-Viveros, U., Muñoz-García, A. M., Castillo-Reyes, O., and Shukla, K. (2021). Machine learning as a seismic prior velocity model building method for full-waveform inversion: A case study from colombia. *Pure and Applied Geophysics*, 178(2):423–448.

Jackson, G. M., Mason, I. M., and Greenhalgh, S. A. (1991). Principal component transforms of triaxial recordings by singular value decomposition. *Geophysics*, 56(4):528–533.

Jenkins, W. and Nayeri, M. (1986). Adaptive filters realized with second order sections. In *ICASSP '86. IEEE International Conference on Acoustics, Speech, and Signal Processing*, volume 11, pages 2103–2106.

Jennings, A. R. (1996). Fracturing Fluids - Then and Now. *Journal of Petroleum Technology*, 48(07):604–610.

Jeong, J., Al-Ali, A. A., Jung, H., Abdelrahman, A., Dhafra, A., Shebl, H. T., Kang, J., Bonin, A., de Perriere, M. D., and Foote, A. (2017). Controls on Reservoir Quality and Reservoir Architecture of Early Cretaceous carbonates in an Abu Dhabi Onshore Field Lekhwair, Kharaib and Lower Shuaiba Formations. In *Abu Dhabi International Petroleum Exhibition & Conference*. Society of Petroleum Engineers.

Jepsen, D. C. and Kennett, B. L. (1991). Three-component analysis of regional seismograms. *Bulletin - Seismological Society of America*, 80(6 B):2032–2052.

Jiang, F.-X., Yang, S.-H., Cheng, Y.-H., Zhang, X.-M., Mao, Z., and Xu, F. (2006). A study on microseismic monitoring of rock burst in coal mine. *Diqiu Wuli Xuebao*, 49.

Jiao, L. and Moon, W. M. (2000). Detection of seismic refraction signals using a variance fractal dimension technique. *Geophysics*, 65(1):286–292.

Jones, G. A., Kendall, J.-M., Bastow, I. D., and Raymer, D. G. (2014). Locating microseismic events using borehole data. *Geophysical Prospecting*, 62(1):34–49.

Jones, G. A., Raymer, D., Chambers, K., and Kendall, J. M. (2010). Improved microseismic event location by inclusion of a priori dip particle motion: A case study from Ekofisk. *Geophysical Prospecting*, 58(5):727–737.

Joshi, Y. V. and Dutta Roy, S. C. (1997). Design of IIR digital notch filters. *Circuits, Systems, and Signal Processing*, 16(4):415–427.

Journel, A. G. (1974). Geostatistics for conditional simulation of ore bodies. *Economic Geology*, 69(5):673–687.

Jurkevics, A. (1988). Polarization analysis of three-component array data. *Bulletin - Seismological Society of America*, 78(5):1725–1743.

Kahraman, S. (2002). The effects of fracture roughness on p-wave velocity. *Engineering Geology*, 63(3-4):347–350.

Karamzadeh, N., Doloei, G. J., and Reza, A. M. (2012). Automatic earthquake signal onset picking based on the continuous wavelet transform. *IEEE Transactions on Geoscience and Remote Sensing*, 51(5):2666–2674.

Kendall, J.-M., Butcher, A., Stork, A. L., Verdon, J. P., Luckett, R., and Baptie, B. J. (2019). How big is a small earthquake? challenges in determining microseismic magnitudes. *First Break*, 37(2):51–56.

Kendall, M., Maxwell, S., Foulger, G., Eisner, L., and Lawrence, Z. (2011). Microseismicity: Beyond dots in a box - Introduction.

Kettlety, T., Verdon, J. P., Werner, M. J., Kendall, J. M., and Budge, J. (2019). Investigating the role of elastostatic stress transfer during hydraulic fracturing-induced fault activation. *Geophysical Journal International*, 217(2):1200–1216.

Kovaleva, Y., Ostadhassan, M., Tamimi, N., and Kovalev, A. (2018). A preliminary optimization of borehole microseismic array design with a multiple criteria decision analysis. *Journal of Applied Geophysics*, 157:87–95.

Krige, D. G. (1951). A statistical approach to some basic mine valuation problems on the witwatersrand. *Journal of the Southern African Institute of Mining and Metallurgy*, 52(6):119–139.

Krischer, L., Megies, T., Barsch, R., Beyreuther, M., Lecocq, T., Caudron, C., and Wassermann, J. (2015). ObsPy: A bridge for seismology into the scientific Python ecosystem. *Computational Science and Discovery*, 8(1).

Kristiansen, T. G., Barkved, O., Pattillo, P., et al. (2000). Use of passive seismic monitoring in well and casing design in the compacting and subsiding valhall field, north sea. In *SPE European Petroleum Conference*. Society of Petroleum Engineers.

Kuang, W., Zhang, W., and Zhang, J. (2013). Locating microseismic events with s-wave data only. In *SEG Technical Program Expanded Abstracts 2013*, pages 2243–2247. Society of Exploration Geophysicists.

Küperkoch, L., Meier, T., Lee, J., Friederich, W., and Group, E. W. (2010). Automated determination of P-phase arrival times at regional and local distances using higher order statistics. *Geophysical Journal International*, 181(2):1159–1170.

Leonard, M. (2000). Comparison of manual and automatic onset time picking. *Bulletin of the Seismological Society of America*, 90(6):1384–1390.

Leonard, M. and Kennett, B. L. N. (1999). Multi-component autoregressive techniques for the analysis of seismograms. *Physics of the Earth and Planetary Interiors*, 113(1-4):247–263.

Li, H. and Chang, X. (2020). A review of the microseismic focal mechanism research. *Science China Earth Sciences*, pages 1–13.

Li, J. and Others (2013). *Study of induced seismicity for reservoir characterization*. PhD thesis, Massachusetts Institute of Technology.

Li, S., Vladimirsky, A., and Fomel, S. (2013). First-break traveltime tomography with the double-square-root eikonal equation. *Geophysics*, 78(6):U89–U101.

Li, X., Shang, X., Wang, Z., Dong, L., and Weng, L. (2016). Identifying P-phase arrivals with noise: An improved Kurtosis method based on DWT and STA/LTA. *Journal of Applied Geophysics*, 133:50–61.

Litsey, L. R., MacBride Jr., W. L., Al-Hinai, K. M., and Dismukes, N. B. (1986). Shuaiba Reservoir Geological Study, Yibal Field, Oman. *Journal of Petroleum Technology*, 38(06):651–661.

Llewellyn, G. T., Dorman, F., Westland, J. L., Yoxtheimer, D., Grieve, P., Sowers, T., Humston-Fulmer, E., and Brantley, S. L. (2015). Evaluating a groundwater supply contamination incident attributed to Marcellus Shale gas development. *Proceedings of the National Academy of Sciences of the United States of America*, 112(20):6325–6330.

Lokajicek, T. and Klima, K. (2006). A first arrival identification system of acoustic emission (AE) signals by means of a high-order statistics approach. *Measurement Science and Technology*, 17(9):2461.

Lolla, S. V. T., Bailey, J., Costin, S., Hons, M., Liu, X., Yam, H., Akhmetov, A., Hayward, T., Brisco, C., et al. (2019). Automated surveillance of subsurface wellbore integrity in a heavy oil field using passive seismic systems. In *SPE Annual Technical Conference and Exhibition*. Society of Petroleum Engineers.

Lomax, A., Satriano, C., and Vassallo, M. (2012). Automatic picker developments and optimization: FilterPicker—A robust, broadband picker for real-time seismic monitoring and earthquake early warning. *Seismological Research Letters*, 83(3):531–540.

Lomax, A., Virieux, J., Volant, P., and Berge-Thierry, C. (2000). Probabilistic earthquake location in 3d and layered models. In *Advances in seismic event location*, pages 101–134. Springer.

Loosveld, R. J. H., Bell, A., and Terken, J. J. M. (1996). The Tectonic Evolution of Interior Oman Unit I : Basement - Pan-African Accretion in the Arabian Peninsula. *GeoArabia Middle East Petroleum Geosciences*, 1(1):28–51.

Maeda, N. (1985). A method for reading and checking phase times in autoprocessing system of seismic wave data. *Zisin*, 38:365–379.

Magotra, N., Ahmed, N., and Chael, E. (1987). Seismic event detection and source location using single-station (three-component) data. *Bulletin of the Seismological Society of America*, 77(3):958–971.

Mahajan, S., Hassan, H., Duggan, T., and Dhir, R. (2018). Compaction and Subsidence Assessment to Optimize Field Development Planning for an Oil Field in Sultanate of Oman. In *Abu Dhabi International Petroleum Exhibition & Conference*. Society of Petroleum Engineers.

Mahmoodi, Y., Kharrat, R., and Hashemi, A. (2009). Study of Thermally Assisted Gas Oil Gravity Drainage in One of Iranian Fractured Reservoirs. In *1st International Petroleum Conference and Exhibition Shiraz 2009*.

Maleki, S., Moradzadeh, A., Riabi, R. G., Gholami, R., and Sadeghzadeh, F. (2014). Prediction of shear wave velocity using empirical correlations and artificial intelligence methods. *NRIAG Journal of Astronomy and Geophysics*, 3(1):70–81.

Marsden, M. (1974). Cubic spline interpolation of continuous functions. *Journal of Approximation Theory*, 10(2):103–111.

Martinez, F. J., Batzle, M. L., and Revil, A. (2012). Influence of temperature on seismic velocities and complex conductivity of heavy oil-bearing sands. *Geophysics*, 77(3):WA19–WA34.

Masse, J. P., Borgomano, J., and Al Maskiry, S. (1998). The platform-to-basin transition of the lower Aptian (Shuaiba Formation) of the northeastern Jebel Akhdar (Sultanate of Oman). *Sedimentary Geology*, 119(3-4):297–309.

Matrullo, E., Amoroso, O., De Matteis, R., Satriano, C., and Zollo, A. (2011). 1D versus 3D velocity models for earthquake locations: a case study in Campania-Lucania region (Southern Italy). *EGU General Assembly*.

Maxwell, S. (2014). *Microseismic Imaging of Hydraulic Fracturing*. Society of Exploration Geophysicists.

Maxwell, S., Bennett, L., Jones, M., and Walsh, J. (2010a). Anisotropic velocity modeling for microseismic processing: Part 1—impact of velocity model uncertainty. In *SEG Technical Program Expanded Abstracts 2010*, pages 2130–2134. Society of Exploration Geophysicists.

Maxwell, S. C., Chorney, D., and Goodfellow, S. D. (2015). Microseismic geomechanics of hydraulic-fracture networks: Insights into mechanisms of microseismic sources. *Leading Edge*, 34(8):904–910.

Maxwell, S. C., Rutledge, J., Jones, R., and Fehler, M. (2010b). Petroleum reservoir characterization using downhole microseismic monitoring. *Geophysics*, 75(5).

Mayerhofer, M. J., Lolon, E., Warpinski, N. R., Cipolla, C. L., and Walser, D andRightmire, C. M. (2010). What is stimulated reservoir volume? *SPE Production & Operations*, 25(01):89–98.

McCormack, M. D., Zaucha, D. E., and Dushek, D. W. (1993). First-break refraction event picking and seismic data trace editing using neural networks. *Geophysics*, 58(1):67–78.

Meert, J. G. and Van Der Voo, R. (1997). The assembly of Gondwana 800-550 Ma. *Journal of Geodynamics*, 23(3-4):223–235.

Minsley, B. J., Willis, M. E., Krasovec, M. L., Burns, D. R., and Toksoz, M. N. (2004). Fracture detection using amplitude versus offset and azimuth analysis of a 3d p-wave seismic dataset and synthetic examples. Technical report, Massachusetts Institute of Technology. Earth Resources Laboratory.

Mitra, S. K. and Kaiser, J. F. (1993). *Handbook for digital signal processing*. Wiley.

Montalbetti, J. F. and Kanasewich, E. R. (1970). Enhancement of Teleseismic Body Phases with a Polarization Filter. *Geophysical Journal of the Royal Astronomical Society*, 21(2):119–129.

Mooney, W. D., Gettings, M. E., Blank, H. R., and Healy, J. H. (1985). Saudi Arabian seismic-refraction profile: a traveltime interpretation of crustal and upper mantle structure. *Tectonophysics*, 111(3-4):173–246.

Moré, J. J. (1983). Recent developments in algorithms and software for trust region methods. In *Mathematical programming The state of the art*, pages 258–287. Springer.

Murat, M. E. and Rudman, A. J. (1992). AUTOMATED FIRST ARRIVAL PICKING: A NEURAL NETWORK APPROACH 1. *Geophysical Prospecting*, 40(6):587–604.

Nabipour, M., Escrochi, M., Ayatollahi, S., Boukadi, F., Wadhahi, M., Maamari, R., and Bemani, A. (2007). Laboratory investigation of thermally-assisted gas-oil gravity drainage for secondary and tertiary oil recovery in fractured models. *Journal of Petroleum Science and Engineering*, 55(1-2):74–82.

Naess, O. E. (2006). Repeatability and 4d seismic acquisition. In *SEG Technical Program Expanded Abstracts 2006*, pages 3300–3304. Society of Exploration Geophysicists.

Negreiros, J. G., Painho, M., Aguilar, F. J., and Aguilar, M. A. (2010). A comprehensive framework for exploratory spatial data analysis: Moran location and variance scatterplots. *International Journal of Digital Earth*, 3(2):157–186.

Nelder, J. A. and Mead, R. (1965). A simplex method for function minimization. *The computer journal*, 7(4):308–313.

Nguyen, V. X., Abousleiman, Y. N., and Hoang, S. (2009). Analyses of Wellbore Instability in Drilling Through Chemically Active Fractured-Rock Formations. *SPE Journal*, 14(02):283–301.

Nussbaumer, R., Mariethoz, G., Gravey, M., Gloaguen, E., and Holliger, K. (2018). Accelerating sequential gaussian simulation with a constant path. *Computers & Geosciences*, 112:121–132.

Obert, L. and Duvall, W. I. (1945). *The microseismic method of predicting rock failure in underground mining*. US Department of the Interior, Bureau of Mines.

Okamoto, K., Yi, L., Asanuma, H., Okabe, T., Abe, Y., and Tsuzuki, M. (2018). Triggering processes of microseismic events associated with water injection in Okuaizu Geothermal Field, Japan.

Olea, R. A. (2006). A six-step practical approach to semivariogram modeling. *Stochastic Environmental Research and Risk Assessment*, 20(5):307–318.

Oliver, M. A. and Webster, R. (1990). Kriging: a method of interpolation for geographical information systems. *International Journal of Geographical Information System*, 4(3):313–332.

Omre, H. (1984). The variogram and its estimation. In *Geostatistics for natural resources characterization*, pages 107–125. Springer.

Osborn, S. G., Vengosh, A., Warner, N. R., and Jackson, R. B. (2011). Methane contamination of drinking water accompanying gas-well drilling and hydraulic fracturing. *Proceedings of the National Academy of Sciences of the United States of America*, 108(20):8172–8176.

Osher, S. (1993). A level set formulation for the solution of the dirichlet problem for hamilton–jacobi equations. *SIAM Journal on Mathematical Analysis*, 24(5):1145–1152.

Ouria, A. and Toufigh, M. M. (2009). Application of nelder-mead simplex method for unconfined seepage problems. *Applied Mathematical Modelling*, 33(9):3589–3598.

Park, C. B., Miller, R. D., and Xia, J. (1999). Multichannel analysis of surface waves. *Geophysics*, 64(3):800–808.

Paul Young, R. and Martin, C. (1993). Potential role of acoustic emission/microseismicity investigations in the site characterization andperformance monitoring of nuclear waste repositories. *International Journal of Rock Mechanics & Mining Sciences & Geomechanics Abstracts*, 30(7):797–803.

Pawar, R. J., Bromhal, G. S., Carey, J. W., Foxall, W., Korre, A., Ringrose, P. S., Tucker, O., Watson, M. N., and White, J. A. (2015). Recent advances in risk assessment and risk management of geologic co2 storage. *International Journal of Greenhouse Gas Control*, 40:292–311.

Peng, P. and Wang, L. (2019). Targeted location of microseismic events based on a 3d heterogeneous velocity model in underground mining. *PloS one*, 14(2):e0212881.

Penney, R. K., Baqi Al Lawati, S., Hinai, R., Van Ravesteijn, Oscar P andRawnsley, K., Putra, P. H., Geneau, M. D., Ikwumonu, A., Harrasy, HaythemandAl-Habsi, M., et al. (2007). First full field steam injection in a fractured carbonate at qarn alam, oman. In *SPE Middle East Oil and Gas Show and Conference*. Society of Petroleum Engineers.

Peters, J. M., Filbrandt, J. B., Grotzinger, J. P., Newall, M. J., Shuster, M. W., and Al-Siyabi, H. A. (2003). Surface-piercing salt domes of interior North Oman, and their significance for the Ara carbonate 'stringer' hydrocarbon play. *GeoArabia*, 8(2):231–270.

Piccinelli, F. G., Mucciarelli, M., Federici, P., and Albarello, D. (1995). The microseismic network of the Ridracoli Dam, North Italy: Data and interpretations. *Pure and Applied Geophysics PAGEOPH*, 145(1):97–108.

Plesinger, A., Hellweg, M., and Seidl, D. (1986). Interactive high-resolution polarization analysis of broad-band seismograms. *Journal of Geophysics*, 59(2):129–139.

Pratt, Brian and D. Smewing, J. (1993). Early Cretaceous platform-margin configuration and evolution in the central Oman mountains, Arabian peninsula. *American Association of Petroleum Geologists Bulletin*, 77(2):225–244.

Pyrak-Nolte, L. J., Myer, L. R., and Cook, N. G. (1990). Anisotropy in seismic velocities and amplitudes from multiple parallel fractures. *Journal of Geophysical Research: Solid Earth*, 95(B7):11345–11358.

Pyrcz, M. and Deutsch, C. (2018). Transforming data to a gaussian distribution. *Geostatistics Lessons. Retrieved from http://geostatisticslessons.com/lessons/normalscore Geostatistics-Lessons.com*.

R. Lynn Kirlin, W. J. D. (1999). *Covariance Analysis for Seismic Signal Processing*, chapter 2, page 9. Society of Exploration Geophysicists.

Rahmoune, R., Sulaimani, M., Stammeijer, J., Azri, S., van Gilst, R., Mahruqi, A., Aghbari, R., and Belghache, A. (2021). Multitemporal sar interferometry for monitoring of ground deformations caused by hydrocarbon production in an arid environment: Case studies from the sultanate of oman. *The Leading Edge*, 40(1):45–51.

Rameil, N., Immenhauser, A., Csoma, A. É., and Warrlich, G. (2012). Surfaces with a long history: The Aptian top Shu'aiba Formation unconformity, Sultanate of Oman. *Sedimentology*, 59(1):212–248.

Rawnsley, K., Gharbi, M., Breiki, M., Bettembourg, S., Putra, P., Sheheimi, A., Maamari, H., Yahyaai, F., Ismaili, I., and Ma'Mary, T. (2013). Fracture modelling & reservoir management of the first full field TAGOGD project with implications for future developments. In *2nd EAGE Workshop Naturally Fractured Reservoirs: Naturally Fractured Reservoirs in Real Life*.

Rawnsley, K., Hadhrami, F., Kok, A., Moosa, R., Swaby, P., Dhahab, S., Bettembourg, S., Engen, G., Richard, P., De Keijzer, M., Penney, R., Boerrigter, P., Pribnow, D., Koning, M., and Hillgartner, H. (2005). Accelerated understanding and modeling of a complex fractured heavy-oil reservoir, oman, using a new 3D fracture-modeling tool. In *2005 International Petroleum Technology Conference Proceedings*, pages 111–116. International Petroleum Technology Conference.

Reading, A. M., Mao, W., and Gubbins, D. (2001). Polarization filtering for automatic picking of seismic data and improved converted phase detection. *Geophysical Journal International*, 147(1):227–234.

Rollinson, H., Searle, M., Abbasi, I., Al-Lazki, A., and Al Kindi, M. (2014). *Tectonic Evolution of the Oman Mountains*, volume 392. Geological Society of London.

Rouy, E. and Tourin, A. (1992). A viscosity solutions approach to shape-from-shading. *SIAM Journal on Numerical Analysis*, 29(3):867–884.

Ruud, B. O. and Husebye, E. S. (1992). A new three-component detector and automatic single-station bulletin production. *Bulletin of the seismological society of America*, 82(1):221–237.

Sabrian, T. A., Saad, R., Saidin, M., Muhammad, S. B., and Yusoh, R. (2018). Empirical Approach in Developing Vs/Vp Ratio for Predicting S-Wave Velocity, Study Case; Sungai Batu, Kedah. In *Journal of Physics: Conference Series*, volume 995, page 12089. IOP Publishing.

Sambridge, M. S. and Kennett, B. L. (2001). Seismic event location: nonlinear inversion using a neighbourhood algorithm. *Pure and Applied Geophysics*, 158(1):241–257.

Santos, R. G., Loh, W., Bannwart, A. C., and Trevisan, O. V. (2014). An overview of heavy oil properties and its recovery and transportation methods. *Brazilian Journal of Chemical Engineering*, 31(3):571–590.

Saragiotis, C. D., Hadjileontiadis, L. J., and Panas, S. M. (2002). PAI-S/K: A robust automatic seismic P phase arrival identification scheme. *IEEE Transactions on Geoscience and Remote Sensing*, 40(6):1395–1404.

Sarkar, S. (2008). *Reservoir monitoring using induced seismicity at a petroleum field in Oman*. PhD thesis, Massachusetts Institute of Technology.

Schorlemmer, D., Wiemer, S., and Wyss, M. (2005). Variations in earthquake-size distribution across different stress regimes. *Nature*, 437(7058):539–542.

Schröder, S., Schreiber, B. C., Amthor, J. E., and Matter, A. (2003). A depositional model for the terminal Neoproterozoic - Early Cambrian Ara Group evaporites in south Oman. *Sedimentology*.

Scott, R. W. (1990). Chronostratigraphy of the Cretaceous carbonate shelf, southeastern Arabia. *Geological Society Special Publication*, 49:89–108.

Searle, M. and Cox, J. (1999). Tectonic setting, origin, and obduction of the Oman ophiolite. *Geological Society of America Bulletin*, 111.

Sena, C. M., John, C. M., Jourdan, A.-L., Vandeginste, V., and Manning, C. (2014). Dolomitization of Lower Cretaceous Peritidal Carbonates By Modified Seawater: Constraints From Clumped Isotopic Paleothermometry, Elemental Chemistry, and Strontium Isotopes. *Journal of Sedimentary Research*, 84(7):552–566.

Sethian, J. A. (1996). A fast marching level set method for monotonically advancing fronts. *Proceedings of the National Academy of Sciences*, 93(4):1591–1595.

Sethian, J. A. and Popovici, A. M. (1999). 3-d traveltime computation using the fast marching method. *Geophysics*, 64(2):516–523.

Sharma, B. K., Kumar, A., and Murthy, V. M. (2010). Evaluation of seismic events detection algorithms. *Journal of the Geological Society of India*, 75(3):533–538.

Shearer, P. M. (2009). *Introduction to Seismology*. Cambridge University Press, Cambridge, 2 edition.

Sherwood, O. A., Rogers, J. D., Lackey, G., Burke, T. L., Osborn, S. G., and Ryan, J. N. (2016). Groundwater methane in relation to oil and gas development and shallow coal seams in the Denver-Julesburg Basin of Colorado. *Proceedings of the National Academy of Sciences of the United States of America*, 113(30):8391–8396.

Shih, X. R., Meyer, R. P., and Schneider, J. F. (1989). An automated, analytical method to determine shear-wave splitting. *Tectonophysics*, 165(1-4):271–278.

Skoumal, R. J., Brudzinski, M. R., and Currie, B. S. (2015). Earthquakes induced by hydraulic fracturing in Poland township, Ohio. *Bulletin of the Seismological Society of America*, 105(1):189–197.

Sleeman, R. and Van Eck, T. (1999). Robust automatic P-phase picking: an on-line implementation in the analysis of broadband seismogram recordings. *Physics of the earth and planetary interiors*, 113(1-4):265–275.

Smith, M. C., Goodfellow, S. D., Huang, J., Maxwell, S. C., Teff, J., Kennedy, B., and Bayliss, B. (2016). Microseismic quality control using synthetic seismograms. In *SPE/AAPG/SEG Unconventional Resources Technology Conference 2016*. Unconventional Resources Technology Conference (URTEC).

Spichak, V. and Goidina, A. (2016). Neural network estimate of seismic velocities and resistivity of rocks from electromagnetic and seismic sounding data. *Izvestiya, Physics of the Solid Earth*, 52(3):371–381.

Staněk, F., Anikiev, D., Valenta, J., and Eisner, L. (2015). Semblance for microseismic event detection. *Geophysical Journal International*, 201(3):1362–1369.

Stork, A. L., Verdon, J. P., and Kendall, J.-M. (2014). Assessing the effect of velocity model accuracy on microseismic interpretation at the in Salah Carbon Capture and Storage site. *Energy Procedia*, 63:4385–4393.

Stork, A. L., Verdon, J. P., and Kendall, J.-M. (2015). The microseismic response at the in salah carbon capture and storage (ccs) site. *International Journal of Greenhouse Gas Control*, 32:159–171.

Strohmenger, C. J., Weber, L. J., Ghani, A., Rebelle, M., Al-Mehsin, K., Al-Jeelani, O., Al-Mansoori, A., and Suwaina, O. (2004). High-resolution sequence stratigraphy of the kharaib formation (lower cretaceous, U.A.E.). In *11th ADIPEC: Abu Dhabi International Petroleum Exhibition and Conference - Conference Proceedings*, pages 637–646. Society of Petroleum Engineers.

Swindell, H. and Snell, N. S. (1977). Station processor automatic signal detection system, phase I: final report, station processor software development, Texas Instruments Report No. *ALEX (01)-FR-77-01*.

Sze, E. K.-M. (2005). *Induced seismicity analysis for reservoir characterization at a petroleum field in Oman*. PhD thesis, Massachusetts Institute of Technology.

Takanami, T. and Kitagawa, G. (1991). Estimation of the arrival times of seismic waves by multivariate time series model. *Annals of the Institute of Statistical mathematics*, 43(3):407–433.

Tang, Z., Liu, X., Li, C., Qin, P., and Xu, Q. (2018). Microseismic characteristic analysis in deep TBM construction tunnels. *Qinghua Daxue Xuebao/Journal of Tsinghua University*, 58(5):461–468.

Tarrahi, M., Jafarpour, B., and Ghassemi, A. (2015). Integration of microseismic monitoring data into coupled flow and geomechanical models with ensemble Kalman filter. *Water Resources Research*, 51(7):5177–5197.

Teanby, N., Kendall, J.-M., and Van der Baan, M. (2004). Automation of shear-wave splitting measurements using cluster analysis. *Bulletin of the Seismological Society of America*, 94(2):453–463.

Terken, J. M., Frewin, N. L., and Indrelid, S. L. (2001). Petroleum systems of Oman: Charge timing and risks. *AAPG Bulletin*, 85(10):1817–1845.

Terken, J. M. J. (1999). The Natih Petroleum System of North Oman. *GeoArabia*, 4(2).

Thakur, G. C. et al. (1997). Heavy oil reservoir management. In *Latin American and Caribbean Petroleum Engineering Conference*. Society of Petroleum Engineers.

Trnkoczy, A. (1999). Topic Understanding and parameter setting of STA/LTA trigger algorithm. *New manual of seismological observatory practice*, 2.

Tsai, Y.-H. R., Cheng, L.-T., Osher, S., and Zhao, H.-K. (2003). Fast sweeping algorithms for a class of hamilton–jacobi equations. *SIAM journal on numerical analysis*, 41(2):673–694.

Usher, P., Angus, D., and Verdon, J. (2013). Influence of a velocity model and source frequency on microseismic waveforms: some implications for microseismic locations. *Geophysical Prospecting*, 61:334–345.

Vaezi, Y. and Van der Baan, M. (2015). Comparison of the STA/LTA and power spectral density methods for microseismic event detection. *Geophysical Journal International*, 203(3):1896–1908.

van Buchem, F. S., Pittet, B., Hillgartner, H., Grötsch, J., Al Mansouri, A., Billing, I. M., Van Steenwinkel, M., Droste, H. J., and Oterdoom, H. W. (2002). High-Resolution Sequence Stratigraphic Architecture of Barremian-Aptian Carbonate Systems in Northern Oman and the United Arab Emirates (Kharaib and Shu ' aiba Formations). *Geoarabia*, 7(3):enclosure.

Van Dok, R. R., Tamimi, N., Fuller, B. N., and Mahrer, K. D. (2016). Do you truly know your geophone's orientation and should you care? In *SEG Technical Program Expanded Abstracts*, volume 35, pages 2647–2651. Society of Exploration Geophysicists.

Verdon, J. (2011). Microseismic monitoring and geomechanical modeling of CO2 storage in subsurface reservoirs. *GEOPHYSICS*, 76(5):Z102–Z103.

Verdon, J., Kendall, J.-M., White, D., and Angus, D. (2011). Linking microseismic event observations with geomechanical models to minimise the risks of storing co2 in geological formations. *Earth and Planetary Science Letters*, 305(1-2):143–152.

Verdon, J., Kendall, J.-M., and Wüstefeld, A. (2009). Imaging fractures and sedimentary fabrics using shear wave splitting measurements made on passive seismic data. *Geophysical Journal International*, 179(2):1245–1254.

Verdon, J. P. and Kendall, J. M. (2011). Detection of multiple fracture sets using observations of shear-wave splitting in microseismic data. *Geophysical Prospecting*, 59(4):593–608.

Verly, G. (1993). Sequential gaussian cosimulation: a simulation method integrating several types of information. In *Geostatistics Troia'92*, pages 543–554. Springer.

Vidale, J. E. (1986). Complex polarization analysis of particle motion. *Bulletin of the Seismological Society of America*, 76(5):1393–1405.

Vilarrasa, V. (2016). The role of the stress regime on microseismicity induced by overpressure and cooling in geologic carbon storage. *Geofluids*, 16(5):941–953.

Vinje, V., Iversen, E., and Gjøystdal, H. (1993). Traveltime and amplitude estimation using wavefront construction. *Geophysics*, 58(8):1157–1166.

Visser, W. (1991). Burial and thermal history of Proterozoic source rocks in Oman. *Precambrian Research*, 54(1):15–36.

Vizuett, K. C. A. and Davis, T. (2017). Application of the seismic quality factor versus offset and azimuth (qvoa) for fractured reservoir characterization. *First Break*, 35(10).

Wadati, K. and Oki, S. (1933). On the travel time of earthquake waves.(part ii). *Journal of the Meteorological Society of Japan. Ser. II*, 11(1):14–28.

Waldhauser, F. and Ellsworth, W. L. (2000). A double-difference earthquake location algorithm: Method and application to the northern hayward fault, california. *Bulletin of the Seismological Society of America*, 90(6):1353–1368.

Walters, R. and Zoback, M. D. (2013). Microseismicity and surface deformation of a heavy oil reservoir undergoing cyclic steam stimulation. In *Society of Exploration Geophysicists International Exposition and 83rd Annual Meeting, SEG 2013: Expanding Geophysical Frontiers*, pages 2218–2222. Society of Exploration Geophysicists.

Warpinski, N. R., Waltman, C. K., Du, J., Ma, Q., et al. (2009). Anisotropy effects in microseismic monitoring. In *SPE annual technical conference and exhibition*. Society of Petroleum Engineers.

Warrlich, G. M., Richard, P. D., Johnson, T. E., Wassing, L. B. M., Gittins, J. D., Ali, A. L., Alexander, D. M., and Murshi, A. R. (2009). From data acquisition to simulator: Fracture modeling a carbonate heavy-oil reservoir (Lower Shuaiba, Sultanate of Oman). In *SPE Middle East Oil and Gas Show and Conference, MEOS, Proceedings*, volume 3, pages 1046–1057. Society of Petroleum Engineers.

Whaley, J. (2008). The Heavy Oil Conundrum. *GEOEXPRO*, pages Vol. 5, No. 6.

Wilson, A. et al. (2013). Reservoir management for world's first thermal gas/oil gravity-drainage project. *Journal of Petroleum Technology*, 65(03):140–143.

Winder, S. (2002). *Analog and Digital Filter Design*. Elsevier.

Withers, M., Aster, R., Young, C., Beiriger, J., Harris, M., Moore, S., and Trujillo, J. (1998). A comparison of select trigger algorithms for automated global seismic phase and event detection. *Bulletin of the Seismological Society of America*, 88(1):95–106.

Wu, B., Doble, R., Turnadge, C., and Mallants, D. (2016). Well Failure Mechanisms and Conceptualisation of Reservoir-Aquifer Failure Pathways. In *SPE Asia Pacific Oil & Gas Conference and Exhibition*. Society of Petroleum Engineers.

Wuestefeld, A., Al-Harrasi, O., Verdon, J. P., Wookey, J., and Kendall, J. M. (2010). A strategy for automated analysis of passive microseismic data to image seismic anisotropy and fracture characteristics. *Geophysical Prospecting*, 58(5):755–773.

Xia, J. and Miller, R. D. (1998). Hum Filter: Power-Line Noise Eliminator for Shallow Seismic Data. In *Symposium on the Application of Geophysics to Engneering and Environmental Problems*, pages 1043–1052.

Yang, C., Luo, Z., Hu, G., and Liu, X. (2007). Application of a microseismic monitoring system in deep mining. *Journal of University of Science and Technology Beijing: Mineral Metallurgy Materials (Eng Ed)*, 14(1):6–8.

Yang, Z.-x., Chen, Y.-t., and Zhang, H.-z. (2002). Relocation and seismogenic structure of the 1998 zhangbei-shangyi earthquake sequence. *Acta Seismologica Sinica*, 15(4):383–394.

Yilmaz, Ö. (2001). *Seismic Data Analysis*. Society of Exploration Geophysicists.

Yu, T. H., Mitra, S. K., and Babic, H. (1990). Design of linear phase FIR notch filters. *Sadhana*, 15(3):133–155.

Yue, T. and Xiao-Fei, C. (2005). A rapid and accurate two-point ray tracing method in horizontally layered velocity model. *Acta Seismologica Sinica*, 18(2):154–161.

Yuko, K. and Kazuo, F. (2001). Some Predictions of Possible Unconventional Hydrocarbons Availability Until 2100. In *SPE Asia Pacific Oil and Gas Conference and Exhibition held in Jakarta, Indonesia, 17–19 April 2001*, volume 5, pages 1–10.

Zhang, C., Qiao, W., Che, X., Lu, J., and Men, B. (2019). Automated microseismic event location by amplitude stacking and semblance. *Geophysics*, 84(6):KS191–KS210.

Zhang, H., Thurber, C., and Rowe, C. (2003). Automatic P-wave arrival detection and picking with multiscale wavelet analysis for single-component recordings. *Bulletin of the Seismological Society of America*, 93(5):1904–1912.

Zhang, J., Liu, H., Zou, Z., and Huang, Z. (2015). Velocity modeling and inversion techniques for locating microseismic events in unconventional reservoirs. *Journal of Earth Science*, 26(4):495–501.

Zhang, Z., Du, J., and Gao, F. (2018). Simultaneous inversion for microseismic event location and velocity model in Vaca Muerta FormationSimultaneous microseismic inversion. *Geophysics*, 83(3):KS23—-KS34.

Zhao, H. (2005). A fast sweeping method for eikonal equations. *Mathematics of computation*, 74(250):603–627.

Zhou, Y., Yue, H., Kong, Q., and Zhou, S. (2019). Hybrid Event Detection and Phase-Picking Algorithm Using Convolutional and Recurrent Neural Networks. *Seismological Research Letters*, 90(3):1079–1087.

Zhu, H. H. X. (2016). Microseismic data analysis in unconventional oil and gas exploration. In *SPG/SEG 2016 International Geophysical Conference, Beijing, China, 20-22 April 2016*, pages 457–458. Society of Exploration Geophysicists.